Nanoscale simulation of crystal defects with application to mantle minerals

Richard Skelton

Submitted: March 2018

A thesis submitted for the degree of Doctor of Philosophy of The Australian National University

The work that appears in this thesis, excepted where otherwise noted, is my own. I have written all of the content in each chapter, and made all of the figures, with comments and proof-reading by supervisors Andrew Walker and Ian Jackson. The `disloPy` code base was developed by me, in discussion with Andrew Walker. I have run all simulations reported on in this thesis.

Signed: Richard Skelton

Word count (not including references): 56,502

Word count (including references): 65,065

Acknowledgements

Many of the computational simulations presented in this thesis were performed on the Terrawulf cluster, a computational facility supported through the AuScope initiative. AuScope Ltd is funded under the National Collaborative Research Infrastructure Strategy (NCRIS), an Australian Commonwealth Government Programme. Special thanks are due to Herb McQueen and Julian Byrne for assistance in compiling DFT codes on Terrawulf. This work also used the ARCHER UK National Supercomputing Service (http://www.archer.ac.uk). During my the PhD, I was supported by an Australian Government Research Training Program (RTP) scholarship, as well as a University Research Scholarship from the ANU and the Jaeger Scholarship, awarded by the Research School of Earth Sciences.

I would like to thank my supervisors, especially Ian Jackson and Andrew Walker. I first met Ian in February of 2011, to work on an experimental project measuring attenuation due to anelastic and viscoelastic relaxation mechanisms in polycrystalline Fo90 olivine. The experience ignited an lasting interest in the physics of multi-lattice crystals, while the 2am experiments in the freezing Canberra winter ensured that this passion would be indulged primarily through computational simulations. Andrew's willingness to supervise me remotely, first for an Honors year project and, later, for this PhD project provided me with the opportunity to enter the world of computational mineral physics. It has been an unusual arrangement, and one that would not have worked without supervisors of the caliber of Ian and Andrew. They have given me the freedom to determine my own research directions, and the guidance to ensure that this does not result in (complete) chaos.

I would also like to acknowledge Maree Coldrick, the patron saint of RSES, my fellow PhD students, especially Morgan, Kathryn, Jen and Jess, Jo, Chris, and Abdulwaheed, for creating a healthy and supportive environment, my parents for supporting and encouraging me from a young age to pursue my love of science, and my wife, Milly Coman, for being my constant companion from start to finish. Without her, this would have been a far more dreary affair.

Abstract

Minor and trace elements can influence the chemical and physical properties of the Earth's mantle, whether by forming separate minerals that can host trace elements at far higher concentrations than major mantle minerals, or by influencing physical properties of major minerals, for instance by enhancing diffusion or pinning topological defects. The present study uses atomistic computational modeling to investigate the properties of calcium phosphate minerals at mantle pressures, and to determine if cation vacancies can lubricate dislocation glide in mantle minerals.

With their large, high-coordination cation sites, calcium phosphate minerals can potentially dissolve large quantities of incompatible elements, and may be an important mantle reservoirs for these elements. Quantum mechanical calculations are used to determine the variation of structure and properties of apatite, a common low-pressure phosphate, with the identity of its channel anion. The crystal structure and compressibility are both found to vary substantially with channel anion identity.

Tuite, which forms by the breakdown of apatite at high pressure, may extend the phosphorous cycle beyond the stability field of apatite and into the lower mantle. DFT calculations are used to show that the pressure at which apatite decomposes to form tuite is sensitive to the identity of the channel anion. The calculated bulk moduli of the calcium-hosting sites in tuite are considerably lower than those of the M site in $CaSiO_3$ perovskite (cpv). Atomistic calculations show that strontium and barium impurities partition strongly from cpv into tuite.

The second part of this thesis considers the role that dislocations play in hosting vacancy-related defects, and influence that these segregated defects may have on the rheology of

mantle minerals. Interatomic potentials are used to calculate energies for the segregation of bare and protonated cation defects to dislocation cores in MgO and forsterite. Vacancies segregate strongly to [100](010) and [001](010) dislocations in forsterite. [100](010) edge dislocations serve as particularly suitable hosts for vacancies on the M1 sub-lattice, while vacant M2 sites, which are energetically unfavorable in the unstrained bulk lattice are more common around [001](010) edge dislocations. Similarly, both $\{\square_{Mg}\}''$ and $\{2H_{Mg}\}^{X}$ defects segregate strongly to all of the major dislocation slip systems in MgO. For both minerals, cation vacancies will be far higher at dislocation core sites than in the unstrained lattice.

Peierls-Nabarro calculations, parameterized using generalized stacking fault energies calculated using plane-wave density functional theory, show that protonated vacancies increase dislocation core widths and reduce the Peierls stresses in MgO. Bare Mg vacancies, especially those on the M2 sub-lattice, similarly reduce γ-line energies and Peierls stresses for the dislocations in olivine. The magnitude of this decrease depends strongly on dislocation and the type of the lattice site (i.e. M1 or M2). Concentrations of vacancy related defects are likely to be elevated particularly in mantle wedge, due to the combination of oxidizing conditions and the availability of liquid water from dehydrating phases in the subducting slab, and changes in the olivine deformation fabric in these regions match those predicted in this study.

Table of Contents

Chapter I. Introduction

I.1 Trace elements and defects in the mantle

In the widely used pyrolite model for mantle composition (Ringwood 1975), the chemistry of the Earth's mantle is dominated by SiO_2, MgO, FeO, CaO, and Al_2O_3, with smaller amounts of Na_2O, TiO_2, and Cr_2O_3. The study of the physical and chemical properties of the mantle is thus predominantly the study of the mineral phases formed by these oxides. Nevertheless, minor and even trace elements can also have a substantial impact on the properties of the Earth's mantle. Where sufficiently abundant to form separate phases, their often radically different crystal chemistry allows them to be a major - even dominant - factor in the dispersal of trace elements (e.g. Bodinier et al. 1996; O'Reilly and Griffin 2000; König et al. 2015). However, even when present as point defects in major phases, these elements may still strongly influence the properties of the mantle, for example, by changing the electrical conductivity (e.g. Dobson and Brodholt 2000; Wang et al. 2006a; Dai and Karato 2009), melting temperature (e.g. Gaetani and Grove 1998), or rheology (e.g. Kronenberg and Tullis 1984; Chen et al. 1998; Faul et al. 2016) of the minerals into which they dissolve.

Phosphorous and trace element distribution in the mantle

Low-abundance elements can influence the chemistry of the mantle by forming separate phases, which may be able to incorporate trace elements at far higher concentrations than is possible in the major mantle silicates and oxides, allowing them to have a potentially greater impact on mantle geochemistry than their overall abundance would suggest. For

instance, the concentration of siderophile elements such as Se and Te in peridotite has been found to be almost entirely controlled by the presence of volumetrically minor sulfides and platinum-group metal phases (see e.g. Lorand and Alard 2010; König et al. 2015). Similarly, calcium phosphate minerals, with their large, highly flexible cation sites, are important hosts for the rare earth elements (REEs), Sr, and the actinides (Pan and Fleet 2002). Indeed, the solubility of REEs is high enough that the presence of apatite in igneous rocks can significantly perturb REE trends (e.g. Watson and Capabianco 1981).

At high pressure, apatite decomposes to form tuite, γ-$Ca_3(PO_4)_2$ (Konzett and Frost 2009), which is thought to be present in some regions of the Earth's deep mantle (Murayama et al. 1986). Like other phosphate minerals, including apatite, tuite has cation sites which are large, flexible, and high coordinated, making it potentially a good host for a wide range of trace elements, including U, Sr, and REEs (Sugiyama and Tokonami 1987) with measured solubilities under ambient conditions similar to those in apatite (Zhai et al. 2014). Tuite is thus expected to play a role in extending the phosphorous cycle beyond the stability field of apatite and into the lower mantle. However, despite the importance of tuite and other calcium phosphate phases, little is known about the structure and stability of tuite at pressures relevant to the Earth's lower mantle. Due to high solubility of the actinides in tuite (Zhai et al. 2014), its presence may locally enrich the mantle in U and Th, with consequent local increases in the production of radiogenic heat.

Hydrous weakening of mantle minerals

Magnesium-rich olivine (with composition approximately $(Mg_{0.9},Fe_{0.1})_2SiO_4$) is the primary mineral phase in the Earth's upper mantle, which is up to 60-70 % olivine, by volume.

Although olivine, like many other mantle minerals, is nominally anhydrous, it can host water (as hydroxyl, $(OH)^-$) at low to moderate concentrations (10-1000 ppmw) under mantle conditions (e.g. Peslier 2010). However, even at low concentrations, hydrous defects can substantially alter the properties of olivine, increasing diffusion in the bulk and at grain boundaries (see e.g. Costa and Chakraborty 2008), changing the relative strengths of different slip systems (Katayama and Karato 2008), and increasing strain rates (e.g. Mackwell et al. 1985). Such hydrolytic weakening is expected to have a substantial effect on the dynamics of the Earth's upper mantle, yet the mechanisms by which it occurs remains poorly understood. When Nabarro-Herring (i.e. lattice diffusion) creep dominates, the weakening mechanism is clear, as hydrous defects increase effective vacancy concentrations and hence diffusion coefficients (Brodholt and Refson 2000). However, significant weakening is also seen in the dislocation creep regime, yet little is known about the ways in which hydrogen is incorporated at and interacts with dislocations in olivine (and in other mantle silicates), despite the observed segregation of water to these defects (Hiraga et al. 2004; Sommer et al. 2009). One possibility is that the hydration of olivine increases the concentration of silicon vacancies, increasing the silicon diffusion coefficient D_{Si} (Mei and Kohlstedt 2000). Dislocation climb is controlled by the diffusion of the slowest species, Si in the case of most silicates, which suggests that hydrogen incorporation may lead to enhanced climb rates. Early studies appeared to show that increased silicon diffusivity in hydrous olivine was the primary cause of hydrolytic weakening (Mackwell et al. 1985), but recent measurements of Si diffusion in a single crystal of forsterite suggest that D_{Si} may be affected far less by hydrous defects than was previously supposed (Fei et al. 2013). This difficulty may be resolved by invoking extrinsic defects, such as protonated M-

site vacancies or the “titano-clinohumite” defect, which consists of two hydrogen atoms located on a Si site and a Ti atom occupying an adjacent M site (Berry et al. 2005; Berry et al. 2007a; Walker et al. 2007). Deformation experiments show that Ti-doped Fo_{90} olivine deforms at higher strain upon hydration to form titano-clinohumite defects (Faul et al. 2016), although the possibility that higher strain rates are attributable to M-site vacancies charge-balancing Fe^{3+} cannot be excluded, given the high fO_2 in platinum wrapped olivine samples (Faul et al. 2017).

Guided by observed changes in lattice preferred orientation (LPO) under hydrous and anhydrous conditions, Katayama and Karato (2008) used high-stress deformation experiments at 2 GPa to show that hydrolytic weakening of olivine also occurs in the exponential creep regime. It has been suggested that interactions between hydrous defects and the dislocation core may enhance dislocation mobility in this creep regime by reducing the Peierls stress, σ_p, required to initiate dislocation glide. By fitting their creep data to an exponential flow law, Katayama and Karato (2008) calculated the σ_p of hydrous olivine to be in the range 1.6-2.9 GPa, compared with a value of 9.1 GPa obtained in an earlier micro-indentation study for dry olivine (Evans and Goetze 1979). A recent study at lithospheric P and lower fH_2O failed to replicate this result, suggesting that high water fugacity may be necessary for hydrolytic weakening in the exponential creep regime (Tielke et al. 2017).

The reduction of flow stresses in the glide-creep regime by point defect-dislocation interactions is of interest outside of the Earth's mantle. For example, increasing the O/U ratio of UO_2, an important fuel material in nuclear reactors, by incorporation of oxygen at interstitial sites changes the relative activities of the primary slip systems (Yust and

McHargue 1971; Seltzer et al. 1972; Keller et al. 1988) and reduces flow strength considerably (Nadeau 1969). Molecular dynamics simulations likewise find that the critical resolved shear stress of dislocations in UO_2 decreases with the concentration of oxygen interstitial defects in stoichiometric UO_2 (Fossati et al. 2013). Electron microscopy has shown that oxygen interstitial defects frequently segregate to dislocation cores in UO_2, and it has been proposed that these defects interact with the dislocation during glide to reduce the energy of intermediate structures, thereby decreasing the Peierls stress (Ashbee and Yust 1982).

I.2 Modeling dislocations

Introduction to dislocations

Dislocations are linear topological defects present in crystals that act as carriers of plastic strain, and are required to explain critical stresses which are orders of magnitude smaller than the shear modulus (e.g. Hirth and Lothe 1982). They are of importance in materials science and geophysics, as they permit plastic deformation to occur at much lower stresses than predicted from slip models. With their large stress fields, edge dislocations often serve as sinks for impurity atoms, as well as fast diffusion pathways (“pipe diffusion”). These large stress fields make them vulnerable to etching where they intersect surfaces, as the removal of material from a dislocation core releases accumulated strain energy, facilitating dissolution through the formation of etch pits (e.g. McLean and Hirth 1968; Brantley et al. 1986; MacInnis and Brantley 1992).

In the original construction of Volterra (Volterra 1907; Taylor 1938), a dislocation is created by introducing a cut into an elastic continuum and displacing the material on either side of

the newly introduced surface. If the displacement vector is normal to the cut line, the dislocation is said to be an edge dislocation, while a dislocation with the displacement vector parallel to the cut line is a screw dislocation. Rotational discontinuities can also be

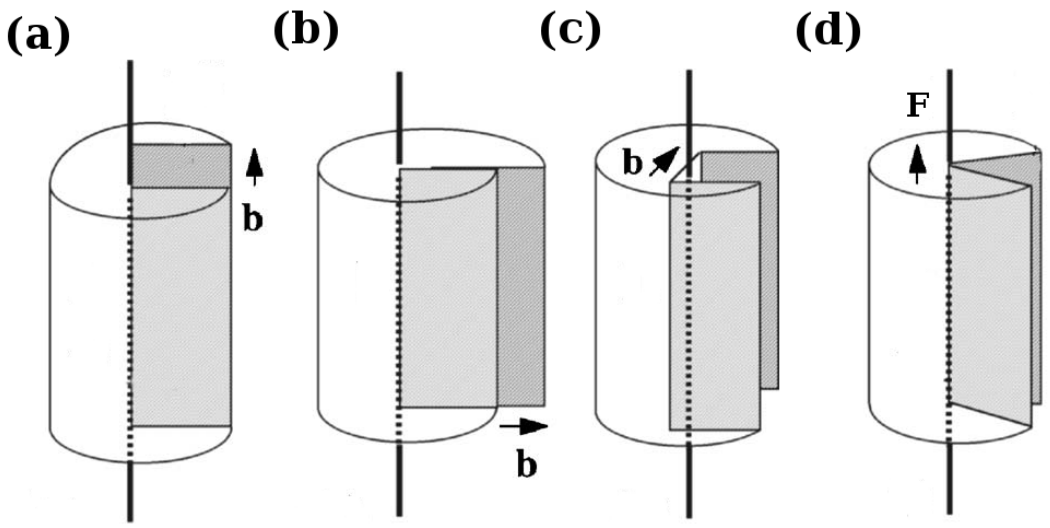

Fig. I.1 Volterra constructions of (a) screw and (b, c) edge dislocations with Burgers vector **b**, and (d) a wedge disclination with Frank vector **F** (modified after Klemen and Friedel 2008).

introduced (Fig. I.1), which are called disclinations. As the displacement induced by a disclination diverges at large *r*, the energies associated with disclinations are much larger than those of dislocations, and isolated disclinations do not occur in real crystals, although they may be found in nanowires and liquid crystals. Moreover, as shown by (Li 1972; Nazarov et al. 2000ab) and recently observed in olivine by Cordier et al. (2014), walls of disclination dipoles can be found at tilt grain boundaries. A dislocation can be characterized by its line vector $\boldsymbol{\xi}$, which gives the direction of the dislocation, and a Burgers vector **b**, which gives the magnitude and direction of the displacement discontinuity (shown in Fig. I.2). For an edge dislocation, **b** and $\boldsymbol{\xi}$ are perpendicular, while they are parallel for a screw

dislocation; dislocations with **b** and ξ inclined at an angle $0 < \theta < 90°$ are said to be of mixed character. The energy per unit length of a dislocation is proportional to $|\mathbf{b}|^2$, so that common dislocations correspond to directions of short translational periodicity.

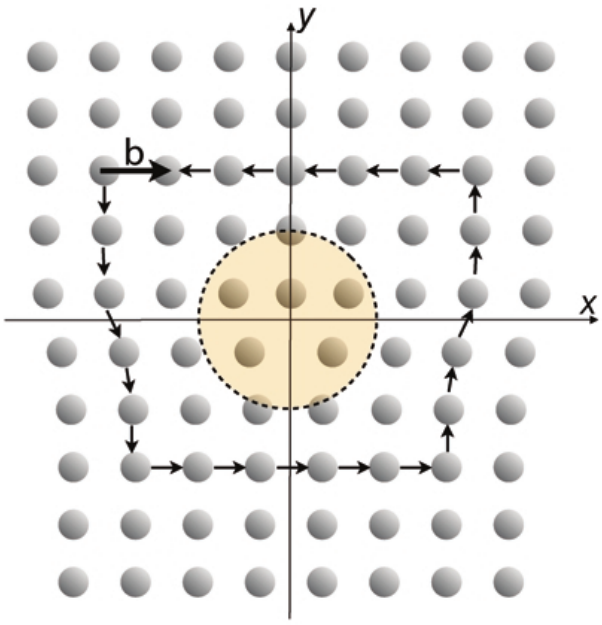

Fig. I.2 Cartoon diagram of an edge dislocation together with its Burgers circuit construction of **b** (reproduced from Walker et al. 2010). **T**he core region of the dislocation is highlighted by the colored circle.

The energy of a dislocation may be decomposed into two parts: an elastic contribution at large range due to the elastic displacement field, and a "core" term which is affected by atomic-scale relaxation near the dislocation line. The elastic contribution can be calculated using classical elasticity theory (with corrections due to non-linear elastic displacement near the dislocation line, see Clouet 2011), while the core energy is an intrinsically atomic-scale property and cannot be computed using continuum mechanics. Experimental observation of dislocation cores is also difficult, and can be done only with techniques capable of achieving atomic-scale resolution, such as transmission electron microscopy

(e.g. Metzger et al. 1998; Hytch et al. 2003). However, advances in atomistic simulation methods, such as density functional theory (DFT; Hohenberg and Kohn 1964; Kohn and Sham 1965) and molecular mechanics force-fields permit simulations of sufficient size to accurately

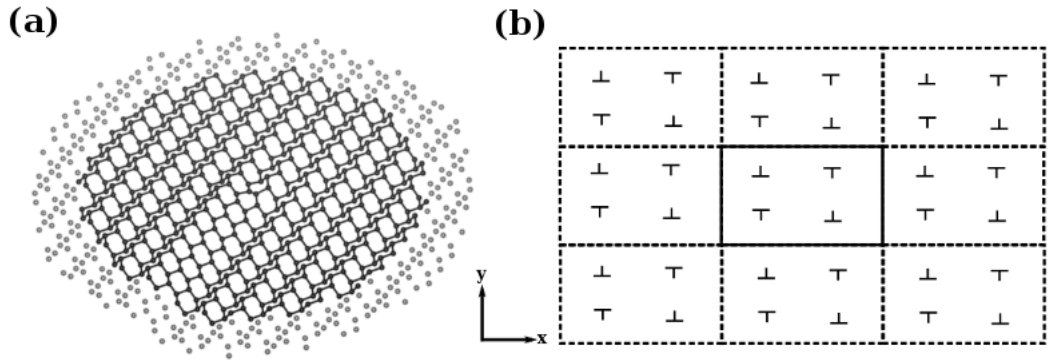

Fig. I.3 Schematic illustration of (a) a screw dislocation embedded in a 1D-periodic cluster of atoms and (b) a quadrupolar configuration of dislocation in a 3D periodic supercell with net Burgers vector 0.

reproduce dislocation core properties. Due to the discontinuity associated with a single dislocation, simulation cells must either be finite in the directions normal to $\boldsymbol{\xi}$, (the cluster-based method, illustrated in Fig. I.3a; e.g. Puls 1980; Walker et al. 2005a) or contain an even number of dislocations whose Burgers vectors sum to zero (the multipole method, illustrated in Fig. I.3b; e.g. Ismail-Beigi and Arias; Cai et al. 2003; Clouet 2009) .

Dislocations in isotropic media

Closed form analytical solutions can be derived for the displacement field $\mathbf{u}(\mathbf{x})$ around a dislocation in an isotropic medium (Hirth and Lothe 1982). For a screw dislocation, the

only non-zero component of the displacement field, **u(x)**, is parallel to the dislocation line. Adopting a coordinate system with *z* parallel to $\boldsymbol{\xi}$ and choosing the branch cut (Fig. I.1) to lie in the z-x plane and contain the positive x-axis, the Burgers circuit construction gives

$$b = \oint u_z(x,y)\,dl = \lim_{\varepsilon \to 0}\left[u_z(x,\varepsilon) - u_z(x,-\varepsilon)\right] \tag{I.1}$$

where $x > 0$ and b is the magnitude of the Burgers vector. Since the displacement field of a screw dislocation in an isotropic medium is axisymmetric (i.e. invariant under rotation θ about *z*, which is parallel to $\boldsymbol{\xi}$), $\partial u_z/\partial\theta$ is constant. This is satisfied by

$$u_z(x,y) = b\theta\frac{(x,y)}{2\pi} = \frac{b}{2\pi}\arctan\left(\frac{y}{x}\right) \tag{I.2}$$

The strain energy per unit length in a cylinder with core radius r_c is accordingly given by

$$E(r) = \frac{\pi}{\mu}\int_{r_c}^{r}\sigma_{\theta z}^2(r)\cdot r\,dr = \frac{\mu b^2}{4\cdot\pi}\ln\left(\frac{r}{r_c}\right) \tag{I.3}$$

where μ is the shear modulus of the material.

For a pure edge dislocation, **b** and $\boldsymbol{\xi}$ are perpendicular and the only non-zero components of the displacement field are u_x and u_y. Force balance requires that

$$u_x(x,y) = \frac{b}{4\pi(1-\nu)}\frac{xy}{(x^2+y^2)} - \frac{b}{2\pi}\arctan\left(\frac{x}{y}\right) \tag{I.4}$$

and

$$u_y(x,y)=\frac{-(1-2\nu)b}{8\pi(1-\nu)}\ln\left(\frac{x^2+y^2}{b^2}\right)+\frac{b}{4\pi(1-\nu)}\frac{y^2}{x^2+y^2} \qquad \text{(I.5)}$$

Using these displacement fields, it can be shown that the strain energy per unit length is

$$E(r)=\int_0^{2\pi} d\theta \int_{r_c}^{r}\left\{\frac{1}{2\mu}\sigma_{xy}^2+\frac{1}{2Y}\left(\sigma_{xx}^2+\sigma_{yy}^2-2\nu\sigma_{xx}\sigma_{yy}-\sigma_{zz}^2\right)\right\}=\frac{\mu b^2}{4\pi(1-\nu)}\ln\left(\frac{r}{r_c}\right) \qquad \text{(I.6)}$$

where Y is the Young's modulus and ν is the Poisson's ratio.

The sextic formulation for a dislocation in an anisotropic medium

The displacement field for a general dislocation in a crystal with anisotropic elasticity can be derived by noting that, around a stationary dislocation, the displacement field **u**(**x**) satisfies the equation of motion

$$\frac{\partial\sigma_{ij}}{\partial x_i}=C_{ijkl}\frac{\partial\varepsilon_{kl}}{\partial x_i}=C_{ijkl}\frac{\partial^2 u_l}{\partial x_i\partial x_k}=0 \qquad \text{(I.7)}$$

where summation over repeated indices is implied. In the sextic formulation of Stroh (1958) and outlined in detail in Hirth and Lothe (1982), the displacement field is assumed to take the form

$$\mathbf{u}(x)=\frac{D_k\mathbf{A}_k}{2\pi\imath}\log\left(\mathbf{m}\cdot\mathbf{x}+p_k\mathbf{n}\cdot\mathbf{x}\right)=\frac{D_k\mathbf{A}_k}{2\pi\imath}\log(\eta_k) \qquad \text{(I.8)}$$

where **m** and **n** are unit vectors normal to the dislocation line $\boldsymbol{\xi}$, $\mathbf{A}_k$ is an unknown vector of unit length, D_k is the magnitude of the displacement field, and $\eta_k = \mathbf{m}\cdot\mathbf{x}+p_k\mathbf{n}\cdot\mathbf{x}$, where p_k is a constant. Substituting this into the equation of motion (equation I.7), the unit vectors $\mathbf{A}_k$ satisfy

$$\{(mm)+p_k[(mn)+(nm)]+p_k^2\}\cdot\mathbf{A}_k=0 \tag{I.9}$$

with

$$(ab)_{jk}=a_i C_{ijkl} b_l \tag{I.10}$$

The p_k are the six roots of the determinant of the matrix in equation (I.9), while the vectors $\mathbf{A}_k$ are its eigenvectors. It can be shown that the roots p_k occur in pairs of complex conjugates. Finding the roots of a general sextic polynomial equation is non-trivial. However, the solution of this problem can be simplified by defining a second set of vectors as

$$\mathbf{L}_k=-\left[(nm)+p_k(nn)\right]\mathbf{A}_k \tag{I.11}$$

The $\mathbf{L}_k$ and $\mathbf{A}_k$ vectors are then combined to form

$$\boldsymbol{\zeta}_k=\begin{pmatrix}\mathbf{A}_k\\ \mathbf{L}_k\end{pmatrix} \tag{I.12}$$

which is an eigenvector of the 6×6 matrix **N** whose upper left and upper right blocks are $-(nn)^{-1}(nm)$ and $-(nn)^{-1}$, with the lower left and right blocks equal to $-[(mn)^{-1}(nn)^{-1}-(mm)]$ and $(mn)(nn)^{-1}$. The corresponding eigenvalues are the roots p_k. Although **N** is not symmetric, it does satisfy the relation

$$\mathbf{N}^T\cdot\mathbf{V}=\mathbf{V}\cdot\mathbf{N} \tag{I.13}$$

where

$$\mathbf{V}=\begin{pmatrix} 0 & \mathbf{I}_{3x3} \\ \mathbf{I}_{3x3} & 0 \end{pmatrix} \tag{I.14}$$

and $\mathbf{I}_{3x3}$ is the 3×3 identity matrix. From the symmetry of the matrix $\mathbf{V}\cdot\mathbf{N}$, it follows that the eigenvectors $\boldsymbol{\zeta}_k$ and eigenvalues p_k of $\mathbf{N}$ satisfy the relation

$$\left(p_j - p_k\right)\boldsymbol{\zeta}_j \cdot \mathbf{V} \cdot \boldsymbol{\zeta}_k = 0 \tag{I.15}$$

for $j \neq k$. Recalling the definition of $\boldsymbol{\zeta}_k$ in terms of $\mathbf{A}_k$ and $\mathbf{L}_k$, this means that

$$\mathbf{A}_j \cdot \mathbf{L}_k + \mathbf{A}_k \cdot \mathbf{L}_k = \delta_{jk} \tag{I.16}$$

where δ_{jk} is the Kronecker delta. It immediately follows that the displacement field is

$$\mathbf{u} = \frac{1}{2\pi\imath}\sum_{k=1}^{6} \pm \mathbf{A}_k\left(\mathbf{L}_k \cdot \mathbf{b}\right)\ln\eta_k \tag{I.17}$$

Using the definition of strain and, hence, stress in terms of the displacement field **u**, the radial dependence of the elastic strain energy $E(r)$ of a dislocation is

$$E(r) = \frac{1}{4\pi}\left(\imath\sum_{k=1}^{6} \pm\left[\mathbf{b}\cdot\mathbf{L}_k\right]\left[\mathbf{L}_k\cdot\mathbf{b}\right]\right)\ln\left(\frac{r}{r_c}\right) \tag{I.18}$$

The term in parentheses is sometimes referred to as the elastic energy coefficient, *K*.

Software Development:* `disloPy`*, a Python package for atomistic modeling of dislocations

A major part of this PhD project has been the development of an extensive library of Python modules (called `disloPy`; https://github.com/andreww/disloPy) designed to

perform dislocation simulations using the cluster-based and supercell methods, as well as the semi-discrete Peierls-Nabarro model. The basic structures and simulation types have been implemented as Python classes, so that subclasses can be implemented with properties that are specific to the external library used to relax the atomic coordinates. This abstract implementation of the basic routines to construct clusters and supercells, with and without dislocations, makes it easier to interface the code with new atomistic simulation software, as the construction of a simulation cell is independent of how the interactions between atoms are handled. Consequently, interfacing to new simulation software requires only functions to parse an input file containing the simulation parameters and unit cell geometry, extracting the unit cell parameters and atomic coordinates, and routines to take the dislocated simulation cell constructed by `disloPy` and convert it into a format accepted by the atomic simulation code.

The geometrical part of the software is built on hierarchy of classes, which are abstractions of the important geometrical properties of a crystal. The foundation is the `Atom`, which has an element symbol and two sets of coordinates associated with it, corresponding to its location in a perfect and dislocated crystal. A `Basis` object contains a list of `Atom`s, and may have an associated displacement field. Associating a `Basis` with a `Lattice` object creates a `Crystal`, which is the typical class manipulated by routines that set up supercell calculations. `PeriodicCluster` is a specialized subclass of **`Basis`** which is 1D periodic, and has a defined cell length. A `TwoRegionCluster` is a subclass of `PeriodicCluster` which has been divided into two radially concentric lists of atoms, which are the free (region I) and fixed (region II) regions in a cluster-based calculation.

For instance, `disloPy` contains routines to interface with the molecular statics code GULP (Gale 1997; Gale and Rohl 2003) by implementing a `GulpAtom` class that inherits all of the variables and function definitions contained in `Atom`, but has additional member variables and functions that handle atomic properties specific to the GULP implementation of atoms. In particular, the `GulpAtom` class has the member variable `GulpAtom.shell_coordinates`, which record the location of a shell relative to the atomic core (and takes the value `None` if the atom does not have a shell), as well as a suite of functions designed to handle shell properties. Additional functions are defined to parse GULP input and output files, set GULP-specific simulation parameters, and write input files for GULP calculations. In addition to GULP, `disloPy` is presently compatible with the molecular dynamics code LAMMPS (Plimpton 1995; http://lammps.sandia.gov), and the plane-wave DFT packages QUANTUM ESPRESSO (QE; Giannozzi et al. 2009) and CASTEP (Clark et al. 2005). Further details about constructing cluster-based atomistic simulations using `disloPy` can be found in Chapter IV.

I have also implemented the Peierls-Nabarro method (Peierls 1940; Nabarro 1947) within the `disloPy` package. The software takes an input file for one of the supported atomic simulation codes and orients it such that the glide plane normal is oriented along *z*. It then constructs a supercell by tiling the unit cell along *z*, in order to minimize interactions between the stacking fault and its periodic images. For small simulation cells, a vacuum layer can be inserted at one end of the simulation cell to isolate the stacking fault. The atoms near the free surface are then fixed in place to simulate the bulk crystal structure. By

default, all other atoms are allowed to relax along *z*, although the user may specify that certain atoms (e.g. O atoms in a silicate mineral) are allowed to relax in three dimensions.

Generalized stacking fault (GSF) energies are calculated by displacing the top half of the slab of atoms cell by **u** and relaxing the atomic coordinates, subject to the applied constraints. The excess energy of the slipped cell is calculated by subtracting the energy of the supercell with **u** = **0** from that of the fully relaxed supercell. If the cell contains a vacuum layer, this is equal to the GSF energy. However, if no vacuum layer has been used, then there is an additional slip plane at z=0. In this case, the GSF energy is 1/2 the total excess energy of the slipped supercell. Calculating GSF energies for a grid of displacement vectors **u** enables us to construct a function, called a γ-line in 1D and a γ-surface in 2D, which relates inelastic displacement to energy. The inelastic component of the core energy of a Peierls-Nabarro dislocation can be parameterized using GSF energies (Christian and Vítek 1970).

In `disloPy`, the γ-lines (or γ-surfaces in 2D) calculated from atomistic simulations, for instance using GULP or QE, are used to parameterize the semi-discrete Peierls-Nabarro model (Bulatov and Kaxiras 1997; Bulatov and Cai 2006). The dislocation core structure is calculated by minimizing the total energy over the core disregistry profile **u**(**x**), which satisfies

$$\oint \left(\partial u_i / \partial l \right) dl = b_i \qquad \text{(I.19)}$$

where the integral is along a closed path containing the dislocation line. Disregistry profiles are expanded as a sum of arctangent functions, with *i*-th component of **u**(**x**) expressed as

$$u_i(x) = \frac{\|\mathbf{b}\|}{\pi} \sum_i A_i \arctan\left(\frac{x - x_{0,i}}{\zeta_i}\right) - u_{i,0} \tag{I.20}$$

where x is the position along the glide plane normal to $\boldsymbol{\xi}$ and A_i, ζ_i, and $x_{0,i}$ are free parameters giving the height, half-width, and location of an individual partial dislocation. The constant $u_{i,0} = \|\mathbf{b}\|/2$ for the component of the disregistry parallel to **b** and 0 for the component perpendicular to it. In `disloPy`, a sensible guess for the initial parameters can be entered by the user or generated automatically. Optimum values for the free parameters are obtained by minimizing the energy of the dislocation using sequential least squares (SLSQP; Carayannis et al. 1983). Using an optimized static dislocation core structure, `disloPy` calculates the Peierls stress using the applied stress method (Bulatov and Kaxiras 1997). In this approach, the stress σ is incrementally increased and the dislocation energy minimized at this new stress state by varying the parameters A_i, ζ_i, and $x_{0,i}$. For $|\sigma| > \sigma_p$, the dislocation glides freely and `disloPy` thus fails to optimize the core structure. The PN model is discussed further in Chapter VI, where it is used to simulate dislocation glide in the fluorite-structured oxide UO_2.

Visualizing dislocation cores using the Nye tensor

In the Volterra construction, a dislocation is located at a single point in the plane normal to x. However, real dislocations are characterized by finite extent over space, with infinitesimal dislocation density (in direction *i*)

$$\rho_i = (\boldsymbol{\alpha} \cdot \mathbf{n})_i \mathrm{d}S \tag{I.21}$$

where dS is an infinitesimal area element, **n** its normal vector, and $\boldsymbol{\alpha}$ is the Nye tensor. Integrating expression (I.21) over a region S including all points with non-zero dislocation density gives the i-th component b_i of the Burgers vector, i.e.

$$b_i = \int_S \rho_i \, \mathrm{d}S = \int_S (\boldsymbol{\alpha} \cdot \mathbf{n})_i \, \mathrm{d}S \tag{I.22}$$

Hartley and Mishin (2005ab) introduced a numerical method for calculating the Nye tensor **a** from a set of atomic coordinates, such as might be produced by an atomic scale simulation of a dislocation, which is briefly summarized here.

In an unstrained crystal, an atom can be characterized by the set bonds $\{\mathbf{P}^{(\beta)}: \beta = 1, 2, ..., n\}$ connecting it to n neighboring atoms a distance $r \le R$, where R is a preset parameter. Large R leads to more stable definition of the bonding environment, at the cost of non-local sampling of the deformation field **u**. In a strained section of the crystal lattice, such as a dislocation core, the set of bonds around a site is $\{\mathbf{Q}^{(\gamma)}: \gamma=1, 2, ..., n'\}$, where n' may be different from n. These bonds can be associated with the bonds in the undeformed lattice by computing the angle

$$\varphi^{(\gamma\beta)} = \arccos\left(\mathbf{Q}^{(\gamma)} \cdot \mathbf{P}^{(\beta)}\right) / \left(\left\|\mathbf{Q}^{(\gamma)}\right\| \left\|\mathbf{P}^{(\beta)}\right\|\right) \tag{I.23}$$

The unstrained lattice vector $\mathbf{P}^{(\beta)}$ for which $|\varphi^{(\gamma\beta)}|$ is a minimum is taken to correspond to $\mathbf{Q}^{(\gamma)}$. Following Hartley and Mishin (2005ab), lattice vectors $\mathbf{Q}^{(\gamma)}$ for which the minimum angle exceeds some predetermined threshold $\varphi_{\max}$ are excluded when calculating the Nye tensor. The default value used by `disloPy` is 0.5 radians.

Hartley and Mishin (2005ab) relate the bonds in the deformed and undeformed regions of the crystal using the lattice correspondence tensor **G**, which relates the lattice vectors d**x** in the undeformed lattice to the lattice vectors d**x**′ in the strained region via

$$\mathrm{d}\,\mathbf{x} = \mathrm{d}\,\mathbf{x}' \cdot \mathbf{G} \tag{I.24}$$

The bonds in the strained and unstrained crystal are related through

$$\mathbf{P}^{(\delta)} = \mathbf{Q}^{(\delta)} \cdot \mathbf{G} \tag{I.25}$$

where $\delta = 1, 2, ..., n''$, with n'' equal to the number of bonds in the strained lattice that can be matched to bonds in the unstrained lattice. Far from the dislocation core, $n'' = \min(n, n')$. However, some atoms may be under-coordinated near the dislocation line, as, for example, with 1/2<110>{110} edge dislocations in MgO (Zhang et al. 2010) or 1/2<110>{110} edge dislocations in UO_2 (Murphy et al. 2014), in which case, n'' is typically less than n or n'. The sets $\{\mathbf{P}^{(\delta)}\}$ and $\{\mathbf{Q}^{(\delta)}\}$ can be cast in matrix form by defining (n″×3) matrices **P** and **Q** whose rows are the individual bonds around an atom. The lattice correspondence tensor is

$$\mathbf{G} = \left(\mathbf{Q}^T \cdot \mathbf{Q}\right)^{-1} \cdot \mathbf{Q}^T \cdot \mathbf{P} = \mathbf{Q}^+ \mathbf{P} \tag{I.26}$$

where $\mathbf{Q}^+$ is the Moore-Penrose inverse. The components of the Nye tensor are calculated from the derivatives of the lattice correspondence tensor as

$$\alpha_{ij} = -\varepsilon_{imn}\,\partial_j G_{mn} \tag{I.27}$$

where ε_{imn} is the permutation tensor. Since the algorithm described above computes **G** only on a discrete lattice, the continuous derivatives $\partial_j G_{mn}$ must be approximated. Following

Hartley and Mishin (2005ab), $\boldsymbol{\alpha}$ is approximated at atom β by defining the tensor $A_{imk} = \partial_k G^{(\beta)}_{im}$. Let $\Delta G^{(\gamma)}_{im} = G^{(\gamma)}_{im} - G^{(\beta)}_{im}$, where γ is an atom bonded to β. Then the column vector $\Delta \mathbf{G}_{im}$ whose components are the $\Delta G^{(\gamma)}_{im}$ can be related to A_{imk} by the finite difference equation

$$\Delta \mathbf{G}_{im} = \mathbf{Q} \cdot \mathbf{A}_{im} \qquad \text{(I.28)}$$

where $\mathbf{A}_{im}$ is the (3×1) column vector whose components are the derivatives of $G^{(\beta)}_{im}$, averaged over the coordination sphere of atom. It can be calculated by taking the Moore-Penrose inverse of $\mathbf{Q}$, i.e. $\mathbf{A}_{im} = (\mathbf{Q}^{+} \cdot \Delta \mathbf{G}_{im})$. The full tensor A_{imk} is obtained by repeating this procedure for the nine components of $\mathbf{G}$, and this then used in equation (I.27) to compute the full Nye tensor.

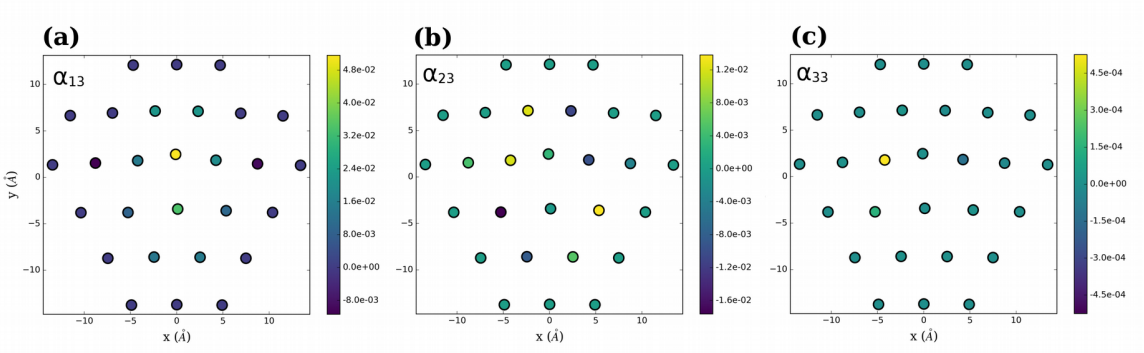

Fig. I.4 Values of the (a) α_{13}, (b) α_{23}, and (c) α_{33} components of the Nye tensor computed at M1 lattice sites around a [100](010) edge dislocation in the orthosilicate Mg_2SiO_4 forsterite.

As suggested by the form of equation (I.21), for coordinate systems with z parallel to the dislocation line vector, $\boldsymbol{\xi}$, the components of $\boldsymbol{\alpha}$ can be associated directly with the infinitesimal dislocation density distribution via $\rho_i = \alpha_{i3}$. For a pure screw dislocation, α_{13}

and α_{23} are zero, and α_{33} is zero for a pure edge dislocation. In dislocations which have mixed character or non-collinear core structures, more than one of the α_{i3} may be non-zero.

In their formulation, Hartley and Mishin (2005ab) compute $\boldsymbol{\alpha}$ for simple metals (Cu and Al) in which all atoms in the unit cell have the same set of bonds **P**. As will be seen in Chapter IV, this approach also works for simple ionic materials, such as MgO (e.g. Issa et al. 2015), or metal alloys (e.g. Bianchini et al. 2016; Rao et al. 2017), as all atoms have equivalent bonds. For complex multi-lattice crystals, the set of bonds **P** typically differs between symmetrically inequivalent sites. More problematically, additional displacements **u** may be superimposed on the displacement field caused by the dislocation. This is the case particularly with crystals containing rigid unit modes (RUMs; Dove et al. 1993; Dove et al. 1995; Hammond et al. 1996). These materials typically contain rigid polyhedra, for which the inter-polyhedral forces are considerably weaker than intra-polyhedral forces. As such, applied strain is accommodated primarily by rigid body rotation or translation of these polyhedra, with only limited changes to their shape or volume. For some atoms, the displacement due to this rigid body motion may exceed the displacement caused by the elastic strain field of a dislocation. In crystals which contain RUMs, `disloPy` computes the Nye tensor using only the sub-lattices which are least affected by their presence. This is illustrated in Fig. I.4 for the [100](010) edge dislocation in forsterite, for which $\boldsymbol{\alpha}$ has been computed using only the M1 sub-lattice, with a neighbor radius R = 7 Å. Integrating α_{13} over the region r < 20 Å gives b_1 = 4.77 Å, comparable to the real value (4.78 Å), while absolute values of the integrals of α_{23} and α_{33} are both < 0.1 Å. While $|\alpha_{33}|$ is close to zero

at all points, α_{23} attains values comparable to those for α_{13}, indicating that shear tension coupling is important for this dislocation (Bulatov and Kaxiras 1997).

I.3 Thesis overview

Atomic scale simulations, employing both *ab initio* DFT and empirical interatomic potentials, are used to investigate aspects of the interplay between minor and trace elements in the Earth's mantle and the chemical and physical properties of mantle assemblages. The thesis has three distinct sections, which address: phase transformations, elasticity, and trace element enrichment of minor phosphate minerals at mantle pressures; segregation of bare and protonated vacancies to dislocations; and the ability of vacancy-related defects to lubricate dislocation glide in mantle minerals. This last section includes a preliminary investigation of the viability of modeling dislocation glide in the important nuclear reactor fuel material UO_2 using the PN model, which is intended to guide future simulations of dislocation glide in hyper-stoichiometric UO_2.

The first section of this thesis details *ab initio* calculations aimed at determining the structure and compressibility of the calcium phosphate minerals apatite and tuite at high pressure. With their large, high-coordination cation sites, phosphate minerals may be able to dissolve large quantities of incompatible elements such as rare earth elements, Sr, Th, and U, and are potentially an important mantle reservoir for these elements. In chapter II, the effect of channel-anion identity on the high pressure compressibility and crystal structure of apatite is determined from DFT calculations. As remarked upon in section I.1, apatite decomposes at high pressure to form the calcium orthophosphate tuite, and I will calculate the pressure at which this decomposition reaction under static (i.e. 0 K)

conditions. This reaction has potentially important implications for the deep transport of phosphorous and other trace elements, as tuite is potentially stable to deep lower mantle pressures. In chapter III, DFT is used to calculate the high pressure structure and elasticity of tuite. Effective radii and Young's moduli for the Ca sites in this mineral are computed and used to parameterize an elastic strain model for impurity substitution (Brice 1975; Blundy and Wood 1994; Wood and Blundy 1997) for impurity substitution into these sites. To test the validity of this approach, I also calculate energies for Sr and Ba partitioning between tuite and $CaSiO_3$ perovskite, the most abundant Ca-bearing phase in the lower mantle, using fully atomistic simulations.

Beginning in chapter IV, I consider the interplay between dislocations and bare or protonated cation vacancies in mantle minerals. In this second part of the thesis, I address the role of dislocations in hosting cation vacancies in MgO periclase (Chapter IV) and Mg_2SiO_4 forsterite (Chapter V). These are the magnesium end-members for two of the most important mantle minerals, magnesiowüstite and olivine, which control the rheology of the lower (e.g. Madi et al. 2005; Girard et al. 2016) and upper mantle (e.g Stocker and Ashby 1973; Karato and Wu 1993), respectively. In chapter IV, I calculate the core structures of 1/2<110>{110} edge, 1/2<110>{100} edge, and 1/2<110> screw dislocations in MgO using the cluster-based method. Segregation energies are calculated for bare (i.e. $\{\square_{Mg}\}''$) and protonated (i.e. $\{2H_{Mg}\}^X$) Mg vacancies for lattice sites around the dislocation core, and these are compared to evaluate the effect of protonation on vacancy-dislocation interactions. Chapter V details similar calculations for the [100](010) and [001](010) edge dislocations and [100] and [001] screw dislocations in forsterite. As with MgO, segregation energies are calculated for both bare and protonated Mg vacancies around different

dislocations. For forsterite, there is an additional layer of complexity, as the lower symmetry of the unit cell means that there are two symmetrically distinct M sites (labeled M1 and M2), for which segregation energies may be different. In the bulk, M1 vacancies are energetically more favorable than M2 vacancies (Brodholt 1997), but this may be different near dislocation cores, with implications not only for dislocation rheology, but also for Mg diffusion in olivine. Although M site vacancies are more common in the mantle, due to the coexistence of olivine with pyroxene minerals, Si vacancies may be present under conditions of high water fugacity or low silica activity (Walker et al. 2007), and so segregation energies are also calculated for the $\{\square_{Si}\}''''$ defect.

In Chapter VI, the PN model is used to calculate σ_p for the industrially important oxide UO_2. Despite the importance of the microstructural features of UO_2 for nuclear reactor safety, the Peierls stresses of the major slip systems of UO_2 remain poorly constrained. The Peierls stress is calculated for 1/2<110>{100}, 1/2<110>{110}, and 1/2<110>{111} dislocations using several literature interatomic potentials. These calculations are intended to serve as a guide for future investigation of dislocation glide in hyper-stoichiometric UO_2.

The third part of this work builds on the results from in the previous section, and investigate ways in which point defects may influence the crystal plasticity in the dislocation glide regime. In the exponential creep regime, where dislocation glide presumably controls deformation, Katayama and Karato (2008) have measured the stress-strain relations in hydrous olivine under conditions where dislocation glide is a dominant contributor to deformation, finding that water reduces the critical stress, which is assumed to be related to the Peierls stress. However, no direct measurements of the Peierls stress for

a single slip system in oxide materials containing protonated defects have ever been obtained. In Chapter VII, DFT calculations used to construct 1/2<110>{110} and 1/2<110>{100} γ-line energies for MgO over a range of mantle pressures, with and without $\{2H_{Mg}\}^{X}$ defects present at the slip plane. These γ-lines are used to parameterize PN models for the edge and screw components of the dominant slip systems in MgO. A similar exercise is undertaken in Chapter VIII for forsterite, where empirical interatomic potentials (Lewis and Catlow 1985; Price et al. 1987) are used to determine the influence of bare Mg vacancies on [100](010) and [001](010) GSF energies. These γ-lines are used to parameterize a PN model, from which the approximate effect of Mg vacancies on dislocation glide in forsterite can be determined.

Finally, Chapter IX contains the conclusions, where the results of the various chapters are assembled to argue that vacancy related point defects, including those associated with the incorporation of water into the crystal structure, may play an important role in the rheology of the Earth's mantle in regions where glide creep dominates strain rates.

Chapter II. The influence of channel anion identity on the high-pressure crystal structure, compressibility, and stability of apatite

This chapter has been accepted for publication in: Mineralogy and Petrology (2018)

II.1 Introduction

The major host mineral for phosphorus in the Earth's crust and upper mantle is apatite, a calcium phosphate mineral with composition $Ca_{10}(PO_4)_6X_2$, where the channel anion, X, is typically F^-, OH^-, or Cl^- (Pan and Fleet 2002). In addition to being the primary ore for phosphorous, apatite is the most important mineral in the global phosphorous cycle, and can help transport incompatible elements such as the rare earth elements (REEs) and large lithophile elements (LILEs) into the Earth's mantle (Konzett et al. 2012). Apatites are also the major mineral components in human and animal bones and teeth, and their mechanical and chemical properties play a prominent, if poorly understood role in tooth durability (e.g. Menendez-Proupin et al. 2011). Because of this, medical implants are often coated in apatite to improve bio-compatibility (Elsinger and Leal 1996; Moore et al. 2001). Natural apatites can contain high concentrations of actinides, and for this reason apatite has been proposed as a potential solid state host for the long-term storage of waste radio-nuclides produced by nuclear reactors (e.g. Arey et al. 1999).

The prototypical calcium apatite unit cell, shown in Fig. II.1, is hexagonal with space group $P6_3/m$. Each unit cell contains 10 Ca^{2+} ions, which are distributed between two symmetry distinct cation sites, labeled CaI and CaII. The CaI sites, of which there are four, are 6+3 coordinated by O^{2-}, while the six CaII sites, which are arranged in triangles around the channel site, are highly asymmetric, with six Ca-O bonds and one Ca-X bond.

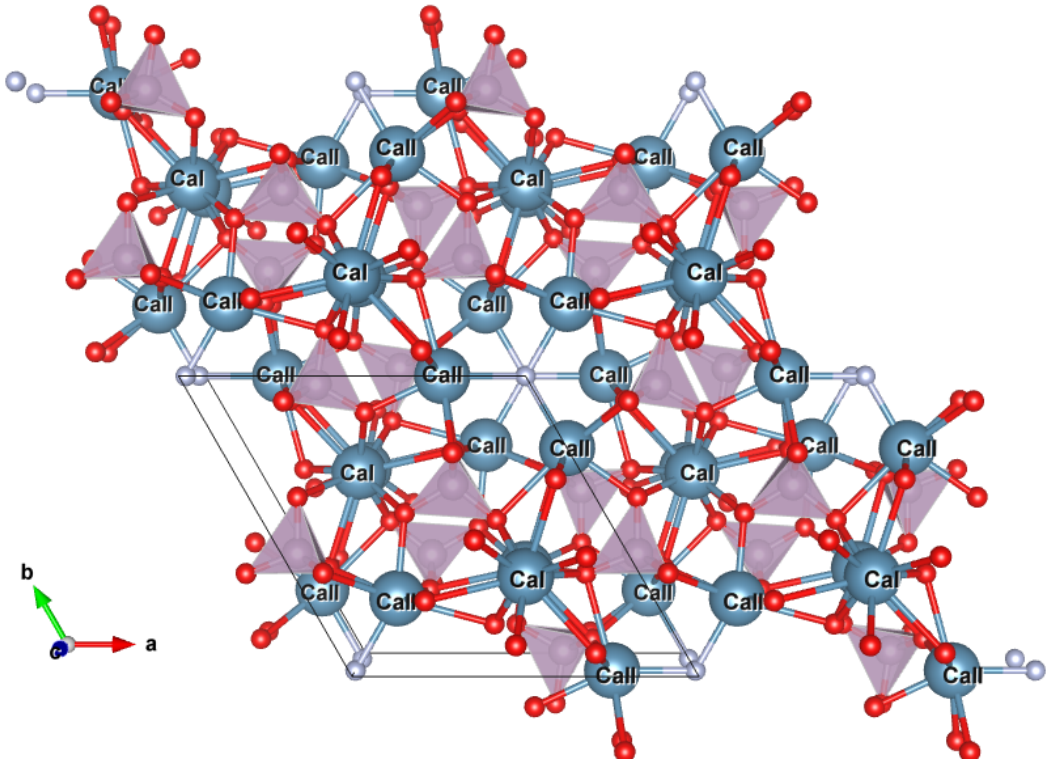

Fig. II.1 Crystal structure of apatite, viewed down the [0001] axis. Image produced using the crystal structure visualization software VESTA 3 (Momma and Izumi 2011)

To minimize interactions between Ca ions, adjacent CaII triangles (along [0001]) are rotated relative to one another by 60°. The channel sites are typically occupied by either F^- (fluorapatite or FAP), OH^- (hydroxyapatite or HAP), or Cl^-, (chlorapatite or CAP). However, other anions may occupy these sites under certain conditions, most notably oxygen (Trombe and Montel 1978), carbonate (Comodi and Liu 2000) and hydrogen-carbonate (Fleet and Yiu 2007). The identity of the channel anion has a significant influence on the crystal structure of apatite. Changing the channel anion species can even change the crystal symmetry and, while FAP only exists in hexagonal form with space group $P6_3/m$, both HAP (Elliott et al. 1973, Ikoma et al. 1999, Ma and Liu 2009) and CAP (Mackie et al. 1972) have monoclinic variants. Due to their large, high-coordination cation

sites and isolated PO_4 tetrahedra, the apatite crystal can accommodate significant distortion and is thus able to host high concentrations of a wide range of elements, including rare earth elements (REEs) and actinides. This makes apatite important in geochemistry, as its presence can significantly alter REE trends in igneous rocks (e.g. Watson and Capabianco 1981).

Although the influence of the channel anion identity on the properties apatite is well established at ambient conditions using theoretical calculations (eg Calderin et al. 2003; Rulis et al. 2004), the relationship between channel anion identity and the compressibility and high-pressure properties of apatite remains poorly understood. X-ray diffraction studies on HAP, FAP, and CAP indicate that the channel anion affects the compressibility of apatite, with CAP having the lowest bulk modulus, while those of HAP and FAP are similar (Brunet et al. 1999). The measured compressibilities of synthetic lead fluorapatite ($Pb_{10}(PO4)_6F_2$) and lead bromapatite ($Pb_{10}(PO_4)_6F_2$) suggest that the channel anion also influences fine features of the response to pressure, such the ratio of the *a* and *c* cell parameters, *a*/*c*, a measure of the anisotropy of compression, which is largely pressure independent for lead fluorapatite (Fleet et al. 2010), but decreases moderately with increasing pressure in lead bromapatite (Liu et al. 2011). Intriguingly, both studies found compressibility anomalies at high pressure, suggesting a change in the compression mechanism.

In experiments, apatite disproportionates at moderately high pressure to form tuite, γ-$Ca_3(PO_4)_2$, a high density calcium orthophosphate, plus an additional phase which depends on the channel anion identity, typically either CaX_2 (X=F, OH, or Cl), or CaO and a fluid

phase (for HAP), and it is thought that this the route by which tuite may form in the mantle (Murayama et al. 1986). Tuite formed by this process could be important for the trace element inventory of the mantle (Zhai et al. 2014; Skelton and Walker 2017b). However, the pressure at which apatite reacts to form tuite varies between studies, from as low as 7.5 GPa (Konzett and Frost 2009) to as high as 12 GPa (Murayama et al. 1986).

In this study, we use quantum mechanical calculations, with and without dispersion corrections, to determine the effect of pressure on the crystal structures of HAP, FAP, and CAP, obtaining the relaxed atomic structures, cell shapes, and cell volumes of the hexagonal phases of HAP, CAP, and FAP in the range 0-25 GPa. Additionally, we compute enthalpies for the monoclinic variants of CAP and HAP, to determine the pressure dependence of the hexagonal to monoclinic phase transition. Valence electron densities were obtained at a range of pressures, showing the effect of pressure on the bond topology of apatite. Ultimately, it is hoped that these calculations will help shed light on the radically divergent high-pressure behavior of the different apatite minerals.

II.2 Methodology

We studied the properties of apatite using plane-wave density functional theory (DFT, Hohenberg and Kohn, 1964; Kohn and Sham, 1965), which is a mean-field approach to solving the Schrödinger equation, as implemented in version 5.2 of the Quantum Espresso software package (Giannozzi et al. 2009). The exchange-correlation (xc) energy was treated using the PBE generalized gradient approximation (GGA) xc-functional (Perdew et al. 1996).

All calculations were performed using a kinetic energy cutoff of 60 Ry (~816 eV) for the wavefunction basis, while reciprocal space sampling is done using the Monkhorst-Pack scheme (Monkhorst and Pack 1976), with grid sizes of 2x2x2 and 2x1x2 for the hexagonal and monoclinic apatites, respectively. These values were found to be sufficient to converge the total energy of the simulation cell to <5 meV/atom. Ionic cores were treated using Vanderbilt ultrasoft pseudopotentials (Vanderbilt 1990), which are smoother than regular norm-conserving pseudopotentials and hence require fewer plane waves for accurate calculations. The plane wave basis used for the auxiliary charge density has a cutoff energy 8 times that used for the wavefunction basis above. Valence configurations were $3s^2 3p^6 4s^2$, $3s^2 3p^3$, $3s^2 3p^5$, $2s^2 2p^4$, $2s^2 2p^5$, and $1s^1$ for Ca, P, Cl, O, F, and H, respectively. At each pressure, the crystal structure was determined by simultaneously relaxing the cell parameters and atomic positions using the BFGS quasi-Newton scheme (Pfrommer et al. 1997). In order to accommodate possible transitions between high- and low-symmetry apatite structures, no symmetry was imposed on the calculations, and the tunnel anions were displaced from high-symmetry locations.

To determine the effect of channel anion identity on the pressure at which apatite decomposes to form tuite, the enthalpy of the following decomposition reaction is computed:

$$Ca_{10}\left(PO_4\right)_6 X_2 \Rightarrow CaX_2 + 3\,Ca_3\left(PO_4\right)_2 \qquad \text{(II.1)}$$

where X=F, Cl, or OH. Murayama et al. (1986), in synthesizing tuite at high pressure and temperature, found that the CaF_2 produced by decomposition of FAP was a solid phase, and that crystalline $Ca(OH)_2$ was produced during decomposition of HAP, at least below 1273

K, above which the decomposition products should be CaO and H_2O. As the calculations here are performed at static conditions (i.e. at 0 K), and since the enthalpies of fluid phases cannot be easily computed with DFT, only decomposition reactions which produce tuite and solid CaX_2, (X=F, OH, Cl) are considered here.

The enthalpies for the products of reaction (II.1) were computed with DFT, with the ionic cores treated using the same set of pseudopotentials as were used for apatite. The kinetic energy cutoff used for apatite (60 Ry) was found to be sufficient to ensure convergence of the total energies of tuite and the CaX_2 phases. For tuite, a 4x4x2 k-point grid was sufficient to guarantee convergence of the total energy to <5meV/atom. CaF_2, $Ca(OH)_2$, and $CaCl_2$ all undergo phase transformations in the pressure interval considered here, and enthalpies were computed for the low-pressure and high-pressure phases. For CaF_2, there is a pressure induced phase transition at ~9 GPa (Qi et al. 2013), from the low density fluorite phase (space group *Fm3m*) to a higher density orthorhombic phase with space group *Pnma*. Converged cell energies were obtained by using a 4x4x4 k-point grid for the fluorite phase and a 6x4x4 grid for the high-pressure *Pnma* phase. For low pressure $Ca(OH)_2$ (portlandite, space group *P*3*m*1), a 6x6x6 k-point grid was sufficient to guarantee convergence of the total cell energy. Like CaF_2, $Ca(OH)_2$ undergoes a phase transformation at high pressure, adopting a structure similar to ZrO_2 baddeleyite (space group $P2_1/c$; Kunz et al. 1996), for which a 4x4x4 k-point grid was used. Finally, $CaCl_2$ also undergoes a phase transformation over the pressure range considered in this study (0-30 GPa), from the low pressure rutile-type phase (space group $P4_2/mnm$) to a high-pressure cotunnite-type phase with space group *Pbcn* (Liu et al. 2007). 6x6x8 and 6x4x4 k-point grids were used for the low and high pressure phases, respectively.

The GGA xc-functional fails to capture the effects of long-ranged dispersive interactions, which contributes to the well-documented tendency of this xc-functional to overestimate cell volumes (see e.g. Otero-de-la-Roza and Luana 2011; Luo et al. 2013). Inclusion of dispersion interactions has been found to be important for layer silicates (Ulian et al. 2013a; Ulian et al. 2014). Their correct treatment is also of more general importance when calculating the properties of ionic materials with DFT, and their inclusion is essential for calculating the correct stable phase of cesium chloride (Zhang et al. 2013). Consequently, we recalculate the atomic positions, cell parameters, and reaction enthalpies for FAP, HAP, and CAP using the DFT-D2 approach (Grimme 2006). In this formulation, the energy of a DFT calculation is modified by adding an additional term, representing energy of the long-ranged dispersion interactions, which has the form

$$E_{\text{dispersion}} = -s_6 \sum_{i=1}^{N} \sum_{j>i}^{N} f(r_{ij}) \frac{C_6^{ij}}{r^6_{ij}} \qquad \text{(II.2)}$$

where s_6 is a xc-functional dependent scaling factor, taken to be 0.75 for the PBE xc-functional (Grimme 2006), r_{ij} is the interatomic distance, and C_6^{ij} is a numerical coefficient giving the strength of the dispersion interaction between atoms *i* and *j*. In the DFT-D2 scheme, this is given by the expression $C_6^{ij} = \sqrt{C_6^i C_6^j}$, where C_6^i is the dispersion coefficient for atom *i*. The taper function f is used to prevent double counting of short-ranged dispersive interactions, and is given by

$$f(r_{ij}) = \frac{1}{1 + e^{-d(r_{ij}/R_{ij}^{vdw} - 1)}} \qquad \text{(II.3)}$$

where d is a steepness parameters and R_{ij}^{vdw} is the sum of the van der Waals radii of atoms i and j. Since dispersion forces may affect apatite minerals and their high-pressure decomposition products differently, enthalpies for the tuite and CaX_2 phases in reaction (I.1) are also calculated using DFT-D2.

II.3 Results and Discussion

Influence of channel anion identity on crystal structure

We begin by examining the relationship between channel anion identity and compressibility of the apatite unit cell using GGA-DFT without a dispersion correction (Table II.1). Calculated cell volumes, a and c parameters, and a/c ratios are plotted in Fig. II.2, where it can be seen that CAP has the largest cell volume and highest compressibility, while HAP and FAP have similar cell volumes and compressibilities at all pressures. To quantify this, the calculated cell volumes are fit to a 3rd order Birch-Murnaghan (BM3) equation of state (EOS)

$$P(V)=\frac{3K_0}{2}\left[\left(\frac{V_0}{V}\right)^{7/3}-\left(\frac{V_0}{V}\right)^{5/3}\right]\times\left[1+\frac{3}{4}\left(K_0^{'}-4\right)\left\{\left(\frac{V_0}{V}\right)^{2/3}-1\right\}\right] \quad \text{(II.4)}$$

where V_0 is the zero pressure volume, K_0 the zero pressure isothermal bulk modulus, and $K_0^{'}$ is the pressure derivative of the bulk modulus at 0 GPa. K_0 and $K_0^{'}$ are covariant, and so we also fit the cell volumes to a second order Birch-Murnaghan EOS, in which $K_0^{'}$ is fixed to 4.0. However, this results in a significant reduction of the goodness of fit for all three apatites. Moreover, whether or not $K_0^{'}$ is allowed to vary, the BM3 EOS

gives a poor fit to the cell volume data of CAP. The fitted BM3 EOS parameters are given in Table II.2. CAP is the softest of the three apatite minerals, with a K_0 of just 55.0 GPa, while FAP is the stiffest, with K_0 = 90.7 GPa. The values for the bulk moduli obtained here are significantly lower than those determined by Brunet et al. (1999), by up to 11% in the case of HAP, and the fitted values of V_0 for FAP and HAP are larger than the experimental values, by 3.5 and 3.7 %, respectively. This is a consequence of the underbinding of the GGA exchange correlation functional. The calculated zero-pressure cell volume of HAP (549.5 Å^3) is larger than the 532 Å^3 found by Ulian et al. (2013b) using all-electron density functional theory with the B3LYP hybrid functional.

Table II.1 Calculated cell volumes and *a* and *c* cell parameters for FAP, HAP, and CAP as functions of pressure.

P (GPA)	FAP			HAP			CAP		
	V (Å^3)	*a* (Å)	*c* (Å)	*V* (Å^3)	*a* (Å)	*c* (Å)	*V* (Å^3)	*a* (Å)	*c* (Å)
0.0	542.74	9.518	6.917	549.52	9.592	6.896	573.07	9.900	6.751
2.5	527.25	9.407	6.880	532.95	9.464	6.871	549.66	9.730	6.704
5.0	514.30	9.317	6.841	519.27	9.363	6.840	531.85	9.588	6.680
7.5	502.86	9.236	6.808	507.57	9.278	6.808	517.71	9.468	6.668
10.0	492.73	9.165	6.774	497.21	9.204	6.777	505.76	9.369	6.654
12.5	483.54	0.100	6.742	487.74	9.136	6.748	495.49	9.286	6.635
15.0	475.43	9.043	6.714	479.20	9.074	6.720	486.20	9.213	6.614
17.5	467.86	8.989	6.687	471.39	9.018	6.694	477.73	9.147	6.593
20.0	460.97	8.939	6.661	4.64.19	8.966	6.668	470.16	9.088	6.573
22.5	454.38	8.891	6.637	4.57.44	8.916	6.644	463.17	9.034	6.554
25.0	448.25	8.846	6.614	451.12	8.870	6.621	456.66	8.984	6.533

The order of the *a* cell parameter lengths at ambient pressure is *a*(CAP) > *a*(HAP) > *a*(FAP), while the order of the *c* cell parameters is *c*(FAP) > *c*(HAP) > *c*(CAP). At high

pressure, the order of the magnitudes of the *a* cell parameters does not change, while the ordering of *c*(HAP) and *c*(FAP) reverses at ~7.5 GPa. As can be seen from the *a/c* ratios of the three apatites (Fig. II.2d), the *a* cell axis is more compressible than the *c* axis, as the *a/c* ratio is strictly decreasing with pressure. The magnitude of this decrease is greatest in the

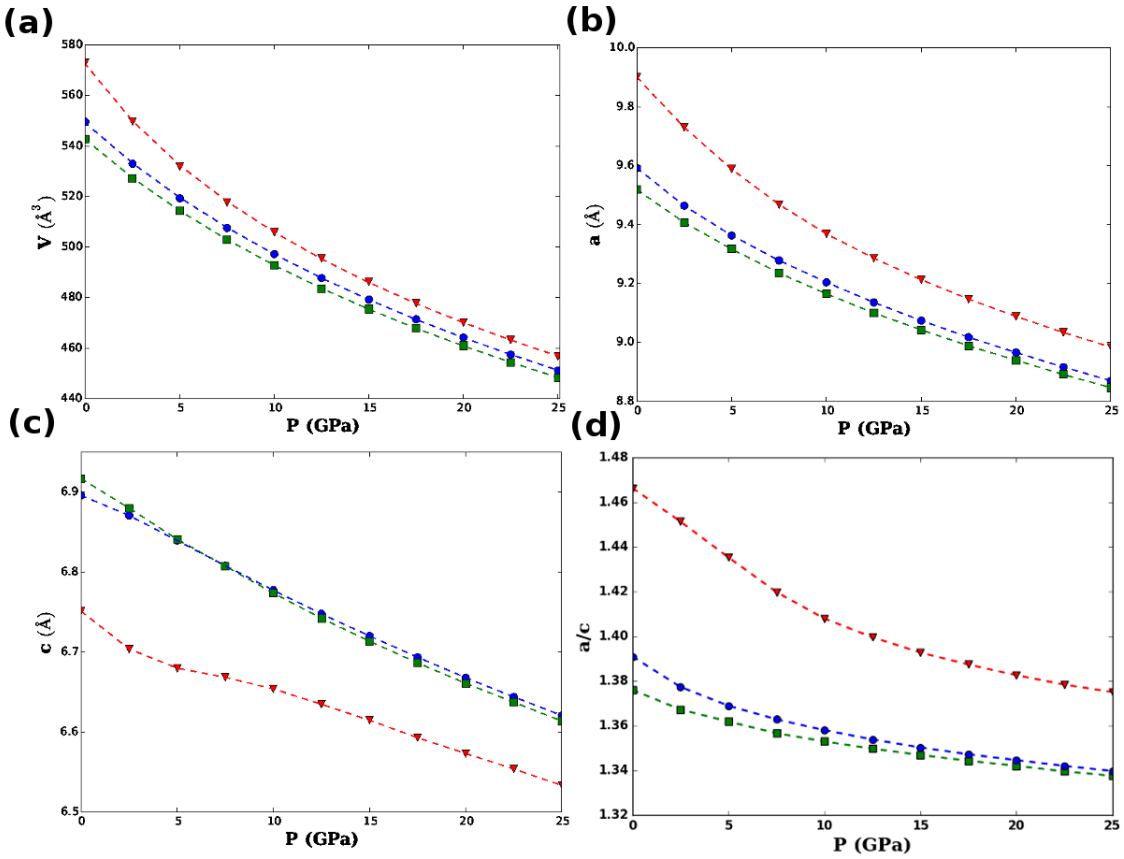

Fig. II.2 Pressure dependence of the (a) cell volumes, (b) *a* cell parameters, (c) *c* cell parameters, and (d) *a*/*c* ratios of FAP (green squares), HAP (blue circles), and CAP (inverted red triangles)

case of CAP. This is consistent with the finding of He et al. (2012), that the incorporation of large radius ions into the apatite structure dilates the *a* axis more than the *c* axis, increasingly the relative compressibility of the *a* axis. To give a quantitative indication of the relative stiffness of the crystal axes of the different apatite minerals, we fit the BM3

EOS (equation II.4) to the cubes of each cell parameter. For the *a* cell parameters, this give effective bulk moduli K_0 of 68.0(16), 60.3(20), and 37.1(21) GPa and K_0' of 4.7(2), 4.9(2), and 5.6(3) for FAP, HAP, and CAP, consistent with the ordering found for the total cell volumes. Fitting the cubes of the *c* cell parameters of FAP and HAP (excluding HAP at 0 GPa, where the curvature is apparently negative) gives bulk moduli of 135.6(42) and 158.9(45) GPa and K_0' of 4.5(4) and 3.4(3) for FAP and HAP, respectively. For CAP, no meaningful fit parameters can be obtained, due to the anomalous stiffening of the *c*-axis at ~7.5 GPa, a result which explains the poor fit obtained for the cell volumes.

Table II.2 BM3 EOS parameters for hexagonal FAP, HAP, and CAP. The final two columns are the 0 GPa bulk modulus and cell volume with K_0' set equal to 4.0. Values in bold are fits to experimental data in Brunet et al. (1999). While Brunet et al. did not compress a sample of CAP, they did compress an apatite with composition $Ca_5(PO_4)_3Cl_{0.7}(OH)_{0.3}$, which had K_0= 93.1 GPa and V_0 = 539.4 Å^3

	K_0 (GPa)	K_0'	V_0 (Å^3)	K_0	V_0 (Å^3)
FAP	82.1(11)	4.9(1)	542.6(3)	90.7(19) **(97.9)**	540.8(12) **(522.4)**
HAP	79.2(14)	4.8(2)	549.1(5)	87.1(17) **(97.5)**	547.4(12) **(526.9)**
CAP	55.0(20)	6.3(3)	572.3(10)	73.9(42)	566.2(39)

This anomaly manifests in the increase of the *z*-coordinate of the Cl^- ion with pressure, from 0.398 at 0 GPa to effectively 0.5 at 7.5 GPa, as can be seen in Fig. II.3. This corresponds to the Cl^- ion being situated exactly halfway between adjacent CaII triangles. This change in compression mechanism is also associated with a change of space group,

which is determined using the program FINDSYM (Stokes and Hatch, 2005), from $P6_3$ at low pressure to $P6_3/m$ at high pressure. This transition is associated with a change in the Wyckoff site occupied by the Cl^- anion, from *2a* to *2b*. Since the z-coordinate approaches 0.5 continuously, but its pressure derivative is discontinuous where the Wyckoff site changes from *2a* to *2b*, the transition from the $P6_3$ to $P6_3/m$ space group is of second order.

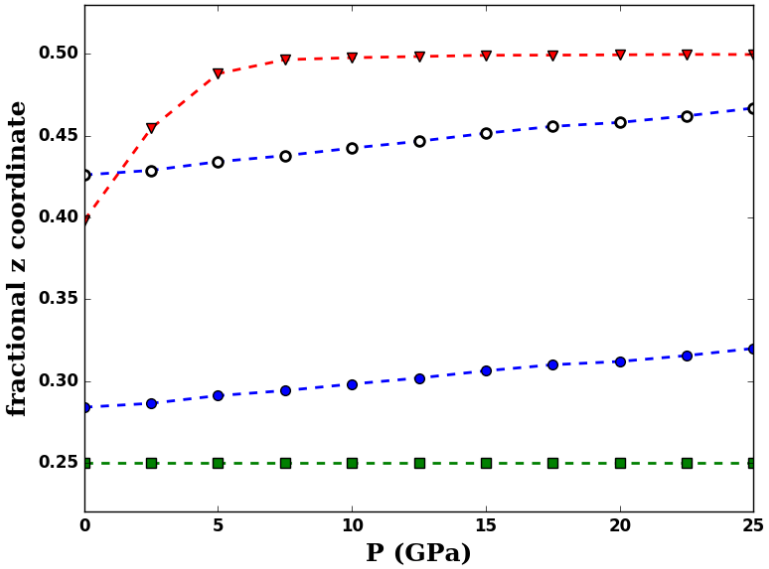

Fig. II.3 Plot of the pressure dependence of *z*-coordinates of the F^- anion in FAP (squares), the Cl^- anion in CAP (inverted red triangles), and the O^{2-} (filled blue circles) and H^+ (hollow blue circles) ions in the $(OH)^-$ group of HAP

Among the apatites considered in this study, this high-pressure transition appears to be unique to CAP, as no similar compressibility anomalies can be seen for either FAP or HAP. In the former case, the F^- ion remains at z = 0.25 (i.e. in the center of a CaII triangle) to 25 GPa. Similarly, in HAP, although the hydroxyl group is displaced along the channel with increasing pressure (Fig. II.3), the pressure derivatives of the O^{2-} or H^+ coordinates do not vary between 0 and 25 GPa. In principle, this could change at pressures substantially above 25 GPa but, as will be shown below, HAP decomposes at high pressure, which means that

any such change in the compression mechanism does not fall within its pressure-stability range.

Unsurprisingly, given the wildly divergent pressure response of the cell parameters for the three apatites, we find that the influence of pressure on the channel is depends strongly on the identity of the channel anion. To illustrate this, we use the trigonally distorted polyhedron whose six corners are the Ca^{2+} atoms from two adjacent CaII triangles and which is centered on a hypothetical ion at z = 0.5 (Fig. II.4a), commonly called the "channel polyhedron" (Fleet et al. 2010). By taking this point to be the center of the polyhedron, we separate the displacement of the channel anion from the distortion of the shape of the channel. At high pressure the channel polyhedron corresponds to the coordination polyhedron of the Cl^- anion in CAP. As can be seen from Fig. II.4b, the pressure dependence of the channel polyhedron's volume varies greatly between FAP, HAP, and CAP. Furthermore, the channel anion identity also affects the shape of the channel polyhedron, as can be seen from the bond angle variance (BAV; Robinson et al. 1971), which is a measure of the angular distortion of the coordination polyhedron, defined as

$$\sigma^2 = \frac{1}{m-1}\sum_{i=1}^{m}\left(\theta_i - \theta_0\right)^2 \qquad \text{(II.5)}$$

where m is equal to 3/2 times the number of faces in the polyhedron. The θ_i are the bond angles made by two Ca atoms at the vertices of the coordination polyhedron with the site at its center, and θ_0 is the ideal bond angle for a regular polyhedron with $2m/3$ faces. BAV values for the channel polyhedra in FAP, CAP, and HAP are plotted in Fig. II.4c. For both FAP and HAP, the BAV of the channel polyhedron increases steadily with pressure,

although the BAV is somewhat greater for FAP, which may be because the channel anions in FAP (i.e. F^-) remain in the faces of the channel polyhedra at all pressures.

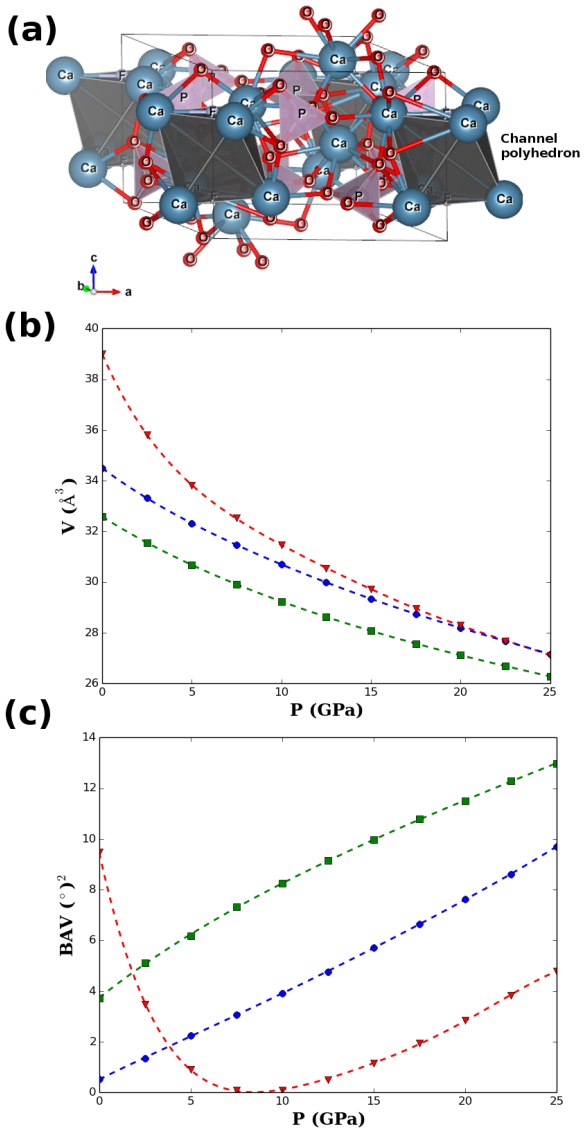

Fig. II.4 (a) Unit cell of fluorapatite with the "channel polyhedron" (defined in the text) highlighted. The pressure dependence of the (b) volumes, and (c) bond angle variances (BAV) of the channel polyhedra in FAP (green squares), HAP (blue circles), and CAP (inverted red triangles) are also shown

The pressure dependence of the shape and compressibility of the CAP channel polyhedron is markedly different from the other apatites. In particular, whereas BAV values for HAP and FAP are monotonic increasing, the BAV of the channel polyhedron in CAP decreases rapidly at low pressure, from 9.47 $(°)^2$ at 0 GPa to <0.1 $(°)^2$ at 7.5 GPa. Thereafter, it increases steadily with P, at a rate similar to that of the BAV for the FAP channel polyhedron. At 0 GPa, the channel polyhedron in CAP is substantially larger than those of HAP or FAP. However, its compressibility is also much greater and, above 15 GPa, the channel polyhedra of CAP and HAP have similar volumes and compressibilities. These differences can be quantified by fitting a BM3 EOS to the calculated polyhedral volumes. Such a fit gives V_0 = 38.6(2), 34.44(3), and 32.58(1) $Å^3$ for CAP, HAP, and FAP, respectively, consistent with Cl^- being the largest of the channel anions and F^- the smallest. Looking now at the bulk modulus and its derivative, we find that, for CAP, K_0 = 28.1(21) GPa and K_0' = 5.5(3). For HAP and FAP, the corresponding values are K_0 = 71.8(11) and 72.4(3) GPa and K_0' = 3.3(1) and 4.53(3), respectively.

The contrasting response to pressure can also be seen by examining the internal parameters of the apatite cell. One quantity of particular interest is the metaprism twist ϕ, which is the angle between the projections of the CaI-O1 and CaI-O2 bonds onto (0001) (illustrated in Fig. II.5*a*). This quantity is known to be sensitive to apatite composition, and is consequently used as a probe for chemical composition and order (Lim et al. 2011). For FAP, the metaprism twist increases from 22.67° at 0 GPa, compared with the value of 24.3° found by Lim et al. (2011). The metaprism twist angle increases with pressure, reaching a maximum of 23.38° at 7.5 GPa, before declining steadily to 22.80° at 25 GPa. Similarly, for

HAP, the value of ϕ increases from 21.57° at 0 GPa, rather less than the value of 23.2° found by Sudarsanan and Young (1972), reaching a maximum value of 23.05° at 10.0 GPa, and decreasing to 22.63° by 25 GPa. While the range of angular values is somewhat greater in HAP than in FAP, in both cases the metaprism twist is only weakly dependent on pressure. However, as can be seen in Fig. II.5a, the effect of pressure on the metaprism twist angle in CAP is radically different, with ϕ increasing rapidly from a value of just 14.37° at 0 GPa, to 20.21° at 22.5 GPa, declining slowly thereafter. Note that, as for the other two apatites, ϕ is rather less than the experimentally determined value of 17.8° (Sudarsanan and Young 1980). However, the relative magnitudes of the metaprism twist angles is reproduced successfully, with ϕ(CAP) < ϕ(HAP) < ϕ(FAP).

Another measure of the response of the apatite crystal structure to pressure is the X-X-CaII angle (illustrated in Fig. II.5*b* for FAP). This quantity, referred to hereafter as the "skew" angle ψ, measures the rotation of the channels relative to one another. If the channels lined up perfectly this would be exactly 120°. Indeed, from Fig. II.5*b* it can seen that, at 0 GPa, this is very nearly the case for FAP and HAP, for which the values of are 120.02° and 119.51°, respectively. However, the effect of increasing pressure is to rotate the channels relative to one another such that, at 25 GPa, the calculated values of *y* are 123.35° for FAP and 123.46° for HAP. As was the case for the metaprism twist, the effect of pressure on the skew angle is rather more pronounced for CAP, for which ψ increases from 115.82° at 0 GPa to 122.32° at 25 GPa.

The differences in the high-pressure responses of the different apatites is apparent not only in the crystal structure but also in the bond topology in the vicinity of the channel. This can

be seen in the differences between the low- and high-pressure valence electron density distributions of HAP with those of CAP, shown in Fig. II.6. In the former, although the channel site shrinks and the hydroxyl group is progressively displaced along the *c*-axis, the

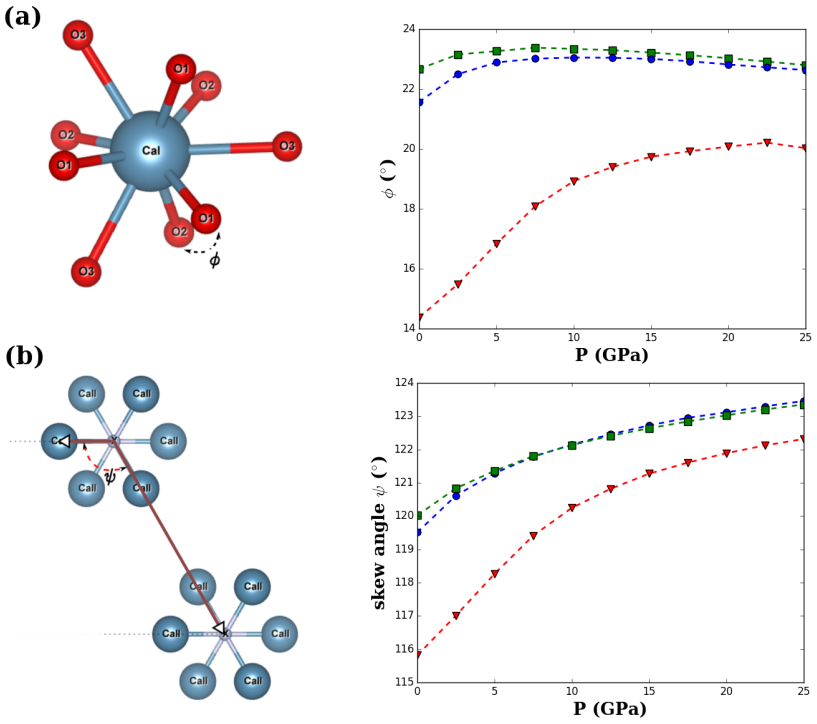

Fig. II.5 Illustrations of (a) the metaprism twist ϕ and (b) the skew angle ψ, together with their calculated pressure dependences, for FAP (green squares), HAP (blue circles), and CAP (inverted red triangles)

bond topology remains unchanged, with the hydroxyl oxygen three-fold coordinated to Ca^{2+} at all pressures between 0 and 25 GPa. At 0 GPa, the electron density distribution of CAP looks very similar to that of HAP, with each Cl^- anion in CAP being linked by bonds with substantial electron density at the bond critical point to Ca^{2+} ions in a only single layer, for a total effective coordination number of three. However, at high pressure the Cl^- anion has clearly defined bonds with all Ca^{2+} ions in the CaII triangles both above and below it, raising the effective coordination number to six. Simultaneously, the channel site

symmetrizes, and a mirror planes develop at z =0.25 and z =0.75, halfway between adjacent Cl^- anions. This symmetrization coincides with (indeed, causes) the substantial stiffening of the CAP *c*-axis seen at ~7.5 GPa in Fig. II.2*c*, and the associated anomaly in the *a*/*c* compression ratio (Fig. II.2d).

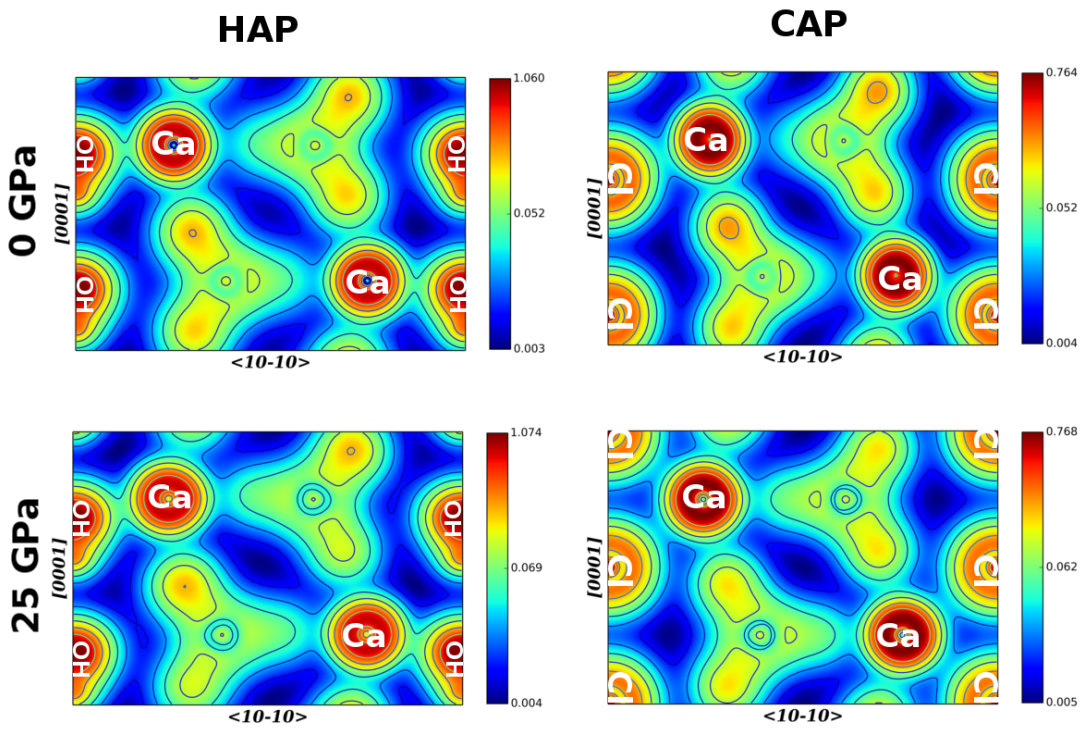

Fig. II.6 Calculated valence electron densities at 0 GPa and 25 GPa for HAP and CAP

A similar anomaly in the *a*/*c* compression ratio has also been observed in synthetic lead fluorapatite (PbFAP; Fleet et al. 2010). Diffraction data shows that, at ambient pressure, the channel ion in PbFAP, much like the channel anions in HAP and CAP, is displaced along [0001] to z = 0.461. While Fleet et al. (2010) were unable to refine the location of the F^- ion at high pressure, as F^- is much lighter than Pb^{2+} and hence difficult to locate in x-ray diffraction, the observed changes in the *a*/*c* compressibility ratio and the substantially

greater compressibility of the channel polyhedron are consistent with progressive displacement of the channel anion along [0001] that stalls as the anion approaches z = 0.5, as was found to be the case here for Ca-CAP. This may also explain similar compressibility anomalies in lead bromapatite (PbBrAp; Liu et al. 2011).

The effect of dispersion forces on the high-pressure structure of apatite

The larger cell volumes and lower zero-pressure bulk modulus of apatite, relative to experiments, reported in the previous section can be attributed to the use of the PBE-GGA xc-functional, which is known to significantly underbind. While several factors contribute to this underbinding, one potentially important source is the failure of the PBE-GGA xc-functional to adequately model long-ranged dispersive interactions. To determine the significance of this for apatite compressibility, cell volumes and cell parameters were calculated using the DFT-D2 approach, as described above. Calculated *a* and *c* cell parameters and cell volumes for FAP, HAP, and CAP are reported in Table II.3 and plotted in Fig. II.7. The inclusion of dispersion forces via the DFT-D2 scheme reduces the cell volumes of all apatites considered here, as well as both the *a* and *c* cell parameters.

The significance of this reduction can be quantified by fitting the BM2 and BM3 equations of state to the cell volumes calculated with DFT-D2. The fitted parameters are reported in Table II.4. The inclusion of dispersion forces does not affect the ordering of the compressibilities of the three minerals, with CAP and FAP remaining the most and least compressible minerals, respectively. However, the DFT-D2 BM2 fit parameters are substantially closer to those obtained by Brunet et al. (1999) for natural apatites, particularly for FAP, whose fitted BM2 K_0 is within error of the value reported by Brunet et

al. (1999). The zero-pressure cell volume V_0 is also substantially better reproduced by the DFT-D2 calculations, with the calculated values for FAP and HAP just 1.3% and 1.4% greater than those obtained by Brunet et al. (1999) by fitting to experimental data.

Table II.3 Cell volumes and *a* and *c* cell parameters for FAP, HAP, and CAP calculated as functions of pressure with the dispersion forces treated using the DFT-D2 scheme.

P	FAP			HAP			CAP		
(GPA)	*V* (Å^3)	*a* (Å)	*c* (Å)	*V* (Å^3)	*a* (Å)	*c* (Å)	*V* (Å^3)	*a* (Å)	*c* (Å)
0.0	530.32	9.453	6.853	535.47	9.501	6.849	552.09	9.734	6.729
2.5	516.83	9.360	6.813	521.53	9.404	6.810	535.28	9.597	6.711
5.0	505.02	9.277	6.775	509.25	9.316	6.775	521.64	9.500	6.675
7.5	494.52	9.204	6.741	498.37	9.238	6.744	509.30	9.415	6.634
10.0	485.10	9.136	6.710	488.63	9.167	6.714	498.62	9.333	6.610
12.5	476.57	9.075	6.682	479.60	9.101	6.686	489.01	9.259	6.586
15.0	468.71	9.018	6.654	471.44	9.031	6.660	480.24	9.191	6.564
17.5	461.48	8.965	6.629	463.92	8.986	6.634	472.16	9.128	6.544
20.0	454.80	8.917	6.605	456.96	8.935	6.609	464.76	9.070	6.523
22.5	448.61	8.871	6.583	450.47	8.887	6.586	457.87	9.016	6.486
25.0	442.72	8.827	6.561	444.46	8.842	6.563	451.47	8.965	6.469

The inclusion of dispersion forces through the DFT-D2 also influences the response of the *a* and *c* cell parameters to pressure. As was done in the previous section for the PBE-GGA calculations, the relative stiffness of the crystal axes can be quantified by fitting the cubes of their values to a BM3 EOS (equation II.4). For the *a* cell parameters, the zero-pressure bulk moduli K_0 are 79.4(3), 73.4(4), and 63.4(11) GPa for FAP, HAP, and CAP, respectively, while the corresponding derivatives $K_0^{'}$ are 4.1(1), 4.2(1), and 4.2(1). For

the cubes of the *c* cell parameters, the BM3 EOS fit parameters are K_0 = 132.3(4) and 147.4(17) GPa and $K_0^{'}$ = 5.7(1) and 4.5(1) for FAP and HAP, respectively.

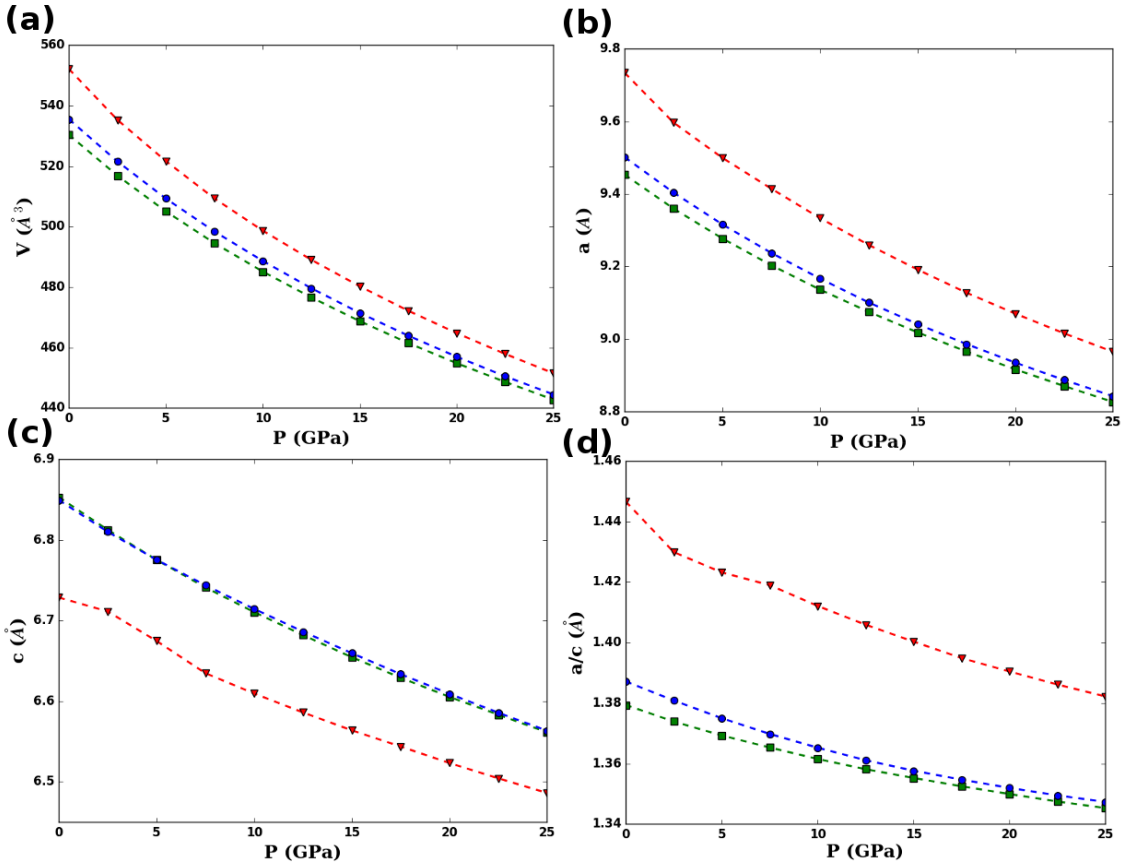

Fig. II.7 Pressure dependence of the (a) cell volumes, (b) *a* cell parameter, (c) *c* cell parameter, and (d) *a*/*c* ratio of FAP (green squares), HAP (blue circles), and CAP (inverted red triangles) calculated with dispersion forces treated using the DFT-D2 scheme

As was found in preceding section using DFT without a dispersion correction, the CAP *c* cell parameter cannot be meaningfully fitted to a BM3 EOS, as the compressibility of this axis changes at ~7.5 GPa. From Fig. II.7c, it can be seen that the DFT-D2 calculations predict that, in contrast to the DFT calculations, the *c* axis actually softens as it approaches this pressure, and then stiffens considerably above it. This anomaly in the *c* axis compressibility can, as in the DFT results, be attributed to the progressive increase of the *z*-

coordinate of the Cl^- ion with pressure. At 0 GPa, the *z*-coordinate is 0.449, greater than the value obtained using DFT with no dispersion correction. However, the DFT-D2 calculations predict a lower pressure sensitivity of the *z*-coordinate of the Cl^- anion, so that the Cl- anion reaches the site halfway between adjacent CaII triangles at approximately the same pressure as was predicted from DFT calculations without a dispersion correction (i.e. ~7.5 GPa). It is likely that this accounts for the qualitatively different response of the *c* axis to increasing pressure below the $P6_3 \rightarrow P6_3/m$ transition predicted by the DFT and DFT-D2 calculations, with the anomaly in the a/c ratios being more pronounced in the latter case, as can be seen by comparing Fig. II.2c and Fig. II.7c). We use FINDSYM (Stokes and Hatch 2005) to determine the space group of CAP. This changes from $P6_3$ to $P6_3/m$ at ~7.5 GPa, similar to the transition pressure determined from the dispersion-uncorrected simulations.

Table II.4 BM3 EOS parameters calculated for hexagonal FAP, HAP, and CAP using the cell volumes calculated using the DFT-D2 scheme. The last two columns are the 0 GPa bulk modulus and cell volume with K_0' set equal to 4.0.

	K_0 (GPa)	K_0'	V_0 (Å^3)	K_0	V_0 (Å^3)
FAP	91.7(2)	4.5(1)	530.3(1)	98.2(6)	529.0(4)
HAP	88.7(3)	4.4(1)	535.6(1)	93.6(5)	534.5(3)
CAP	78.4(4)	4.6(1)	551.7(1)	85.3(7)	549.9(5)

The monoclinic-hexagonal phase transition

Although only hexagonal apatite structures have so far considered here, both HAP (Elliott et al. 1973; Ma and Liu 2009) and CAP (Mackie et al. 1972) are known to have monoclinic symmetry at room pressure. Given the different behavior found for the hexagonal phases of

these two apatites, it is likely that the pressure dependence of the boundary between their hexagonal and monoclinic phases will also differ. To test this, we compute enthalpies of the monoclinic phases to 25 GPa and compare the enthalpy changes of the monoclinic to hexagonal phase transitions. In addition, to account for the possibility of a monoclinic FAP phase, the cell has been relaxed with F^- anion initially displaced along the [0001] axis (with opposite sense in adjacent channels) from its position at (0.0, 0.0, 0.25). However, at all pressures, it was found that FAP relaxes to the hexagonal crystal structure with space group $P6_3/m$.

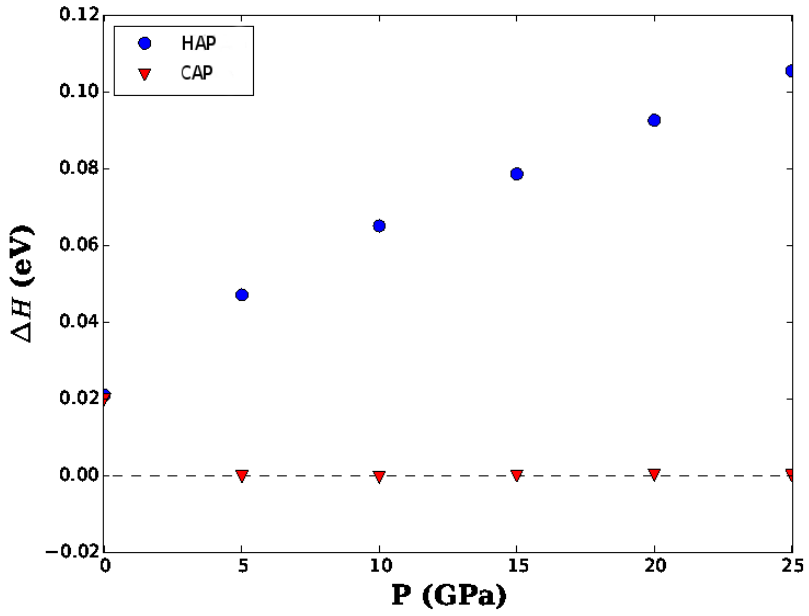

Fig. II.8 Plot of ΔH (per hexagonal cell) against pressure, for the phase transition from the monoclinic to hexagonal forms of HAP (blue circles) and CAP (inverted red triangles)

As can be seen from Fig. II.8, the stability of the monoclinic phase of HAP increases with pressure. This can be attributed to the fact that increasing pressure decreases the distance between adjacent channels, thereby strengthening the coupling between channel sites. In contrast, monoclinic CAP has the same enthalpy as hexagonal CAP above 7.5 GPa. Indeed,

analysis of the monoclinic and hexagonal crystal phases using the program FINDSYM (Stokes and Hatch, 2005) shows that they are structurally identical above this pressure (i.e. hexagonal with space group $P6_3/m$ and the Cl^- ion in the *2b* Wyckoff site). The well-established underbinding of GGA-type xc-functionals leads to overestimation of transition pressures. Consequently, the stability of monoclinic HAP relative to the hexagonal phase should be somewhat greater at constant pressure predicted using just the PBE-GGA xc-functional. The inclusion of dispersion forces using the DFT-D2 scheme has no substantial effect on the relative stabilities of the monoclinic and hexagonal phases, although the enthalpy difference between the hexagonal and monoclinic variants of HAP increases, from 0.02 eV/ hexagonal cell to 0.06 eV/hexagonal cell at 0 GPa and 0.11 eV/hexagonal cell to 0.19 eV/hexagonal cell at 25 GPa. The energy difference between the monoclinic and $P6_3$ hexagonal forms of CAP at 0 GPa calculated with DFT-D2 (0.06 eV/hexagonal cell) is also slightly higher than the ΔH of 0.02 eV/hexagonal cell calculated without a dispersion correction. While the energy difference between monoclinic and hexagonal cells is calculable, we note that ΔH is not large, being comparable to the thermal energy at ambient temperature, which means that the orientations of adjacent channels are not tightly coupled and considerable disordering of the channel orientations is to be expected at realistic temperatures.

Previous studies have suggested that hydroxyapatites may have ordered channels. Disordering of the orientations of the (OH)- groups in the channels has been proposed to be responsible for the high-T transition from $P2_1/b$ to $P6_3/m$ (Hochrein et al. 2005). However, de Leeuw (2010) noted that the coupling energy between adjacent columns is relatively small. Consequently, increasing the temperature should mean that, while the hydroxyl

groups within a channel should remain ordered, the orientations of the hydroxyl groups in adjacent channels are no longer correlated. This increases the symmetry of the crystal from $P2_1/b$ to $P6_3/m$. In this model, the disordering temperature depends (to first order) on the coupling between channels, which is roughly proportional to the relative stability of the monoclinic and (ordered, i.e. $P6_3$) hexagonal phases. Consequently, from the relative stabilities of the hexagonal and monoclinic phases calculated in this study, it is expected that the temperature at which the transition from monoclinic to hexagonal HAP occurs should increase with pressure.

By the same reasoning, CAP should form the disordered (i.e. $P6_3/m$) hexagonal phase at progressively lower temperatures as the pressure increases. The symmetrization of the channel site at high pressure means that the monoclinic phase can no longer exist, and above the transition pressure CAP will have the ordered hexagonal structure (with Cl at z=0.5) at all temperatures where apatite is stable. More detailed analysis on the effect of pressure on the temperature of the monoclinic to hexagonal phase transition would require a study of the free energy change across the phase boundary informed by molecular dynamics or lattice dynamics calculations. However, this is beyond the scope of the present work.

The apatite-tuite phase boundary

Enthalpies for the reaction whereby apatite decomposes to produce tuite and CaX_2 are calculated from using the enthalpies calculated with PBE-GGA without the DFT-D2 dispersion correction. As discussed in the Methodology section, CaF_2, $Ca(OH)_2$, and $CaCl_2$ all undergo phase transitions in the pressure range considered in study. Consequently, for

each pressure, we use the enthalpy of the stable CaX_2 phase at that pressure. Calculated enthalpies for reaction (II.1) are plotted in Fig. II.8, where it can be seen that the formation of tuite is quite sensitive to the identity of the channel anion in apatite, with CAP remaining stable to far higher pressures than either HAP or FAP. The transition pressure is lowest when the channel anion is F and highest when it is Cl, with transition pressures of 13.8, 15.5, and 26.9 GPa for FAP, HAP, and CAP, respectively. The ordering of the phase transition pressures is unchanged by the inclusion of a dispersion correction using the DFT-D2 scheme, although their values are reduced modestly to 8.0, 9.6, and 19.3 GPa for FAP, HAP, and CAP. These results suggests that, while HAP and FAP will disproportionate to form tuite + CaX_2 somewhere between the deep upper mantle and the upper transition zone, CAP may potentially remain stable into the lower mantle. In natural apatites, the occupancy of the channel depends on the origin of the apatite, with those in metasomatized mantle peridotites being more Cl^- rich and F^- poor, while those crystallized from magma at high-pressure are relatively F^- rich (O'Reilly and Griffin 2000; O'Reilly and Griffin 2013). Thus, the origin of an apatite crystal may influence the pressure at which it potentially decomposes to form tuite in the mantle.

HAP and CAP both have monoclinic polymorphs, which may influence the pressure of the apatite → tuite transition. Given that the monoclinic variant of CAP disappears at pressures well below the calculated apatite → tuite phase boundary, this will not affect the result when $X=Cl^-$. However, as shown above, in the case of HAP, pressure increases the stability of the monoclinic structure over the hexagonal structure, which will shift the apatite → tuite phase boundary to higher pressures. Nevertheless, as can be seen in Fig. II.8, this is a minor effect, and not enough to influence the relative ordering of the high-pressure

stabilities for the three apatite compositions. The pressure derivatives of the enthalpies for each of the three apatites are nearly identical. In contrast, the enthalpy per atom of $CaCl_2$ increases much more rapidly with pressure than either $Ca(OH)_2$ or CaF_2. Consequently, the strong dependence of the decomposition pressure on the channel anion is driven by the enthalpy of the CaX_2 phase, rather than that of apatite.

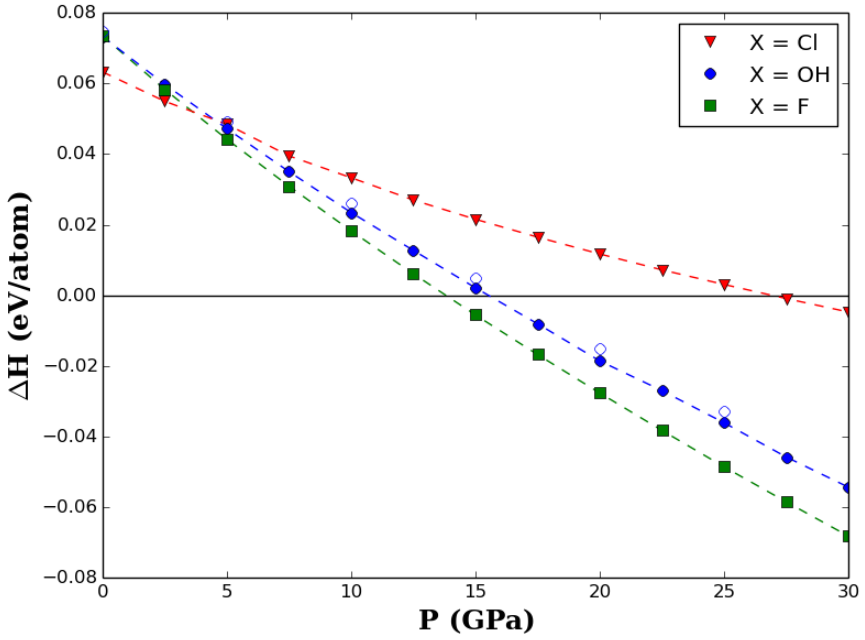

Fig. II.9 Calculated ΔH (per atom), obtained using DFT, for the decomposition of FAP (green squares), HAP (blue circles), and CAP (inverted red triangles) to produce tuite and CaX_2 (X=F, OH, Cl). Hollow symbols give the reaction enthalpy for monoclinic HAP

Clearly, the identity of the channel anion has a significant influence on the relative stability of the apatite and tuite assemblages. Indeed, our calculations predict that, while HAP and FAP decompose to form tuite + CaX_2 at pressures comparable to those in the upper transition zone, CAP can remain stable to considerably greater depths. Konzett and Frost (2009) reported the decomposition pressure of HAP in a system with a mid-ocean ridge basalt (MORB) composition, finding that tuite was produced at 7.5 GPa, lower than the

value reported by Murayama et al. (1986), which is halfway between the values calculated here with DFT and DFT-D2. Similarly, Konzett et al. (2012) reported, in an assemblage containing chlorapatite and phlogopite, tuite formed was present at below 9 GPa, significantly lower than the value reported in this study. In this case, the decomposition products included a Cl-rich fluid, which may be responsible for destabilizing CAP. This suggests that the presence of coexisting phases, whether minerals (Konzett and Frost 2009) or fluids (Konzett et al. 2012), can affect the pressure at which tuite forms from apatite, particularly in the case of CAP. Temperature will also reduce the pressure at which these decomposition reactions occur, but is unlikely to alter their relative order, with FAP decomposing at the lowest pressure and CAP persisting to greater depths.

II.4 Conclusions

In this study, *ab initio* calculations were used to examine the effect of different common channel anion species on the compressibility of apatite. It was found that channel anion identity has a substantial influence on the compressibility of apatite, as all three apatites displayed different pressure dependences of the cell parameters, bond lengths, and polyhedral volumes, as well as subtle structural features such as the metaprism twist and channel skew angles. However, the differences between CAP and the other apatites were far more significant than those between FAP and HAP. Moreover, the qualitative nature of the compression mechanism varied between the three apatites, with FAP compressing uniformly, HAP compressing through progressive displacement of the hydroxyl groups along the channels. In CAP, meanwhile, the Cl^- shifted along the channel at low pressure, but were constrained by symmetry to remain stationary above 7.5 GPa, greatly increasing

the stiffness of the *c*-axis. While the inclusion of dispersion forces using the DFT-D2 method decreases the cell volumes of all three apatites and increases their bulk moduli (at constant pressure), the ordering of these parameters does not change. The pressure at which the Cl^- site in CAP becomes 6-fold coordinated is also not significantly affected by the inclusion of dispersion forces, although the evolution of the CAP *c* axis compressibility below 7.5 GPa is modestly different.

This meant that, although the space groups of hexagonal FAP and HAP ($P6_3/m$ and $P6_3$, respectively) do not change over the pressure range studied, hexagonal CAP, whose space group is $P6_3$ at ambient conditions, has space group $P6_3/m$ above 7.5 GPa, associated with the development of a mirror planes at z = 0.25 and z = 0.75. This is associated with an increase in the coordination of the Cl^- channel anion from three to six-fold coordinated by the CaII sites. By calculating the enthalpies of the monoclinic structures, it was found that the compression anomaly in CAP coincides with a change in symmetry from monoclinic to hexagonal. While monoclinic HAP becomes more stable than hexagonal HAP with increasing pressure, monoclinic CAP ceases to exist above 7.5 GPa.

Chapter III. *Ab initio* crystal structure and elasticity of tuite, γ-$Ca_3(PO_4)_2$, with implications for trace element partitioning in the lower mantle

*This work was published as: R. Skelton and A. M. Walker, Contrib Mineral Petrol **172**, 87 (2017).*

III.1. Introduction

γ-$Ca_3(PO_4)_2$, whose mineral form is called tuite, is a high-pressure calcium orthophosphate with the palmierite structure (Murayama et al. 1986; Sugiyama and Tokonami 1987). It is the high-pressure polymorph of β-$Ca_3(PO_4)_2$ whitlockite although, unlike tuite, natural whitlockite invariably contains additional elements, principally Mg (Ionov et al. 2006). Tuite can also be formed through pressure-induced decomposition of apatite, and this is the route by which tuite is usually synthesized in experiments (e.g. Zhai et al. 2009; Zhai et al. 2013). Owing to its high-density crystal structure, tuite may occur in some parts of the Earth's mantle, and naturally occurring tuite has also been found in meteorite shock-melt veins (Xie et al. 2003; Xie et al. 2016).

If tuite is present in some regions of the Earth’s mantle, this would have implications for the storage and transport of trace elements, as tuite, like other calcium phosphate minerals, has large, high-coordination cation sites, permitting easy accommodation of a diverse range of impurity atoms, including U, Sr, the rare earth elements (REEs), and large ion lithophile elements (LILEs) (Sugiyama and Tokonami 1987). Indeed, Zhai et al. (2014) measured trace element concentrations in tuite crystals synthesized by decomposition of a natural apatite crystal at high pressure and temperature, finding high concentrations of Sr, Th, and

the REEs, with concentrations of the latter exceeding those of garnet and pyroxene by 2-3 orders of magnitude.

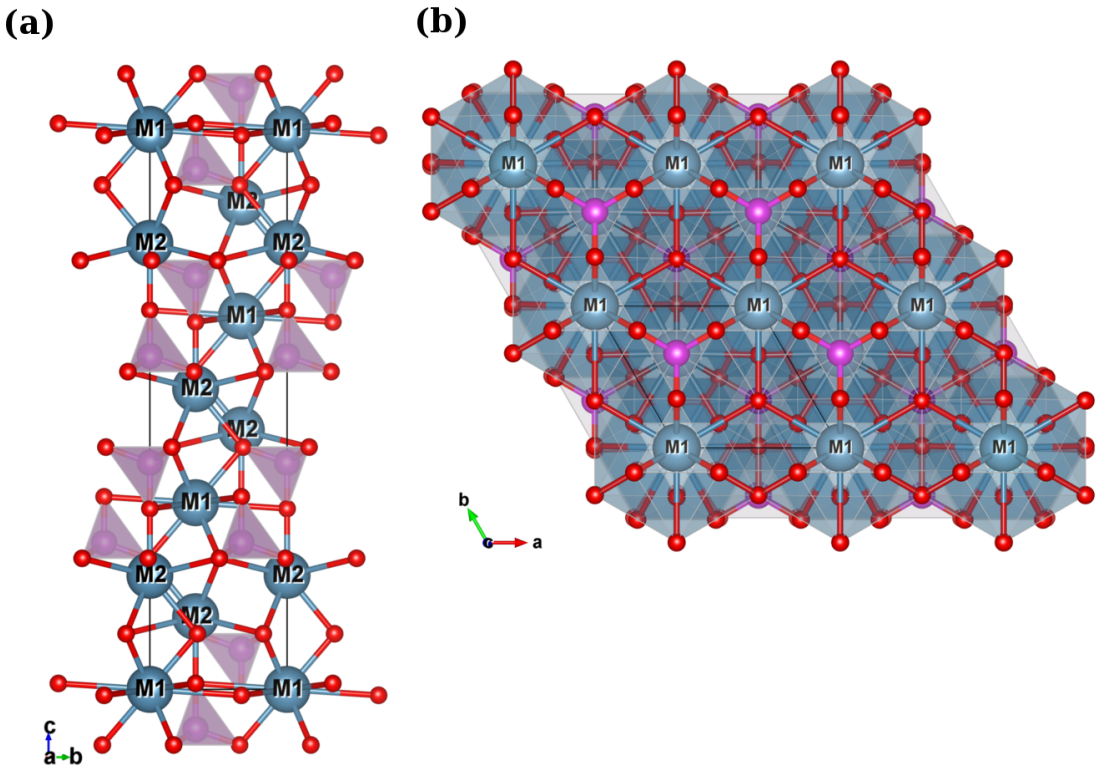

Fig. III.1 Crystal structure of tuite viewed along the (a) *a*-axis, and (b) *c*-axis. Images produced using the program VESTA 3 (Momma and Izumi, 2013)

The crystal structure of tuite has trigonal-high symmetry, with space group *R3m*. There are two distinct cation sites occupied by Ca, labeled M1 and M2, which are 12- and 10-fold coordinated by O, respectively. The unit cell contain 3 M1 site and 6 M2 sites, arranged in columns which have a characteristic “pinwheel” shape when viewed down [0001] (see Fig. III.1). P atoms are tetrahedrally coordinated by oxygen, with one bond aligned parallel to [0001], and the other three creating links between adjacent columns of polyhedra. The tuite crystal structure also occurs in other chemical systems, notably the strontium and barium

orthophosphates (Sugiyama and Tokonami 1990). In contrast to tuite, both γ-$Ba_3(PO_4)_2$ and γ-$Sr_3(PO_4)_2$ are stable under ambient conditions, and the latter has been used as a low pressure analogue for tuite (Zhai et al. 2011).

Despite its potential importance as a host for trace elements at high pressure, limited data is available on the effect of pressure on the crystal structure of tuite. Existing studies have tended to focus either on the crystal structure of tuite at ambient pressure, well away from the conditions at which it is expected to be an important host for trace elements (e.g. Sugiyama and Tokonami 1987; Thompson et al. 2013), or have obtained only cell volumes and lattice parameters at high pressure, as in Zhai et al. (2009; 2013). However, the potential significance of tuite for trace element hosting in the Earth's mantle is a consequence of size and compressibility of the Ca-O_n polyhedra, about which little is known at high pressure.

In this study, plane-wave density functional theory (DFT) is used to study the crystal structure and elasticity of tuite to pressures representative of the Earth's deep lower mantle. To evaluate its relative importance as a potential host for trace elements in the lower mantle, these properties are contrasted with those of $CaSiO_3$-perovskite (cpv), which is the dominant calcium bearing phase in the Earth's lower mantle, and the only other known mineral likely to contribute substantially as a host for trace elements at these pressures. In addition to the qualitative guidance facilitated by comparing the crystal structure and elastic properties of tuite and cpv, atomistic simulations of strontium and barium partitioning between the two minerals are performed, in order to probe the importance of atomic scale relaxation around the cation sites in tuite for trace element accommodation.

III.2. Computational methods

All atomistic calculations are performed using density functional theory (DFT, Hohenberg and Kohn, 1964; Kohn and Sham, 1965), which is a mean-field approach to solving the Schrödinger equation, as implemented in version 5.2.0 of the QUANTUM ESPRESSO software package (Giannozzi et al. 2009). The exchange-correlation (xc) energy was treated using the PBE generalized gradient approximation (GGA) xc-functional (Perdew et al. 1996). In all calculations, a kinetic energy cutoff of 60 Ry (~816 eV) was used, as this is sufficient to ensure convergence of the total energy of all phases studied to within <5meV/atom. Reciprocal space sampling was performed using the Monkhorst-Pack scheme (Monkhorst and Pack 1976). For the cubic phase of cpv, a grid size of 6x6x6 was sufficient to ensure convergence of the total energy to within <5 meV, while a grid size of 4x4x2 was sufficient to give converged energy values for tuite and the tetragonal variant of cpv. Ionic cores were treated using Vanderbilt ultrasoft pseudopotentials (Vanderbilt 1990), which are smoother than norm-conserving pseudopotentials, and hence require fewer plane waves for accurate calculations. The plane wave basis used for the auxiliary charge density has a cutoff energy 8 times that used for the wavefunction basis above. Valence configurations were $3s^2 3p^6 4s^2$, $3s^2 3p^3$, $3s^2 3p^5$, $2s^2 2p^4$, $2s^2 2p^5$, and $1s^1$ for Ca, P, Cl, O, F, and H, respectively. In point defect calculations valence configurations were $4s^2 4p^6 4d^1 5s^1$ and $5s^2 5p^6 6s^2$ for Sr and Ba, respectively. Cell parameters and atomic coordinates were relaxed using the BFGS quasi-Newton scheme (Pfrommer et al. 1997).

One key problem with GGA-DFT is that underbinding of the total energy results in larger cell volumes at a given pressure than are found experimentally. However, the pressure

dependence of cell parameters and material properties (including elastic constants, etc.) is well reproduced, and good agreement with experiment is achievable through the application of an Empirical Energy Correction (EEC; see e.g. Otero-de-la-Roza and Luaña 2011; Luo et al. 2013). The simplest such correction is the P_{SHIFT} EEC, in which an additional term E = $P_{SHIFT}V$ is added to the energy of the cell (Otero-de-la-Roza et al. 2011). In the case of GGA functionals, $P_{SHIFT} > 0$, which reduces the cell volume at constant (real) pressure. This correction works because the derivative of the total energy with respect to volume is computed more accurately than is the cell volume at constant pressure (Vanderbilt 1998), and has seen wide application in computational mineral physics (e.g. Oganov et al. 2001; Walker et al. 2008; Li et al. 2014). The value of P_{SHIFT} can be determined easily by comparing the computed cell volumes to experimental data, shifting the values of the former to the lower pressures to minimize the difference between the computed and experimental P-V curves.

The elastic constants relate stress to strain in the small-strain approximation (where Hooke's law is valid). They can be calculated from the total energy as $C_{ij}=\frac{1}{V}\frac{\partial^2 E}{\partial \epsilon_i \partial \epsilon_j}$. However, the accurate calculation of second derivatives in DFT is computationally expensive, and it is more common to apply a strain to the unit cell and relax its internal coordinates (i.e. atomic positions), from which the elastic constants are extracted by fitting to the linear stress-strain relation $\sigma_i = C_{ij}\epsilon_j$, a technique which has seen wide use in computational mineral physics (e.g. Karki et al. 1999; Stackhouse et al. 2005;). The number and type of strain patterns required to extract the elastic constants C_{ij} depends on

the number of independent, non-zero components the matrix has, which in turn depends on the symmetry of the crystal.

For tuite, which has rhombohedral (or trigonal-high) symmetry, the elastic constants matrix is

$$C_{ij}=\begin{pmatrix} C_{11} & C_{12} & C_{13} & C_{14} & 0 & 0 \\ C_{12} & C_{11} & C_{13} & -C_{14} & 0 & 0 \\ C_{13} & C_{13} & C_{33} & 0 & 0 & 0 \\ C_{14} & -C_{14} & 0 & C_{44} & 0 & 0 \\ 0 & 0 & 0 & 0 & C_{44} & C_{14} \\ 0 & 0 & 0 & 0 & C_{14} & C_{66} \end{pmatrix} \qquad \text{(III.1)}$$

where $C_{66}=(C_{11}-C_{12})/2$. As can be seen, this matrix has only six independent elastic constants, which can be uniquely determined using just two distinct strain patterns:

$$\varepsilon_1=\pm\delta\begin{pmatrix} 1 & 0 & 0 \\ 0 & 0 & 0 \\ 0 & 0 & 0 \end{pmatrix} \quad ; \quad \varepsilon_1=\pm\delta\begin{pmatrix} 0 & 0 & 0 \\ 0 & 0 & 1/2 \\ 0 & 1/2 & 1 \end{pmatrix} \qquad \text{(III.2)}$$

where δ is the magnitude of the applied strain. This applied strain cannot be too large, as the assumption of linear elasticity breaks down for large strain amplitudes. However, if δ is too small, the induced stress will be similar in magnitude to the errors introduced by the finite convergence criteria used in the ab initio calculations. In this study, six strain magnitudes of ±0.0333, ±0.0667, and ±0.1 a.u were used to fit the elastic constants.

The ability of tuite to act as a host for trace elements at lower mantle pressures was probed by calculating the energies of strontium and barium impurities in the tuite M1 and M2 sites,

and comparing these with equivalent defects sitting in the M site of tetragonal cpv. To minimize interactions between the inserted impurity and its periodic images, the calculations (for both tuite and cpv) were performed in 2x2x1 supercells, which corresponds to a minimum distance between defects at 100 GPa of 9.13 angstroms in the *a*-*b* plane and 17.2 angstroms along *c* in tuite. For cpv, the minimum distance between defects at 100 GPa was 6.7 angstroms along *c* and 9.3 angstroms in the *a*-*b* plane.

III.3. Results and Discussion

High pressure crystal structure and equation of state

The crystal structure of tuite was calculated using DFT at applied pressures in the range 0-125 GPa. As described in section 2, the underbinding of the PBE-GGA xc-functional is corrected using the P_{SHIFT} EEC, which is determined by fitting the calculated cell volumes to the high pressure cell volumes reported in Zhai et al. (2009, 2013), giving P_{SHIFT} = -3.6 GPa. In Table III.1, cell parameters and internal coordinates calculated for tuite at 0 GPa pressure (nominal and pressure corrected) are compared with x-ray diffraction data from Sugiyama and Tokonami (1987) and Thompson et al. (2013). As is usual for GGA xc-functionals, the uncorrected cell parameters are substantially larger than the experimental values. After the application of the P_{SHIFT} EEC, the match between the experimental and calculated cell parameters is much closer, although the predicted *a*-parameter is marginally larger than those found by Sugiyama and Tokonami (1987) and Thompson et al. (2013), while the *c*-parameter is smaller.

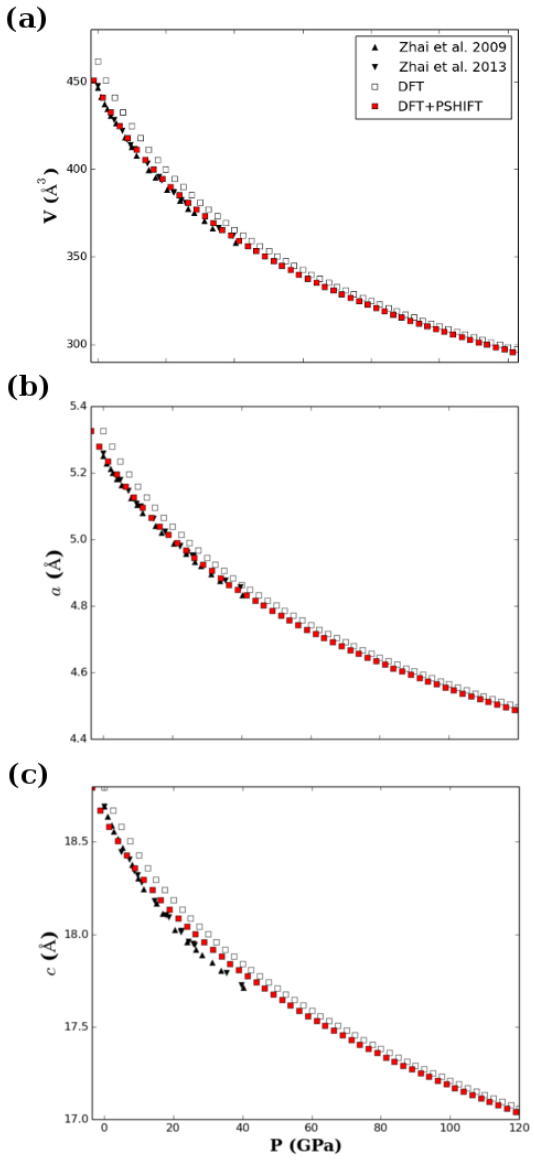

Fig. III.2 Calculated pressure dependence of the (a) volume, and (b) *a* and (c) *c* cell parameters, compared with x-ray diffraction measurements of synthetic tuite (Zhai et al. 2009; Zhai et al. 2013)

The calculated *P*-*V* data for tuite (with and without the P_{SHIFT} EEC) is then fit to a BM3 equation of state (EOS)

$$P(V)=\frac{3K_0}{2}\left[\left(\frac{V_0}{V}\right)^{7/3}-\left(\frac{V_0}{V}\right)^{5/3}\right]\times\left[1+\frac{3}{4}\left(K_0^{'}-4\right)\left\{\left(\frac{V_0}{V}\right)^{2/3}-1\right\}\right] \qquad \text{(III.3)}$$

Table III.1 Cell parameters and atomic positions from DFT calculations at 0 GPa applied and nominal pressure, compared with experimental values

	DFT	DFT+EEC	Expt.[a]	Expt.[b]
a (Å)	5.3260	5.2588	5.2487	5.2522
c (Å)	18.7942	18.6341	18.6735	18.690
V (Å^3)	461.7	446.3	445.5	446.5
Ca2 z	0.20358	0.20293	0.2036	0.20359
P z	0.40481	0.40501	0.4052	0.40508
O1 z	0.32275	0.32243	0.3235	0.32372
O2 x	0.17315	0.17185	0.1742	0.17370
O2 z	0.09930	0.09978	0.0994	0.09950

[a] Sugiyama and Tokonami (1987)

[b] Thompson et al. (2013)

where V_0 is the cell volume, K_0 is the bulk modulus, and K_0' is the pressure derivative of K_0, all at zero pressure. Since the calculated cell volumes extend to high compression ratios, where the BM3 equation of state can be inadequate (due to the assumption of infinitesimal strain), the *P*-*V* data is also fit to a Vinet EOS (Vinet et al. 1986), which has the form

$$P(V) = \frac{3K_0\left(1-\left(V/V_0\right)^{1/3}\right)}{\left(V/V_0\right)^{2/3}} \exp\left[\frac{3}{2}\left(K_0'-1\right)\left(1-\left(V/V_0\right)^{1/3}\right)\right] \quad \text{(III.4)}$$

where the symbols have the same meaning as for the BM3 equation of state. BM3 and Vinet EOS fit parameters are presented in Table III.2.

Table III.2 Parameters for the Vinet and BM3 EOS fit to the DFT and DFT+EEC cell volumes from this study and the cell volumes measured experimentally by Zhai et al. (2009) (Vinet EOS parameters have been recalculated here from the published data)

EoS		DFT	DFT+EEC	Zhai et al. (2009)
BM3	K_0 (GPa)	104.2(9)	119.4(8)	100.2(13)
	$K_0^{'}$	4.56(2)	4.38(2)	5.48(16)
	V_0 (Å^3)	460.3(5)	445.8(3)	446.3(1)
Vinet	K_0 (GPa)	97.2(6)	114.1(6)	101.2(44)
	$K_0^{'}$	5.04(1)	4.87(2)	5.57(3)
	V_0 (Å^3)	461.8(3	446.5(2)	446.1(9)

The pressure-uncorrected zero-pressure cell volume, V_0, is greater than the experimental value (Zhai et al. 2009), although the value of K_0 agrees closely with experiments. In contrast, while the values of V_0 obtained from BM3 and Vinet fits to the DFT+EEC data shown in Fig. III.2 agree closely with the corresponding values obtained by fitting to the experimental data of Zhai et al. (2009), the fitted values of the zero pressure bulk modulus, K_0, exceeds those obtained by fitting to experimental data, by 19 GPa when using the BM3 EOS and 13 GPa when using the Vinet EOS. The fitted value of the pressure derivative of the bulk modulus, $K_0^{'}$, is also substantially different from that obtained from experimental measurements. For instance, the Vinet EOS gives $K_0^{'}$ = 4.87 for the *ab initio P-V* data, whereas the value obtained for the cell volume data of Zhai et al. (2009) is 5.57. In consequence, the calculations here suggest that tuite is stiffer at ambient pressure

than reported in experiments, but that its bulk modulus is considerably less sensitive to pressure.

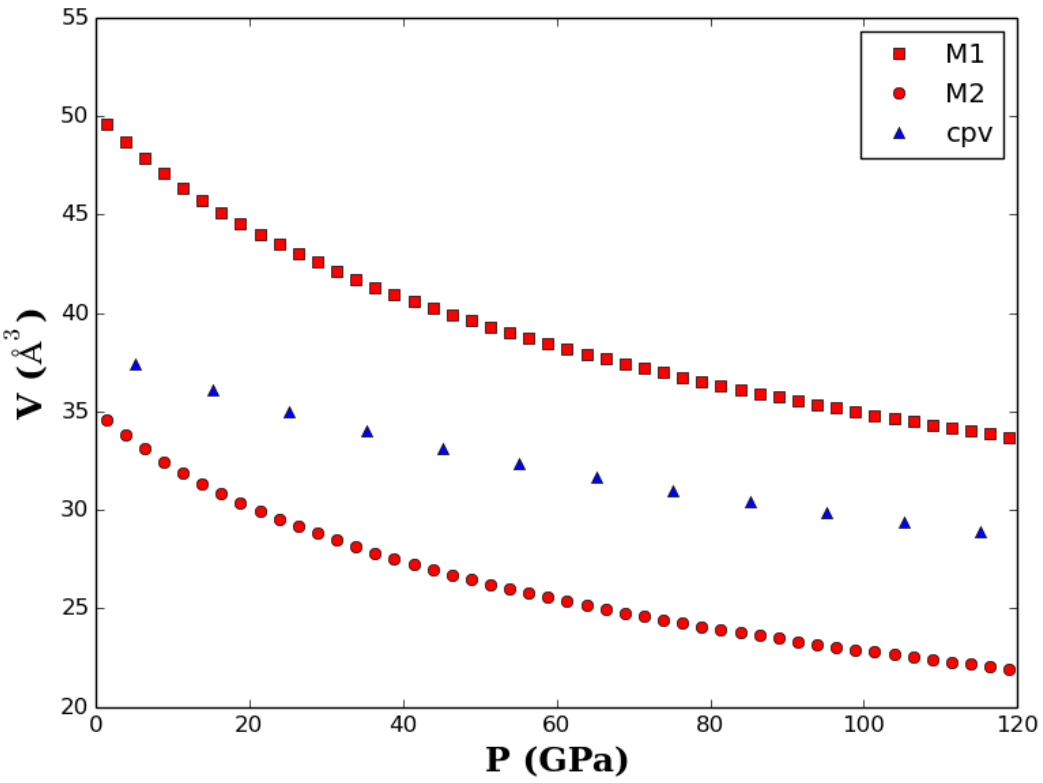

Fig. III.3 Volumes of the M1 (12-coordinated) and M2 (10-coordinated) Ca-O_n polyhedra in tuite, compared with the volume of the Ca site in tetragonal cpv

The relative flexibility and compressibility of the cation sites in phosphate minerals enables them to serve as excellent hosts for impurity ions. However, to determine the compressibility of a site, its volume needs to be defined. Here, the site volume is defined to be that of the polyhedron whose vertices are the oxygen ions surrounding the site. The volumes of the M1 and M2 sites calculated in this way are shown in Fig. III.3. Fitting Vinet equations of state to the calculated pressure-volume relationships of the two M sites gives

K_0 = 116.1 GPa, K_0' = 4.97, and V_0 = 50.2 for M1, and K_0 = 94.2 GPa, K_0' = 4.44, and V_0 = 35.1 for M2. Thus , M1 is the larger, but more incompressible cation site. M1 has two bond types, six connecting with O1 oxygen and 6 six connecting to O2 oxygen atoms. The M2 site has three distinct bond types, one connecting with O1, 3xCa-O2(a), and 6xCa-O2(b) bonds, where the bonds for each polyhedron have been listed in order of increasing length. In M1, the compressibility of each bond is similar while, for M2, the Ca-O1 bond is considerably stiffer than the other bond types, while the Ca-O2(a) bonds are both shorter and more compressible than the Ca-O2(b) bonds and much more compressible at low pressure, with the difference between the two diminishing at high pressure.

Table III.3 Vinet EoS fit parameter for the M1 and M2 cation sites in tuite, and the M site in *Pm*-3*m* and *I*4/*mcm* cpv. Values in bold are fits are for the pressure-corrected cation site volumes

	K_0 (GPa)	K_0'	V_0 (Å^3)
M1	98.1(1)/**116.1(1)**	5.15(2)/**4.98(3)**	51.93(5)/**50.23(3)**
M2	78.9(6)/**94.2(7)**	4.62(2)/**4.44(2)**	36.61(3)/**35.13(3)**
cpv (*P*m-3m)	213.6(25)/**234.1(23)**	4.40(6)/**4.30(5)**	39.15(3)/**38.34(2)**
cpv (*I*4/mcm)	212.0(14)/**232.3(13)**	4.36(3)/**4.26(3)**	39.09(2)/**38.25(1)**

Fitting the computed volumes of the PO_4 tetrahedra to a Vinet EOS, giving K_0 = 363.6(32) GPa, V_0 = 1.9498(8), and K_0' = 5.47(7). As expected, the PO_4 tetrahedra are significantly more incompressible than either of the Ca-bearing sites. Each PO_4 tetrahedron has two distinct bond types: one P-O1 bond and three P-O2 bonds. Of these, the P-O1 bond, which

is parallel to [0001], is found to be the less compressible, with the consequence most of the shortening of the c-cell parameter with increasing pressure is achieved by compressing and distorting the M1 and M2 polyhedra.

Elasticity

The first step in determining the elastic stability of tuite is to calculate its anisotropic elastic constants, which is achieved here using the finite strain approach described in the methods section. The calculated zero-pressure elastic constants are tabulated in Table III.4, where it can be seen that C_{33} is significantly greater than any of the other elastic constants, consistent with the fact that the principal structural motifs in tuite are chains of linked Ca polyhedra and PO_4 tetrahedra that sit parallel to [0001].

Table III.4 Calculated elastic constants of tuite at 0 GPa applied and nominal pressure. K^{VRH} and G^{VRH} are the Voigt-Reuss-Hill averages of the isotropic bulk and shear moduli, respectively

	DFT	DFT+EEC
C_{11}	151.0(30)	181.1(29)
C_{12}	68.2(5)	74.7(6)
C_{13}	58.3(11)	74.1(12)
C_{14}	5.5(4)	6.7(4)
C_{33}	208.0(36)	249.2(31)
C_{44}	21.9(5)	37.0(4)
K^{VRH}	97.1(9)	116.4(9)
G^{VRH}	35.0(5)	49.0(4)

Looking now at their pressure dependence (Fig. III.4a), we see that C_{33} remains greater than the other elastic constants across the pressure range 0-125 GPa. In particular, the gap

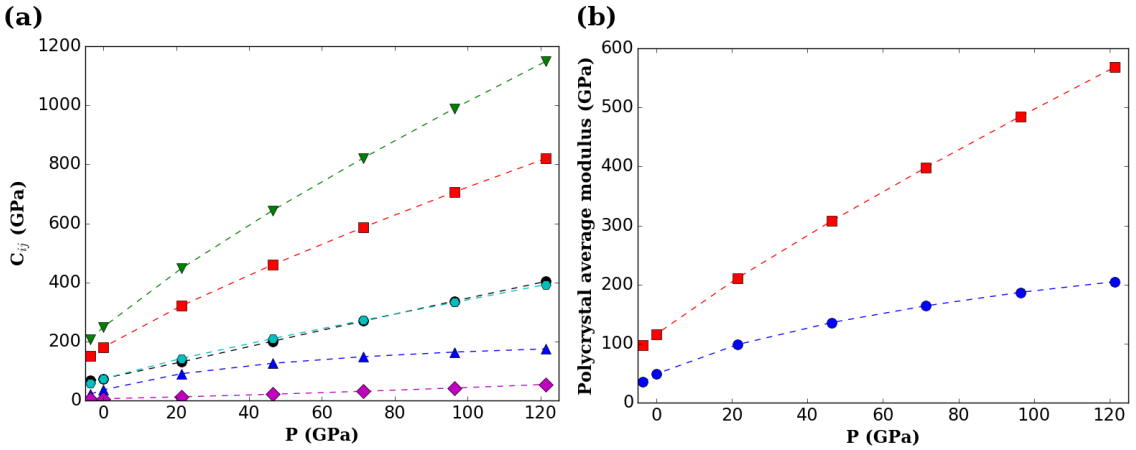

Fig. III.4 (a) C_{11} (inverted triangles), C_{33} (red squares) C_{13} (cyan circles), C_{12} (black circles), C_{14} (blue triangles), and C_{44} (purple diamonds) anisotropic elastic constants, and (b) Voigt-Reuss-Hill average bulk (red squares) and shear (blue circles) moduli of tuite, as functions of pressure

between C_{33} and C_{11} increases with pressure, showing that the *c*-axis stiffens more with increasing pressure than does the *a*-axis. C_{13}, although less than C_{12} under ambient conditions, stiffens much more rapidly with pressure and quickly exceeds the value of the latter. This trend reverses at high pressure, however, such that $C_{12} > C_{13}$ above 100 GPa. Finally, C_{14} and C_{44} are largely independent of P, although the latter does increase moderately at low pressure. The wide disparity in the pressure dependence of the different elastic constants suggests that tuite is a highly anisotropic mineral. This can be demonstrated quantitatively by calculating the Universal Anisotropy Index, defined as (Ranganathan and Ostoja-Starzewski 2008)

$$A^U = 5\frac{G^R}{K^R} + \frac{G^V}{K^V} - 6 \qquad \text{(III.5)}$$

where G is the shear modulus, K is bulk modulus, and the superscripts R and V refer the Reuss (homogeneous stress) and Voigt (homogeneous strain) bounds, respectively. For an

elastically isotropic crystal, A^U = 0, and it increases with any departure from isotropy. At 0 GPa applied pressure, A^U=1.186, decreasing rapidly to 0.520 at 3.6 GPa applied pressure (0 GPa nominal pressure). It then increases gradually with increasing pressure, reaching a value of 0.707 at 125 GPa applied pressure (121.4 GPa nominal pressure). By way of comparison, Walker (2012) used DFT to calculate the elastic constants of diopside, one of the more anisotropic minerals in the Earth's upper mantle, and found that for this mineral, A^U has a value of just 0.495 at 0 GPa, which decreases to 0.312 at 20 GPa.

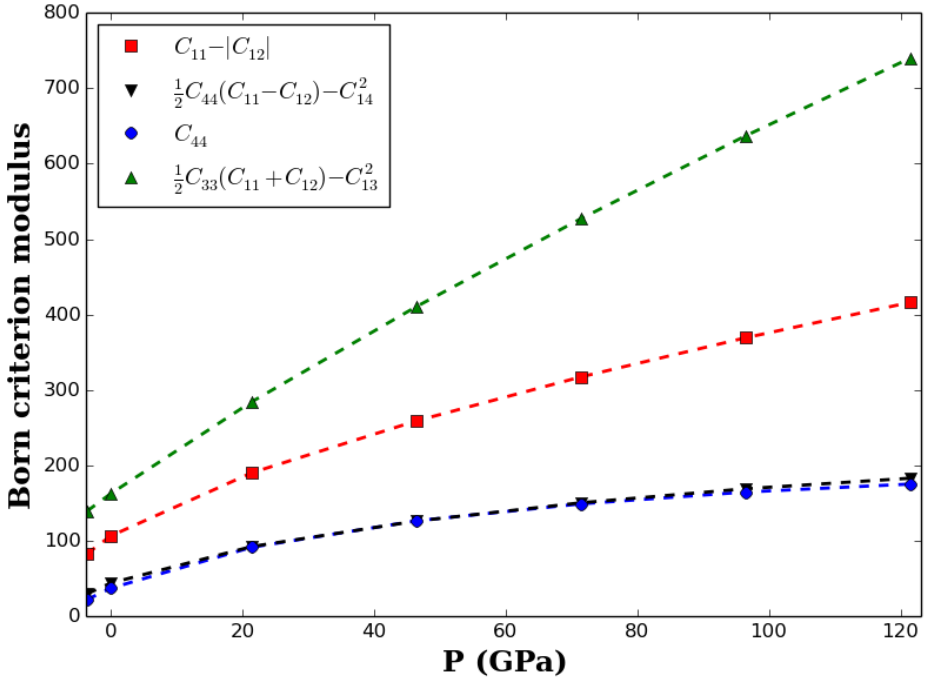

Fig. III.5 Born criteria for tuite, computed from the calculated anisotropic elastic constants. The criteria represented by blue circles and red squares have units of GPa, while values for the remaining Born criteria are given in units of GPa^2

Knowledge of the elastic constants permits the computation of the Born stability criteria for tuite, which give a measure of the elastic stability of a crystal. Originally formulated for crystals with cubic symmetry (Born 1940), the stability criteria are constraints which the

elastic constants must satisfy in order for a crystal to be stable against perturbations of its cell volume or shape. This is equivalent to requiring that any applied strain increase the internal energy of the crystal, which is satisfied when the eigenvalues of the elastic constants matrix are greater than zero. From these considerations, Mouhat and Coudert (2014) have derived the Born stability criteria for low-symmetry crystals; the relevant expressions for tuite (which has trigonal-high symmetry) are

$$\begin{aligned} C_{11} - |C_{12}| &> 0 \\ C_{44} &> 0 \\ \frac{1}{2} C_{33}(C_{11} + C_{12}) - C_{13}^2 &> 0 \\ \frac{1}{2} C_{44}(C_{11} - C_{12}) - C_{14}^2 &> 0 \end{aligned} \qquad \text{(III.6)}$$

The Born stability criteria for tuite calculated using the calculated using DFT are plotted in Fig. III.5. As can be seen, all four stability criteria are positive and monotonic increasing over the pressure range 0-125 GPa, showing that tuite is *elastically* stable at all pressures relevant to the Earth's mantle. This does not, however, preclude the possibility that it is only metastable at high pressure, or that there are symmetry reducing instabilities associated with imaginary phonon modes.

Comparison with $CaSiO_3$ perovskite

$CaSiO_3$ perovskite (cpv) is the third most abundant phase in the lower mantle (after bridgmanite, $(Mg,Fe)SiO_3$, and ferropericlase, (Mg,Fe)O), comprising approximately 5% of the region's mass (e.g. Wood 2000). It consists of corner-linked network of SiO_6 octahedra, with 12-coordinated Ca ions filling the voids. This cation site is larger than those in bridgmanite and ferropericlase, and $CaSiO_3$ perovskite is thus likely to be an important

reservoir for trace elements such as Sr and the rare earth elements (REEs) in the lower mantle (Corgne et al. 2005). There is some disagreement about its crystal structure, and the stable phase has been proposed to be either cubic or tetragonal, with some researchers finding a space group of *Pm-3m* (Wentzcovitch et al. 1995), while others report space group to be *I4/mcm* (e.g. Shim et al. 2002; Jung and Oganov 2005; Adams and Oganov 2006). Recent molecular dynamics simulations have tried to reconcile these conflicting views by showing, while the tetragonal phase is stable at lower temperatures, the cubic (*Pm*-3*m*) phase may be entropically stabilized at mantle temperatures (Sun et al. 2014).

As cpv is considered to be a major host for trace elements, any evaluation of the effectiveness of tuite as a host for trace elements will be determined by its relative ability to accommodate impurities over cpv. To perform this comparison, we have computed the crystal structure of $CaSiO_3$ perovskite to an applied pressure of 130 GPa. To compensate for the underbinding of the GGA, a P_{SHIFT} EEC was applied by fitting the calculated cell volumes of the *I4/mcm* phase to experimental data (Shim et al. 2002), from a value of P = -4.8 GPa was obtained. The *Pnam* phase has the lowest enthalpy for $P < 15$ GPa, while above that the *I4/mcm* phase has the lowest enthalpy. At no pressure in the range 0-130 GPa is the cubic polymorph the most stable structure. However, as was found by Caracas et al. (2005), the enthalpies of the three polymorphs are very similar.

From the crystal structures, it is possible to compute volumes for the CaO_{12} polyhedra in each polymorph, for which BM3 and Vinet EOS fit parameters are presented in Table III.3. The values obtained for the zero-pressure cell volume V_0 and compressibility K_0 of the CaO_{12} polyhedra are nearly identical for the two polymorphs. Consequently, while we use

only the lower enthalpy *I*4/*mcm* structure to determine point defect substitution energies, the insensitivity of the M site properties to cell symmetry mean that the results are equally relevant for cubic cpv.

Comparing the cpv Ca-O_{12} polyhedron with those of the cation sites in tuite, we see that the cpv M site is larger than the M2 polyhedron in tuite, but smaller than the M1 polyhedron. It is also significantly more incompressible than either of the Ca-O_n polyhedra in tuite, which causes the volumes of the cpv Ca-O_{12} and tuite M1 polyhedra to converge at high pressure, with V_{M1}/V_{cpv} = 1.31 at 0 GPa, but 1.17 at 120 GPa. For the same reason, the volumes of the cpv Ca-O_{12} and the tuite M2 polyhedron diverge with increasing pressure, so that V_{M2}/V_{cpv} = 0.92 at 0 GPa, but only 0.76 at 120 GPa. Although the M sites in tuite compress more rapidly than the cpv M site, their bulk moduli are more pressure sensitive, causing K_{M1}/K_{cpv} to increase from 0.51 at 0 GPa to 0.87 at 120 GPa, while K_{M2}/K_{cpv} increases from 0.41 to 0.76 over the same pressure range. This should affect trace element partitioning between the two minerals, with the partition coefficients expected to be closer to unity at high rather than low pressures.

Modeling the lattice strain energy

A qualitative guide to the relative impurity substitution energies in cpv and tuite can be obtained using the lattice strain model of Brice (1975). To look at trace element partitioning, we compute the elastic substitution energies for defects with a range of different ionic radii using the model developed by Brice (1975) and applied to trace element partitioning in minerals by Blundy and Wood (1994). In this model, the impurity

atom is modeled as a spherical defect inserted into an isotropic elastic continuum, whose energy is

$$E_i(r) = 4\pi Y\left(\frac{r_0}{2}(r-r_0)^2 + \frac{1}{3}(r-r_0)^3\right) \quad \text{(III.7)}$$

where Y is the Young's modulus, r_0 the radius of crystallographic site i, and r is the ionic radius of the substituted ion. Since ionic radii are poorly defined, the factors of $(r\text{-}r_0)$ in equation (III.7) are sometimes written in terms of metal-oxygen bond lengths, R, as

$$E_i(r) = 4\pi Y\left(\frac{r_0}{2}(R-R_0)^2 + \frac{1}{3}(R-R_0)^3\right) \quad \text{(III.8)}$$

This expression is not, however, completely independent of the ionic radius, which still appears in the pre-factor of the quadratic term. Using this expression, the difference between the energy of an impurity element with metal-oxygen bond length R substituting for calcium in site M_i in tuite and that same element substituting for Ca in cpv is

$$\Delta E_{M_i}(R) = E_{M_i-tuite}(R) - E_{M-cpv}(R) \quad \text{(III.9)}$$

where the energy of the impurity in each site is calculated using equation (III.8), with the appropriate Young's modulus and equilibrium Ca-O bond length.

To calculate substitution energies, we use the average Ca-O bond lengths calculated for the M1 and M2 sites in tuite and the *I4/mcm* cpv polymorph. The Young's modulus, Y, for a polyhedral site is approximately $K/(1-\nu)$, where K and ν are the bulk modulus and compressibility, respectively. For tuite, ν is nearly constant across the entire pressure range

studied, decreasing from 0.34 at 0 GPa to 0.30 at 25 GPa, before gradually increasing to 0.34 at 125 GPa while the Poisson's ratio of *I4/mcm* cpv is 0.28 at 0 GPa, increasing monotonically with pressure to reach 0.33 at 125 GPa. For simplicity, it is assumed that the contribution of the impurity to the volume of the system is negligible (i.e. that we are working in the dilute limit), so that the enthalpy of the substitution reaction is entirely due to the internal energy of the defect in the lattice. The ionic radius r_0 of Ca^{2+} is taken to be 1.37 Å for 10-fold coordinated and 1.48 Å in 12-fold coordination (Shannon 1976).

From these parameters, the energies of impurity elements in the tuite M1 and M2 sites, relative to their energy in the cpv M site, can be calculated using equation (III.9), and are plotted as functions of pressure and impurity atom metal-oxide bond length (relative to the average Ca-O bond length in cpv) in Fig. III.6. As can be seen, impurities with relatively large metal-oxygen bond lengths will strongly prefer the M1 site in tuite over the cpv M site, an effect that increases with pressure. Smaller impurities, however, have a lower energy when substituting into the cpv M site than the tuite M1 site. The picture is more complicated for the M2 site. At low pressures, both large and small impurities have significantly lower energies when sitting in the tuite M2 site than in the cpv M site. However, at high pressures, as the bulk moduli and, hence, Young's moduli of the two sites converge, $\Delta E(R)$ increases for impurities whose metal-oxygen bond length exceeds that of the cpv M site, and decreases for impurities with shorter metal-oxygen bond lengths, so that small impurities partition more strongly into the tuite M2 site.

Consequently, at all pressures found in the Earth's mantle, impurities whose metal-oxygen bond lengths differ from the average Ca-O bond length found in cpv may be expected to

partition strongly from that mineral into tuite, and tuite, where present, should be a major reservoir for trace elements throughout the mantle. However, the site occupancy of these trace elements in tuite will be pressure dependent. At low pressure, the lattice strain

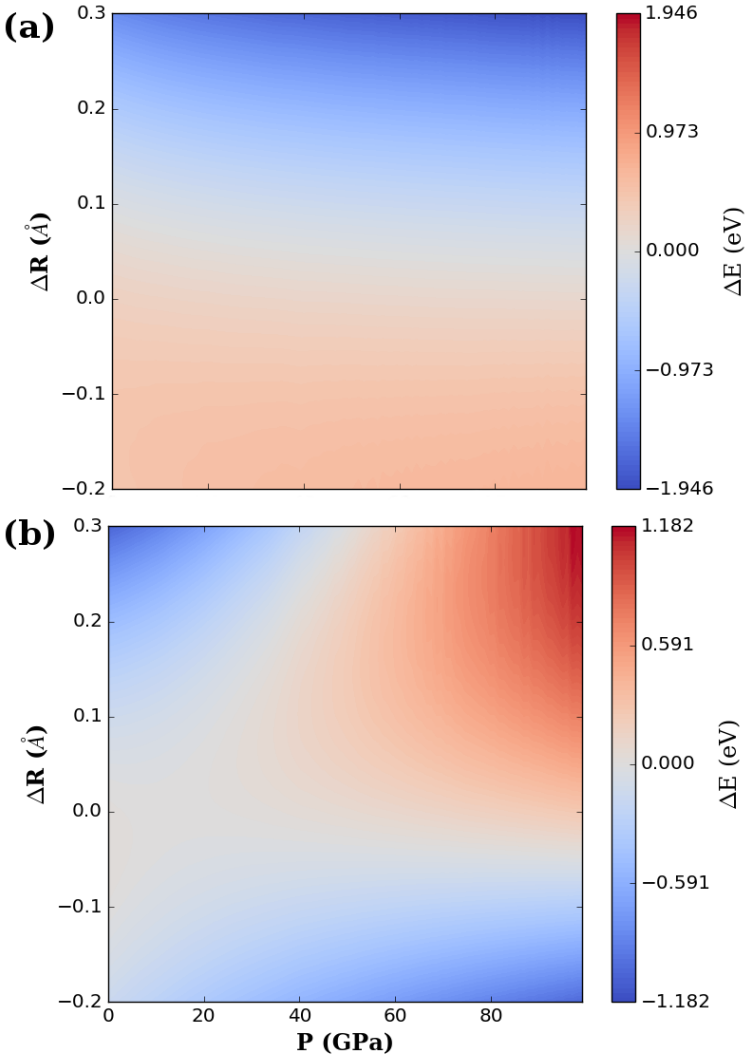

Fig. III.6 Differences between elastic strain energies for defects in the (a) the M1, and (b) M2 sites in tuite, and defects in the cpv M site. Here, Δ*R* is the difference between the average Ca-O bond length in cpv and the metal-oxygen bond length of the impurity

energies calculated for large cations are broadly similar for the M1 and M2 sites, suggesting no significant partitioning between the two sites. As the pressure increases, the lattice strain energies of large cations in the M2 site, relative to that calculated for the M1 site, increases substantially, with the consequence that trace elements with large radii will partition strongly into the latter site. Conversely, the site occupancy of small cations is predicted to be comparatively pressure insensitive, as the lattice strain energy of the M2 site is significantly lower than that of the M1 site for small *R*, at all pressures.

While the above analysis assumed that the substituting ion was divalent, the conclusions can readily be extended to other impurities since, as shown by Hazen and Finger (1979), the Young's modulus of a site is proportional to the charge of the substituting ion. For monovalent impurities (e.g. Na^+ and K^+), the tuite-cpv partitioning energies can be obtained by scaling those shown in Fig. III.6 for divalent impurities by a factor of 0.5, while scaling the energies in Fig. III.6 by a factor of 1.5 gives the partitioning energies for trivalent impurities, such as the REEs. As the latter have considerably smaller radii than calcium (Shannon 1976), it immediately follows that they should partition from cpv into tuite, and will partition more strongly at high pressure.

Partitioning of divalent impurities between γ-$Ca_3(PO_4)_2$ and $CaSiO_3$

The elastic substitution model has been used to predict trace element partitioning between phases, encompassing a wide range of different minerals and impurity atoms (see e.g. Wood and Blundy 1997; van Westrenen et al. 2000). However, impurity energies calculated this way are inherently qualitative, as they do not take into account the specifics of local atomic relaxation around a substitution site to accommodate an impurity atom, the elastic

anisotropy of the crystal, or changes in the nature of the bonding. To see how these effects may influence partitioning of trace elements between tuite and cpv, substitution energies were calculated for strontium and barium defects sitting in the cation sites of both of these minerals, over the pressure range 0-100 GPa. As the properties of the cpv M site are largely independent of the exact symmetry group (cf. Table III.3), defect energies were calculated only for the tetragonal phase.

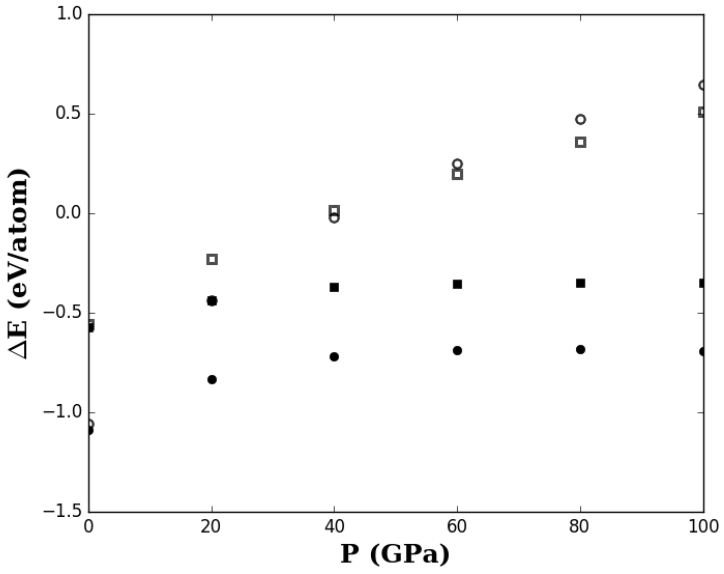

Fig. III.7 Difference between the enthalpy of strontium (circles) or barium (squares) impurity substituting for calcium in tuite, and an equivalent defect in cpv. Filled symbols correspond to the M1 site in tuite (12-fold coordination), while hollow symbols correspond to the M2 site (10-fold coordination)

The calculated energies of strontium and barium defects in the tuite M1 and M2 sites are compared with those of equivalent in defects sitting in the M site of cpv in Fig. III.7. The energy of a strontium ion sitting in the tuite M1 site is -0.57 eV lower than the energy of the corresponding defect in the cpv M site, while the energy of a strontium impurity in the tuite

M2 site is -0.56 eV lower. For barium defects sitting in the tuite M1 and M2 sites the relevant values are -1.09 and -1.06 eV, respectively. Consequently, strontium and barium should partition strongly into tuite at low pressures, displaying no particular preference for either of the two cation sites.

Although similar partitioning energies are found for the two cation sites in tuite at ambient pressure, the relative energies of strontium and barium defects in M1 and M2 diverge as the pressure increases. For divalent impurities in the M2 site, their energies relative to equivalent defects in cpv increase with pressure. Above ~40 GPa, strontium and barium have lower energies in the cpv M site than the tuite M2 site, and the energy difference between the two sites reaches 0.51 eV (strontium) and 0.64 eV (barium) at 100 GPa. Similarly, the energies of strontium and barium defects in the tuite M1 site relative to those the cpv M site increase with pressure, although in this case the energy differences remain negative across the entire pressure range considered here, Ultimately, as can be seen in Fig. III.7, the energy difference converges to a constant value above ~60 GPa, which is -0.35 and -0.69 eV/atom for strontium and barium, respectively. This behavior contrasts sharply with that seen for the M2 site, where the energy difference between impurities in that site and the M site of cpv continues to increase rapidly even at the highest pressures. Consequently, although tuite remains the principal host of strontium and barium at higher pressures, the relative solubility of both elements in tuite compared with cpv should decrease, both because of the converging substitution energies in the two minerals and because of the reduced ability for the tuite M2 site to host large cations at high pressure.

The partition coefficient D_J for a species J between site Mi (i=1,2) in tuite and the cpv M site is

$$D_J = 1/3 \cdot \exp\left(-\Delta G_{M1}/k_B T\right) + 2/3 \cdot \exp\left(-\Delta G_{M2}/k_B T\right) \quad \text{(III.10)}$$

where T is temperature, k_B is Boltzmann's constant, and ΔG_1 and ΔG_2 are the free energies of the exchange reaction between the cpv M site and tuite sites M1 and M2, respectively. Following Lee et al. (2009), the vibrational entropy term S_{vib} in the Gibbs free energy difference of the exchange reaction between the two sites, ΔG_i, will approximately cancel, in this case because tuite and cpv are assumed to coexist. In the dilute limit considered here, the configurational entropy is much smaller than the enthalpy of reaction, and so can be neglected. Since the excess volume of the impurity element is should also be approximately equal in the two phases, ΔG_i can thus be replaced by the internal energy difference, ΔE_i. Partition coefficients for strontium and barium partitioning between cpv and tuite can be computed using the reaction energies calculated above for strontium and barium partitioning from cpv into the M1 and M2 sites of tuite (Fig. III.7). From the temperature profile computed by Ono (2008), the mantle temperature at 20 GPa is ~2000 K, so that the partition coefficient D_{Sr} = 6.8. At 60 GPa and 2300 K, representative of mid-mantle conditions, it decreases to 2.2, and is ~1 at 100 GPa and 4000 K, approximately the conditions of the lowermost mantle. As expected, given its larger ionic radius, barium partitions more strongly than strontium into tuite, with D_{ba} = 51.4 at 20 GPa and 2000 K, decreasing to 11.1 at 60 GPa and 2300 K (mid-mantle conditions) and reaching 2.6 at 100 GPa and 4000 K (i.e. at lowermost mantle conditions). The calculated partition coefficients show tuite is potentially an important reservoir for barium over the entire depth of the

mantle. Conversely, while strontium is expected to partition strongly into tuite at shallower depths, cpv is an equally good host for this element under PT conditions of the lowermost mantle.

As the pressure dependence of the Sr-O and Ba-O bond length is unknown, we cannot make a quantitative comparison between the partitioning energies determined here using atomistic calculations with those obtained using the elastic strain model in section 3.4. Nevertheless, a qualitative comparison between the two can be made, and reveals substantial agreement between the two approaches to modeling trace element partitioning between cpv and tuite. At low pressure, both the elastic strain model and the atomistic calculations predict that large cations preferentially partition into tuite, with little difference between the M1 and M2 sites, and the magnitude of the partitioning energy increases with cation size. Similarly, the elastic strain model predicts that, at high pressure, the energy of large cations substituting on the M1 site in tuite will be lower than that for substitution into the cpv M site although, in contrast to the atomistic calculations, the elastic strain model shows that the magnitude of the partitioning increases with pressure. The pressure dependence of the energy difference for large-radius impurities partitioning between the tuite M2 site and the cpv M site also shows substantial agreement. Consistent with the atomistic calculations, the lattice strain model shows that the energy of the exchange reaction for the M2 site at low pressure decreases with increasing impurity size, and that the energy of large cations increases more rapidly with pressure. At lower mantle pressures, the energy of large cations is predicted to be lower in cpv than in the tuite M2 site, as was found for both strontium and barium in the DFT calculations. The qualitative agreement found between the lattice strain model and the DFT calculations suggests that the former

can be a useful guide for trace element partitioning between cpv and tuite, allowing us to conclude that the latter is likely to be an important reservoir for a wide range of incompatible trace elements. While its importance for large ions, including strontium and barium, is likely to decrease at high pressure, due to their declining stability in the M2 site, Fig. III.6b suggests that the partitioning of small ions from cpv into tuite will actually increase with pressure.

III.4 Conclusions

Tuite is of potential significance in the Earth's mantle because its chemistry and crystal structure make it an ideal candidate for hosting incompatible elements. In this study, we used density functional theory calculations to determine the structure and elasticity of tuite to lower mantle pressures. Comparison of the properties of the M1 and M2 sites in tuite with those of the M site in cpv, the major phase most important for hosting incompatible elements in the lower mantle, revealed that the former are significantly more compressible than the cpv M site. Since impurities preferentially occupy flexible sites, it follows that defects should partition from cpv into tuite. This conclusion was supported by modeling of partition energies between cpv and the cation sites of tuite using the lattice strain model of Brice (1975), parameterized using the polyhedral volumes and Young's moduli calculated in this study, from which it was found that defects of any size will prefer either the M2 site (or both) over the M site at all pressures relevant to the Earth's mantle.

Density functional theory was used to calculate the energies of strontium and barium defects in tuite, and these were compared to the energies of strontium and barium impurities occupying the M site in cpv. It was found that, at low pressure, both divalent

impurities will partition strongly to tuite, although no preference for either the M1 or M2 site was observed. While increasing pressure created a preference for the cpv M site over the M2 site, the lowest energy substitution site (for both impurities) remained the tuite M1 site. Consequently, tuite may serve as a reservoir for both strontium and barium in the Earth's mantle, with the magnitude of the partitioning energies between tuite and cpv great enough to compensate for entropic effects except at extreme temperatures.

Chapter IV. Segregation of bare and protonated Mg vacancies to dislocation cores in MgO

IV.1. Introduction

MgO is the Mg end-member of the magnesiowüstite (or ferropericlase) solid solution (Mg,Fe)O, the second most abundant mineral in the Earth's lower mantle. Ferropericlase is thought to accommodate most of the strain in the deforming lower mantle (Madi et al. 2005; Girard et al. 2016) and is probably also the primary source for the observed seismic wave anisotropy in this region (Karki et al. 1999; Marquardt et al. 2009). Dislocations serve as sinks for point defects, including both bare and protonated Mg site vacancies in MgO. These may be bare (i.e. contain no impurity atoms), or protonated, in which case the Mg atom is replaced by one or more protons (i.e. H^+). Dislocations are also important for the transport of defects, as their cores serve as fast diffusion pathways. In MgO, measured cation self-diffusion coefficients for such pipe diffusion are more than an order of magnitude larger than coefficients for cation self-diffusion in the bulk lattice (Sakaguchi et al. 1992). The presence of vacancy-related defects near dislocations may influence strain rates, especially under conditions of low temperature or high stress, where deformation is controlled by dislocation glide. Peierls-Nabarro modeling has shown that vacancy-dislocation core interactions can produce glide weakening in Al metal, while high-stress experiments have found that the incorporation of protonated defects (often referred to as "water") in $(Mg,Fe)_2SiO_4$ olivine may reduce the Peierls stress by up to a factor of two (Katayama and Karato 2008).

Dislocations act as sinks for vacancies, interstitial atoms, and impurities due to interactions between the elastic fields induced by dislocations and point defects; this effect is more pronounced for edge dislocations, due to their higher stress fields. Impurity atoms can also modify the structures of the dislocations to which they segregate. Density functional theory calculations have shown that the segregation of interstitial C impurities to 1/2<111> screw dislocations in bcc Fe can cause reconstruction of the core structure from the easy configuration to the higher energy (in pure Fe) "hard" core configuration (Ventelon et al. 2015). Pipe diffusion along dislocation cores can be significantly faster than in the bulk, as for example in the case of Mg vacancies in MgO (Zhang et al. 2010), H in Pd metal (Heuser et al. 2014), and oxygen diffusion in albite (Yund et al. 1981).

In nominally anhydrous minerals (NAMs), water is commonly incorporated as protonated defects. In MgO, the typical substitution mechanisms include the partial or full protonation of a vacancy defect, for instance the replacement of a divalent cation M^{2+} (e.g. Mg^{2+}, Fe^{2+}) with either a single proton $\{H_M\}^{\cdot}$, or pair of protons $\{2H_M\}^X$. In silicates, $\{4H_{Si}\}^X$ defects can also be created by replacing a Si^{4+} ion with four protons. *Ab initio* calculations show that the protonation of existing vacancies is highly exothermic (de Leeuw 2001b).

While long-range interactions between point defects and dislocations can be understood on the basis of elasticity theory, segregation of impurities to dislocation cores is an inherently atomistic phenomenon, driven by the dislocation core structure. Although the clouds of impurities segregated to dislocation cores can be observed experimentally using atom probe tomography (e.g. Miller 2006), routine measurements remain difficult because of the small length scales involved. However, atomistic modeling techniques enable easy treatment of atomic-scale phenomena.

Several popular techniques exist for modeling the atomic-scale properties of dislocations. In the dislocation multipole approach, several dislocations are inserted into a simulation cell with 3D-periodic boundary conditions. To maintain continuity at the cell boundaries, the Burgers vectors of the dislocations must sum to zero. This approach makes possible the use of *ab initio* methods, such as density functional theory (DFT; Hohenberg and Kohn 1964; Kohn and Sham 1965), to calculate the energy of a dislocation. However, due to the use of 3D-periodic boundary conditions, dislocations in a simulation cell interact not only with other dislocations in the multipole, but also with their periodic images. These interactions can affect the structure of the dislocation core, and a rigorous calculation of dislocation energy requires the elastic interactions between dislocations to be subtracted from the total energy (Cai et al. 2003). This approach has been used to calculate the core structure and energy of 1/2<110> screw dislocations in MgO to lower mantle pressures (Carrez et al. 2015).

An alternative is to embed a single dislocation in a cylindrical cluster of atoms, subject to periodic boundary conditions along the axis of the cylinder, *z*. This cluster is aperiodic normal to the dislocation line vector ξ. In this approach, the cluster of atoms is divided radially into two regions: an inner cylinder where atoms are permitted to relax freely and an outer region where they are held fixed at the locations predicted from elastic strain field of the dislocation. There are several limitations to this method: a large inner radius is required to fully converge the dislocation core properties; the outer surface of the cluster may become charged when modeling ionic materials; and interactions between a moving dislocation and the surface separating region I from region II render accurate calculation of the Peierls stress σ_p difficult. Additionally, because the simulation cell includes surfaces, the

core energy cannot easily be calculated using DFT, as the energy will include a component due to relaxation of the electron density at the surface (although see Tarrat et al. 2014). However, the absence of dislocation-dislocation interactions in the cluster-based approach, combined with its ease of implementation, has made it a valuable tool for simulating dislocations in ionic materials. It has, for example, used to determine the structure and energy of screw dislocations in Mg_2SiO_4 forsterite (Walker et al. 2005b) and natural zeolites (Walker et al. 2004). A detailed exposition of the cluster-approach and its use in computational mineral physics may be found in Walker et al. (2005a). The cluster based method has been applied extensively to MgO, including to study the core structure and mobility of 1/2<110>{110} edge dislocations (Puls and Norgett 1976), segregation of cation and anion vacancies to 1/2<110>{110} edge dislocation (Puls 1980, 1983), pipe diffusion along 1/2<110>{110} edge dislocations (Zhang et al. 2010), and the core structure of <100> screw dislocations (Walker et al. 2005b).

In this chapter, core structures and energies of several important dislocations in MgO, including 1/2<110>{110} and 1/2<110>{100} edge dislocations, and screw dislocations with Burgers vector 1/2<110>, are calculated using the cluster-based approach, described briefly in Chapter I and in more detail below, with the interatomic interactions modeled using empirical pair potentials. Energies for segregation of vacancy-related point defects to each dislocation are calculated. For each dislocation type, we take the lowest energy core structure and calculate the energies of $\{\square_{Mg}\}''$ and $\{2H_{Mg}\}^X$ defects occupying cation sites in the vicinity of the dislocation line. Segregation energies are calculated by comparing these energies with those of equivalent point defects in the bulk crystal. Finally, migration barriers are calculated for $\{\square_{Mg}\}''$ diffusing along the dislocation lines in MgO, which has

previously been done by Zhang et al. (2010) for 1/2<110>{110} edge dislocations, but is here extended to edge and screw dislocations with line vector, $\boldsymbol{\xi}$, parallel to <110>. For these dislocations the influence of pipe diffusion is expected to be more pronounced because the minimum energy path through the crystal is parallel to the dislocation, so that diffusing atoms do not have to take high-energy paths away from the dislocation core.

IV.2. Computational methods

Cluster-based simulation of dislocations

In the cluster-based approach, a single dislocation is inserted along the axis of a cylinder of atoms, which is 1D-periodic along its axis (Fig. IV.1). The first step is to displace atoms according to the elastic displacement field $\mathbf{u}(\mathbf{r})$ calculated for the dislocation. Here, we use the sextic formulation for a dislocation in an anisotropic medium (Stroh 1958), the details of which are recalled in section I.2. For edge dislocations, this is a non-conservative algorithm and atoms must be removed from the simulation cell to obtain a physically reasonable initial dislocation structure. To do this, a branch cut is created that is normal to both the Burgers and dislocation line vectors. Any atoms that are displaced across this branch cut by the displacement field $\mathbf{u}(\mathbf{r})$ are deleted. Additionally, atoms in close proximity to the branch cut are merged with any nearby atoms, if the distance between them falls below a specified threshold $d_{\min}$. Once the elastic displacement field has been applied to the cluster, it is divided into two concentric regions whose radii are R_{I} and R_{II}, respectively. During the geometry optimization step, atoms in region I will be permitted to relax freely, while those in region II are held fixed at the coordinates determined from elasticity theory.

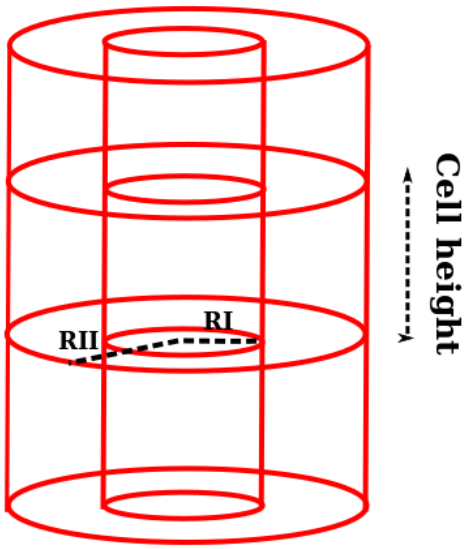

Fig. IV.1 Illustration of a simulation cell used for cluster-based modeling of a dislocation .

The total excess energy per unit length, E_{dis}, contained within radius r of an isolated dislocation is

$$E_{dis}(r) = E_{core} + \frac{Kb^2}{4\pi}\log(r/r_c) \qquad \text{(IV.1)}$$

where K is the elastic energy coefficient (given in equation I.18 for an anisotropic material), E_{core} is the energy contained within the core region (termed the core energy), and r_c is the radius of the dislocation core, within which the displacement field diverges from the predictions of linear elasticity. The core radius r_c is an undetermined parameter, whose value cannot determined from the radial excess energy of the dislocation. Its value must be chosen in order to set a gauge for the core energy. In this study, we use a core radius of $2b$, where b is the absolute magnitude of the Burgers vector.

The core energy is determined from atomistic cluster-based simulations by fitting equation (IV.1) to the calculated radial dependence of the excess energy, which is the difference between the energy of a cluster containing the dislocation and a reference system containing an identical number of atoms. E_{core} is also the excess energy of the dislocation at $r = r_c$. For screw dislocations, this is straightforward, as the undeformed and deformed simulation cells contain the same number of atoms. However, as the insertion of an edge dislocation is non-conservative (i.e. atoms are removed from the initial simulation cell), the excess energy must be calculated from the energies of the individual atoms as

$$E_{excess}(r) = E_{dis}(r) - \sum_{species} n_{species}(r) E_{species} \qquad \text{(IV.2)}$$

where $E_{dis}(r)$ is the total energy of the atoms within r of the dislocation line, the sum runs over the different atomic species present, $n_{species}(r)$ gives the number of atoms of each species within r, and E_{species} is the energy of the species in the bulk lattice. In single-component crystals, E_{species} is just the energy of the unit cell divided by the number of atoms it contains. In multicomponent crystals, such as MgO, this is equal to

$$E_{species} = 1/2\left(E_{supercell} + E_{isolated} - E_{vac}\right) \qquad \text{(IV.3)}$$

where E_{vac} is the energy of a supercell from which one atom of the specified type has been removed, without relaxing the coordinates of the remaining atoms, $E_{supercell}$ is the energy of the supercell without a vacancy, and $E_{isolated}$ is the energy of an isolated atom of the specified type.

The core energy and core displacement field of a dislocation in a two-region cluster depends on the value of r_I, the radius of the relaxed region. Although the initial coordinates for all atoms are set using a purely elastic displacement field, atoms close the dislocation core experience a significant inelastic component of displacement due to atomic-scale relaxation near the dislocation core. Consequently, for small r_I, some component of the total displacement will be missed, leading to higher core energies than if all atoms were permitted to move during relaxation. For all dislocations examined in this study, values of r_I and r_{II} were chosen to ensure convergence, to within <25 meV/Å, of the E_{core} determined by fitting equation (IV.1) to the calculated excess energy curve. For all three dislocation slip systems, region I and region II radii of 30 Å and 45 Å were sufficient to achieve this level of convergence. The coordinates of atoms in region I were relaxed using the Broyden-Fletcher-Goldfarb-Shanno (BFGS) algorithm (Shanno 1970), as other minimizers, such conjugate gradients, relax the dislocation core into high-energy local minima with highly distorted core structures.

In this study, we treat the interatomic interactions using a widely used potential model, which was parameterized by fitting to experimental data and theoretical data (Sanders et al. 1984; Lewis and Catlow 1985; Schröder et al. 1992), and reproduces the physical properties of forsterite reasonably well (Price et al. 1987). Following Wright and Catlow (1994), we model hydroxyl using the parameters developed by Schröder et al. (1992) to treat $(OH)^-$ groups in zeolite. This potential, labeled THB1, has been widely used to model point and extended defects in forsterite, including Mg point defects (Walker et al. 2009), surface structures and energetics (de Leeuw et al. 2000), and screw dislocation core structures and energies (Walker et al. 2005b). The THB1 model uses formal charges for the

Mg^{2+} and Si^{4+} cations, while the polarizable oxygen anion is modeled as a positively charged core coupled by a harmonic potential to a negatively-charged massless shell (Dick and Overhauser 1958). Each cation-anion pair interacts through a Buckingham potential, while the rigidity of the SiO_4 tetrahedra is replicated using a short-ranged three-body

Table IV.1 Parameters defining the THB1 interatomic potential. The cutoff distance for the potentials is 10 Å

	q_{core} (e^-)	q_{shel} (e^-)	k_s (eV/Å^2)
Mg	2.0	-	-
Si	4.0	-	-
O	0.84819	-2.84819	74.92038
O_H	-1.426	-	-
H	0.426	-	-
	Buckingham potential		
	A (eV)	ρ (Å)	C_{ij} (eV•Å^6)
Mg-O	1428.5	0.29453	0.0
Mg-O_H	1060.5	0.29453	0.0
Si-O	1283.90734	0.32052	10.66158
Si-O_H	983.556	0.32052	10.66128
O-O[a]	22764.0	0.149	27.88
O-H[b]	311.97	0.25	0.0
	Morse potential		
	D_{ij} (eV)	α (Å^{-1})	r_0 (Å)
O_H-H	7.02525	2.03	0.9485
	Three-body potential		
	k_3	θ_0	
O-Si-O	7.02525	109.47	

[a] O_H-O and O_H-O_H pairs also use this potential

[b] Also used for O_H-H bonds

harmonic potential. All atomistic calculations are performed using the molecular mechanics program GULP (Gale 1997; Gale and Rohl 2003). THB1 simulates the covalent part of the

O-H bond in a hydroxyl group using a Morse potential, and treating the participating oxygen ion (labeled O_H in Table IV.1) as a partially ionic point charge. Values for the parameters defining the THB1 potential are given in Table IV.1.

The Coulomb interaction is treated using the Wolf summation approach (Wolf et al. 1999), which has been found to produce physically reasonable properties for dense solid state materials without 3D periodic boundary conditions (Demontis et al. 2001; Gdoutos et al. 2010). In all calculations, we use a damping factor of 0.2 and a cutoff radius of 15.0 Å, which was found to be sufficient for convergence of the elastic constants and cell energy of defect-free MgO within <1% of the value calculated using the Ewald summation technique.

Modeling point defect segregation

The energy required to move a point defect from the bulk lattice to a site near a dislocation core is termed the segregation energy, $E_{seg.}$ In an atomistic simulation, this is equivalent to the difference between the excess energy ΔE_{dis} of a point defect of the specified type in a simulation cell containing a dislocation, and the excess energy ΔE_{perf} of the point defect in a 3D-periodic supercell of the material. Here, E_{seg} is calculated as

$$E_{seg} = \left(E_{dfct+dis} - E_{dis}\right) - \left(E_{dfct+supercell} - E_{supercell}\right) \quad \text{(IV.4)}$$

where E_{dis} is the energy of a cluster containing a dislocation, $E_{dfct+dis}$ is the energy of that same cluster with a single point defect inserted, $E_{supercell}$ is the energy of a defect-free 3D-periodic supercell, and $E_{dfct+supercell}$ is the energy of a supercell containing a point defect.

Due to the 1D periodic boundary conditions imposed on the simulation cell, each point-defect interacts with periodic images of itself along the dislocation line. Consequently, calculating $E_{dfct+dis}$ for a single point defect adsorbed to a dislocation core requires that the thickness of the 1D-periodic simulation cell along the dislocation line vector ξ be increased, which is done by stacking n simulation cells along ξ. The value of n was checked to ensure that defect energies converged. For the 1/2<110>{100} edge and 1/2<110> screw dislocations, a stack thickness of n = 5 was used, giving a distance of 14.8 Å between a point defect and its nearest periodic image. Calculations for defects segregating to the 1/2<110>{110} edge dislocation used a cell thickness of n = 4, so that the shortest distance between adjacent point defects was ~16.8 Å. The 3D-periodic supercell used to calculate the excess energy of an isolated point defect in the bulk lattice must also be sufficiently large to minimize interactions between the point defect and its periodic images. For this purpose, a 4x4x4 simulation cell, for which the shortest distance between point defects is ~16.8 Å, was sufficient for convergence of the defect energy with same precision obtained for simulations of vacancy-dislocation interactions. Interactions between charged defects (i.e. $\{\square_{Mg}\}''$ defects) are corrected using the method of Leslie and Gillan (1985).

Due to the large size of the simulation cell and the $O(N^2)$ scaling of the BFGS algorithm used to minimize the total energy, where N is the number of atoms permitted to relax, it is computationally expensive to calculate the energy of a point defect near a dislocation core. However, the perturbation of the dislocation displacement field by the point defect is large only in the immediate vicinity of the point defect. Atoms outside this region may be fixed at the positions predicted for a dislocation without segregated point defects, without changing

the calculated dislocation-point defect interaction energy significantly. In this study, all atoms a distance less than or equal to r from the inserted point defect are allowed to move freely during relaxation. Due to the shorter range of the elastic field of a point defect, relative to a dislocation, r is smaller than the region I radius r_I used to determine the dislocation core structure, reducing the number of atoms whose coordinates need to be relaxed. The calculated segregation energy is strictly decreasing with increasing relaxation radius, which must therefore be varied to test for convergence. For all dislocations and point defects considered in this study, the radius of the relaxed region is r = 10 Å, sufficient to converge the energies of the tightest binding sites to <0.05 eV.

Calculating the segregation energy of a bare Mg vacancy is straightforward, as this defect can be inserted into a simulation cell by deleting one of the Mg ions. However, setting up a segregation energy calculation is less straightforward if the vacancy is protonated. This is because the interatomic potential employed here models the oxygen ion in a hydroxyl group differently from other oxygen ions: with a partially ionic charge, and without a polarizable shell (Table IV.1). Creating a protonated vacancy entails not only the removal of an Mg^{2+} ion and insertion of two H^{+} ions in the cation, but also the replacement of two oxygen anions around the Mg site with oxygen ions tailored for membership of a hydroxyl group. Additionally, unlike a bare vacancy, a protonated defect has an orientation, defined by the direction of the O-H bond for which the defect energy is minimized. There are thus several symmetrically distinct configurations of the $\{2H_{Mg}\}^{X}$ defect for each site around a dislocation, corresponding to the different O-H bond orientations. Determining the minimum segregation energy for $\{2H_{Mg}\}^{X}$ to a particular site near a dislocation core entails calculating segregation energies for each of these configurations, as is done below.

Pipe diffusion

Dislocation cores are not only sinks for vacancy-related defects, but also fast diffusion pathways by which they can be transported through a crystal, a process referred to as pipe diffusion. To probe the relative importance of the three major dislocation slip systems in MgO for vacancy diffusion, we calculate migration barriers for pipe diffusion along all three 1/2<110> dislocations in MgO. This is done by moving a magnesium ion into a neighboring vacant M site in sequential steps. At each step, the coordinates of atoms in the vicinity of the migrating ion are relaxed, with the constraint that they are restricted to move perpendicular to the dislocation line. Mg vacancies diffusing along the cores 1/2<110> screw dislocations and 1/2<110>{100} edge dislocations can migrate parallel to ξ. However, for Mg vacancies diffusing along 1/2<110>{110} dislocations, the short diffusion paths (along 1/2<110>) make an angle of $\pi/4$ to the dislocation line (which is <100>). The translational symmetry of the crystal perpendicular to ξ is broken by the dislocation, are there are thus four distinct diffusion paths for a vacancy migrating along a 1/2<110>{110} edge dislocation. Energy barriers for all possible migration paths of an Mg vacancy diffusing along a 1/2<110>{110} edge dislocation are calculated.

IV.3. Dislocation core properties

For each of the three dislocation slip systems considered in this study, there are multiple possible core structures, corresponding to the different high-symmetry locations in the appropriately oriented unit cell. These are shown in Fig. IV.2a for dislocations gliding on {110} and in Fig. IV.2b for dislocations gliding on {100}. To obtain stable structures for

each of the three dislocation slip systems, radial excess energy profiles were calculated for dislocations centered at a number of different locations using the methods described in section 2.1, and their core energies E_{core} extracted by fitting to equation (IV.1). The locations shown in Fig. IV.2 have the lowest values of E_{core}. Radial excess energies for the stable dislocation slip systems are shown in Fig. IV.5, together with the fitted excess energy curves $E(r)$.

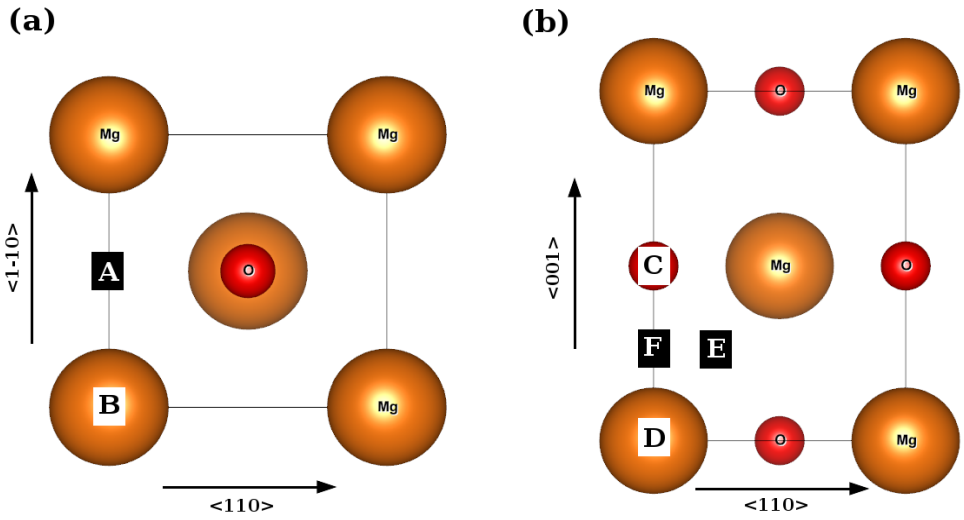

Fig. IV.2 Crystal structure of MgO, viewed down (a) <100> and (b) <110> with possible high-symmetry dislocation locations marked. The high symmetry locations corresponding to the lowest energy dislocation structures are labeled.

All three dislocation types considered in this study were found to have multiple core structures, corresponding to different possible locations of the dislocation line within the unit cell (Fig IV.2ab), which have identical core energies. In this study, the 1/2<110>{110} edge dislocation was found to have two core structures with indistinguishable energies, both with fitted core energies of 1.35 eV/Å. For one such stable structure, the dislocation

line is located along the channel parallel to <100> (site A in Fig. IV.2a). The other is centered on the column of alternating oxygen and magnesium ions parallel to the <100>

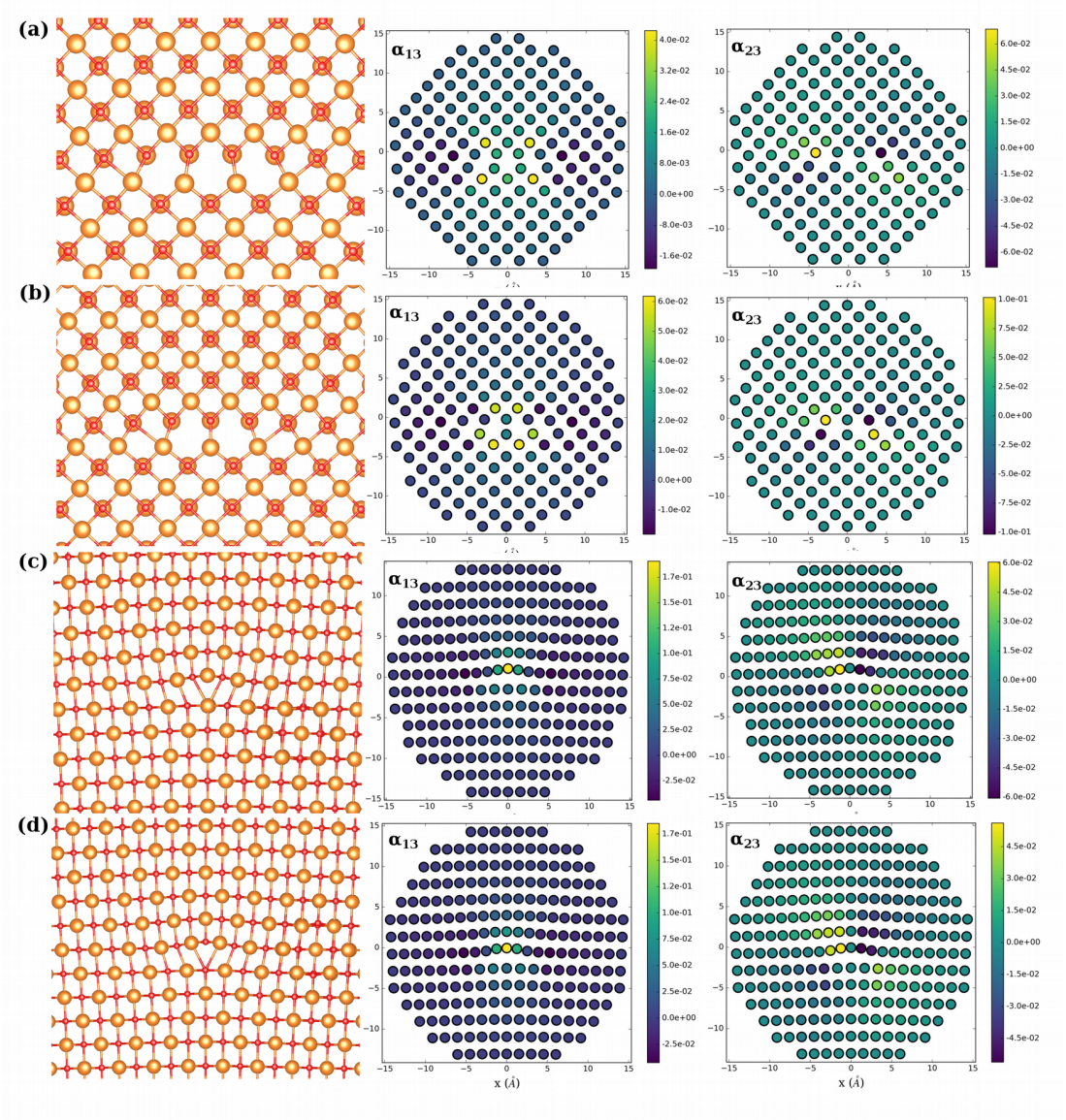

Fig. IV.3 Atomic structures of the (a) <100>-channel-centered and (b) ion-centered polymorphs of the 1/2<110>{110} edge dislocation, and of the (c) Mg-centered and (d) O-centered polymorphs of the 1/2<110>{100} edge dislocation. Also shown are the edge components α_{13} and α_{23} of the Nye tensor $\boldsymbol{\alpha}$.

lattice direction, and intersects the {100} plane (site B in Fig. IV.2a). In the discussion that follows, these two polymorphs are referred to as the <100>-channel-centered (Fig. IV.3a) and ion-centered (Fig IV.3b) structures, respectively. While the existence of energy degenerate core structures contrasts with previous theoretical studies, in which the ion-centered structure is reported to be the unique stable core structure (Zhang et al. 2010), polymorphism of the 1/2<110>{110} edge dislocation slip system has been observed in MgO bicrystals by transmission electron microscopy (Wang et al. 2014). The Nye tensor α, which describes the distribution of dislocation density in a crystal and can be used to characterize the spreading of the dislocation core, is calculated here using the method of Hartley and Mishin (2005ab). As can be seen from the edge component α_{13} in Fig. IV.3ab, both polymorphs of the 1/2<110>{110} edge dislocation have undissociated cores. However, the non-zero value of α_{23} indicates that the atoms are relaxed away from the glide plane due to shear-tension coupling, as described by Bulatov and Kaxiras (1997) for Si. The magnitude of the screw component α_{33} is negligible at all lattice points.

1/2<110>{100} edge dislocations similarly have two energy-degenerate core structures, one centered on the <110>-parallel column of oxygen anions (site C in Fig. IV.2b) and the other on a column of Mg cations (site D in Fig. IV.2b), both with core energies of 1.91 eV/Å. In the discussion that follows, these two polymorphs are referred to as the O-centered (Fig. IV.3c) and Mg-centered (Fig. IV.3d) structures. In contrast to the 1/2<110>{110} edge dislocation, for which the two degenerate core structures differ significantly from one another, the O-centered and Mg-centered 1/2<110>{100} edge dislocation structures are nearly identical, except that the positions of the Mg and O ions

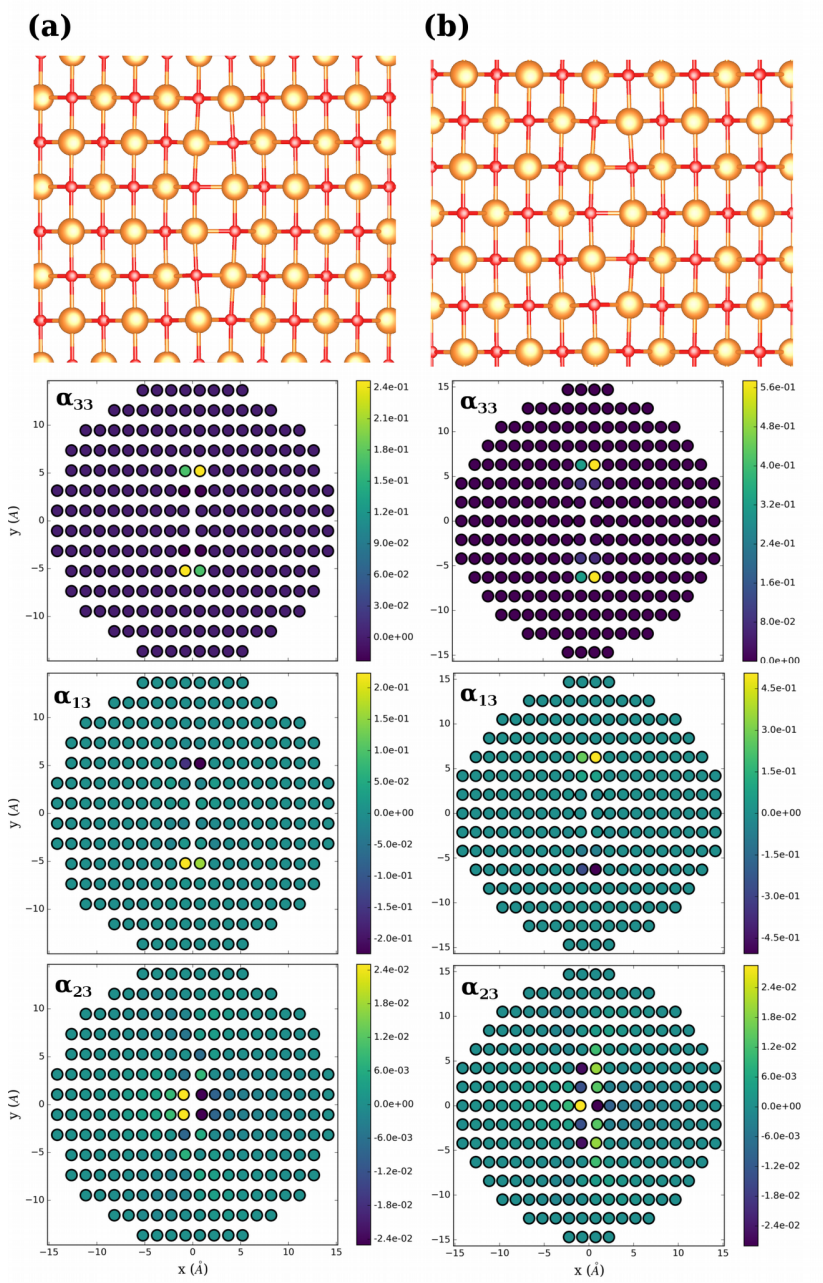

Fig. IV.4 Relaxed core structure of the 1/2<110> screw dislocation in the (a) <110>-channel-centered and (b) edge-A-centered configurations. The screw (α_{33}) and edge (α_{13} and α_{23}) components of the Nye tensor are also shown.

are reversed. This can be easily seen by comparing the α_{13} and α_{23} components of the Nye tensor (Fig. IV.3de), which are visually indistinguishable. As was found for 1/2<110>{110}

edge dislocations, α_{23} is non-zero, indicating the presence of shear-tension coupling within the dislocation core, and and the screw component α_{33} is effectively zero.

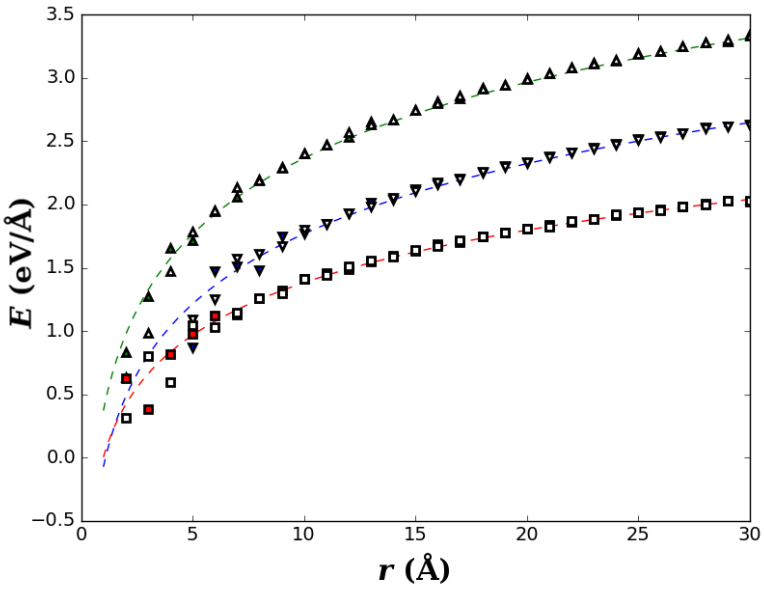

Fig. IV.5 Radial excess energies $E(r)$ for the lowest core energy polymorphs of the 1/2<110>{110} (inverted triangles) and 1/2<110>{100} edge dislocations (triangles), and the 1/2<110> screw dislocation (squares). Atomistic energies for <110>-channel-centered 1/2<110> screw dislocations, ion-centered 1/2<110>{110} edge dislocations, and Mg-centered 1/2<110>{100} edge dislocations are shown as filled symbols. Empty symbols denote the atomistic energies of edge A-centered 1/2<110> screw dislocations, <100>-channel-centered 1/2<110>{110} edge dislocations, and O-centered 1/2<110>{100} edge dislocations. Dashed lines show the lines of best fit of equation (IV.1) to the atomistic energies.

Finally, the 1/2<110> screw dislocation also has two degenerate core structures, each with a fitted core energy of 1.07 eV/Å. The first of these is centered on the <110>-oriented channel (site E in Fig. IV.2b), while the second intersects the Mg-O bonds with non-zero projection onto the dislocation line (site F in Fig. IV.2b). These are labeled the <110>-channel-centered (Fig. IV.4a) and edge A-centered (Fig. IV.4b) core structures, respectively.

The relative insensitivity of the core energy of the 1/2<110> screw dislocation to its origin in the unit cell agrees with the earlier calculations of Watson et al. (1999), who also calculated the core energy of the 1/2<110> screw dislocation to be 1.21 eV/Å (when corrected to the core radius used in this study). The screw component of the Nye tensor, α_{33}, is dissociated on the {110} plane (Fig. IV.4) for both stable core structures. Whereas the screw components α_{33} of the Nye tensor $\boldsymbol{\alpha}$ is zero for both edge dislocations in MgO, the edge components, α_{12} and α_{13}, are non-zero for the 1/2<110> screw dislocation, meaning that the displacement field for the 1/2<110> screw dislocation has a significant edge character.

The supercell method has previously been used to evaluate the core structure and energy of the 1/2<110> screw dislocation, with interatomic interactions simulated using a partially ionic rigid ion model of Henkelman et al. (2005), finding that the core energy is 1.10 eV/Å (Carrez et al. 2015), within error of the value calculated here. In contrast to this study, Carrez et al. predict that only the channel-centered structure is stable at 0 GPa, while the edge A-centered polymorph has a lower core energy at higher pressures. However, this may be a consequence of the relatively small cell size used by Carrez et al. (2015), as substantial dislocation-dislocation interactions may alter the core structure.

IV.4. Segregation energies

Bare vacancies

The tightest binding site for $\{\square_{Mg}\}''$ defects around a 1/2<110>{110} edge dislocation has a segregation energy of -1.51 eV (Fig. IV.6), similar to but slightly higher than the value of

-1.7 eV found by Zhang et al. (2010) using a breathing shell potential. In both cases, the tightest binding sites are located immediately above the dislocation line. Spread out on the {110} plane directly below the dislocation line is an array of sites with low segregation energies (< -1.0 eV), consistent with the wide core spreading predicted for this dislocation by DFT-parameterized Peierls-Nabarro calculations (Amodeo et al. 2011).

Table IV.2 Minimum segregation energies (in eV) for point defects around MgO dislocations

	1/2<110>{110} edge dislocation		1/2<110>{100} edge dislocation		1/2<110> screw dislocation	
	channel-centered	ion-centered	O-centered	Mg-centered	channel centered	edge A-centered
vacancy	-1.51	-1.51	-2.84	-3.54	-0.97	-0.98
$[2H_{Mg}]_{plane}$	-	-	-5.74	-6.06	-1.15	-1.14
$[2H_{Mg}]_{norm}$	-	-	-3.39	-3.60	-1.51	-1.53
$[2H_{Mg}]_{cross}$	-1.12	-1.06	-	-	-	-
$[2H_{Mg}]_{para}$	-2.22	-2.21	-	-	-	-

$\{\square_{Mg}\}''$ defects bind more tightly to lattice sites around 1/2<110>{100} edge dislocations, with maximum binding energies for the O-centered and Mg-centered polymorphs exceeding those calculated for the 1/2<110>{110} edge dislocation, by ~2 eV in the case of the Mg-centered polymorph (Fig. IV.7). Additionally, in contrast to the 1/2<110>{110} edge dislocation, segregation energies were found to differ markedly between the two polymorphs for the 1/2<110>{100} edge dislocation slip system, so that Mg vacancies bind more strongly to the core of the Mg-centered polymorph than the O-centered polymorph.

This suggests that the presence of Mg vacancies may stabilize the former core structure relative to the latter, lifting the energy degeneracy of the 1/2<110>{100} edge dislocation.

As the magnitudes of the strain fields around screw dislocation cores are, in general, less than those for similarly oriented edge dislocations, the binding energies calculated for Mg vacancies are lower for the 1/2<110> screw than for either of the edge dislocation slip systems. Nevertheless, as can be seen in Table IV.2, binding energies are close to -1.0 eV, indicating moderately strong binding between $\{\square_{Mg}\}''$ defect and the screw dislocation core. The lowest energy sites are located close to the {110} plane normal to {100} glide plane (Fig. IV.8ab). This is likely a consequence of core spreading of 1/2<110> screw dislocations (Carrez et al. 2015), which can be seen in the associated Nye tensor distribution α (Fig. IV.4). Semi-continuum Peierls-Nabarro-Galerkin calculations suggest that 80% of the dislocation core b_i is distributed on this plane (Amodeo et al. 2011).

$\{2H_{Mg}\}^X$ defects

The H^+ ions in the most stable configuration of the $\{2H_{Mg}\}^X$ defect in MgO are bonded to O^{2-} ions on opposite sides of the MgO_6 octahedron, with the O-H bonds parallel and pointing towards the center of the site. Due to the high symmetry of the MgO unit cell, there are three possible symmetry-equivalent configurations of this defect, corresponding to the three pairs of opposing O^{2-} ions around the Mg site. However, the insertion of a dislocation into the MgO lattice breaks its rotational symmetry, thereby lifting the three-fold degeneracy of the $\{2H_{Mg}\}^X$ point defect. For both <110> and <100> oriented dislocations, this results in two symmetrically distinct defect structures, one of which is doubly degenerate.

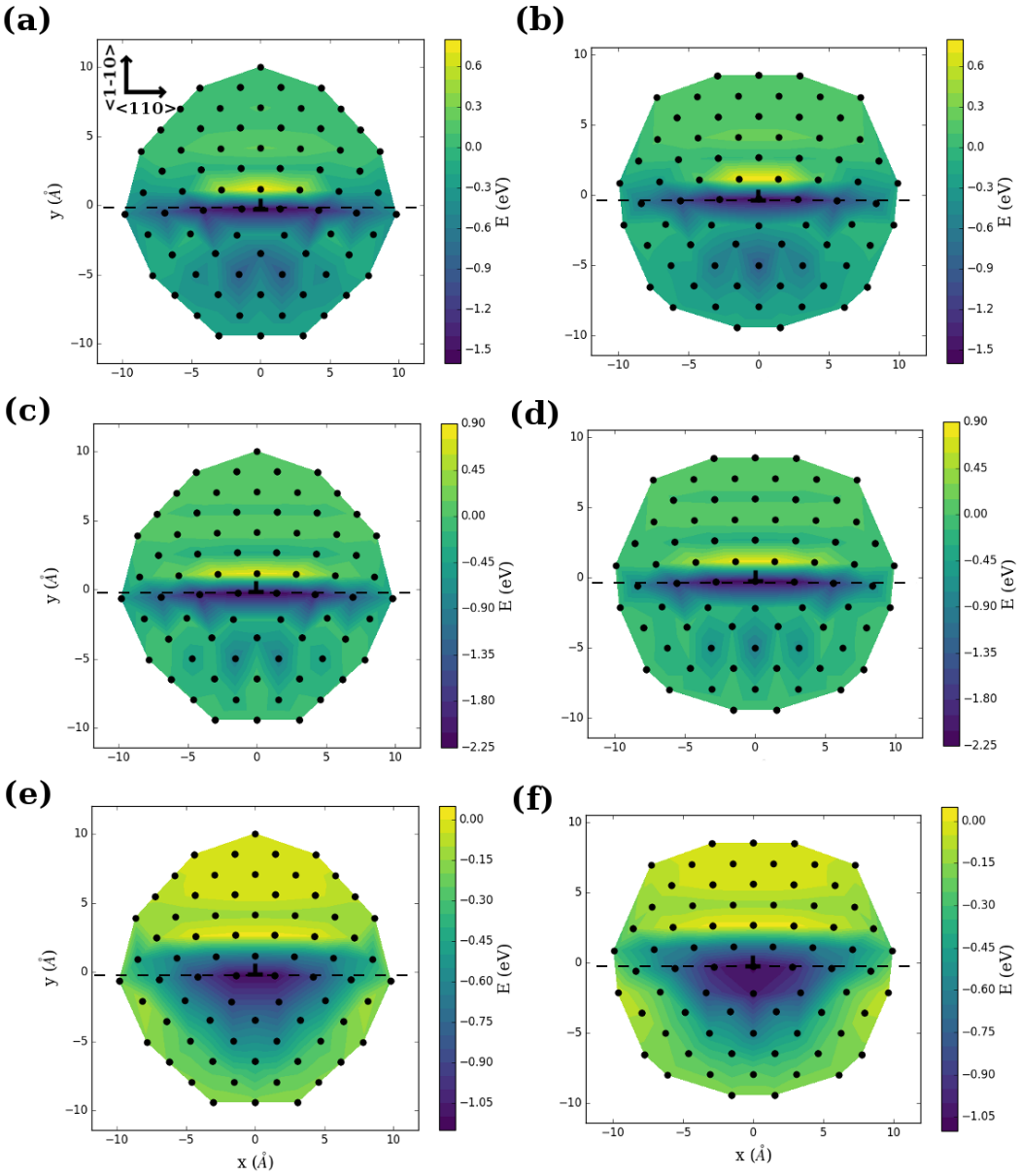

Fig. IV.6 Energies for segregation of (a, b) $\{\square_{Mg}\}''$ defects, and $\{2H_{Mg}\}^{X}$ defects in the (c, d) HPARA and (e, f) HCROSS configurations to Mg sites around 1/2<110>{110} edge dislocations. (a), (c), and (e) were calculated using the <100>-channel-centered core structure, while (b), (d), and (f) were calculated using the ion-centered structure. The {110} glide plane has been indicated with a dashed line.

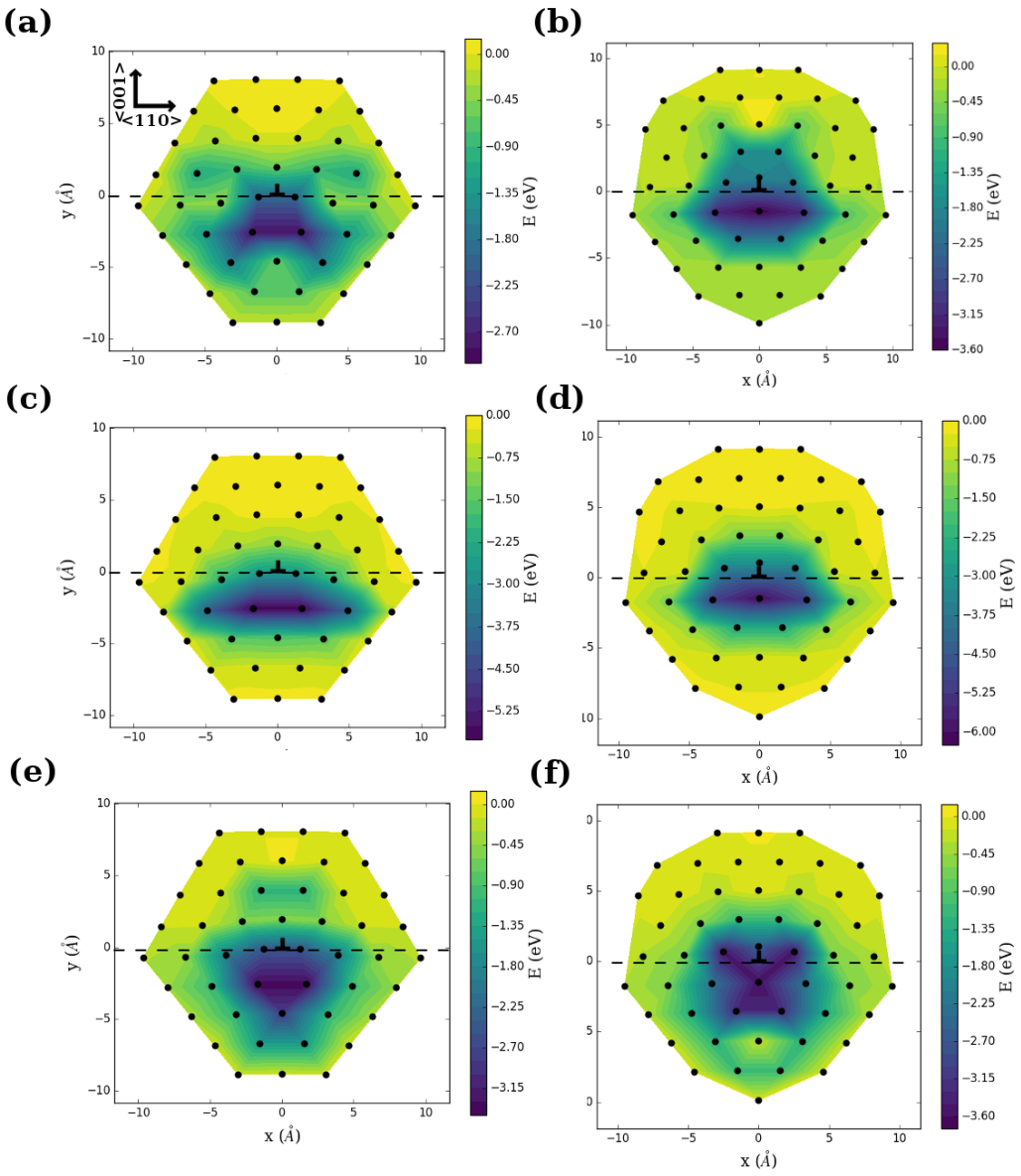

Fig. IV.7 Energies for segregation of (a, b) $\{\square_{Mg}\}''$ defects, and $\{2H_{Mg}\}^{X}$ defects with the (c, d) HPLANE and (e, f) HNORM configurations to Mg sites around 1/2<110>{100} edge dislocations. (a), (c), and (e) were calculated for the O-centered core structure, while (b), (d), and (f) were calculated for the Mg-centered structure. The {100} glide plane has been indicated with a dashed line.

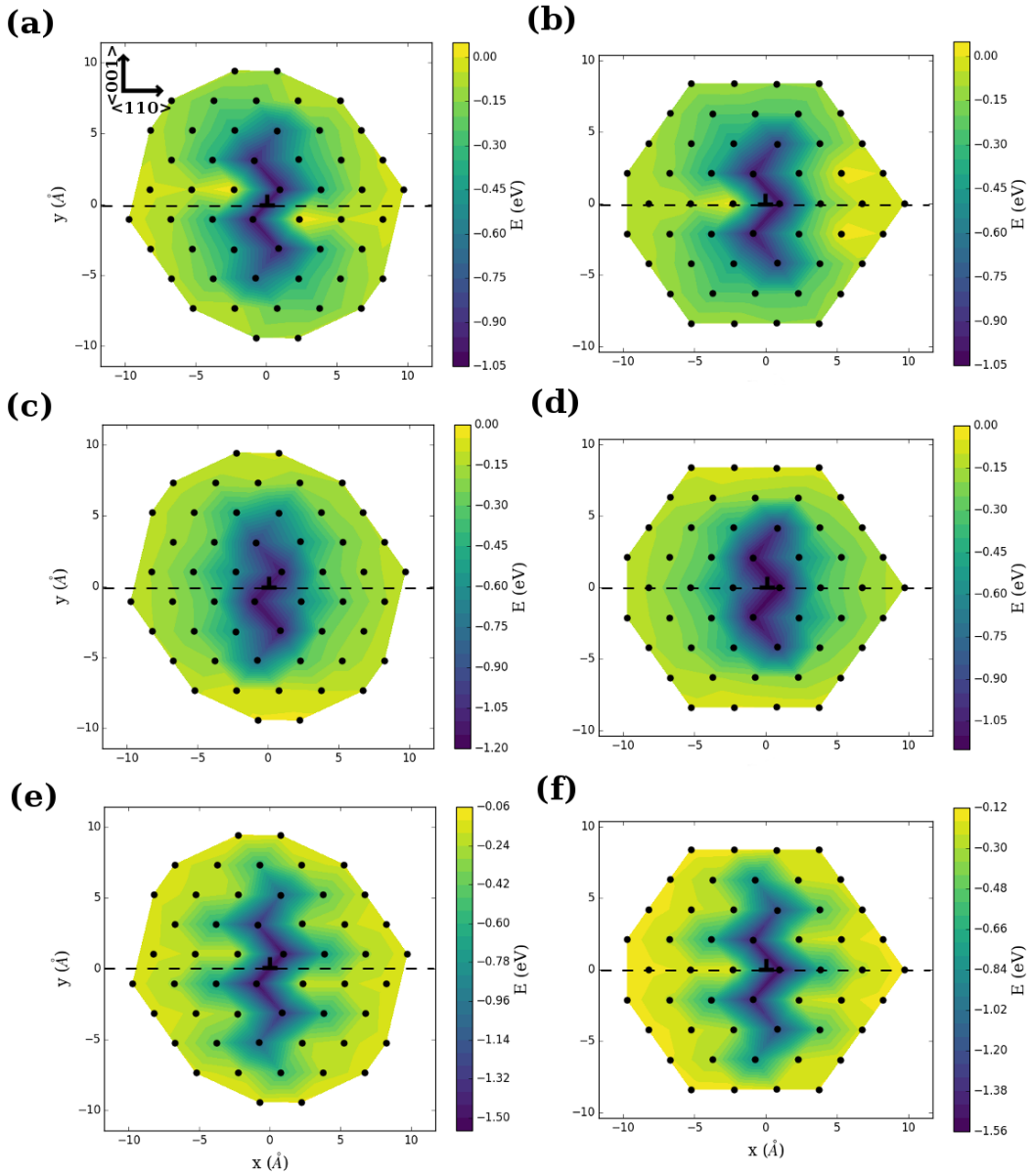

Fig. IV.8 Energies for segregation of (a, b) $\{\square_{Mg}\}''$ defects, and $\{2H_{Mg}\}^{X}$ defects with the (c, d) HPLANE and (e, f) HNORM configurations to Mg sites around 1/2<110> screw dislocations. (a), (c), and (e) were calculated for the <110>-channel-centered core structure, while (b), (d), and (f) were calculated for the edge-A structure. The {100} glide plane has been indicated with a dashed line.

We begin by considering the 1/2<110>{110} edge dislocation slip system. In the first of the two possible $\{2H_{Mg}\}^X$ configurations around this dislocation, the O-H bonds lie in the plane normal to the dislocation line ξ, oriented at 45° relative to the glide plane. Due to the mirror symmetry of the dislocation, this defect, referred to hereafter as HCROSS, is doubly degenerate. The second possible $\{2H_{Mg}\}^X$ configuration corresponds to the case when the O-H bonds are oriented parallel to the dislocation line, and will be referred to hereafter as the HPARA configuration. As shown in Table IV.2, the minimum segregation energy calculated for the HPARA defect is >1 eV lower than that calculated for the HCROSS defect. Given the relative mobility of hydrogen ions within a crystallographic site, this means that $\{2H_{Mg}\}^X$ defects segregating to 1/2<110>{110} dislocation cores will be polarized by the dislocation, with the O-H bonds parallel to the dislocation line.

For 1/2<110>{100} edge dislocations, the two symmetrically distinct $\{2H_{Mg}\}^X$ configurations are HPLANE, in which the O-H bonds are contained within the {100} glide plane and inclined at 45° with respect to ξ, and HNORM, in which the O-H bonds are perpendicular to the glide plane and normal to ξ. As can be seen in Fig. IV.8, the segregation energies are generally lower for the HPLANE configuration than the HNORM configuration. Comparing the minimum energies for the two defect configurations, the tightest binding site for a $\{2H_{Mg}\}^X$ defect in the HPLANE is 0.6 eV lower than for the tightest binding site of the HNORM defect. As was found for $\{\square_{Mg}\}''$ defects, the calculated maximum $\{2H_{Mg}\}^X$ binding energies differ between the two 1/2<110>{100} edge dislocation core structure polymorphs, with lowest segregation energies calculated for sites near the Mg-centered core structure.

The symmetrically distinct configurations of the $\{2H_{Mg}\}^X$ defect around a 1/2<110> screw dislocation are identical to those already described for the 1/2<110>{100} edge dislocation. However, in contrast to the 1/2<110>{100} edge dislocation, the lowest energy site was associated with the HNORM defect configuration (Table IV.2), although the energy difference between the two configurations is smaller than was found for the 1/2<110>{100} edge dislocation. The differing orientation of the O-H bonds in the screw and edge dislocations can be explained in terms of the interaction between the stress fields induced by the dislocation and the point defect. For $\{2H_{Mg}\}^X$ point defect in undeformed MgO, there is a compressive stress in the direction of the O-H bonds and tensile stresses perpendicular to them. Since the elastic energy of a crystal is

$$E_{elastic} = \int \sigma_{ij}\,\epsilon_{ij}\,dV = \int S_{klmn}\,\sigma_{ij}\,\epsilon_{mn}\,dV \qquad \text{(IV.5)}$$

where S_{klmn} is the compliance tensor for the material, it follows that the highest energy configuration will have the O-H bond oriented normal to $\boldsymbol{\xi}$ for edge dislocations and parallel to $\boldsymbol{\xi}$ for screw dislocations. In the case of the 1/2<110>{100} edge dislocation, this corresponds to the HPLANE defect should have the lowest segregation energy, while the HNORM defect should have the lowest segregation energy for the 1/2<110> screw dislocation, as was found here.

For 1/2<110>{110} edge dislocations and 1/2<110> screw dislocations, the calculated minimum segregation energies are essentially independent of the particular core structure, although in the case of the screw dislocation this appears to be due to reconstruction of the dislocation core induced by the presence of a vacancy. However, as seen in Table IV.2,

calculated minimum segregation energies for $\{\square_{Mg}\}''$ and $\{2H_{Mg}\}^{X}$ defects around a 1/2<110>{100} edge dislocation are markedly different for the two polymorphic core structures of this dislocation. For both defect types, calculated minimum segregation energies are lowest for the Mg-centered polymorph. The energy difference is 0.32 eV for the low-energy planar configuration of the $\{2H_{Mg}\}^{X}$ defect and 0.7 eV for the $\{\square_{Mg}\}''$ defect. While the calculated segregation energy differences between the two polymorphs are relatively small in comparison with the total segregation energy, they represent a significant fraction of the core energy E_{core}. Consequently, the energy degeneracy of the two polymorphic 1/2<110>{100} edge dislocation core structures is lifted by the addition of vacancy-related defects, as segregation of these defects to Mg-centered dislocations is preferred. This can be easily explained by considering the strain field around a dislocation For both polymorphs, the lowest energy site(s) lie below the glide plane. However, because the lowest energy site for the Mg-centered structure is directly below the dislocation line, it is closer to the center of the dislocation core than are either of the lowest energy sites for the O-centered dislocation, and thus relieves more strain in the Mg-centered structure than the O-centered one.

IV.5. Pipe diffusion

In the bulk lattice, the shortest diffusion path for Mg vacancies is along the <110> direction. The activation energy for diffusion along this path has been calculated with LDA-DFT to be 2.26 eV (Karki and Khanduja 2006), nearly identical to the 2.28 eV barrier found by fitting to measured (Mg, Fe)O ionic conductivity (Sempolinski and Kingery 1980). Previous calculations using interatomic potentials have predicted a lower activation

energy of ~1.9 eV (Catlow et al. 1976; Zhang et al. 2010), whereas the value computed here (2.24 eV) is comparable to values obtained in experiments and DFT calculations.

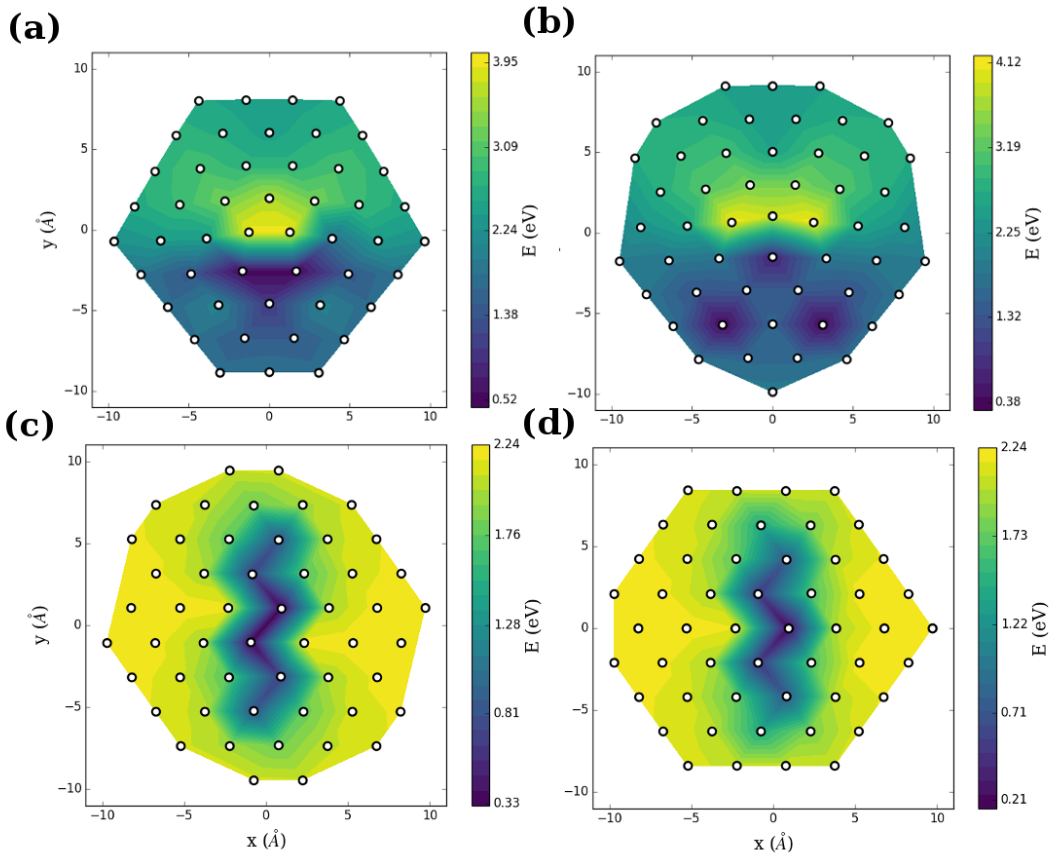

Fig. IV.9 Migration barriers for Mg vacancies diffusing along 1/2<110>{110} edge dislocations with the (a) O-centered and (b) Mg-centered core structures. Migration barriers for diffusion along 1/2<110> screw dislocations with (c) the channel-centered and (d) the edge A-centered core structures.

Dislocation cores often serve as significant reservoirs of point defects, potentially increasing the solubility limit. However, this is not the only way in which dislocations are able to affect defect concentrations, as higher diffusion coefficients along the dislocation line enable them to act as fast diffusion pathways. Migration barriers for pipe diffusion

along a 1/2<110>{110} edge dislocation have previously been calculated using a breathing shell model (Zhang et al. 2010), and were found to be reduced by up to ~15%, relative to the migration barrier for bulk diffusion, for sites close to the dislocation core. This is comparable with the calculations presented here, in which the lowest energy migration barrier for pipe diffusion along this dislocation is 1.91 eV, a reduction of 14.7% relative to bulk diffusion barrier.

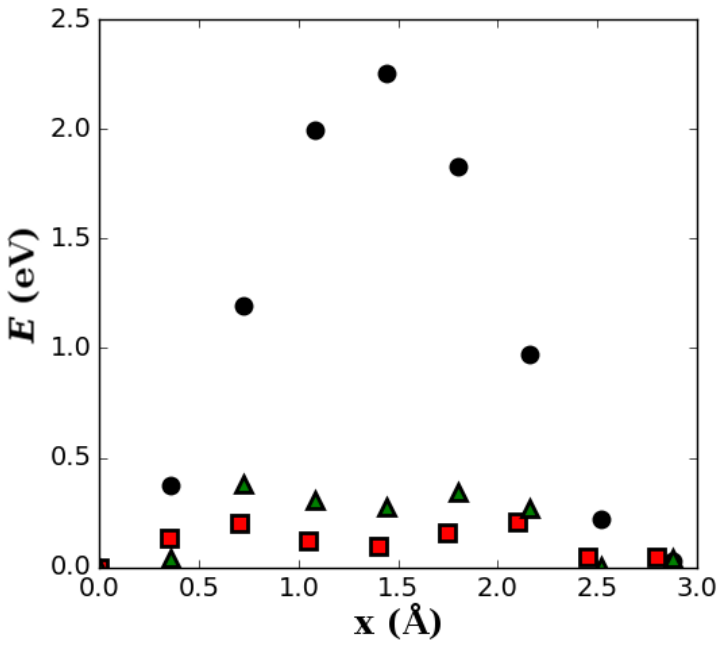

Fig. IV.10 Energy profiles of the lowest energy diffusion paths for vacancies migrating a Mg-centered 1/2<110>{110} edge dislocation (triangles) and a edge-A 1/2<110> screw dislocation (squares). For reference, the energy profile along the minimum energy diffusion path in the bulk lattice is also shown (circles).

Vacancy segregation energies were found to differ between the two degenerate polymorphs of the 1/2<110>{100} edge dislocation core. As can be seen by comparing the migration energy barriers calculated for the two polymorphs (Fig. IV.9), pipe diffusion is likewise

sensitive to the core structure for this slip system. The highest mobility site around the Mg-centered structure has a migration barrier of 0.38 eV, whereas the minimum energy pathway for vacancy diffusion along the oxygen-centered polymorph has an energy barrier of 0.52 eV. This matches the ordering of segregation energies calculated for the two polymorphs calculated in section 4.1. Whereas segregation energies for $\{\square_{Mg}\}''$ defects around 1/2<110> screw dislocations are independent of the core structure, pipe diffusion of these defects along 1/2<110> screw dislocation cores is sensitive to the core structure. The highest mobility site in the core of the channel-centered polymorph has a migration barrier of 0.33 eV. However, pipe diffusion along the edge A-centered structure is more favorable, as the migration barrier of the highest mobility site is just 0.21 eV.

The higher barrier for the minimum energy path along the 1/2<110>{110} edge dislocation compared with the 1/2<110> screw and 1/2<110>{100} edge dislocations is due to the differing alignments of the line vectors ξ. The shortest diffusion path in for Mg vacancies in MgO is along 1/2<110> which, for the latter two dislocations, corresponds to the dislocation line vector. However for 1/2<110>{110} edge dislocations the shortest diffusion path is at an angle of $\pi/4$ with the dislocation line. Consequently, the diffuse path involves a jump either towards or away from the dislocation line. Where the diffusion path takes the vacancy closer to the dislocation core, diffusion transports the vacancy from a high to a low energy site, and the migration barrier is small. In contrast, when the vacancy hops to a site further away from the dislocation core, it jumps from a low to a high energy site, and the migration barrier is correspondingly much larger. Since diffusion along the dislocation involves sequential jumps towards and away from the dislocation line, the activation energy is that of the least favorable individual step. This means that pipe diffusion along

1/2<110>{110} edge dislocations is less favorable than pipe diffusion along 1/2<110>{100} edge or 1/2<110> screw dislocations.

IV.6. Conclusions

In this chapter, I have used empirical interatomic potentials to simulate the segregation of bare and protonated Mg vacancies to dislocation cores in MgO. It was found that the both $\{\square_{Mg}\}''$ and $\{2H_{Mg}\}^X$ defects segregate strongly to all three of the major dislocation slip system, with segregation energies up to several electron volts. For all three dislocations, protonated vacancies segregate more strongly than bare vacancies, with the segregation energy nearly doubling for defects around a 1/2<110>{100} edge dislocation. The presence of the dislocation was found to lift the three-fold degeneracy of the $\{2H_{Mg}\}^X$ defect, an effect attributed to interactions between the stress field of the dislocation and the anisotropic stress field of the point defect. Vacancy related defects can migrate along dislocation cores via pipe diffusion. Dislocations oriented along <110> (i.e. 1/2<110> screw dislocations and 1/2<110>{100} edge dislocations) provide fast diffusion pathways for $\{\square_{Mg}\}''$ defects, with activation energies for pipe diffusion up to an order of magnitude lower than the activation energy for bulk diffusion of Mg vacancies and considerably lower than the lowest migration barrier for pipe diffusion along a 1/2<110>{110} edge dislocation. Migration barriers are not the only contributor to diffusion rates, as the attempt frequency also determines the mean time for a migration event to occur, and calculation of site and transition state normal modes would be essential to determine pipe diffusion rates from the migration barriers computed here.

The segregation of vacancies (bare and protonated) to dislocation cores in MgO can potentially influence its high-stress rheology, by reducing the Peierls stress required to initiate dislocation glide. As we have shown here, vacancy-related defects segregate strongly to all three major dislocation slip systems in this mineral. The calculated binding energies are often considerable, with the lowest energy sites having binding energies of several electron volts, ensuring that defect concentrations at dislocation cores will be far greater than in the bulk lattice, even at high temperature. Consequently, it is possible that dislocation mobility may be enhanced when the chemical environment is suitable for the generation of vacancy-related defects, such as under hydrous or oxidizing conditions. Moreover, vacancy lubrication may be possible even for low bulk concentrations of Mg vacancy-related defects, as the large segregation energies mean that vacancies may be orders of magnitude more abundant in the dislocation than the undeformed bulk lattice. The possibility of vacancy lubrication of dislocation is investigated in more detail in chapter VIII.

Chapter V. Atomistic simulations of point-defect segregation to dislocation cores in forsterite

1. Introduction

Olivine is an orthosilicate mineral (space group *Pbnm*) of composition $(Mg,Fe)_2SiO_4$, and is the most abundant mineral in the Earth's upper mantle, comprising ~60-70% of the region. Although nominally anhydrous, under mantle pressure and temperature conditions, it can incorporate modest amounts of water into its crystal structure, primarily as protonated vacancies (e.g. Martin and Donnay 1972; Bai and Kohlstedt 1993; Kohlstedt et al. 1996; Lemaire et al. 2004). Water-related defects are important for understanding olivine rheology because, even at low concentrations, they substantially alter its physical properties, increasing the diffusivity of cations (Costa and Chakraborty 2008), reducing its creep strength (Girard et al. 2013; Faul et al. 2016), and even reducing the pressure at which olivine transforms into wadsleyite (Chen et al. 2002). Bare vacancies are frequently invoked to achieve balance in the oxidation of Fe^{2+} to Fe^{3+} (Stocker and Smyth 1978; Nakamura and Schmalzried 1983).

Early deformation experiments showed that the presence of hydrous defects can cause water weakening of olivine, with crystals deformed under wet conditions at 1300°C with a flow stress reduced ~1.5-2.5-fold relative to crystals deformed at the same temperature and strain rate under dry conditions (Mackwell et al. 1985). In the low temperature-high stress creep regime, deformation is controlled by dislocation glide, with dislocation climb enabling dislocations to move past obstacles in the lattice (Boioli et al. 2015). Hydrous

conditions increase experimental strain rates in this creep regime, potentially indicating that protonated defects segregated to dislocation cores are able to lubricate dislocation glide in olivine (Katayama and Karato 2008). Dislocation glide may also be important for grain boundary sliding under some conditions, by relaxing stress concentrations at asperity contacts (Hansen et al. 2011; Hansen et al. 2012ab). For olivine, the most common dislocations have Burgers vectors [100] or [001]. At low pressure, the easiest slip system is [100](010) (Hilairet et al. 2012), but the [001](010) slip system becomes more active at high pressure (Couvy et al. 2004; Hilairet et al. 2012). In the power law creep regime, where dislocation climb predominates, the [001](010) slip system is the more important contributor to strain rates (Tielke et al. 2016).

Dislocations can also influence the chemistry of minerals, by acting as reservoirs for trace or incompatible elements. They interact elastically with other defects in the crystal lattice, including point defects such as vacancies and substitutional impurities. Segregation phenomena can also affect the bulk chemistry of minerals, as for example in the formation of striped chemical zoning in olivine during low strain-rate deformation, due to Fe^{2+} segregation to the sub-grain boundaries formed by arrays of edge dislocation (Ando et al. 2001). Some defects may enhance dislocation glide by reducing the Peierls stress, σ_p. In particular, hydrous defects are thought to reduce σ_p in olivine, as the σ_p measured for hydrated olivine is ~1.6-2.9 GPa (Katayama and Karato 2008), considerably lower than values measured for dry olivine polycrystals, which range from at least 3.8 GPa (Idrissi et al. 2016) to as much as ~15 GPa (Demouchy et al. 2013). Although there is presently no definitive evidence that hydrous defects segregate to dislocation cores in olivine, high-resolution synchrotron images show that concentrations of protonated defects in olivine are

greatest around grain boundaries and cracks, demonstrating that water in olivine will tend to segregate to locally strained regions of the crystal lattice (Sommer et al. 2008).

The short length scales characteristic of impurity segregation to dislocation cores mean that it can be difficult to study experimentally, although developments in the field of atom probe tomography mean that it is now possible to visualize impurity clouds around dislocation lines (Miller et al. 2006). Theoretical modeling offers an alternative approach, allowing direct access to the atomic scale and control over system chemistry. Interactions between dislocations and point defects far from the dislocation line can be adequately modeled using linear elasticity theory; close to the dislocation line (i.e. within the 'core' of the dislocation) atomic-scale relaxation is significant within the dislocation core. One way to model a dislocation is to insert two or more dislocations into a 3D-periodic simulation cell, with their Burgers vectors **b** summing to zero to ensure continuity at the boundaries. Limited system size permits the use of *ab initio* methods, but dislocation-dislocation interactions may be substantial. An alternative is to embed a single dislocation in an isolated cluster of atoms with periodic boundary conditions along the dislocation line (Walker et al. 2005a). Both the cluster-based (Walker et al. 2005b) and supercell (Mahendran et al. 2017) approaches have been used to simulate [100] and [001] screw dislocations in forsterite, producing comparable dislocation core structures, although the latter study did not report core energies for either slip system.

While atomistic modeling is a powerful tool for studying dislocations and their interactions with point defects, there are several limitations that restrict its range of applicability. Firstly, obtaining a converged dislocation core structure and energy may require the use of very

large simulation cell, containing many hundreds or thousands of atoms, for which the computational cost of using quantum chemical methods such as DFT can be prohibitive. Instead, as in this study, interatomic potentials are more commonly used, which are parameterized by fitting to experimental data or *ab initio* calculations. The second problem is that the dislocation itself breaks the translational symmetry of the crystal, meaning that interactions between point defects cannot be parametrized using any of the techniques available for solid solutions, such as cluster expansion (Sanchez et al. 1984) or Special Quasirandom Structures (Zunger et al. 1990), and the dislocation energy must be obtained from fully atomistic calculations. In practice, this limits calculations to the dilute limit.

In this study, we use the cluster-based approach to determine segregation energies for dry and hydrated cation vacancies to dislocation cores in the forsterite (Mg_2SiO_4) end-member of the olivine solid solution. Interatomic interactions are modeled using a widely applied interatomic potential for hydrous forsterite. Segregation energies are calculated for Mg vacancies located on the M1 and M2 sub-lattices, and for Si vacancies. Additionally, we consider protonated M site vacancies, to determine if the decoration of cation vacancies in olivine with protons changes their segregation properties.

V.2. Computational methods

Dislocation core structures and segregation energies were calculated using the cluster-based approach, described in more detail in Chapter IV. The core energy and core displacement field of a dislocation in a two-region cluster depends on the radius of the relaxed region. A region I radius R_I = 25 Å was sufficient to guarantee convergence of the calculated core energies of the [100](010) edge and [100] and [001] screw dislocations to <10 meV/Å,

while a larger region I with radius R_I = 35 Å was needed to achieve similar precision for the [001](010) edge dislocation. The coulomb energy was calculated using the Wolf summation method (Wolf et al. 1999), which uses a charge neutralizing term to guarantee convergence of the energy at a finite distance, and has been found to produce more physically reasonable properties for systems without 3D periodic boundary conditions than the computationally more demanding Ewald method (Demontis et al. 2001; Gdoutos et al. 2010). A cutoff range of r_{cut} = 15 Å and damping parameter ξ = 0.2 $Å^{-1}$ were used, giving lattice parameters and elastic constants that differ from the values calculated using the Ewald method by <1%. As electrostatic interaction between ions is truncated at r_{cut}, the region II radius R_{II} of R_I+r_{cut} is used for all cluster calculations. Due to the large size of the simulation cell, all calculations are performed using empirical interatomic potentials in the program GULP (Gale 1997; Gale and Rohl 2003). The interatomic potentials used are from the THB1 model (Sanders et al. 1984; Catlow and Price 1985), which was used in Chapter IV to calculate energies for segregation of $\{\square_{Mg}\}''$ and $\{2H_{Mg}\}^X$ defects to dislocations in MgO. Its parameters are summarized in Table IV.1.

$\{\square_{M1}\}''$, $\{\square_{M2}\}''$, and $\{\square_{Si}\}''''$ defects are inserted into a simulation by removing atoms of the specified type. As these defects are charged, a charge-neutralizing background was applied to the simulation cell, to maintain overall charge neutrality. In addition to calculating segregation energies for Mg and Si vacancies, segregation energies were also calculated for protonated Mg site vacancies (written $\{2H_{Mg}\}^X$ in the Kroger-Vink notation), which may be expected to exist in mantle olivine wherever the oxygen fugacity is high, owing to the high a_{SiO2} associated with the presence of coexisting pyroxene minerals.

Constructing a $\{2H_{Mg}\}^X$ defect involves not only deletion of the Mg ion occupying the specified M site, and its replacement with two H ions, but also the replacement of two of the O ions around the site with oxygen ions using the hydroxyl potential. There are three symmetrically distinct O sites in olivine labeled O1, O2, and O3, leading to a large number of possible configurations of the $\{2H_{M1}\}^X$ and $\{2H_{M2}\}^X$ defects. For each site, protonated defects are created in the configuration predicted by Walker et al. (2006) to have the lowest energy. In a protonated M1 vacancy, the hydrogen atoms are bonded to oxygen in the O2 site, while the hydrogen atoms in a protonated M2 vacancy are bonded to oxygen atoms on the O2 and O3 sites. Excess energies of isolated empty and protonated M-site vacancies were calculated using a simulation cell with dimensions 4*a*x2*b*x4*c*, where *a*, *b*, and *c* are the forsterite cell parameters, was found to be sufficiently large to converge the calculated excess energies of the point defects to <0.05 eV.

In cluster calculations, the segregation energy of a single point defect at an atomic site in a dislocation core is determined by embedding it in a simulation cell whose length is a multiple of the unit cell edge parallel to the dislocation line vector, ξ, and comparing its energy with that of an isolated defect in the bulk lattice. The segregation energies for the tightest binding site of the $\{\square_{M1}\}''$, $\{\square_{M2}\}''$, $\{2H_{M1}\}^X$, and $\{2H_{M2}\}^X$ defects for all four dislocations were converged to <0.05 eV by using supercells with length n = 3. The distance between a point defect and its closest periodic image is thus 17.960 Å for dislocations with line vector [001] and 14.346 Å for those with line vector [100]. The energy of the $\{\square_{Si}\}''''$ defect is comparatively high, and so larger simulation cells with length n = 5 were used for dislocations with line vector [100] and n = 4 for those with line vector

[001]. These cell lengths give minimum distances between point defects and their periodic images of 23.909 Å and 23.946 Å for [100] and [001] oriented dislocations, respectively.

V.3. Dislocation core properties

The energy of a given dislocation depends on its coordinates within the crystallographic plane normal to $\boldsymbol{\xi}$. For each of the dislocations considered in this study, there are several possible symmetrically distinct origins (labeled in Fig. V.1). In the case of edge dislocations, which also break any rotational symmetry of the crystal about the line vector $\boldsymbol{\xi}$, the number of symmetry distinct origins for a dislocation can be even higher. Core energies for the most stable configuration found for each dislocation obtained by fitting the computed radial variation of the excess energy (Fig. V.3) to equation (IV.1) are reported in Table V.1. Also shown are their associated elastic energy coefficients *K*, which are determined from the elastic constant C_{ij} using the Stroh sextic theory (Stroh 1958). Stable core structures are displayed in Fig. V.2.

Table V.1 Calculated core energies and elastic energy coefficients for dislocations in forsterite

	E_{core} (eV/Å)	*K* (GPa)
[100](010) edge dislocation	2.42±0.04	135.0
[001](010) edge dislocation	2.46±0.07	92.3
[100] screw dislocation	1.78±0.02	79.1
[001] screw dislocation	1.50±0.03	57.4

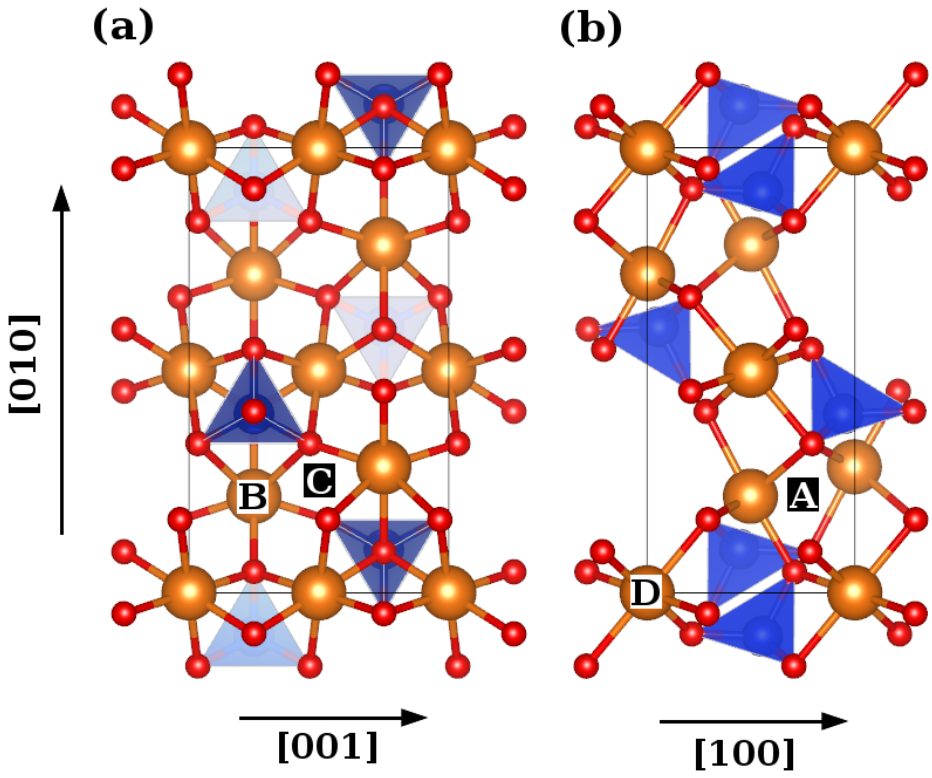

Fig. V.1 Olivine unit cell viewed down (a) the [100] cell direction, and (b) the [001] cell direction. Locations A, B, C, and D are, respectively, the points in the unit cell through which the most stable core structures for the [100](010) edge, [001](010) edge, [100] screw, and [001] screw dislocations pass. Visualization produced using VESTA 3 (Momma and Izumi 2011).

[100] screw dislocations have higher core energies, E_{core}, than [001] screw dislocations. The calculated core energies for the [100](010) and [001](010) edge dislocation slip systems are comparable. However, the core radius r_c depends on the length of the Burgers vector, which is shorter for the [100](010) edge dislocation, and E_{core} therefore corresponds to the energy of a smaller region. As can be seen in Table V.1, the [001] screw dislocation has the lowest core energy (1.50 eV/Å) and elastic energy coefficient (57.4 GPa) among the dislocations

considered in this study. Consistent with these results, atomistic calculations of generalized stacking fault energies show that both the relative volume change of SiO_4 tetrahedra and the displacement of atoms away from the fault surface, which serve as measures of nonelastic strain, are greater for [100](010) slip than [001](010) slip (Durinck et al. 2005). Thus, we expect [100](010) dislocations to have higher core energies than [001](010) dislocations.

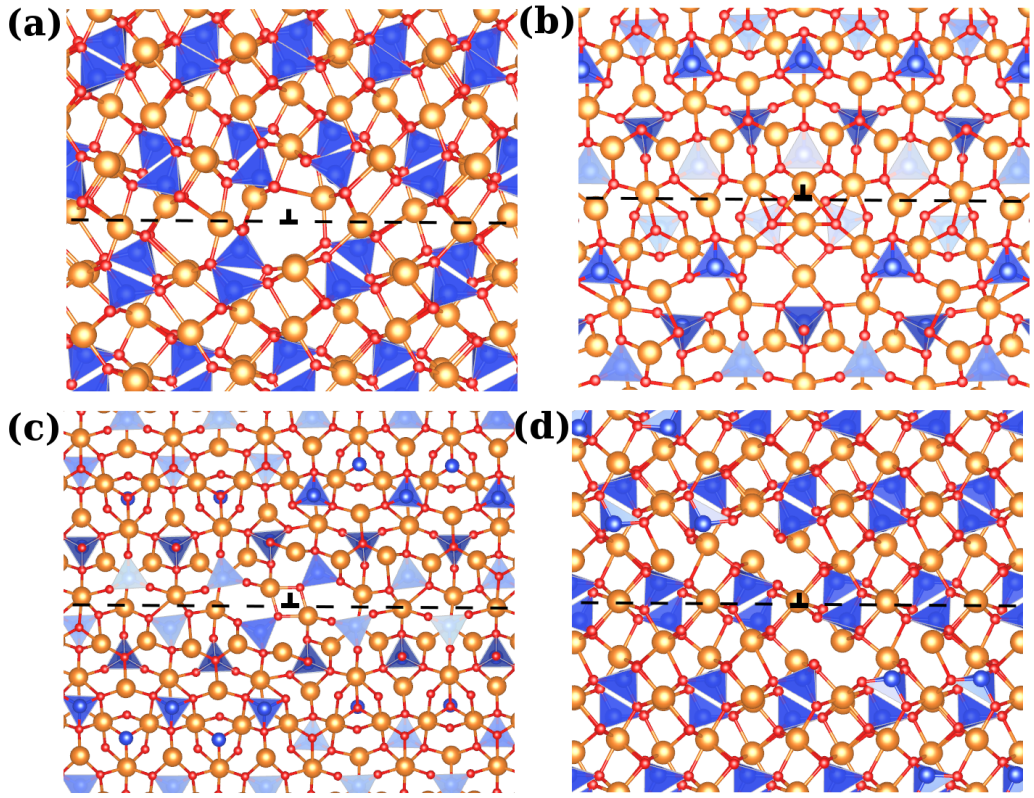

Fig. V.2 Atomic structures for the most stable core polymorphs of the (a) [100](010) and (b) [001](010) edge dislocations, and (c) [100] and (d) [001] screw dislocations in forsterite. The dislocation line and (010) glide plane have been marked. Visualization produced using VESTA 3 (Momma and Izumi 2011).

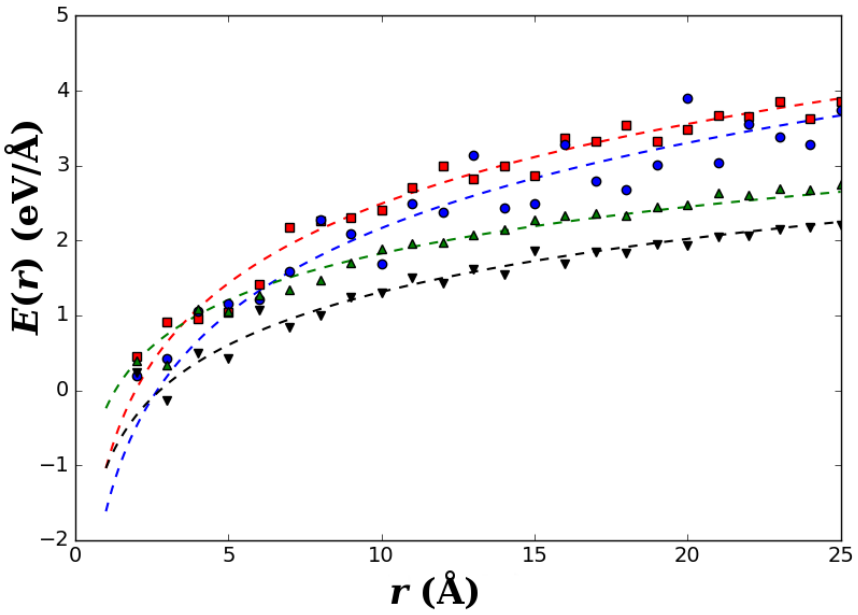

Fig. V.3 Dislocation line energies as a function of distance *r* from the dislocation line, together with the energy curve fitted using equation (V.1). [100](010) edge, [001](010) edge, [100] screw, and [001] screw dislocations energies are shown using squares, circles, triangles, and inverted triangles, respectively.

Equilibrium core structures for the [100](010) and [001](010) edge dislocations are shown in Fig. V.2ab. As can be seen in Fig. V.2a, the [100](010) edge dislocation has an asymmetric core structure, a consequence of the absence of mirror planes parallel to [100]. The algorithm for creating an edge dislocation creates something similar to a vacant M2 site near the [100](010) dislocation line. Inserting an Mg atom at this site increases the core energy by 0.2 eV/Å. As a consequence, the [100](010) edge dislocation has an empty channel parallel to ξ, causing the oxygen ions closest to the dislocation line to be under-coordinated. In contrast to the [100](010) edge dislocation, the stable core structure of the [001](010) edge dislocation is symmetric, due to the existence of mirror planes parallel to (001) located at z = 0.25 and z = 0.75, passing through the row of Si atoms parallel to

[010]. Both edge dislocations lie on the median planes of the $M2O_6$ polyhedra (y = 0.25/0.75). This is consistent with quantum mechanical calculations of generalized stacking fault energies, which find that ideal shear stresses for [100](010) and [001](010) slip are lowest when slip is localized at y = 0.25 (Durinck et al. 2005).

For the [100] screw dislocation, we find that the origin of the most stable core structure is (0.5, 0.25), halfway between adjacent M2 sites (Fig. 1a), which has a calculated core energy of E_{core} = 1.78 eV/Å. This core structure was also reported by Mahendran et al. (2017), who used the alternative supercell approach. Earlier work using the cluster-based approach, by contrast, found that the dislocation centered on the M1 site has a lower energy (Walker et al. 2005b), for which we compute a relatively high core energy of 1.97 eV/Å. The discrepancy is likely due to the fact that Walker et al. (2005b) searched for the minimum energy core structure using single point energy calculations at each possible core position, whereas the core structures were relaxed in this study. Local atomic-scale structure thus has a determining effect on the relative stability of the different core configurations for the [100] screw dislocation in forsterite.

Whereas other dislocations gliding on (010) are located on the median plane of the sheet of $M2O_6$ octahedra, the most stable core structure of the [001] screw dislocation is centered on the column of $M1O_6$ polyhedra running parallel to [001], consistent with previous theoretical calculations (Walker et al. 2005b; Mahendran et al. 2017). As found in previous studies (Carrez et al. 2008), the [001] screw dislocation has a non-planar core. This is can be seen clearly in the sub-periodic modulation of the displacement **u** of M1 sites located in the lattice plane a distance 1/2b above and below the glide plane. These atoms are displaced

normal to the (010) glide plane, with the sense of this displacement alternating along [001] (see Fig. V.2d). The SiO_4 tetrahedra in this plane undergo significant rotation, with the sign of this rotation alternating in the fashion as the sign of the displacement of neighboring M1 sites. This modulation causes the two-fold rotation center at z = 0.5, where *z* is the coordinate along the dislocation line, to disappear. In what follows, the region in which 0.0 <= *z* < 0.5 is referred to as the "lower" region, and the region with *z* satisfying 0.5 <= z < 1.0 as the "upper" region. In this labeling scheme, the lower region corresponds to those M1 sites that relax away from the (010) glide plane, and the upper region to the sites that relax toward it.

V.4. Segregation of Mg vacancies to dislocations

Excess energies of defects in the bulk lattice

Segregation energies are calculated from equation (V.4), which requires the excess energy of a point defect in the bulk lattice. This excess energy is defined as the difference between the energies of forsterite supercells of the same size, with and without a point defect. The excess energy of an $\{\square_{M1}\}''$ defect, corrected for the interactions between charged defects, is 24.0 eV, while a $\{\square_{M2}\}''$ defect has a modestly higher excess energy of 25.9 eV, reflecting the lower energy of a magnesium ion in M2 site. Similarly, the excess energy of a $\{2H_{M2}\}^X$ defect in the bulk lattice is 51.4 eV, significantly greater than the 49.5 eV excess energy calculated for the $\{2H_{M1}\}^X$ defect. These excess energies are uniformly lower than those reported by Wright and Catlow (1994) using the Mott-Littleton procedure (Mott and Littleton 1938), perhaps because of the larger number of atoms used in this study.

Table V.2 Minimum segregation energies (in eV) for defects around dislocations in forsterite. In each of these cases, the minimum energy site is close to the dislocation core, where atomic-scale effects dominate over elastic terms such the size-effect and inhomogeneity interactions

	[100](010) edge dislocation	[100] screw dislocation	[001](010) edge dislocation	[001] screw dislocation
$\{\square_{M1}\}''$	-3.00	-0.87	-1.74	-0.76
$\{2H_{M1}\}^X$	-2.28	-1.71	-1.50	-0.77
$\{\square_{M2}\}''$	-3.93	-1.91	-3.64	-1.89
$\{2H_{M2}\}^X$	-2.61	-2.12	-2.48	-0.99
$\{\square_{Si}\}''''$	-4.00	-2.28	-3.57	-1.99

Creating an M1 vacancy, whether protonated or bare, is thus more energetically favorable than creating an M2 vacancy. $\Delta H_{M1\rightarrow M2}$, the enthalpy of the required to exchange an Mg vacancy between the M1 and M2 sub-lattices is 1.9 eV, identical to previous values of $\Delta H_{M1\rightarrow M2}$ calculated using empirical potentials (Jaoul et al. 1995; Walker et al. 2009), but higher than the 0.81 eV energy difference predicted by DFT calculations (Brodholt 1997). The energy difference $\Delta H_{M1\rightarrow M2}$ between the $\{2H_{M1}\}^X$ and $\{2H_{M2}\}^X$ defects is also 1.9 eV. As the relative concentrations of vacancies on the two sites is $\exp(-\Delta H_{M1\rightarrow M2}/k_BT)$, M1 vacancies, bare and protonated, will be considerably more abundant than similar M2 vacancy-related defects in the bulk lattice. However, the magnitude of the stress field around the $\{\square_{M2}\}''$ and $\{2H_{M2}\}^X$ defects, which are of comparatively high energy, is considerably greater than around the low energy $\{\square_{M1}\}''$ and $\{2H_{M1}\}^X$ defects. M2 vacancy-related defects can thus be expected to interact more strongly with dislocation core fields, leading to higher relative abundance of M2 defects close to the dislocation line.

Segregation of M1 vacancies

The segregation energy for the $\{\square_{M1}\}''$ defect around a [100](010) edge dislocation is lowest for the three sites located directly below the dislocation line (Fig. V.4a). The $\{\square_{M1}\}''$ defect binds particularly tightly to the site at x = 0, with segregation energy -3.00 eV, compared with -0.96 eV for the two adjacent sites below the glide plane. Segregation energies for the $\{2H_{M1}\}^X$ defect are similarly lowest for the three sites immediately below the glide plane, although their segregation energies are more similar in value. E_{seg} = -2.28 eV for the site at x = 0, while E_{seg} = -1.85 eV for the adjacent sites.

Segregation energies for M1 defects around [001](010) edge dislocations are shown in Fig. V.5. $\{\square_{M1}\}''$ defects bind to the sites immediately above the glide plane of [001](010) edge dislocations, with segregation energy -1.74 eV. As was found for $\{\square_{M1}\}''$ around the [100](010) edge dislocation, segregation energies increase markedly away from the most stable binding site; the next lowest energy is -1.05 eV, corresponding to the M1 sites on either side of the tightest binding sites. As was found for [100](010) dislocations, $\{2H_{M1}\}^X$ defects segregating to [001](010) edge dislocations preferentially bind to sites directly below the glide plane and close to the dislocation line, albeit with considerably higher segregation energies than found for [100](010) edge dislocations. For the tightest binding site, which is located directly below the dislocation line, E_{seg} = -1.51 eV. E_{seg} = -1.50 eV for the M1 sites on either side of the lowest energy site. Despite the strong attraction of the $\{2H_{M1}\}^X$ defect to sites close to the [001](010) edge dislocation core, segregation energies for some sites can be as high as +0.84 eV. At these sites, the concentration of $\{2H_{M1}\}^X$ defects will be lower than in the bulk lattice.

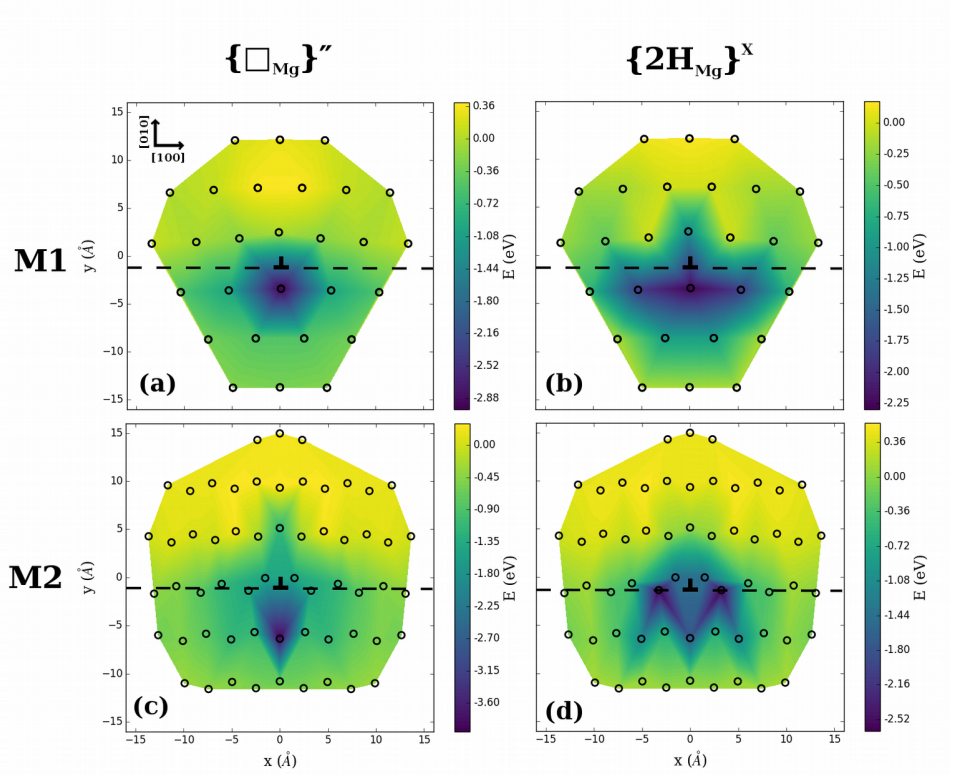

Fig. V.4 Contoured energy for segregation of bare and protonated Mg vacancies to the forsterite [100](010) edge dislocation. The [001] lattice vector is normal to the image plane. Note that segregation energies for M2 defects are computed relative to the corresponding defect in the bulk lattice, and are generally higher in energy than M1 defects. Both the dislocation line and (010) glide plane are displayed.

The calculated minimum segregation energies for M1 vacancies binding to screw dislocation cores are higher than those for the edge dislocations, consistent with the lower stresses induced by a screw dislocation. For the [100] screw dislocation, the low energy sites are distributed radially around the dislocation core (Fig. V.6), with the tightest binding sites being those closest to the (010) glide plane. The tightest binding sites for the $\{\square_{M1}\}''$ defect, at $\mathbf{r} \approx \pm[(1/2)\mathbf{c}+(1/4)\mathbf{b}]$ (**b** in this context referring to the unit cell length rather than

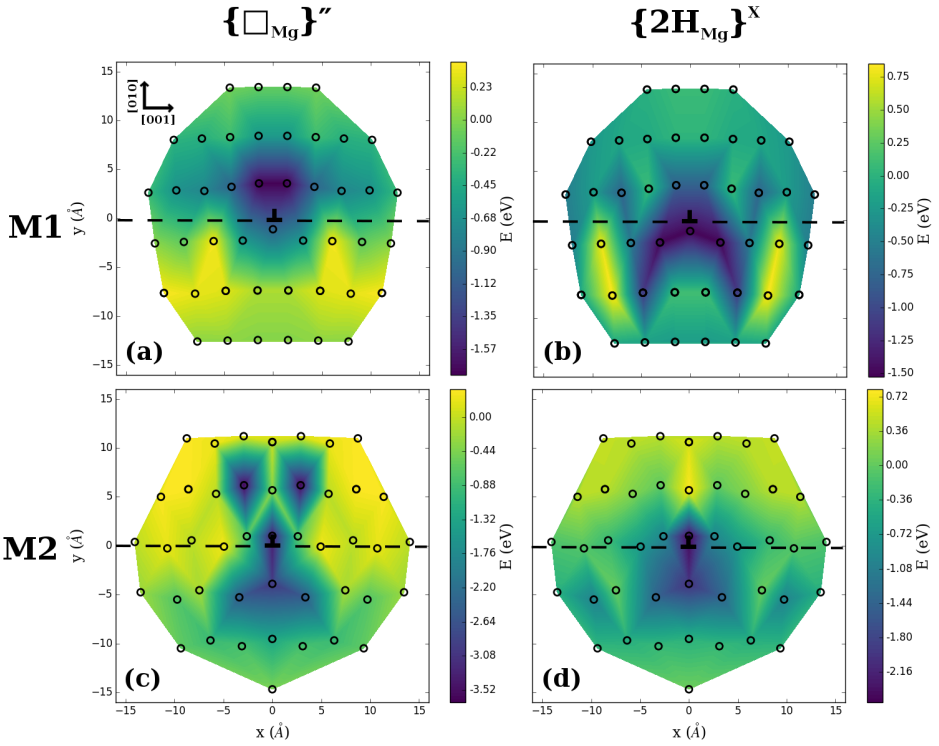

Fig. V.5 Contoured energy for segregation of bare and protonated Mg vacancies to the forsterite [001](010) edge dislocation. The [100] lattice vector is normal to the image plane.

the Burgers vector), have E_{seg} = -0.87 eV, while E_{seg} = -0.81 eV for the next most tightly bound sites, which are located at **r** ≈ ±[(1/2)**c**-(1/4)**b**]. However, the sites closest to the dislocation line, at **r** ≈ ±[δ**c**+(1/4)**b**], with δ << 1, have a comparatively high segregation energy (-0.20 eV). Comparing Fig. V.6a and Fig. V.6b, it can be readily seen that distribution of low energy sites for the $\{2H_{M1}\}^X$ defect is qualitatively similar to that computed for the $\{\square_{M1}\}''$ defect, although the relative energies of the sites at **r** ≈ ±[(1/2)**c**+(1/4)**b**] and **r** ≈ ±[(1/2)**c**-(1/4)**b**] are reversed, with E_{seg} = -1.07 eV for the former and E_{seg} = -1.71 eV for the latter. As is the case for bare M1 vacancies, energies for

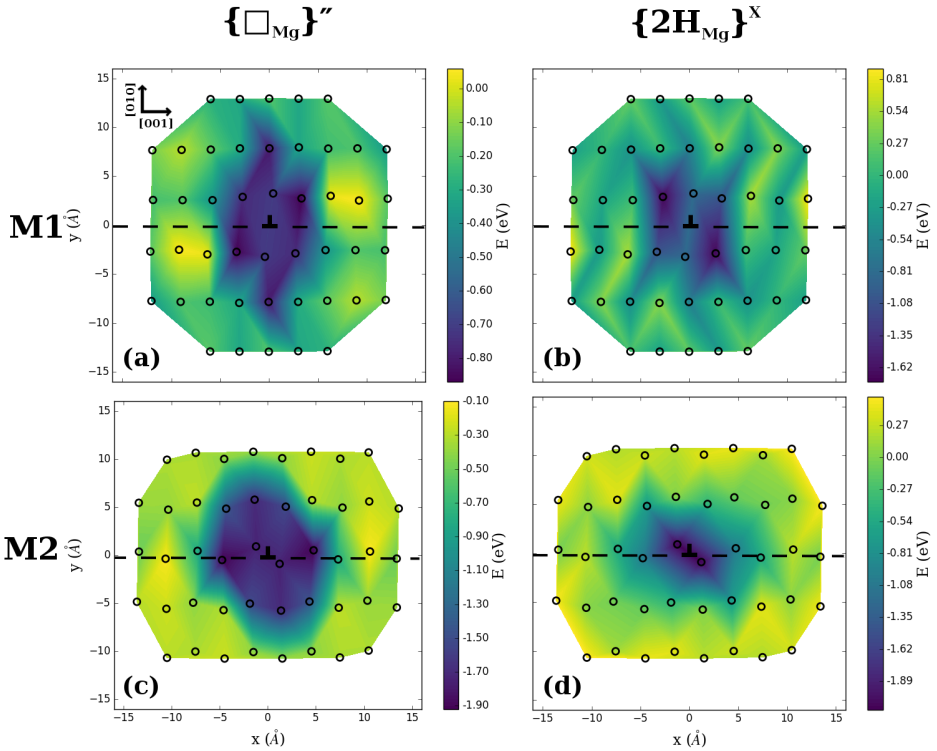

Fig. V.6 Contoured energy for segregation of bare and protonated Mg vacancies to the forsterite [100] screw dislocation. The [100] lattice vector is normal to the image plane.

segregation of $\{2H_{M1}\}^X$ defects to the sites at $\mathbf{r} \approx \pm[\delta\mathbf{c}+1/4\mathbf{b})$ are relatively high. In fact, E_{seg} = 0.23 eV, indicating modest anti-binding of the $\{2H_{M1}\}^X$ defect to these sites.

Segregation energies for defects around the [001] screw dislocation (Fig. V.7) depend not only on their location in the plane normal to the line vector $\boldsymbol{\xi}$, but also on their position along the $\boldsymbol{\xi}$, due to the modulation of the crystal structure along the dislocation line. For the bare M1 vacancy the lowest segregation energy site is -0.77 eV within the lower half of the

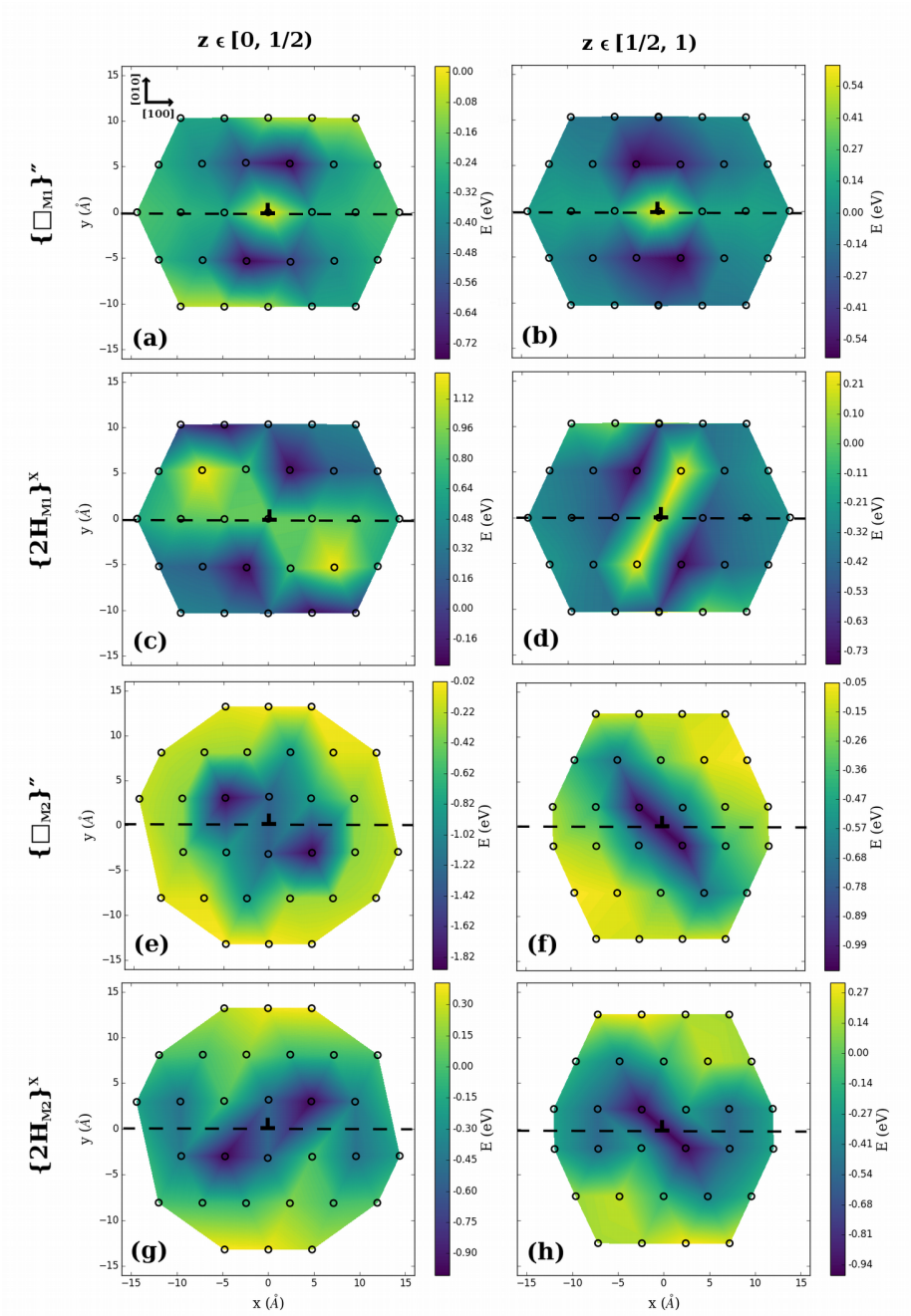

Fig. V.7 Contoured energy for segregation of $\{\square_{M1}\}''$, $\{2H_{M1}\}^{X}$, $\{\square_{M2}\}''$, and $\{2H_{M2}\}^{X}$ defects to atomic sites around [001] screw dislocations. To reflect the modulated crystal structure of this dislocation along **x**, segregation energies for the "lower" (z ϵ [0, 0.5)) and "upper" (z ϵ [0.5, 1.0)) regions are plotted separately separately.

cell, compared with -0.61 eV in the upper half. Segregation energies for the $\{2H_{M1}\}^X$ defect are more sensitive to location along the dislocation line. E_{seg} = -0.77 eV for the tightest binding site in the upper region, while the lowest segregation energy found for any site in the lower region is only -0.28 eV. This difference is reflected more generally in the segregation energy surfaces, with values near the dislocation core generally negative for the upper region, whereas E_{seg} is typically positive for sites in the lower region. For both bare and protonated defects, the segregation energy for the M1 sites through which the dislocation passes are generally near zero. Segregation energies for M1 vacancy-related defects in the upper and lower regions of the [001] screw dislocation are anti-correlated, which may inhibit pipe diffusion along this dislocation, in much the same way that diffusion of Mg vacancies along 1/2<110>{110} edge dislocations in MgO are inhibited by migration between high and low energy sites. This anti-correlation is greater for protonated than bare vacancies.

Segregation of M2 vacancies

The lowest segregation energy site for $\{\square_{M2}\}''$ around the [100](010) edge dislocation is not at the glide plane, but at x = 0 on the first sheet of $M2O_6$ octahedra below the dislocation (Fig. V.4). The segregation energy of the most stable binding site (-3.93 eV) is considerably lower than that calculated at any other location in the dislocation core, matching the behavior found for $\{\square_{M1}\}''$ defects segregating to this dislocation. The energies of the next tightest binding sites, those immediately adjacent to the dislocation on the glide plane, are considerably higher, with E_{seg} = -1.4 eV. As was found for the M1 defects segregating to this dislocation, the segregation energy surface of the $\{2H_{M2}\}^X$ defect is profoundly

different to that of the $\{\square_{M2}\}''$ defect. Unlike $\{\square_{M2}\}''$, $\{2H_{M2}\}^X$ binds to sites near the glide plane, with the lowest energies found for the four sites closest to the dislocation line. Of these, the two sites closest to the dislocation line, which are above the glide plane, have E_{seg} = -1.76 eV, while E_{seg} = -2.61 eV for the two sites below the glide plane. Above the glide plane, segregation energies rapidly decay to zero.

The tightest binding sites for $\{\square_{M2}\}''$ defects segregating to [001](010) edge dislocations are in the sheet of $M2O_6$ octahedra above the glide plane (Fig. V.5). For these sites, the segregation energy is -3.64 eV. The M2 site ~6 Å above the glide plane is the next closest in energy, with E_{seg} = 3.40 eV, while the segregation energy for the site below the glide plane that is closest to the dislocation line is -3.00 eV. The segregation energy for $\{2H_{M2}\}^X$ defects is lowest for the site directly above the dislocation line, with E_{seg} = -2.48 eV for this site. The site directly below the dislocation line is also favorable for segregation of $\{2H_{M2}\}^X$, with E_{seg} = -2.00 eV.

The low energy sites for $\{\square_{M2}\}''$ and $\{2H_{M2}\}^X$ defects around the [100] screw dislocation are distributed radially around the dislocation line (Fig. V.6). However, for both defects the tightest binding sites are located near the (010) glide plane. The energy for segregation of $\{\square_{M2}\}''$ defects to the sites closest to the dislocation line is -1.74 eV. The lowest segregation energies correspond to the next closest sites to the dislocation line, for which E_{seg} = -1.91 eV. The lowest segregation energies for the $\{2H_{M2}\}^X$ defect are found for the sites immediately adjacent to the dislocation and have E_{seg} = -2.12 eV. Segregation energies for protonated vacancies increase more markedly with distance from the dislocation line than for bare M2 vacancies.

As was found for defects on the M1 sub-lattice around [001] screw dislocations, M2 segregation energies vary along the dislocation line (Fig. V.7). The sites for which the segregation energy of $\{\square_{M2}\}''$ is a minimum are found in the lower region. For these sites, E_{seg} = -1.89 eV, whereas the lowest segregation energy for any site in the upper region is -1.06 eV. At upper mantle temperatures, the concentration of $\{\square_{M2}\}''$ defects will therefore be orders of magnitude greater in the lower region than the upper region, due to the exponential variation of relative concentrations on ΔH. As can be seen in Fig. V.7, the segregation energy surfaces for the $\{2H_{M2}\}^X$ in the upper and lower regions are spatially distinct. However, segregation energies for the tightest binding sites in the two regions are more similar for protonated than bare vacancies, with E_{seg} = -0.98 eV and E_{seg} = -0.99 eV in the lower and upper regions, respectively.

Comparing segregation energies for M1 and M2 defects

Relative to equivalent defects in the bulk lattice, $\{\square_{M2}\}''$ defects bind more tightly to core sites than $\{\square_{M1}\}''$ defects for all dislocations considered in this study (see Table V.2). The difference between the minimum segregation energies for the two defects around a [100] (010) edge dislocation is 0.93 eV. Comparable values of 1.04 and 1.18 eV are found for the [100] and [001] screw dislocations, respectively. Like their bare counterparts, $\{2H_{M2}\}^X$ defects bind more strongly to dislocation cores, relative to the equivalent defect in the unstrained lattice, than $\{2H_{M1}\}^X$ defects. M2 vacancy-related defects will be more strongly concentrated near a dislocation core, relative to the bulk, than M1 defects, although in most cases the lower absolute energies of M1 vacancies mean that these defects will remain more abundant near dislocation cores than M2 vacancies. However, the ratio of defect

concentrations on the two sites, $[\{\square_{M1}\}'']/[\{\square_{M2}\}'']$ and $[\{2H_{M1}\}^{X}]/[\{2H_{M2}\}^{X}]$, will be lower near a dislocation than in the bulk lattice.

The [001](010) edge dislocation represents a partial exception, as $\{\square_{M2}\}''$ defects bind particularly well to the core sites of this dislocation. The segregation energy (relative to an equivalent defect in the bulk) of the tightest binding site for $\{\square_{M2}\}''$ defects in the core region of this dislocation is 1.9 eV lower than that of the tightest binding M1 site, indistinguishable from $\Delta H_{M1\rightarrow M2}$ in the bulk lattice. This means that the energies for $\{\square_{M1}\}''$ and $\{\square_{M2}\}''$ defects segregating to [001](010) edge dislocation cores are identical, relative to a $\{\square_{M1}\}''$ defect in the bulk lattice, and their near-dislocation concentrations will be equal. The low energy of the tightest binding M2 vacancy for this defect is readily explained by the fact that the dislocation runs through an M2 site. Thus, the region of highest strain coincides with an M2 site. Protonation of the vacant M2 site reduces its stability relative to the lowest energy site for the $\{2H_{M1}\}^{X}$ defect. The energy difference between the lowest energy $\{2H_{M1}\}^{X}$ and $\{2H_{M2}\}^{X}$ defects around the [001](010) edge dislocation is 0.98 eV, so that the former will be more abundant.

However, while this means that the concentration of M2 vacancies, relative to M1 vacancies, is greater in the vicinity of a dislocation core than in the bulk, this does not necessarily imply that they are lower energy. Indeed, only in the case of [001](010) edge dislocations are the differences between the lowest segregation energies of the $\{\square_{M1}\}''$ and $\{\square_{M2}\}''$ defects comparable to $\Delta H_{M1\rightarrow M2}$ for the bulk lattice. The energy difference for protonated M1 and M2 vacancies is lower than the bulk $\Delta H_{M1\rightarrow M2}$ for all four dislocations, so that creation of a protonated M1 vacancy near the dislocation core is still more favorable

than creation of a protonated M2 vacancy. Assuming that vacancy-related defects can lubricate glide of dislocations in olivine, it is probable that the effect will vary with the distance of the vacant site from the glide plane. In forsterite, this implies that M2 vacancies will have a greater lubrication effect for dislocations gliding on (010) than M1 vacancies, as glide occurs primarily on the (010)-parallel sheet of $M2O_6$ octahedra. However, as shown here, with the exception of the [001](010) edge dislocation, M2 vacancies are much less abundant than M1 vacancies near dislocation cores, which could limit the magnitude of the glide lubrication effect.

V.5. Segregation energies of bare versus protonated defects

Among dislocations in forsterite gliding on (010), segregation energies are lower for edge than screw dislocations and, in general, lower for dislocations with Burgers vector **b** = [100] than those with **b** = [001]. Considering only the sites with the lowest segregation energies, bare and protonated M1 and M2 vacancies should be more abundant near [100](010) than [001](010) edge dislocations, and with generally higher concentrations for [100] screw dislocations than [001] screw dislocations. The spatial distribution of segregation energies for protonated and bare M site vacancies for a specific dislocation are similar. However, as noted in the previous section, the fine details of the segregation energy surfaces can vary considerably and non-trivially between $\{\square_{M1}\}''$ and $\{2H_{M1}\}^X$, and $\{\square_{M2}\}''$and $\{2H_{M2}\}^X$. In this section, we will attempt to quantify the degree to which protonation changes segregation energies.

The degree to which the segregation energies for two defects around a particular dislocation are similar to one another can be quantified by computing a similarity measure for the

segregation energy surfaces around the dislocation core. One such measure is the cosine similarity measure, which is computed for two vectors $\mathbf{x}_1$ and $\mathbf{x}_2$ as

$$s_{12}(\mathbf{x}_1, \mathbf{x}_2) = \mathbf{x}_1 \cdot \mathbf{x}_2 / (\|\mathbf{x}_1\| \|\mathbf{x}_2\|) \quad \text{(V.1)}$$

The similarity s_{12} = -1 when the vectors are anti-correlated, while s_{12} = 1 for perfectly correlated vectors. The cosine similarity measure is widely used in data mining to compare data sets, with applications ranging from facial verification (e.g. Nguyen and Bai 2010), to comparing linguistic data sets (e.g. Liao and Xu 2015) and automated text classification (e.g. Song et al. 2009). Here, we represent a segregation energy surface for a single point defect around a dislocation as a vector of length equal to the number of sites, whose entries correspond to the segregation energies of each site. Thus bare and protonated vacancies around the same dislocation can be compared provided that segregation energies have been computed for the same list of sites, as is the case in this study. However, the similarity measure cannot be straightforwardly compared between slip systems, as the list of sites will be different. Values of s_{12} for the M1 and M2 sites around each of the dislocation types are given in Table V.3.

Table V.3 Values of the cosine similarity measure for bare and protonated M sites around the various dislocations in forsterite

	[100](010) edge dislocation	[100] screw dislocation	[001](010) edge dislocation	[001] screw dislocation
M1	0.848	0.610	0.379	-0.244
M2	0.741	0.556	0.671	0.562

The similarity s_{12} of the M2 sub-lattice is strictly positive for all dislocations, meaning that the segregation energies of $\{\square_{M2}\}''$ and $\{2H_{M2}\}^X$ defects to dislocations in forsterite are invariably positively correlated. While s_{12} is negative for the M1 sub-lattice in the vicinity of a [001] screw dislocation, because of the modulated core structure of this dislocation, its properties are anomalous, and s_{12} is positive for the [100](010) and [001](010) edge and [100] screw dislocations. Bare and protonated Mg vacancies around [100](010) edge dislocations have relatively similar energies for both sub-lattices. However, the similarity s_{12} between $\{\square_{M1}\}''$ and $\{2H_{M1}\}^X$ defects is modestly higher than that for the corresponding defects on the M2 sub-lattice, with a ratio of similarity measures $s_{12}(M1)/s_{12}(M2) = 1.1$. The similarity between bare and protonated defects around [100] screw dislocations is similarly greater for the M1 sub-lattice, and the ratio between the similarities between bare and protonated defects for the two M sites is likewise 1.1. Conversely, for the [001](010) edge dislocation, s_{12} is greatest for the M2 sub-lattice, with $s_{12}(M1)/s_{12}(M2) = 0.6$.

While the segregation energy surfaces for protonated and bare M2 vacancies around a [001] screw dislocation are similar ($s_{12} = 0.526$), the cosine similarity for the M1 site is negative, meaning that the energies are moderately anti-correlated. The dislocation has a modulated structure and defects on M1 sites that are adjacent along [001] have different segregation energies, as seen in Fig. V.7. Considering the segregation energies for the M1 sites at y = 0.0 (Fig. V.7ab) and y = 0.5 (Fig. V.7cd) separately, we find similarities s_{12} = -0.520 and s_{12} = 0.347. Thus, for the M1 sites which displace away from the (010) glide plane, $\{\square_{M1}\}''$ and $\{2H_{M1}\}^X$ segregation energies are modestly anti-correlated, while they are weakly correlated for the M1 sites that are displaced towards the glide plane. Segregation energies for the M2 site also vary between the upper and lower regions of the [001] screw

dislocation. For the lower region, s_{12} = 0.471, while s_{12} = 0.791 in the upper region. As was found for the M1 sub-lattice, bare and protonated Mg vacancies are more similar in the upper than the lower plane.

V.6. Si vacancy segregation

Due to the strength of an Si-O bond in an SiO_4 group, the excess energy of a $\{\square_{Si}\}''''$ defect is considerably greater than that of either bare Mg vacancy, and calculated here to be 98.6 eV. This is consistent with values obtained for the $\{\square_{Si}\}''''$ defect formation energy using both empirical (Walker et al. 2006) and quantum chemical calculations (Berry et al. 2007). The stresses induced by an Si vacancy are significantly greater than those caused by an Mg vacancy, so stronger partitioning of this defect from the bulk lattice to dislocation core sites is expected. Note that, because the form of the O-Si-O three-body potential is harmonic, dissociation energies must be treated with some skepticism. However, no other potential models presently exist that can reproduce the stiffness of the SiO_4 tetrahedron without employing a harmonic potential for the O-Si-O bonding angle.

Segregation energies for the Si vacancies around [100](010) and [001](010) dislocations are shown in Fig. V.8. Comparing the minimum segregation energies for the five vacancy-related defects considered in this study, we see that segregation energies are higher for protonated Mg vacancies than bare Si vacancies, but bare Mg and Si vacancies have similar segregation energy minima (Table V.2). In the vicinity of [100](010) dislocation cores, $\{\square_{Si}\}''''$ defects likewise bind particularly to the T-sites immediately below the dislocation line, with a segregation energy E_{seg} = -4.00 eV. Segregation energies on either side of the tightest binding site are similarly low (-3.24 and -3.18 eV), and there is another low energy

site above the glide plane, which has E_{seg} = -3.46 eV. However, there is also a strongly anti-binding T-site near the dislocation line (Fig. V.8a), for which E_{seg} = 2.17 eV. The high energy of this site can be attributed to orientation of the SiO_4 group, three of whose oxygen atoms are adjacent to the [001]-parallel channel along the dislocation, and hence severely under-coordinated. Thus, the removal of an Si ion at this site is energetically highly unfavorable.

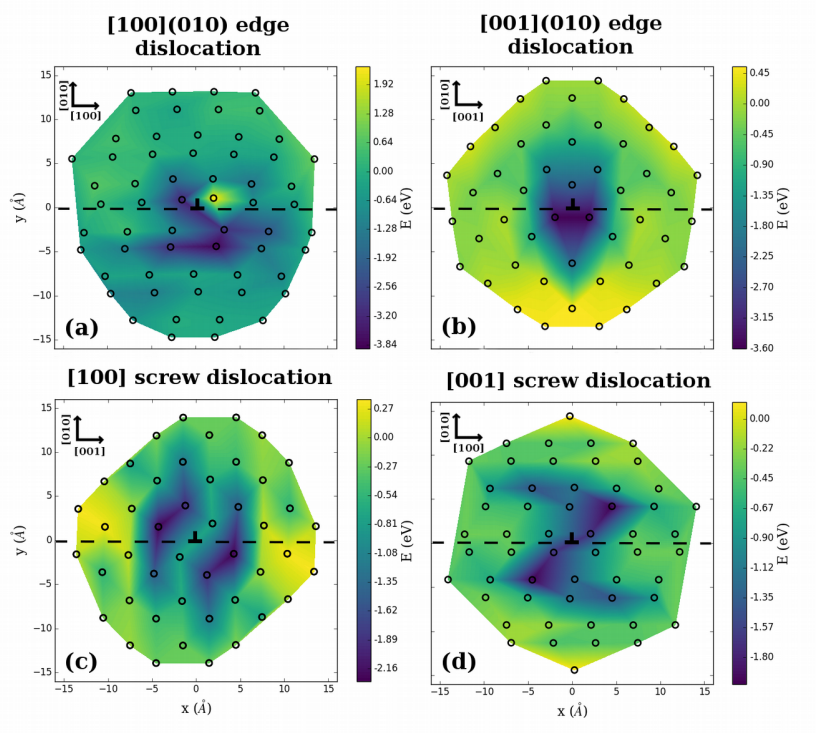

Fig. V.8 Contoured energy for segregation of $\{\square_{Si}\}''''$ defects to (a) [100](010) edge dislocations, (b) [001](010) edge dislocations, (c) [100] screw dislocations, and (d) [001] screw dislocations in forsterite.

Among the core sites of [001](010) edge dislocations, $\{\square_{Si}\}''''$ defects bind most tightly to those immediately below the glide plane. For these sites, the lowest segregation energies are found for sites directly below the glide plane, separated from the dislocation line by a

distance r = 2.2 Å, where E_{seg} = -3.57 eV. The next tightest binding site, for which E_{seg} = -2.27 eV, is above the glide plane and a distance 2.57 Å from the dislocation line. That $\{\square_{Si}\}^{\prime\prime\prime\prime}$ defects partition from the bulk lattice into the compressional and tensional regions (i.e. above and below the glide) around edge dislocations indicates that linear elastic interactions are of secondary importance in determining segregation energies for this defect.

As measured by minimum segregation energies, $\{\square_{Si}\}^{\prime\prime\prime\prime}$ defects bind less tightly to screw dislocations than to edge dislocations. For [100] screw dislocation cores, the minimum segregation energy is -2.28 eV, although segregation energies for the T-sites closest to the dislocation line are higher (-0.72 eV). For the [001] screw dislocation, the lowest energy sites are spread out along the [110] direction. The segregation energy of the most stable sites, which are one lattice plane removed from the glide plane, is -1.99 eV, while the lowest segregation energy on the lattice plane closest to the glide plane is -1.69 eV.

The absolute magnitudes of these segregation energies are considerably lower than those reported for the most favorable sites in edge dislocation cores. However, it is worth noting that relative concentrations of Si vacancies on core versus bulk sites, $c_{core}/c_{lattice}$, computed as $\exp(-\Delta H/k_B T)$, where ΔH is the energy to move a Si vacancy from the bulk lattice to a dislocation core site, may be quite substantial. At 1273 K $c_{core}/c_{lattice}$ will be ~10^7 for [001] and ~10^{10} for [100] screw dislocations. Thus, provided that Si vacancies can diffuse through the lattice, the probability of finding a vacant T-sites near any dislocation core is higher, even when bulk concentrations are extremely low (<1 ppm).

Particularly for the [100] screw and [001](010) edge dislocations, the sites with the lowest segregation energy, which have the highest probability of being occupied by a $\{\square_{Si}\}''''$ defect, can be found immediately above or below the (010) glide plane. The lowest energy sites around the [100](010) edge dislocation are two lattice planes away from the (010) glide plane. However, several atomic sites immediately adjacent to the glide plane and near the dislocation line have strongly negative segregation energies. A similar observation can be made about the [001] screw dislocation. Thus, for all dislocations gliding on (010), there will be a finite concentration of Si vacancies near the dislocation, potentially lubricating glide. However, the (010) easy glide plane does not intersect any SiO_4 tetrahedra, so the effect may be less than for M2 vacancy-related defects.

V.7. Discussion

The interaction between the elastic strain field of an edge dislocation in an elastically isotropic medium and point defect whose strain field contains no component of shear (i.e. is purely dilatational) is given by (Eshelby 1957)

$$E_{hydrostatic} = A_1 \frac{\sin\theta}{r} \qquad \text{(V.2)}$$

where A_1 depends on the shear modulus of the materials, Burgers vector of the dislocation, and the magnitude of the strain induced by the point defect. As this size-effect interaction is purely hydrostatic, it is clearly zero for screw dislocations. However, this is not the only interaction between a point defect and a dislocation; the discrepancy between the elastic constants of the bulk crystal and those of the defect result in an "inhomogeneity" effect, which was shown by Bullough and Newman (1962; 1963) to have the form

$$E_{inhomogeneity} = \frac{A_2}{r^2} \qquad \text{(V.2)}$$

where A_2 depends on the elastic properties of the material and defect. For point defects that are smaller than the atom for which they substitute or, as is the case for vacancies, considerably more flexible, A_2 is negative, while rigid inclusions have positive A_2 (Bullough and Newman 1963). This latter group includes primarily large atoms/ions. The strength of interactions due to the inhomogeneity effect decays much more strongly with increasing distance from the dislocation line than the size-effect interaction. It is, however, the dominant term for screw dislocations, and can predominate for certain types of point defect, such as vacancies, for which elastic constants of the matrix and the reference phase for the dissolved defect species are significantly different.

The coefficients A_1 and A_2 depend on the elastic constants C_{ij} of the crystal, the geometry of the dislocation, and the force moment tensor of the point defect (Cottrell and Bilby 1949; Clouet 2006; Clouet et al. 2008), but can also be calculated by fitting the sum of equations (V.2) and (V.3) to the segregation energy surfaces calculated in sections 4 and 6. As these equations are undefined at $r = 0$, we limit the fit to atoms a distance $r > 2$ Å from the dislocation line for which segregation energies have been calculated, which in this study includes all atoms with $r < 15$ Å. Values for A_1 and A_2 for the dislocations considered in this study are presented in Table V.4. The fitted size-effect coefficient A_1 is zero for defects segregating to [100] and [001] screw dislocations, as the dilatational strain field induced by a point defect does not interact with the stress field of a screw dislocation, for which only the shear components are non-zero.

Only for $\{2H_{M1}\}^X$ defects segregating to [001] screw dislocation cores is the fitted inhomogeneity coefficient A_2 non-negative. However, in section 3.2 it was shown that Mg vacancy segregation energies for sites in the core of this dislocation depend on position along the dislocation line, and can be partitioned into upper and lower regions. Using only segregation energies calculated for $\{2H_{M1}\}^X$ defects in the upper region of the dislocation, we find an inhomogeneity coefficient of A_2 = -13.6±3.1 eV·Å^2. For the sites in the lower region, A_2 = 21.5±5.3 eV·Å^2. Conversely, for $\{\square_{M1}\}''$ defects segregated to sites in the lower region A_2 = -17.0±2.1 eV·Å^2, and -7.5±1.9 eV·Å^2 for sites in the upper region. Thus, M1 and M2 vacancy-related defect concentrations oscillate between high and low values along the [001] screw dislocation. The amplitude of this oscillation is greater for $\{2H_{M1}\}^X$ than $\{\square_{M1}\}''$ defects, and relative populations of the two defects are anti-correlated.

Table V.4 Calculated coefficients for the contributions of the size-effect and inhomogeneity terms to the segregation energy of selected point defects to dislocation cores in forsterite

		[100](010) edge dislocation	[100] screw dislocation	[001](010) edge dislocation	[001] screw dislocation
A_1 (eV·Å)	$\{\square_{M1}\}''$	5.3±0.2	0.0±0.3	3.5±0.3	0.0±0.4
	$\{2H_{M1}\}^X$	4.1±0.4	0.0±0.6	1.1±0.7	0.0±0.9
	$\{\square_{M2}\}''$	5.1±0.8	0.0±0.4	4.1±1.7	0.0±0.7
	$\{2H_{M2}\}^X$	5.0±0.6	0.0±0.7	5.4±0.5	0.0±0.7
	$\{\square_{Si}\}''''$	6.2±1.3	0.0±0.6	-0.7±0.7	0.0±0.8
A_2 (eV·Å^2)	$\{\square_{M1}\}''$	-14.7±0.6	-11.5±1.2	-14.5±1.4	-12.05±1.6
	$\{2H_{M1}\}^X$	-17.4±1.4	-11.8±2.8	-15.6±2.8	3.0±3.9
	$\{\square_{M2}\}''$	-22.9±2.9	-45.7 ±1.9	-16.9±4.5	-14.9±2.2
	$\{2H_{M2}\}^X$	-17.8±0.6	-9.5±3.4	-12.8±1.4	-6.8.1±1.2
	$\{\square_{Si}\}''''$	-12.0±3.8	-14.6±1.9	-18.6±1.4	-12.1±1.6

For point defects segregating to screw dislocations, binding energies are governed by the inhomogeneity effect. However, when the defect species is substantially different from the species for which it substitutes, the inhomogeneity effect can also dominate segregation energies even around edge dislocation cores. This is certainly the case for bcc metals, in which vacancies bind to sites above and below the glide plane of 1/2<111>{110} edge dislocations (Ingle and Crocker 1968). With the exception of the $\{2H_{M1}\}^{X}$ defect segregating to the [001] screw dislocation core (discussed below), the fitted inhomogeneity coefficient for each defect-dislocation pair is negative, with considerably greater absolute values than the size-effect coefficient A_1. As such, elastic interactions between vacancy-related defects and dislocations are purely attractive for all sites a distance $r < |A_2|/|A_1|$ from the dislocation core. Sites with positive segregation energies near the dislocation line, such as that found for $\{\square_{Si}\}^{''''}$ segregating to [100](010) edge dislocations, are those where the energy is dominated by atomic-scale effects.

The solubility limit of vacancy-related defects in the olivine crystal lattice is relatively high, and can reach nearly 0.9 % for protonated vacancies at 12 GPa pressure (Smyth et al. 2006). Accordingly, the presence of dislocations will not substantially change the solubility of H, even in highly deformed samples which have significant dislocation densities. However, the strongly negative segregation energies calculated for all dislocation slip systems mean that the concentration of vacancy-related defects will be many times greater in the dislocation core than in the bulk crystal lattice. Consequently, dislocation cores may

contain a large number of vacancy-related defects even in olivine crystals where their bulk abundance is low.

Vacancy-lubrication of dislocation glide has been reported in a range of different materials. Generalized stacking fault energy (GSFE) parametrized Peierls-Nabarro calculations have suggested that interstitial H may facilitate dislocation glide in Al metal, while the presence of interstitial O in hyper-stoichiometric UO_2 (i.e. UO_{2+x}, $x > 0$) is known to reduce the critical resolved shear stress (Keller et al. 1988), an effect attributed to interactions between the interstitial impurities and the dislocation core (Ashbee and Yust 1982). One possible explanation is that interactions between the dislocation core and an adsorbed vacancy defect reduce the Peierls stress, although the precise mechanism remains unclear. Deformation experiments in the glide-controlled creep regime show that the critical resolved shear stress decreases from 3.8-15.0 GPa in dry olivine (Idrissi et al. 2016; Demouchy et al. 2013) to 1.6-2.9 GPa for olivine under water-saturated conditions (Katayama and Karato 2008). This CRSS represents the stress required for deformation at 0 K, and is referred to by Katayama and Karato as the Peierls stress, although it actually represents a weighted average of the Peierls stresses for several active slip systems.

Although it is difficult to establish whether or not the critical stress measured by Katayama and Karato (2008) does in fact correspond to the Peierls stress of a dislocation or dislocations, there is evidence that the relative activities of the main olivine slip systems are affected by water. As a plastically anisotropic mineral, olivine develops a strong lattice preferred orientation (LPO) when deformed by dislocation creep, which is different under wet and dry conditions (Katayama and Karato 2008). Under dry conditions and at low

pressure, the LPO is consistent with [100](010) slip, due to the low Peierls stress of this slip system (Durinck et al. 2007; Mahendran et al. 2017). However, when water is present, the B-type deformation fabric is observed, which develops when the most active slip system is [001](010) (Jung and Karato 2001). Natural examples of olivines from subduction zone-derived rocks show this B-type fabric (Mizukami et al. 2004), and the change in deformation fabric with hydration has been used to explain the development of trench-parallel alignment of the polarizations of fast shear waves propagating sub-vertically within the mantle wedges above subducting slabs (Ohuchi et al. 2012).

While this change in LPO could be caused by hardening of the [100](010) slip system, perhaps due to pinning of the dislocation by point defects, this is inconsistent with the low flow stresses measured in deformation experiments under hydrous conditions (Katayama and Karato 2008). An alternative explanation is that protonated defects may enhance the mobility of the [001](010) slip system by lowering its critical resolved shear stress, relative to that of the [100](010) slip system, whether by reducing the Peierls stress σ_p or enhancing the rate of kink-pair nucleation. As we have shown, segregation energies are comparable for [001](010) and [100](010) edge dislocations, and substantially lower for [100] than [001] screw dislocations. Thus, [001](010) slip cannot be enhanced relative to [100](010) by differences in concentration of vacancy-related defects near the dislocation core. However, as discussed in section 4, the location of the vacancy will determine its ability to influence dislocation glide. For dislocations gliding on (010), M2 vacancies are expected to have greatest effect. In this study, we have found that segregation energies for vacancy-related defects to the M2 sites closest to the dislocation line are lower for [001](010) edge dislocations than for [100](010) edge dislocations, by ~0.7 eV. In the dilute limit, the

concentration of $\{2H_{M2}\}^X$ defects in the tightest-binding site around a [001](010) edge dislocation will thus be ~700 times greater than for the tightest binding sites in the [100](010) edge dislocation core, so that the former will experience a greater reduction of its Peierls stress than the latter. In reality, a mixture of differential lubrication of the two slip systems and different defect distributions around the dislocation core probably contribute to the development of the B-type fabric.

V.5. Conclusions

Vacancy related defects are important for understanding the material properties of olivine. The addition of small quantities of water to Fo_{90} olivine deforming in the glide creep regime increases strain rates, indicating a reduction of the Peierls stress. This has been plausibly attributed to lubrication of dislocation glide by protonated cation vacancies interacting with the dislocation, a process similar to the vacancy lubrication phenomenon invoked to explain flow stress variations for a range of materials. Concentrations of protonated vacancies or similar vacancy-related defects present at the dislocation core need to be high for the lubrication effect to be substantial. However, H concentration in mantle olivine is typically low, with <1000 ppm H/Si, although water contents may reach higher values in the deep upper mantle, as much as 0.9 wt % at 12 GPa (Smyth et al. 2006). Ferric iron, an important source of bare vacancies in silicate minerals, has a similarly low abundance, except in the most oxidized regions of the mantle (Kelley and Cottrell 2009). Consequently, vacancy lubrication is possible only if vacancy related defects bind strongly to sites around dislocation cores.

In this study, we have used cluster-based computational simulations to compute segregation energies for both bare and protonated Mg vacancies around dislocations in forsterite. These segregation energies can be < -1 eV, suggesting that vacancy-related defect concentrations near the dislocation core may be orders of magnitude higher than in the bulk lattice, especially at low to moderate T. These are precisely the temperature conditions at which dislocation glide is most important for the deformation of olivine. However, not all vacancies are equal and, while the energy of an $\{\square_{M2}\}''$ or $\{2H_{M2}\}^{X}$ defect is considerably lower near an edge or screw dislocation line than an equivalent defect in the bulk lattice, Mg vacancies preferentially occupy M1 sites. However, even though concentrations of vacancy related defects at the dislocation core may be high, they may occupy sites whose ability to directly influence dislocation glide is limited. The easy glide plane for dislocations gliding on (010) is the median plane of the sheet of $M2O_6$ octahedra, and M2 vacancies located this glide plane may play a critical role in lubricating dislocation glide. Such strategically located vacancies are expected to be most abundant around [001](010) dislocations.

Chapter VI. Peierls-Nabarro modelling of dislocations in UO_2

This work was published as: R. Skelton and A. M. Walker, Journal of Nuclear Materials ***495****, 202 (2017).*

VI.1. Introduction

UO_2 is a common oxide of uranium, and the primary fuel material for nuclear reactors. Under normal conditions, UO_2 adopts the fluorite (CaF_2) structure, with the U^{4+} ions arranged in a face centered cubic lattice and eight-fold coordinated by O^{2-}. UO_2 also occurs naturally as a mineral, known as uraninite or pitchblende. Uraninite is the most abundant uranium bearing mineral, and is an important economic source of uranium. Dislocations, a type of linear topological defect that act as carriers of plastic strain, are produced by interaction with radiation during burn-up (Nogita and Une 1995; Baranov et al. 2014) and are important for understanding the mechanical properties of UO_2, especially at low temperatures. Additionally, due to the substantial distortion of the crystal lattice in the vicinity of a dislocation, they can also serve as hosts for impurity atoms in UO_2, including fission products such as Ru (Goyal et al. 2013) and the noble gas Xe (Nerikar et al. 2011).

There are four main dislocations observed in UO_2, 1/2<110>{100}, 1/2<110>{110}, and 1/2<110>{111} edge dislocations, and a screw dislocation with Burgers vector 1/2<110> (Ashbee and Yust 1982; Keller et al. 1988). Of these, the 1/2<110>{100} edge dislocation is the weakest (i.e. moves under the application of the lowest resolved shear stress), while the 1/2<110>{110} is the strongest. Computational studies show that the screw dislocation has the lowest energy, while the 1/2<110>{110} edge dislocation has the highest energy

(Parfitt et al. 2010; Murphy et al. 2014). Under the action of an applied shear stress, a dislocation can be displaced from its equilibrium position and, if the stress exceeds some critical value (referred to as the Peierls stress, σ_p), the dislocation may begin to move. The Peierls stress and elasticity tensor together determine dislocation mobility below the athermal limit (the temperature above which dislocation velocities are controlled by dislocation-dislocation interactions rather than the Peierls stress), and can be used to model the critical resolved shear stresses, dislocation velocities, and strain rates for a given slip system, as functions of temperature. At stresses below σ_p, dislocation glide occurs through the thermally activated nucleation and migration of kink-pairs (Koizumi et al. 1993). The velocity at which a dislocation glides is related to the rate of sustainable kink-pair nucleation, the activation energy of which depends on the elastic constants of the material, and on the Peierls barrier. If the activation energy for sustainable kink-pair nucleation at zero applied stress ΔE_0 is known, the stress dependence of the activation energy is

$$\Delta E(\sigma) = \Delta E_0 \left(1 - \left(\sigma / \sigma_p\right)^p\right)^q \quad \text{(VI.1)}$$

where p and q are exponents whose values must be determined by fitting to experimental or simulation data (Kocks et al. 1975).

Despite their importance for modeling dislocation velocities and hence strain rates during glide-controlled creep, the Peierls stresses of the major dislocation slip systems in UO_2 remain poorly constrained. However, one previous study has used atomistic simulations to calculate the Peierls barriers (which are approximately proportional to σ_p) of edge dislocations in UO_2, whose values have the relative ordering 1/2<110>{100} <

1/2<110>{111} < 1/2<110>{110} (Parfitt et al. 2010). High-temperature molecular dynamics calculations of critical shear stresses show that the Peierls stresses of the edge dislocations in UO_2 follow the same relative ordering seen in Parfitt et al. (2010), and indicate σ_p is at least several GPa for all three slip systems (Fossati et al. 2013). Atomistic simulations have also shown that glide of 1/2<110>{100} edge dislocations occurs via a thermally activated mechanism below 2000 K, which is consistent with a relatively high (>1 GPa) Peierls stress for this slip system (Lunev et al. 2017). Hyper-stoichiometry is known to affect the slip systems of UO_2, reducing the critical resolved shear stress (Keller et al. 1988; Yust and McHargue 1971). The magnitude of this effect is greater on the {111} slip plane than on the {100} slip plane (Keller et al. 1988), causing their critical resolved shear stresses to converge at high temperature and oxygen fugacity.

Peierls stresses can be calculated directly using atomistic methods, either by applying a stress/strain to a supercell and determining the stress required to move the dislocations or by calculating the energies of structures intermediate between adjacent dislocation energies, giving an energy profile whose derivative is proportional to the Peierls stress. A simpler alternative to the fully atomistic approach is the Peierls-Nabarro (PN) model, which uses a hybrid continuum-atomistic approach to model dislocations. In the PN model, a dislocation is represented as a finite distribution of partial dislocations, whose elastic interactions are balanced by some inelastic restoring force (Peierls 1940; Nabarro 1947). Atomistic simulation methods can be used to parameterize this force by introducing a generalized stacking fault (GSF) into a simulation cell, which is done by displacing one half of the cell with respect to the other (Christian and Vítek 1970). One clear advantage of the PN model over fully atomistic simulations is that the bulk of the computational cost is incurred in the

generalized stacking fault (GSF) calculations used to parameterize the inelastic forces. As these contain far fewer atoms than are found in the simulation cells used to perform fully atomistic calculations of dislocation properties, the PN method can be used to calculate dislocation widths and Peierls stresses far more quickly and at lower computational cost than is possible with fully atomistic calculations.

The Peierls stress is an important parameter governing glide mobility of dislocations, knowledge of which is essential to accurately model glide-controlled creep processes during, for example, burn-up of UO_2. In this study, we use the Peierls-Nabarro model to calculate the dislocation misfit profiles and Peierls stress for the most important slip systems in UO_2 To do this, we first calculate the γ-surfaces (i.e. GSF energies over a range of different stacking fault vectors) corresponding to the main slip systems, using seven different interatomic potentials for UO_2. This subset of potentials was chosen to cover the range of possible parameterizations available in the literature and typically used to model UO_2. The models include full- and partial-charge models, rigid ions, shell models, and a recent many-body model, and allow us to infer the general behavior of these classes of parameterizations for modeling dislocations in UO_2. From the Peierls-Nabarro model, we are then able to use these γ-surfaces to calculate misfit profiles and Peierls stresses for the 1/2<110>{100}, 1/2<110>{110}, and 1/2<110>{111} edge dislocations and the 1/2<110>{110} screw dislocations in UO_2. In addition to providing intrinsic dislocation properties, allowing us to compare the suitability of different interatomic potentials for dislocation modeling, and evaluate the viability of using the PN method to study dislocations in UO_2.

VI.2. Computational methods

The Peierls-Nabarro Model

In the Peierls-Nabarro (PN) model, a dislocation with finite core-width is represented as a distribution of partial dislocations along the glide plane, whose shape is determined by the balance between the elastic energies acting between its constituent partial dislocations and the inelastic energy introduced by the presence of a disregistry **u** in the material at the glide plane, with the former acting to broaden the dislocation distribution and the latter serving to constrain it. The PN model, as used in this study, is briefly summarized below. For a more complete treatment, see Bulatov and Cai (2006).

The value of the total energy of such a finite distribution of dislocations at a distance R from the dislocation line is

$$E_{TOT}(R) = E_{ELASTIC} + E_{MISFIT} + E_{WORK} + Kb^2 \ln R \qquad \text{(VI.2)}$$

where K is an energy pre-factor whose value depends on the elastic constants and the dislocation orientation, and b is the Burgers vector magnitude. E_{ELASTIC} is the elastic interaction energy between the partials, E_{MISFIT} the energy due to the inelastic displacement of atoms at the glide plane, E_{work} the work energy and the final term gives the strain energy due to the long-ranged elastic strain field of the dislocation. As the long-ranged term is independent of the core structure and $\mathrm{E_{WORK}}$ is zero in the absence of an applied stress, the solution to PN model is the dislocation distribution that to minimizes the energy function

$$E_{INTERNAL} = E_{ELASTIC} + E_{MISFIT} \qquad \text{(VI.3)}$$

If **u**(x) is the disregistry across the slip plane and $\rho(x)=d\,u_i(x)/dx$ is the associated dislocation density distribution, then the elastic energy of the dislocation is the work required to insert this disregistry into an infinite elastic medium:

$$E_{ELASTIC}[\rho(x)]=-K\iint \rho(x')\rho(x)\ln|x-x'|\,dx'\,dx \qquad \text{(VI.4)}$$

It is worth noting that the effect of the elastic energy is to cause the dislocation to spread out so that, if there were no restoring force, the dislocation density distribution would be zero everywhere (but with finite integral). In real crystals, it is the energy penalty associated with introducing misfit on either side of the slip plane that provides this opposing force, and constrains dislocations to have finite width. For a given disregistry profile **u**(x), the inelastic energy is

$$E_{MISFIT}=\sum_n \gamma\left(u\left(na_p\right)\right)a_p \qquad \text{(VI.5)}$$

where a_p is the spacing between adjacent atomic planes and γ, called a γ-line in one dimension and the γ-surface in two, is a function that gives the energy required to displace one half of a crystal with respect to the other by **u** (Christian and Vítek 1970). The misfit energy can also be written as an integral, in which case the dislocation energy is invariant under translation, implying that the dislocation is mobile under the application of an infinitesimal external stress. When calculating the dislocation core structure numerically, the misfit profiles is expanded as a sum of arctangent functions (i.e. partial dislocations), as

$$u(x)=\frac{b}{\pi}\sum_i A_i \arctan\left(\frac{x-x_{0,i}}{c_i}\right)-C \qquad \text{(VI.6)}$$

where C is *b/2* for the component of misfit parallel to the Burgers vector and zero otherwise. The parameters $x_{0,i,}$ A_i, and c_i are found by minimizing equation (VI.3), with the elastic and misfit terms represented by equations (VI.4) and (VI.5), respectively, with the disregistry function given in the form of equation (VI.6).

The evolution of the disregistry profile under the action of an applied stress σ is computed by adding $E_{WORK} = -\sigma \int u(x)dx$ to the total internal energy (equation VI.3) of the dislocation and minimizing the energy functional as before. At the Peierls stress, σ_p, the energy barrier inhibiting free translation of the dislocation disappears, allowing it to glide indefinitely.

There are two key assumptions in the PN model as given in the preceding discussion. The first is that non-linear interactions between adjacent partial dislocations in the dislocation density distribution $\rho(x)$ are negligible, so that equation (VI.5) can be written as a linear sum of GSF energies, and this is generally true. The second assumption is that the dislocation core structure is planar, and localized on the glide plane. This is generally correct in the case of pure edge dislocations, but may fail for some screw dislocations if they spread on multiple glide planes, as is the case for [001] screw dislocations in forsterite (Carrez et al. 2008), which glide via a locking-unlocking mechanism (Nabarro 1997). If a screw dislocation exhibits non-planar core-spreading, the PN model still provides a lower bound on the Peierls stress, as dislocations with planar cores are more mobile than those with non-planar cores.

Generalized stacking fault calculations

The γ-surface energy used to calculate the inelastic energy of a dislocation density distribution is constructed from generalized stacking fault (GSF) energies obtained from atomistic calculations. This is done for each slip system by taking an appropriately oriented supercell of UO_2 and displacing the top half of the construction simulation cell along a grid of stacking fault vectors and relaxing the atomic coordinates, subject to the constraint that both U and O can only relax perpendicular to the slip plane. The excess energy of the slipped cell is obtained by comparing the energy of the undeformed crystal with that of the fully relaxed supercell. As the simulation cell is 3D periodic, this construction actually inserts a pair of equivalent stacking faults into the cell (at z=0 and z=0.5), so that the GSF energy is 1/2 the calculated excess energy of the deformed supercell.

The dependence of the generalized stacking fault energies on the simulation cell thickness (perpendicular to the slip plane) was tested for each lattice orientation. For {100} and {111} slip planes, atomic slabs 10 unit cells thick were sufficient to converge the calculated 1/4<110> stacking fault energies on each surface to within < 2%, while for the {110} slip plane, the fully converged simulation cell was 14 unit cells. These simulation cells are displayed in Fig. VI.1.

In this study, seven different interatomic potentials are used to calculate the properties of dislocations in UO_2. In addition to the highly-accurate embedded atom potential developed by Cooper et al. (2014a), we use the Arima potential (Arima et al. 2005), which is a rigid-ion model that treats all interatomic interactions using the Buckingham potential, and the Goel potential (Goel et al. 2008), which is similar to the potential developed by Arima et

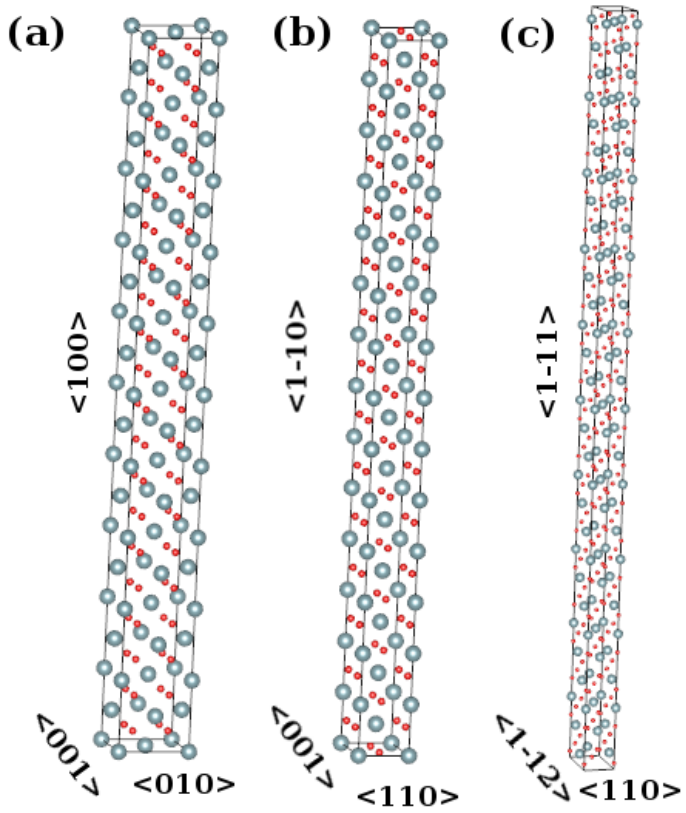

Fig. VI.1 Simulation cells used to calculate (a) {100}, (b) {110}, and (c) {111} γ-surface energies for UO_2.

al., but treats the polarizability of the O ions using a shell model (Dick and Overhauser 1958). Additionally, we use the Morelon potential (Morelon et al. 2003), which simulates the O-O interactions with a Buckingham 4-range potential, and has previously been used by Parfitt et al. (2010) to study dislocation motion atomistically, and the potentials developed by Basak et al. (2003) and Yakub et al. (2009, 2010), which are rigid ion models, including Morse terms to simulate the covalent part of U-O pair interactions. Finally, we also use the Read potential, in which a Buckingham 4-range potential is used to model the O-O interactions and includes shells for the O ions (Read and Jackson 2010). Both the Arima and Read potentials take the charges on the U and O atoms to be equal to their formal

charges, while the other five potentials are partially ionic. For convenience, these potentials will be referred to henceforth as Arima05, Basak03, Cooper14, Goel08, Morelon03, Read10, and Yakub10. All atomistic calculations of GSF energies are performed using the molecular mechanics code GULP (Gale 1997; Gale and Rohl 2003).

VI.3. Results and discussion

The {100}, {110}, and {111} γ-surfaces calculated using the seven interatomic potentials are displayed in Fig. VI.2, with the important stable and unstable stacking fault energies listed in Table VI.1. Note that the shape of the {111} gamma surface presented here differs from that in Fossati et al. (2013) because there are two non-equivalent heights at which the slip plane may intersect the simulation cell, either separating a layer of U atoms and a layer of O atoms, or two adjacent layers of O atoms. Here, the latter choice is used as it gives lower generalized stacking fault energies and a simpler γ-surface shape, whereas Fossati et al. (2013) appear to have placed the slip plane between the U and O layers. These layers are closely spaced, such that atoms sometimes pass close to one another, resulting in an irregular γ-surface characterized by high maximum GSF energies.

As can be seen from Fig. VI.2, the seven potentials can be separated into two broad groups based on the shape of the {100} γ-surface. In the first group, which comprises Arima05, Goel08, Morelon03, and Read10, the 1/4<110> generalized stacking fault corresponds to a saddle point of the γ-surface. In contrast, this stacking fault vector is associated with a local

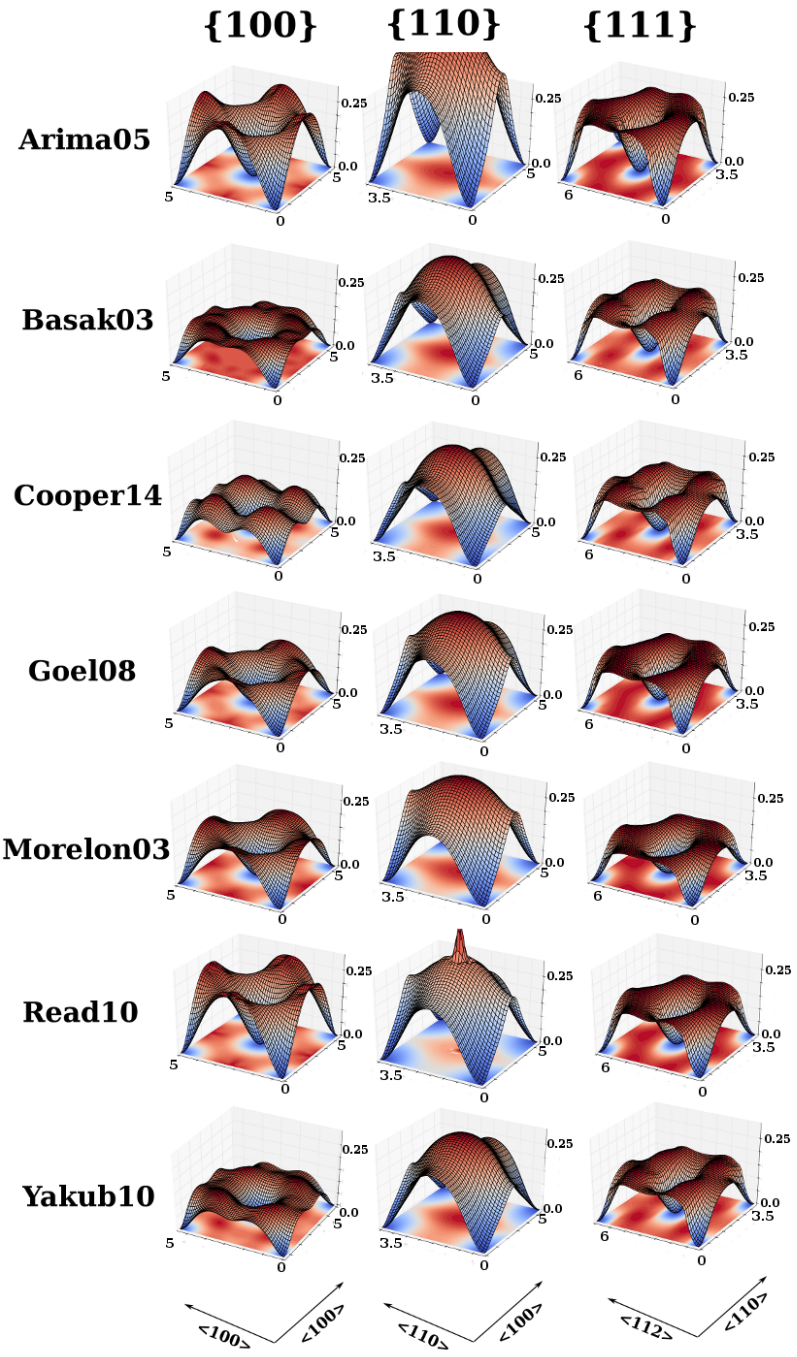

Fig. VI.2 Calculated {100}, {110}, and {111} γ-surfaces (in eV/Å) for the seven different interatomic potentials used in this study. For ease of comparison, all γ-surfaces have been plotted on the same energy scale**.** Horizontal axes in units of Å

maximum of the γ-surface energy for the Basak03, Cooper14, and Yakub10 potentials. Furthermore, this group of potentials all show a local minimum along <100>, which is deepest for the Cooper14 potential and shallowest for the Basak03 potential. Despite the disparity in the shapes of the γ-surfaces calculated using the different potentials, the 1/2<110>{100}, 1/2<110>{110}, and 1/2<110>{111} γ-lines remain qualitatively similar (see Fig. VI.3), although the range of stacking fault maxima predicted for each line is quite large. The shape of these γ-lines will largely determine the properties of their associated slip systems, indicating that the qualitative features predicted for the major slip systems in UO_2 are likely to be similar for all seven potential models, although the dislocation widths and Peierls stresses may vary greatly.

Table VI.1 Key generalized stacking fault energies for the {100}, {110}, and {111} planes

	1/4<110>{100} (eV/Å^2)	**1/4<110>{110} (eV/Å^2)**	**1/4<110>{111} (eV/Å^2)**
Arima05	0.2121	0.3754	0.2252
Basak03	0.1202	0.2701	0.1760
Cooper14	0.1522	0.2477	0.1620
Goel08	0.1358	0.2434	0.1445
Morelon03	0.1410	0.2156	0.1224
Read10	0.2090	0.2327	0.1598
Yakub10	0.1300	0.2372	0.1533

From these γ-surfaces, dislocation misfit profiles were calculated for the three types of edge dislocation and 1/2<110> screw dislocations gliding on {100}, {110}, and {111}. Although

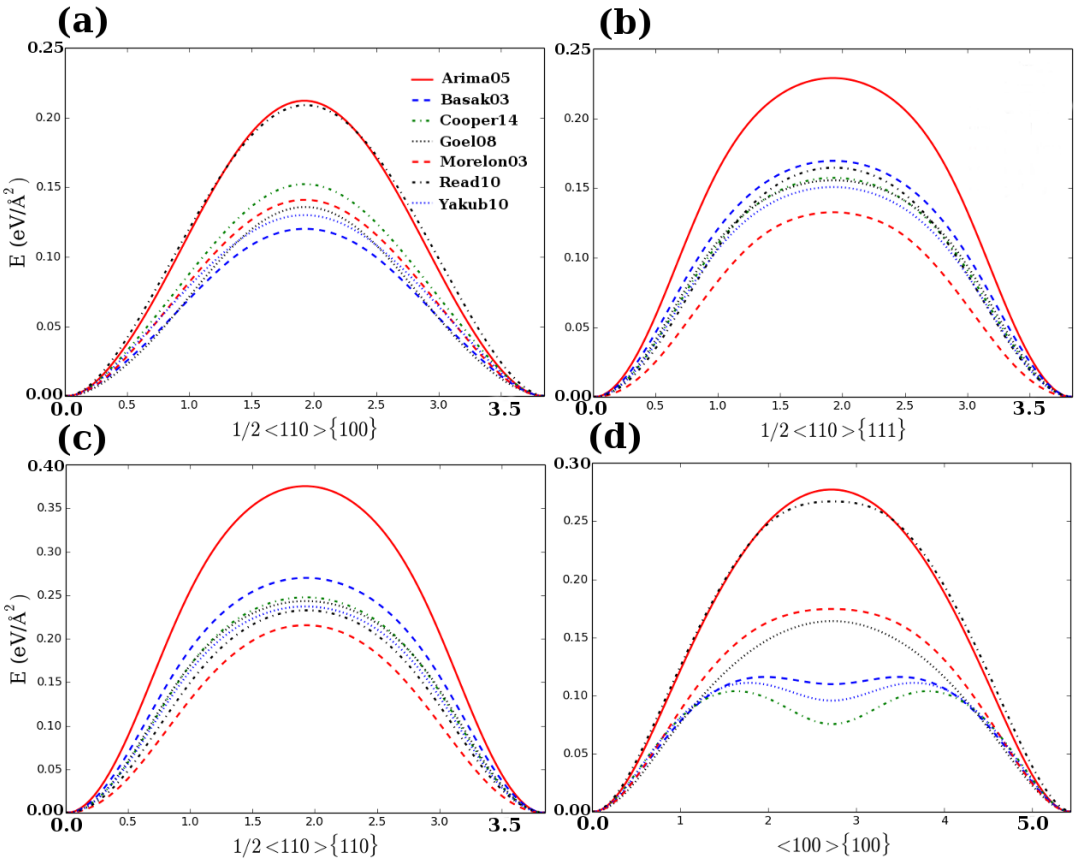

Fig. VI.3 (a) 1/2<110>{100}, (b) 1/2<110>{111}, (c) 1/2<110>{110}, and (d) <100>{100} γ-lines for UO_2**.** Horizontal axes in units of Å

all calculations were performed using the 2D Peierls Nabarro model, no spreading perpendicular to **b** was found for any of the slip systems (i.e. for all *i* corresponding to the perpendicular component). This means that the three edge dislocations are not predicted to have a screw component, while the 1/2<110> screw dislocation has no edge component. For consistency between the static structures and Peierls stresses, the misfit energy has been calculated using a sum over discrete lattice planes rather than the integral formulation. For the edge dislocations, the interlayer spacing is *b*, the Burgers vector thickness. For 1/2<110> screw dislocations gliding on {100}, the interlayer spacing is likewise *b*, while for screw dislocations spreading on {110} or {111}, the interlayer spacing is a/2 (where *a* is

the lattice parameter) and $b\sqrt{(2)}/2$, respectively. Calculated dislocation widths and dislocation energies are listed in Table VI.2 for all of the potentials, while representative disregistry profiles and their associated dislocation density distributions (obtained using the Cooper14 potential) are plotted in Fig. VI.4.

One of the key parameters defining a dislocation core is the core width, defined as distance over which the disregistry field changes from **-b**/4 to **b**/4. For all potentials examined in this study, the 1/2<110>{100} edge dislocation had the widest core and the <110>{110} screw dislocation the narrowest. The Arima05, Goel08, and Morelon03 potentials had unusually narrow 1/2<110>{100} and 1/2<110>{111} edge dislocations, while the Basak03 potential predicted an unusually wide core for the 1/2<110>{100} edge dislocation, compared with the other potentials. Predictions for the shape of the 1/2<110>{111} misfit profile were particularly consistent between the different potentials, with a minimum width of 2.471 Å (Basak03) and a maximum width of 2.776 Å (Morelon03). The shapes of the 1/2<110>{110} edge and screw dislocations were remarkably consistent between the seven potentials. As can be seen in Table VI.2 and Fig. VI.4d, the 1/2<110> screw dislocations has a particularly narrow core, and the widths of screw dislocations spreading on {110} and {111} are considerably less than that of a screw dislocation spreading on {100}. This indicates that the 1/2<110> screw dislocation is essentially planar, and that its Peierls stress can thus be calculated using the PN method.

Table VI.2 Dislocation core widths (ξ) and core energies calculated with each potential model

Slip system		Arima05	Basak03	Cooper14	Goel08	Morelon03	Read10	Yakub10
1/2<110>{100} edge	ξ (Å)	2.926	3.552	2.932	3.090	2.776	2.478	2.929
	E (eV/Å^2)	-0.472	-0.385	-0.298	-0.405	-0.227	-0.152	-0.269
1/2<110>{100} screw	ξ (Å)	2.772	3.089	2.624	2.935	2.468	2.323	2.697
	E (eV/Å^2)	-0.307	-0.268	-0.143	-0.282	-0.089	-0.062	-0.168
1/2<110>{110} edge	ξ (Å)	2.310	2.317	2.469	2.472	2.468	2.478	2.466
	E (eV/Å^2)	-0.154	-0.097	-0.158	-0.140	-0.140	-0.196	-0.137
1/2<110>{110} screw	ξ (Å)	1.694	1.699	1.698	1.699	1.774	1.781	2.158
	E (eV/Å^2)	0.216	0.172	0.39	0.137	0.089	0.099	0.132
1/2<110>{111} edge	ξ (Å)	2.618	2.471	2.624	2.626	2.776	2.633	2.620
	E (eV/Å^2)	-0.301	-0.184	-0.233	-0.221	-0.282	-0.250	-0.209
1/2<110>{111} screw	ξ (Å)	2.156	2.085	2.161	2.163	2.237	2.168	2.158
	E (eV/Å^2)	-0.052	-0.015	-0.033	-0.043	-0.088	-0.042	-0.029

While the ordering of the energies for the three edge dislocations considered here agrees with the fully atomistic calculations of Murphy et al. (2014), we find that the 1/2<110>{100} edge dislocation has a lower energy than a 1/2<110> screw dislocation spreading on {100}, whereas they reported that screw dislocations have the lowest line energy. However, this disparity can be attributed to the fact that Murphy et al. (2014) report the relative ordering of the dislocation energies at a distance 40 Å from the dislocation line. In atomistic simulations, the dislocation energy as a function of radius is $E_{TOT} = E_{CORE} + Kb^2 \ln\left(R/R_{core}\right)$. At large distances from the dislocation line, the total energy is dominated by the second term, which is the elastic energy of the dislocation strain

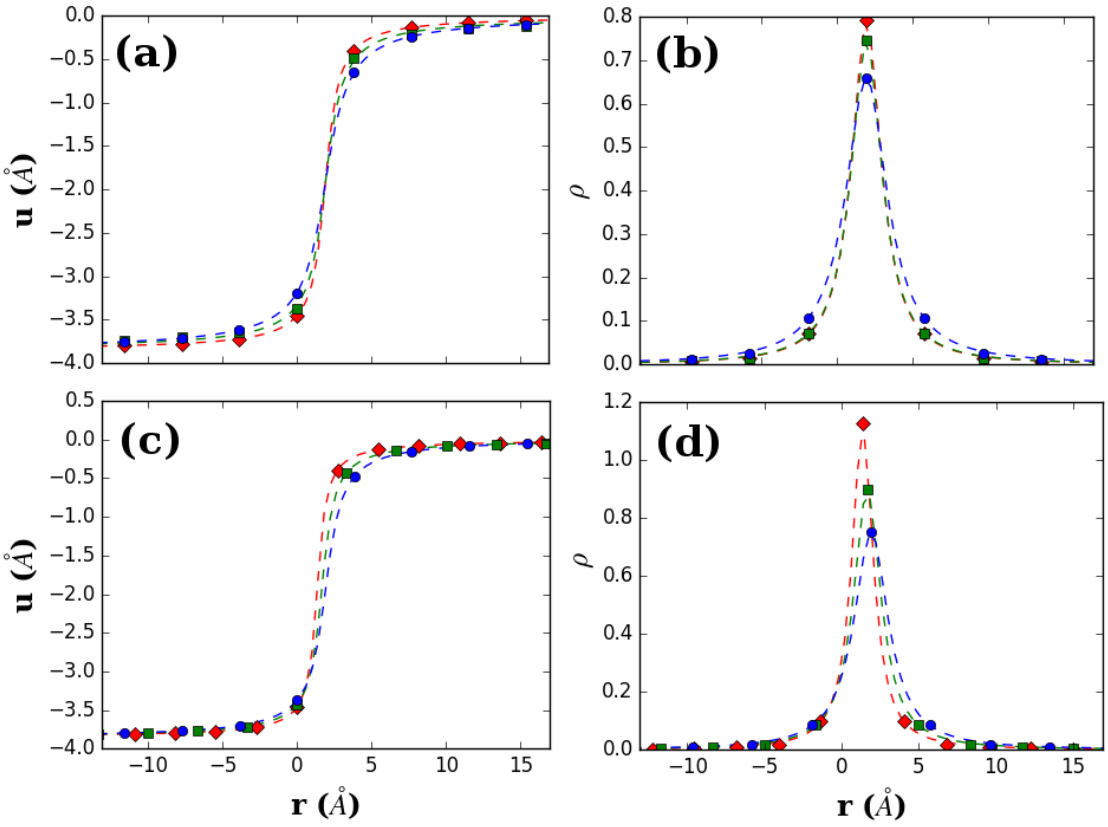

Fig. VI.4 (a) Misfit profiles for 1/2<110>{100} (circles), 1/2<110>{110} (diamonds), and 1/2<110> edge dislocations in UO_2, calculated using the Cooper14 potential. (b) Misfit profiles calculated using the Cooper14 potential for 1/2<110> screw dislocations spreading on the {100} (circles), {110} (diamonds), and {111} (squares) planes. The dislocation density distributions corresponding to these misfit profiles are plotted in (b) and (d) for the edge and screw dislocations, respectively.

field. Since the energy coefficient *K* for a screw dislocation is necessarily lower than that of an edge dislocation (for an isotropic material, $K_{edge} = K_{screw}/(1-\nu)$, where $\nu > 0$ is the Poisson's ratio) the energy of a screw dislocation at a distance of 40 Å from the dislocation line (the distance at which Murphy et al. calculated dislocation line energy) will usually be lower than that of an edge dislocation with the same magnitude Burgers vector.

Perhaps more relevant are the core (i.e. inelastic) energies obtained by Parfitt et al. (2010), where the order of the calculated core energies is $E_{<110>\{110\}} > E_{<110>\{111\}} > E_{<110>\{100\}}$, a result identical to that found for five of the seven potentials in this study. The exceptions are the Morelon03 and Read10 potentials, with the former predicting that the 1/2<110>{111} is the lowest energy dislocation, whereas the latter actually predicts that the 1/2<110>{100} dislocation has the highest energy of the three major slip systems. In contrast to fully atomistic calculations (Parfitt et al. 2010; Murphy et al. 2014), the PN model predicts that 1/2<110> screw dislocations in UO_2 have higher core energies than any of the 1/2<110> edge dislocations. However, this discrepancy may be attributed to the presence of the elastic energy term, as Parfitt et al. (2010) and Murphy et al. (2014) use a cutoff radii of 30 Å and 40 Å, respectively, to fit the core energy. The trade-off between the parameters E_{CORE} and R_{CORE} mean that their reported core energies contain a substantial contribution from elastic strain energy of the region $R < R_{\mathrm{CORE}}$.

Peierls stresses are calculated using the applied stress method for all three edge dislocation slip systems, and for 1/2<110> screw dislocations gliding on {100}, {110}, and {111}. The values calculated are listed in Table VI.3. For all seven potentials, slip on the {110} plane is associated with the highest Peierls stresses, consistent with experimental observations of relative slip system strengths, with predicted stresses for glide of the edge dislocation in this direction as great as 32.3 GPa (Arima05), although the other six potentials predict somewhat lower values (16.4-22.9 GPa). Of the potential models used in this study, six predict that the 1/2<110>{100} slip is weakest, as has been found in experiments. The lone exception is the Read10 potential, for which the 1/2<110>{100} edge dislocation has a Peierls stress of 12.9 GPa, compared with a σ_p of 8.1 GPa for glide of the 1/2<110>{111}

edge dislocation. Comparing calculated Peierls stresses for Read10 with those of the other six potential, it appears that the specific problem is that Read10 overestimates the strength of the 1/2<110>{100} slip systems, as the calculated Peierls stresses for dislocation glide on {110} and {111} are broadly similar to those obtained with other potentials. While the Morelon03 potential still predicts that 1/2<110>{100} will be softer than 1/2<110>{111}, the contrast is much less than for the other potentials.

Table VI.3 Calculated Peierls stresses (in GPa) for the 1/2<110> edge and screw dislocations gliding on {100}, {110}, and {111}. Numbers in parentheses are uncertainties, related to small asymmetries in the underlying parameterization of the disregistry function, to which the absolute energy is relatively insensitive, but have a modest effect on the calculated Peierls stress. Values for the uncertainties are derived by applying both positive and negative stress to the dislocation, and calculating the Peierls stress in that direction

Potential	**1/2<110>{100}**		**1/2<110>{110}**		**1/2<110>{111}**	
	edge	**screw**	**edge**	**screw**	**edge**	**screw**
Arima05	3.4(1)	10.6(1)	32.3(0)	31.0(2)	11.2(1)	13.9(2)
Basak03	2.7(1)	3.9(0)	22.9(1)	21.6(1)	11.0(2)	12.8(2)
Cooper14	5.2(0)	7.9(0)	19.4(1)	20.1(1)	13.6(1)	12.3(2)
Goel08	3.0(0)	8.3(3)	19.7(1)	18.7(1)	6.8(0)	8.9(0)
Morelon03	5.8(1)	9.0(1)	17.0(1)	16.6(0)	8.6(0)	10.2(2)
Read10	12.9(0)	16.2(1)	16.4(2)	16.7(0)	8.1(0)	11.1(1)
Yakub10	3.8(0)	5.4(0)	18.7(1)	18.0(1)	11.1(2)	12.7(2)

For screw dislocations, the line vector $\boldsymbol{\xi}$ and Burgers vector **b** are parallel. Consequently, screw dislocations can glide on any plane whose normal is perpendicular to **b**. For the 1/2<110> screw dislocation in UO_2, possible glide planes include {100}, {110}, and {111}, and the calculated Peierls stresses for these possible slip systems are presented in Table VI.3. As can be seen, the relative ease of screw dislocation glide on the different planes is

strongly dependent on the interatomic potential used. The Basak03 and Yakub10 potentials both predict that 1/2<110> screw dislocations glide most easily on {100}, while glide is most difficult on {110}. The calculated value of σ_p for glide on {111} is intermediate between the two. This is also the case for calculations performed using the Cooper14 potential, although in this case the Peierls stresses for glide on {100} and {111} are more similar. While the Arima05, Goel08, and Morelon03 potentials find that {110} glide has the highest Peierls stress, all three give almost identical Peierls stresses for glide on {100} and {111}. For the Arima05, Cooper14, Goel08, and Morelon03 potentials, the similarity of the Peierls stresses for slip on {100} and {111} suggests that cross-slip between these planes should be possible. Finally, as is the case for the edge dislocation slip systems, the Read10 potential predicts substantially different relative ordering of the Peierls stresses, with the Peierls stress for glide on {111} (11.1 GPa) is lower than those for glide on {100} or {110}, for which the calculated values of σ_p are 16.2 and 16.7 GPa, respectively.

There is no apparent systematic variation in the Peierls stress with the oxygen polarizability, except that shell models predict marginally a lower value for the Peierls barrier of the 1/2<110>{111} edge dislocation. However, the difference is no larger than the variation seen within the rigid models. Similarly, there is no systematic difference between models with formal charges and those that use partial ionic charges. From this, we conclude that variations between the different models are a consequence of the values of the fitted parameters, rather than the style of model used.

While, of the seven potentials considered in this study, for only one (Read10) are the calculated values of σ_p inconsistent with the known relative strengths of the {100}, {110},

and {111} glide planes, the scatter in the calculated values is quite high. Below the athermal limit, the activation energy for glide creep is given by the expression for the critical energy for sustainable kink-pair nucleation (equation VI.1). This depends on the value of σ_p which, as has been shown, depends on the choice of potential. Indeed, since dislocation velocities and strain rates have an Arrhenius relationship to the activation energy, high temperature simulations of glide-controlled creep will be more sensitive to the choice of potential than might be expected judging from the Peierls stresses alone. This means that future attempts to model deformation via glide-controlled mechanism will have to be careful in interpreting their results, as these will depend on the potential used.

The Peierls potential is the energy barrier separating adjacent minima of the dislocation. For undissociated dislocations, the approximate shape of the Peierls potential may be calculated from the Peierls stress and Burgers vector magnitude as

$$W_P(X) = \frac{\sigma_p b^2}{2\pi}\left[1 - \cos\left(\frac{2\pi x}{b}\right)\right] \qquad \text{(VI.5)}$$

It follows that the maximum height of the Peierls potential (also called the Peierls barrier) is simply $W_{p,max} = \frac{\sigma_p b^2}{\pi}$. For the Morelon03 potential, using the Peierls stresses from Table VI.3 and the Burgers vector magnitude b = 3.852 Å, the Peierls barriers for glide on 1/2<110>{100}, 1/2<110>{110}, and 1/2<110>{111} edge dislocations are 0.17 eV/Å, 0.50 eV/Å, and 0.25 eV/Å, respectively. For comparison, Parfitt et al. (2010) used fully atomistic calculations (with interatomic interactions treated using the Morelon03) potential, together with the nudged elastic band (NEB) method to directly calculate Peierls barriers

for the three edge dislocations, obtaining values of 0.25 eV/Å, 0.46 eV/Å and 0.31 eV/Å for 1/2<110>{100}, 1/2<110>{110}, and 1/2<110>{111} edge dislocation. The value for the Peierls barrier of the 1/2<110>{110} slip system is well reproduced by the PN model. In contrast, the 1/2<110>{100} and 1/2<110>{111} slip systems are moderately lower than those found by Parfitt et al. (2010), which may be because slip paths found in their NEB calculations do not correspond to the global minimum energy pathways or a consequence of the relatively small radius (25 Å) used for the fully relaxed region in their simulations, which may have allowed the dislocations to interact with the boundary of the simulation cell, creating an artificial barrier to glide. Alternatively, the difference may indicate the presence of non-planar dislocation core spreading in the atomistic calculations which, as previously discussed, would result in higher Peierls stresses than those found for the labile planar dislocations produced by PN modeling. Nevertheless, it should be noted that the Peierls barriers calculated using the PN model are of the same order of magnitude as those found by Parfitt et al. (2010), and that both methods predict the same order for the slip system strengths.

The close comparison between the results presented here and fully atomistic calculations suggest that the PN model can be used to accurately model the mobility of dislocations in UO_2. However, previous studies of dislocation glide have all used the same potential (Morelon03) to model interatomic interactions (Parfitt et al. 2010; Fossati et al. 2013; Lunev et al. 2017). Murphy et al. (2014) compared UO_2 dislocation core structures predicted by a range of different potentials, and found that several of them produced highly disordered dislocation core structures, with a substantially non-planar character. As discussed in the methods section, the particular formulation of the PN model used here is

applicable only to dislocations with a planar core, as it assumes that the disregistry field is localized on the glide plane. However, the disordered cores found for some of the potentials are likely a consequence of the fact that the input displacement fields were derived from classical elasticity theory, leading to high stresses near the dislocation line (especially for the 1/2<110>{110} edge dislocation), and substantial forces on some of the individual atoms. Given the large number of degrees of freedom available in a fully atomistic calculation, it is plausible that the non-compact, disordered core structures found in (Murphy et al. 2014) for some of the potentials actually reflects relaxation of the dislocation into a local energy minimum. That this might be the case is supported by the fact that the core width predicted for each dislocation is relatively consistent across the seven potentials, with the greatest spread (~1 Å) seen for the 1/2<110>{100} edge dislocation. Moreover, all of the potentials predict that the 1/2<110> screw dislocation and the 1/2<110>{100}, 1/2<110>{110}, and 1/2<110>{111} edge dislocations in UO_2 have narrow cores, with no apparent splitting into partial dislocations. Fully atomistic calculations using improved initial structures for the dislocations and numerical solver will be required to resolve this discrepancy.

In this study, we have focused on dislocations moving in point defect-free UO_2. However, the PN method of modeling dislocation glide also allows the effect of point defect-dislocation interactions on the Peierls stress of a dislocation to be calculated straightforwardly. To do this, point defect of the desired type are inserted at or near the slip planes in generalized stacking fault calculations, whose energies are processed to produce the γ-line/surface which enters the expression for the inelastic misfit energy (equation VI.5) in a PN model. This approach has been used previously to help explain the mechanisms by

which interstitial hydrogen atoms (Lu et al. 2001) and vacant lattice sites (Lu and Kaxiras 2002) lubricate dislocation glide in fcc Al. The PN model has also been used to show that Sn alloying reduces the Peierls stress of basal dislocations in Zircaloy materials, relative to pure Zr (Udagawa et al. 2011), and that alloying with Yt similarly enhances basal glide in Mg metal (Tsuru et al. 2013). In UO_2, oxygen hyper-stoichiometry (i.e. O/U > 2) reduces the measured critical resolved shear stress, and changes the relative strengths of the 1/2<110>{100} and 1/2<110>{111} slip systems by enhancing the mobility of the latter (Yust and McHargue 1971; Keller et al. 1988). The precise mechanism by which this occurs is unclear, but one possibility is that the presence of oxygen defects incorporated at interstitial sites reduces the Peierls stress (Nadeau 1969). Since the PN method can be used to calculate σ_p for the major edge dislocation slip systems in stoichiometric UO_2 returning values comparable to those calculated from atomistic simulations, it is likely that the PN will also be can also be applied to dislocation glide in hyper-stoichiometric UO_{2+x}.

VI.4. Conclusions

Using several commonly used interatomic potential models, we studied the structures and mobilities of the major dislocation slip systems found in UO_2 using the Peierls-Nabarro model parameterized with generalized stacking fault energies obtained from atomistic calculations. It was found that all three edge dislocations have no screw component, and that the screw dislocation had no edge component. For all seven potentials, the 1/2<110>{110} edge and screw dislocations had the highest core energies. For the Read10 and Morelon03 potentials, it was found that the calculated core energies for 1/2<110>{111} edge dislocations exceed those of the 1/2<110>{100} edge dislocations, contradicting the

results for the other five potentials as well as previous computational studies (Parfitt et al. 2010; Murphy et al. 2014).

Of the seven potential models considered here, only Read10 fails to correctly identify the 1/2<110>{100} slip system as having the lowest Peierls stress. Looking at the other six potentials, we found that the Peierls stresses are strongly dependent on the model used with, for instance, σ_p for the dominant 1/2<110>{100} slip system varying from as little as 2.7 GPa (Basak03) to as much as 5.8 GPa (Morelon03). However, all six predict that the order of the dislocation slip systems, from weakest to strongest, is 1/2<110>{100} < 1/2<110>{110} < 1/2<110>{111}, consistent with both experiments (Ashbee and Yust 1982; Keller et al. 1988) and fully atomistic calculations (Parfitt et al. 2010; Fossati et al. 2013) showing that, where suitable potentials are available, the Peierls-Nabarro approach can be used to predict dislocation properties in UO_2. Unfortunately, since there are no experimental measurements or *ab initio* calculations of Peierls stresses for individual dislocation slip systems in UO_2, it is presently impossible to determine which of the potentials considered here is best suited for modeling dislocations in UO_2.

Chapter VII. Lubrication of dislocation glide in MgO by hydrous defects

This work is in press: R. Skelton and A. M. Walker, Phys Chem Minerals 1 (2018).

VII.1. Introduction

Dislocations are linear topological defects in a crystal lattice that act as carriers of plastic strain. The stress required to move a dislocation by glide is lower than the ideal shear strength of a crystal, and glide-controlled creep can be a significant contributor to deformation, especially under conditions of moderate to high stress or low temperature. Dislocations can also act as reservoirs for point defects, as the strain fields around the core induce elastic and inelastic interactions between point defects and dislocations that cause segregation of point defects to dislocation cores. This can diminish dislocation mobility through the phenomenon of solute drag, whereby the additional energy required to either pull a solute cloud along with a translating dislocation or break free from it altogether increases the stress required for dislocation creep (Cottrell and Bilby 1949). Alternatively, in the glide-creep regime, point defects can enhance dislocation mobility, by reducing the Peierls stress σ_p required to initiate glide at 0 K.

Vacancies have been found to reduce stacking fault energies and lubricate dislocation glide in a variety of metals, including fcc Al (Lauzier et al. 1989; Lu and Kaxiras 2002), Ni, Cu, Fe (Asadi et al. 2014). Vacancies can also reduce the Peierls stress in non-metals, such as the superconductor MgB_2 (Shen et al. 2015). Theoretical calculations show that hydrogen can lubricate dislocation glide in fcc metals such Al (Lu et al. 2001) and Fe (Taketomi et al.

2008), which may explain the ubiquitous phenomenon of hydrogen induced local plasticity in these metals. Chemical impurities, in the form of interstitial oxygen defects, can also lubricate dislocation glide in oxides such as UO_2, decreasing the critical resolved shear stress and changing the relative strength of its major slip systems (Keller et al. 1988). This is attributed to interactions between dislocation cores and the interstitial oxygen ions reducing the Peierls barrier to glide (Ashbee and Yust 1982).

(Mg, Fe)O is thought to be the second most abundant mineral in the Earth's lower mantle, after the perovskite-structured mineral (Mg, Fe)SiO_3 bridgmanite, comprising slightly less than 20% of the region's volume (e.g. Lee et al. 2004). Despite being less abundant than bridgmanite, the relatively low strength of (Mg, Fe)O means that it may accommodate the majority of the strain in lower-mantle rocks (Girard et al. 2016). Along a mantle geotherm, MgO deforms athermally to ~2000km depth, with dislocation-dislocation interactions governing flow rates. At greater depths, the rheology is in the thermally activated regime and the Peierls stress becomes important for determining strain rates (Cordier et al. 2012). In MgO, the dominant slip system at ambient pressure is 1/2<110>{110}, with a modest additional contribution from the 1/2<110>{100} slip system. High pressure creep experiments show that the relative activity of the 1/2<110>{100} slip system in MgO gradually increases with pressure and, above ~23 GPa, this slip system comes to dominate over the 1/2<110>{110} slip system (Girard et al. 2012).

In some mantle silicates and oxides, dissolved water-related defects, in the form of chemically bound hydroxyl, may enhance strain rates by reducing the Peierls stress. For instance, under dry conditions the measured Peierls stress of olivine, the most abundant

mineral in the Earth's upper mantle, is between 3.8 GPa (Idrissi et al. 2016) and ~15 GPa (Demouchy et al. 2013), although more typical values are in the range 5-10 GPa (e.g. Evans and Goetze 1979; Kranjc et al. 2016; Proietti et al. 2016). In contrast, high-stress, low-temperature deformation experiments designed to measure the Peierls stress of hydrated olivine report its value to be in the range 1.6-2.9 GPa (Katayama and Karato 2008), significantly below the range of Peierls stresses measured for dry olivine. These experiments have measured only an average Peierls stress for olivine, which does not correspond to any individual slip system. However, changes in the deformation fabric with water content suggest that some slip systems are more sensitive to water content than others (Jung and Karato 2001; Katayama et al. 2004).

In pure MgO, hydrogen is incorporated via the charge-neutral substitution of an Mg^{2+} ion by a pair of protons, represented in the Kroger-Vink notation as $\{2H_{Mg}\}^{X}$ (Kroger and Vink 1956). Analogous defects, in which a divalent cation (typically Mg or Fe) is replaced with two protons are also found in (Mg, Fe)-silicates in the mantle, including olivine (Bai and Kohlstedt 1993; Kohlstedt et al. 1996). The solubility of hydrogen in MgO is very low, and under conditions of ambient pressure and water saturation, the concentration of hydrated Mg vacancies is <10 wt ppm H_2O (Joachim et al. 2012). However, concentrations of hydrated vacancies may be much higher in regions of the crystal under compressional strain, as is the case directly above the glide plane of an edge dislocation. This is certainly the case for bare Mg vacancies (i.e. vacancies without protons present), which in cluster-based simulations segregate strongly to 1/2<110>{110} edge dislocation cores in MgO, with a segregation energy of -1.7 eV for the tightest binding site (Zhang et al. 2010). *Ab initio* calculations show that $\{2H_{Mg}\}^{X}$ defects in MgO bind to {310} tilt grain boundaries,

which can be modeled as an array of dislocation, with minimum segregation energies on the order of -1 eV at 0 GPa (Karki et al. 2015).

A number of different methods exist for calculating Peierls stresses from atomistic simulations. While fully atomistic calculations are possible, one approach that has seen considerable use in materials science is the Peierls-Nabarro (PN) method (Peierls 1940, Nabarro 1947). This model uses a hybrid continuum-elastic approach in which a dislocation is represented as a discrete distribution of dislocation density which interact with each other elastically, held together by inelastic restoring forces representing the shear strength of the crystal. These restoring forces can be calculated using atomistic simulations by introducing the concept of a generalized stacking fault (GSF), which is a translational discontinuity across the glide plane of the crystal, whose energy can be calculated using any one of the numerous atomic simulation techniques available (Christian and Vítek 1979).

The PN approach has been applied to calculation of dislocation properties, including Peierls stresses, of dislocations in pure MgO, and is able to reproduce experimentally observed dislocation properties with some accuracy. Carrez et al. (2009) used an *ab initio* parameterized continuous PN model of relative slip strength in MgO, predicting that the 1/2<110>{110} slip system is approximately an order of magnitude weaker than the 1/2<110>{100} slip system, consistent with experimental observations (e.g. Foitzik et al. 1989). *Ab initio* parameterized Peierls-Nabarro-Galerkin (PNG; Denoual 2004) simulations show that Peierls stress of the 1/2<110>{110} slip system is lower than that of the 1/2<110>{100} slip system at low pressure, but that the strengths of the two slip systems converge at lower mantle pressures (Amodeo et al. 2012). This approach was used as the

basis for simulations of dislocation mobility by kink-nucleation in MgO (Cordier et al. 2012).

In this study, we use the PN model to compare Peierls-stresses in MgO with and without dissolved $\{2H_{Mg}\}^X$ defects, in order to determine whether hydrous defects can reduce the Peierls stress in mantle minerals, and to determine the possible significance of this for deformation of MgO. To do this, we use density functional theory (DFT; Hohenberg and Kohn, 1964; Kohn and Sham, 1965) to calculate generalized stacking fault energies for slip in the 1/2<110> direction on the {100} and {110} planes, with and without $\{2H_{Mg}\}^X$ defects present at the slip plane. These GSF energies, together with elastic constants calculated *ab initio* are used to parameterize PN models for 1/2<110>{100} and 1/2<110>{100} dislocations in both hydrous and anhydrous MgO.

VII.2. Computational details

Ab initio calculations

All atomistic calculations performed in this study use plane-wave density functional theory (DFT), as implemented in version 5.2.0 of Quantum Espresso (Giannozzi et al. 2009). Core and semi-core electrons were represented using the projector augmented wave (PAW) method (Blöchl 1994), while the exchange correlation (xc) energy was treated using the PBEsol xc-functional (Perdew et al. 2008). This xc-functional, which was developed to correct biases in earlier parameterizations towards isolated systems, was chosen for its ability to accurately predict the structure and properties of crystalline solids (see e.g. Ropo et al. 2008; Demichelis et al. 2010). The PAW data sets for Mg, H, and O atoms are from

version 1.0.0 of `pslibrary` (Dal Corso 2014); details of their generation parameters can found therein. The kinetic energy cutoff and spacing of the Monkhorst-Pack grid used to sample reciprocal space (Monkhorst and Pack 1976) were chosen to ensure convergence of the total energy to with <5 meV/atom. This required a kinetic energy cutoff of 80 Ry (~1090 eV) and a Monkhorst-Pack grid spacing that corresponds to a 4x4x4 grid for the 8-atom rock salt unit cell. The charge density kinetic energy cutoff was 8 times the cutoff for the wave functions In all calculations, free parameters (atomic positions and, where applicable, cell parameters) were relaxed using the BFGS quasi-Newton scheme (Pfrommer et al. 1997).

In the bulk crystal, the lowest energy configuration of $\{2H_{Mg}\}^X$ defect is one in which the two hydrogen ions are bonded to opposing oxygen ions within the M-site octahedron, with the O-H bonds in each defect parallel and pointing towards the center of the site. This is consistent with the DFT calculations of Hernández et al. (2013), who similarly found the linear hydrogen configuration to be the most stable. There are three possible arrangements and all possible configurations of this defect are symmetry equivalent in a perfect crystal. However, as discussed below, the insertion of a topological defect such as a dislocation or generalized stacking fault breaks the symmetry of the crystal, leading to multiple symmetry-inequivalent configurations of the $\{2H_{Mg}\}^X$ defect.

The elastic constants C_{ij} determine the strength of the repulsive elastic interactions between components of the dislocation density in the PN model. These were calculated using the finite strain approach, in which a small strain is applied to the simulation cell and the internal coordinates (i.e. atomic positions) are relaxed. The elastic constants can then be

extracted by fitting the residual stress to the Hooke's law relation $\sigma_i = C_{ij}\epsilon_j$. Linear elasticity breaks down at large strain amplitudes whereas, if the strain amplitude is too small, the numerical error due to the use of finite convergence criteria may be of the same order as the residual stresses, leading to high uncertainties in the fitted values of the C_{ij}. The number of distinct imposed strains depends on the symmetry of the crystal; for MgO, which has cubic symmetry, a single strain was sufficient to determine all of the C_{ij}. In addition to the elastic constants of anhydrous MgO, we also calculated elastic constants for 1x1x1 and 2x2x2 supercells, each containing a single $\{2H_{Mg}\}^X$ defect, to assess the possible influence of hydrated defects on the elastic self-interaction of a Peierls-Nabarro dislocation.

Peierls-Nabarro calculations

The Peierls stress is calculated here using the Peierls-Nabarro method (described in more detail in Chapter VI), with the inelastic restoring force parameterized using *ab initio* calculations of GSF energies. Recall that a GSF is a planar defect in a crystal across which the crystal is offset by some vector **u**, perpendicular to the normal of the GSF plane, which is created **i**n an atomistic simulation by cutting an appropriately oriented simulation cell and displacing one half of it with respect to the other by **u**. The atomic coordinates are then to relaxed to their minimum energy configuration, subject to the constraint Mg^{2+} and O^{2-} ions can only move in the direction of the stacking fault normal. It is common to incorporate a vacuum layer into the simulation cell, to prevent direct interactions between stacking faults along the slab axis. In all GSF calculations described here, the vacuum layer was 15 Å thick, and the coordinates of all atoms within 2.5 Å of the vacuum layer were fixed during relaxation. For {100} and {110} oriented simulation cells, the energies of the

γ-line maxima to within 10 meV/Å^2 by the use of a slab cell whose thickness (in units of the fault normal vector) was n = 6. GSF cell geometries for simulating slip on {100} and {110} are shown in Fig. VII.1.

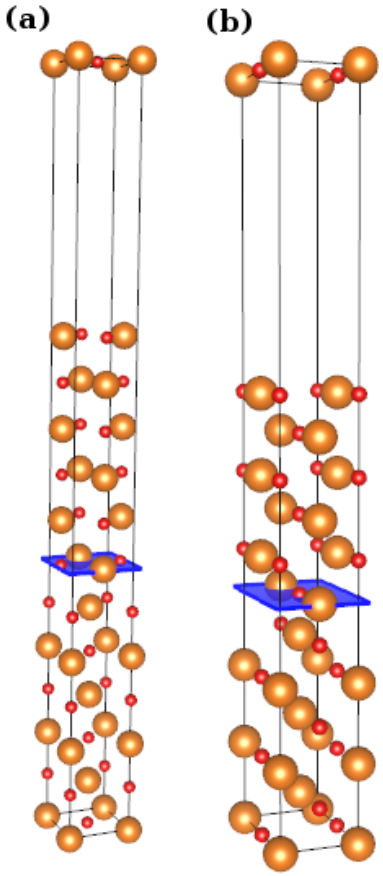

Fig. VII.1 Simulation cells containing 1/4<110> generalized stacking faults on the (a) {100} and (b) {110} planes.

To calculate the effect of protonated Mg vacancies on GSF energies, all γ-line calculations were repeated with simulation cells containing a single $\{2H_{Mg}\}^X$ defect at the slip plane, with the cell dimensions in the *x*- and *y*-directions doubled to reduce interactions between

the defect and its periodic images. Consistent with the fact that the strain field induced by a point defect decays more quickly with distance than that of an unstable stacking fault, the slab cell thickness used in calculations of GSF energies without adsorbed point defects were sufficient to ensure convergence of those with $\{2H_{Mg}\}^{X}$ defects present at the slip plane. For the {100} GSF calculations, this corresponds to a cross-sectional area of $\sqrt{2}a$x$\sqrt{2}a$, where a is the unit cell parameter of MgO, while the cross-sectional area of the cell used in the {110} GSF calculations was $\sqrt{2}a$x2a. However, although the differently oriented simulation cells have different cross-sectional areas, the number of defects per lattice site at the slip plane is the same for the {100} and {110} oriented simulation cells, permitting a direct comparison of the effects of protonated Mg vacancies on glide of 1/2<110>{100} and 1/2<110>{110} dislocations.

Parameterizing the inelastic restoring force using calculations of GSF energies in which a point defect has been inserted allows us to investigate the potential influence that point defects might have on the core structure and mobility of a particular dislocation. The dislocation properties calculated using this represent only an approximation to the true effect that the point may have, as the point defect is effectively spread out across the entire dislocation core. This is less of a problem for dislocations in MgO, which have narrow, undissociated cores, than it would be for dislocations with widely dissociated cores, for example [001] dislocations in olivine (Durinck et al. 2007) and [010] dislocations in wadsleyite (Metsue et al. 2010). Additionally, because the PN model does not simulate an individual point defect, it is impossible to calculate the binding energy between the point defect and a dislocation. However, the PN model has some advantages over fully atomistic calculations, the most important of which is that GSF simulation cells contain fewer atoms

than those used in fully atomistic simulations of dislocations, so that it is possible to use DFT instead of empirical potentials, which may be inaccurate for highly deformed regions of a crystal, such as in the vicinity of a dislocation core.

VII.3. Results and Discussion

Elastic constants

The shape and mobility of a Peierls-Nabarro dislocation are controlled by the balance between the repulsive elastic interactions between components of the dislocation density and the inelastic restoring force parameterized using GSF calculations. Before addressing the effects of adsorbed $\{2H_{Mg}\}^X$ defects on GSF energies, we will address the question of how sensitive the elastic constants C_{ij} - and through them the elastic prefactor K in equation (VI.2) - are to the concentration of these defects.

Compared with the experimental measurements (taken from Sinogeikin and Bass, 1999), the PBEsol xc-functional predicts modestly lower elastic stiffness, with the calculated 0 GPa elastic constants less than their experimental values by 1.6% (C_{11}) and 6.9% (C_{44}). To determine the effect of water on the elastic constants of MgO, we compare the C_{ij} calculated for anhydrous MgO above with those calculated using 1x1x1 and 2x2x2 supercells, each containing a single $\{2H_{Mg}\}^X$ defect (Table VII.1). In the 1x1x1 supercell, one quarter of the Mg sites are replaced with $\{2H_{Mg}\}^X$, while the 2x2x2 supercell contains one $\{2H_{Mg}\}^X$ per 32 Mg sites. The Voigt-Reuss-Hill average of the isotropic shear modulus, G^{VRH}, for the 1x1x1 cell is ~18% softer than the dry shear modulus at 0 GPa, compared with a ~4% shear modulus relaxation for the 2x2x2 simulation cell. Pressure increases the

relative shear modulus deficit of the 1x1x1 simulation cell slightly, to ~19.5%, while that of the 2x2x2 simulation cell is essentially pressure invariant. However, while the effect of water on the isotropic shear modulus is relatively pressure insensitive, this is not the case for the individual elastic constants. For instance, the value of C_{12} for the 1x1x1 simulation cell is ~34.7% lower than that of dry MgO at 0 GPa, but only 18.7% lower at 100 GPa.

Table VII.1 Calculated elastic constants (in GPa) of anhydrous MgO, compared with those of 1x1x1 and 2x2x2 supercells containing a single $\{2H_{Mg}\}^X$ defect. Measured elastic constants of dry MgO at ambient pressure given for reference. For each set of elastic constants, we have computed the elastic energy coefficients for 1/2<110>{100} and 1/2<110>{110} dislocations. While the edge coefficients (K_e) differ between the two slip systems, the screw energy coefficient (K_s) does not.

		C_{11}	C_{12}	C_{44}	G^{VRH}	K_e		K_s
						1/2<110> {100}	1/2<110> {110}	
anhydrous (DFT)	0 GPa	293.2	89.8	143.8	125.1	160.7	147.7	120.9
	125 GPa	1281.5	253.1	204.7	299.0	381.2	446.1	324.4
anhydrous (expt.)[a]	0 GPa	297.9(15)	95.8(10)	154.4(20)	130.2(1)	168.8	152.0	124.9
1x1x1 supercell	0 GPa	277.8	58.6	98.1	102.6	125.0	128.2	103.7
	125 GPa	1112.3	205.8	153.1	240.7	306.1	365.3	263.4
2x2x2 supercell	0 GPa	283.6	85.3	135.8	119.7	153.3	142.0	116.0
	125 GPa	1224.7	246.6	196.3	285.8	365.2	426.7	309.8

[a] Sinogeikin and Bass (1999)

For a more rigorous quantification of the effect of defect chemistry on the elasticity of a material, we can compute the Euclidean distance between the elasticity tensors of the pure material and the supercells containing protonated vacancies. To do this, the elasticity tensor is represented as a 21-dimensional vector, corresponding to the number of linearly independent elastic constants C_{ij} for a triclinic crystal, with appropriate pre-factors to

maintain invariance under coordinate transformations (Browaeys and Chevrot 2004). The distance between two elasticity tensors is then $||\mathbf{C}_1-\mathbf{C}_2||$, where $\mathbf{C}_1$ and $\mathbf{C}_2$ are the vector representations of the two tensors, and the relative deviation of $\mathbf{C}_1$ from $\mathbf{C}_2$ is $||\mathbf{C}_1-\mathbf{C}_2||/||\mathbf{C}_2||$. For MgO, which has cubic symmetry, only the first 9 components of the vectorial representation of the elasticity tensor are non-zero, with components 1-3 equal to C_{11}, components 4-6 equal to $\sqrt{2}C_{12}$, and components 7-9 equal to $2C_{44}$. This technique has been used to calculate the effect of chemistry and order on the elasticity of metal alloys (e.g. Xie et al. 2012; Zhou et al. 2013). Using the elastic constants reported in Table VII.1, we calculate the normalized distance between the elasticity tensor of dry MgO and a 1x1x1 supercell to be 0.239 at 0 GPa, decreasing to 0.15 at 125 GPa. The elasticity tensor of the 2x2x2 supercell is even closer to that of dry MgO, reflecting the 8-fold reduction in the defect concentration, with a normalized distance between the dry and wet **C** of just 0.046 at ambient pressure, decreasing only slightly with pressure to 0.043 at 125 GPa.

Crystal elasticity affects the core properties of a dislocation through the elastic energy coefficient K in equation (VI.2), which depends both on the elastic constants C_{ij} and the dislocation geometry. Elastic energy coefficients for the 1/2<110>{100} and 1/2<110>{110} edge dislocations, and for the 1/2<110> screw dislocation (whose coefficient is the same for glide on {100} and {110}) are calculated from the elastic constants of dry and protonated vacancy-containing MgO. As expected, the elastic energy coefficients calculated from the elastic constants of supercells containing a $\{2H_{Mg}\}^X$ defect are systematically lower than those calculated for dislocations in dry MgO (Table VII.1). At 0 GPa, K_e for the 1/2<110>{100} slip system is 22.2 % lower when calculated using the elastic constants for the 1x1x1 supercell. However, the K_e for this slip system computed

using the elastic constants of the 2x2x2 supercell differs from the dry value by only -4.6 %, comparable to the difference between the DFT and experimental values. The value of K_e calculated for the 1/2<110>{110} slip system at ambient pressure is even less sensitive to the concentration of $\{2H_{Mg}\}^X$ defects, with the values calculated using the elastic constants of the 1x1x1 and 2x2x2 supercells differing from the dry K_e by -13.2 % and -3.9 %, respectively. However, the deficit increases modestly with pressure, reaching -18.1 % and -4.3 % at 125 GPa. The effect of $\{2H_{Mg}\}^X$ concentration on K_s, the elastic energy coefficient of the 1/2<110> screw dislocation, is similar to that reported for K_e.

For MgO, as for magnesium silicates such as forsterite (Liu et al. 2009) and wadsleyite (Mao et al. 2008; Chang et al. 2015), the incorporation of water as protonated vacancies softens the elasticity tensor. However, this effect decreases rapidly with decreasing water content. Consequently, since the simulation cells used for GSF calculations in this study have relatively large cross-sections and bulk water solubilities are extremely low in both MgO (<10 ppmw; Joachim et al. 2012) and (Mg, Fe)O (<100 ppmw; Bolfan-Casanova et al. 2003), the elastic energy coefficients for all PN simulations in this study were calculated using the elastic constants of dry MgO.

Generalized stacking fault energies

To determine the effect of $\{2H_{Mg}\}^X$ defects on inelastic stacking faults in MgO, it is first necessary to calculate the energies of these stacking faults in the absence of adsorbed point defects (shown in Fig. VII.2). At 0 GPa, the maximum energy computed along the 1/2<110> γ-line is associated with the 1/4<110> stacking fault vector for slip on both the {110} and {100} families of of planes, with values of 0.0691 eV/Å^2 and 0.1434 eV/Å^2,

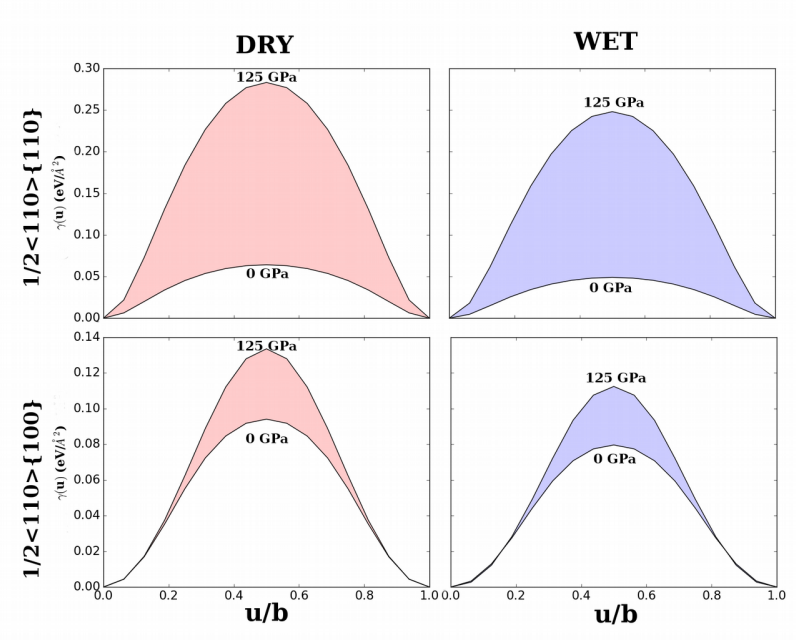

Fig. VII.2 Pressure evolution of wet and dry 1/2<110>{110} (top) and 1/2<110>{100} (bottom) γ-lines in MgO.

comparable to the values of 0.0655 and 0.1361 eV/Å^2 calculated for these GSFs using the PBE xc-functional in a previous study (Carrez et al. 2009). However, {110} GSF energies are more pressure sensitive than {100} GSF energies. Comparing the energies of the 1/4<110> stacking fault vector on {110} and {100} as functions of pressure (Fig. VII.3), it can be seen that, in the former case, the calculated GSF energy increases almost six-fold over the pressure range 0-125 GPa, reaching 0.3907 eV/Å^2 at the highest pressure, whereas the energy of the 1/4<110> stacking vector on {100} is roughly doubled, reaching 0.2605 eV/Å^2 at 125 GPa. This causes a reversal of the relative heights of the 1/2<110>{110} and 1/2<110>{100} γ-lines, which occurs at ~54 GPa. Since the γ-line functions influence the dislocation energy (equation VI.2) through the inelastic misfit energy (equation VI.5), this means that the relative strengths for dislocation glide on {110} and {100} will invert at high pressure.

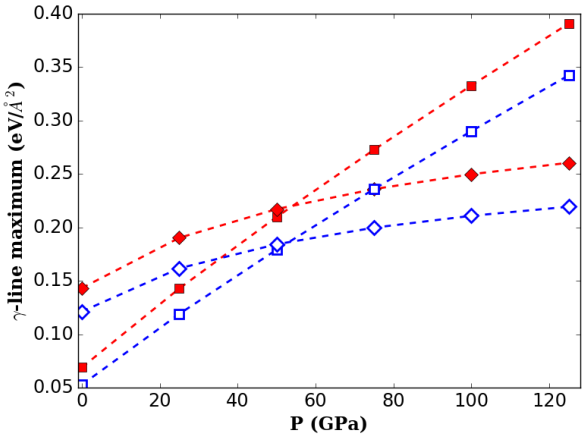

Fig. VII.3 Pressure dependence of the γ-line maximum for slip along 1/2<110> on the {100} (diamonds) and {110} (squares) planes, with dry and wet values plotted with full and empty symbols, respectively. For wet γ-lines, values are shown only for the lowest energy $\{2H_{Mg}\}^{X}$ configuration for each slip plane.

Due to the high symmetry of MgO, there are three possible symmetry equivalent – and thus energy degenerate – configurations of the $\{2H_{Mg}\}^{X}$ defect in the bulk crystal. However, this energy degeneracy is lifted by the insertion of a stacking fault. There are two distinct configurations of the $\{2H_{Mg}\}^{X}$ defect for GSFs on {110}. In one, the O-H bonds lie within the stacking fault plane, but are normal to the stacking fault vector (Fig. VII.4a). For the other, the O-H bonds intersect the glide plane with an angle of 45° (Fig. VII.4b). There are likewise two symmetrically distinct configurations for a protonated vacancy located near the {100} plane: one with the O-H bonds in the fault plane and inclined 45° with respect to the GSF vector (Fig. VII.4c), and the other with O-H bonds normal to the fault plane (Fig. VII.4d). For both {100} and {110} oriented fault planes, the configuration whose O-H bonds are make an angle of 45° with respect to 1/2<110> is doubly degenerate.

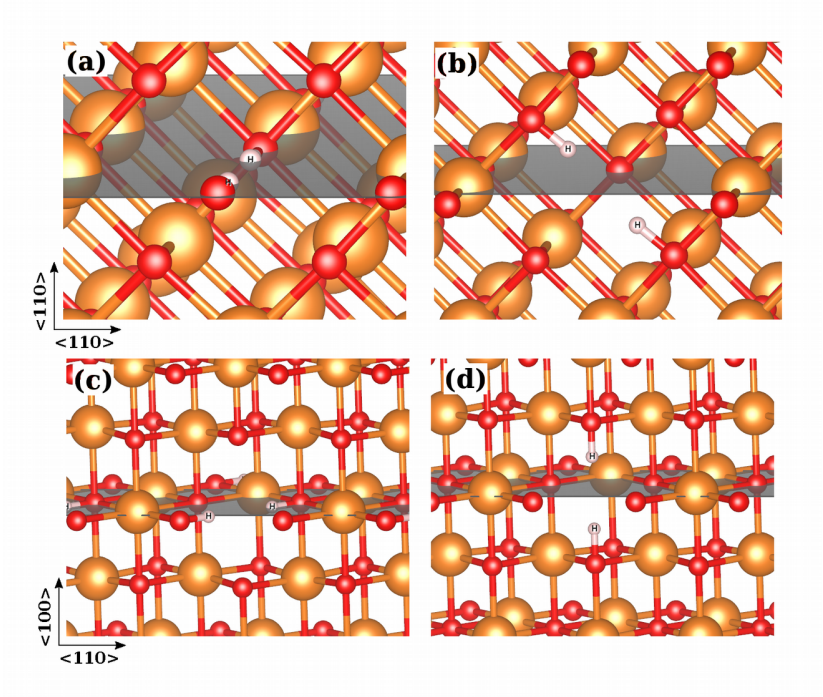

Fig. VII.4 The **s**ymmetrically distinct configurations of the $\{2H_{Mg}\}^X$ defect relative to the {110} stacking fault plane correspond to the cases when the O-H bonds are either (a) in the slip plane and parallel to **b**, or (b) crossing the slip plane. For a $\{2H_{Mg}\}^X$ defect on a {100} stacking fault, the two symmetry distinct configurations are those with (c) the O-H bond in the slip plane and (d) normal to the slip plane.

The orientation of the O-H bonds in the $\{2H_{Mg}\}^x$ defect, relative to the slip plane, influences the calculated GSF energy, as can be seen by comparing the wet and dry γ-lines (Fig. VII.2). For slip on {110}, the defect configuration in which the O-H bonds cross the slip plane has a γ-line maximum of 0.0923 eV/Å^2, higher than the calculated γ-line maximum for dry MgO. In contrast, the γ-line maximum is reduced by the presence of the defect with the O-H bonds within the {110} plane, to just 0.0529 eV/Å^2. At 125 GPa applied pressure, the corresponding values for the two defect configurations are 0.3572 and 0.3423 eV/Å^2. For slip on {100}, meanwhile, the γ-line maximum at 0 GPa is 0.1447 eV/Å^2 when O-H bonds are aligned normal to the glide plane compared with 0.1214 eV/Å^2 when the O-H

bonds are parallel to it. At 125 GPa, the corresponding energies are 0.2378 eV/Å^2 and 0.2194 eV/Å^2 so that, while the absolute and relative differences in energy are reduced, the defect with O-H bonds in the slip plane remains lower in energy. In summary, for slip along 1/2<110> on {110} and {100}, it is clear that the orientation of the O-H bonds relative to the slip plane influences the degree of water weakening, with lower energies when the configuration of the adsorbed $\{2H_{Mg}\}^X$ defect has O-H bonds parallel to the slip plane. In the following section, where we calculate Peierls stresses for dislocations in hydrous MgO, we will use the γ-lines calculated for these $\{2H_{Mg}\}^X$ defects.

One way to quantify the impact of a protonated vacancy on a generalized stacking fault is to consider the relative reduction of the γ-line maximum by the addition of a single defect at the stacking fault plane. For the 1/2<110>{110} γ-line, the energy maximum at 0 GPa is reduced by 23% by the addition of a $\{2H_{Mg}\}^X$ defect, the deficit decreasing steadily with pressure to 12% at 125 GPa. In contrast, the 1/2<110>{100} γ-line is less affected by the presence of a protonated defect at 0 GPa, and the maximum energy decreases by 15%. However, the relative magnitude of the γ-line relaxation increases slightly with pressure, to 16% at 125 GPa.

As mentioned at the end of section 2.2, it is impossible to calculate the binding energy between a point defect and a dislocation with the PN formalism. However, by taking the difference between dry and wet GSF energies with the same stacking fault vector **u**, it possible to determine the segregation energy E_{seg} of a protonated vacancy from the bulk to a generalized stacking fault. For the 1/4<110>{100} GSF, the segregation energy at 0 GPa is -0.78 eV, rising to -1.14 eV at 125 GPa. At 0 GPa, the segregation energy to a

1/4<110>{110} GSF is -0.81 eV, but rises more quickly with pressure, reaching -1.90 eV at 125 GPa. While a direct quantitative comparison with the results of Karki et al. (2015) for $\{2H_{Mg}\}^{X}$ segregation to {310} tilt boundaries is not possible, the magnitudes of the segregation energies reported at 0 GPa in that study are comparable to those found here (approximately -1 eV), and increase with pressure.

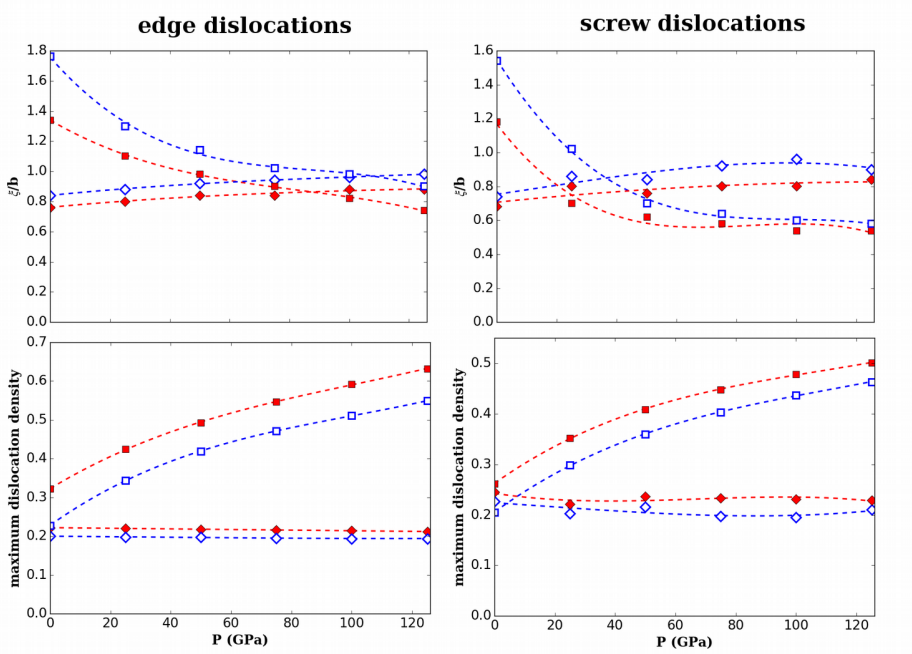

Fig. VII.5 Pressure dependence of the dislocation core width, as a fraction of the Burger's vector magnitude |**b**| (top) and maximum dislocation density along the glide plane (bottom). Results for the 1/2<110>{110} and 1/2<110>{100} slip systems are shown with square and diamond symbols, respectively, while values for hydrous MgO are indicated with hollow symbols.

Peierls-Nabarro dislocations

Using the γ-lines calculated in section 3.2, Peierls-Nabarro dislocation core structures can be obtained by minimizing equation (VI.2) with applied stress $\sigma = 0$. A static dislocation can be characterized by its core width ξ, which is defined to be the width of the region

within which $|\mathbf{b}|/4 < |\mathbf{u}(x)| < 3|\mathbf{b}|/4$, and its maximum dislocation density, ρ_{max}. In anhydrous MgO, both of these parameters are nearly constant for the 1/2<110>{100} edge dislocation and the 1/2<110> screw dislocation spreading on {100}, whereas ξ and ρ_{max} respectively decrease and increase for the 1/2<110>{110} edge dislocation and the 1/2<110> screw dislocation spreading on {110} (Fig. VII.5). Relaxing the static dislocation core structure using the wet γ-lines increases core spreading, particularly on the {110} plane, with a corresponding decrease in the value ρ_{max}. However, this hydrogen-induced dislocation core spreading has no significant effect on the pressure derivatives of either ξ or ρ_{max}.

From these static dislocation core structures, Peierls stresses for the different slip systems can be obtained by minimizing equation (VI.2) with $|\sigma| > 0$, using the static disregistry profile $\mathbf{u}(x)$ as input. Within the 1/2<110>{110} slip system, the Peierls stress of the 1/2<110>{110} edge dislocation is lower than that of the 1/2<110> screw dislocation gliding on {100}, which controls mobility in this slip system. The Peierls stress of the edge dislocation at ambient pressure is 0.06 GPa, similar to the 0.02 GPa (Carrez et al. 2009) and 0.04 GPa (Liu et al. 2012) calculated for this dislocation in previous studies. For the 1/2<110> screw dislocation, σ_p for glide on {110} is 0.26 GPa at ambient pressure. Previous computational studies have found values for this slip system ranging from 0.04 GPa (Carrez et al. 2009) to 0.16 GPa (Liu et al. 2012). For the 1/2<110>{100} slip system we find that, across the entire pressure range 0-125 GPa, a 1/2<110> screw dislocation gliding on {100} has lower Peierls stress than 1/2<110>{100} edge dislocation. At 0 GPa, the screw dislocation has σ_p = 1.7 GPa for the screw dislocation, comparable to the value of 1.53 GPa calculated by Carrez et al. (2009) using a continuous 1D PN model. Carrez et al.

determined the Peierls stress of the 1/2<110>{100} edge dislocation at ambient pressure to be 1.16 GPa, markedly lower than the 2.8 GPa computed in this study.

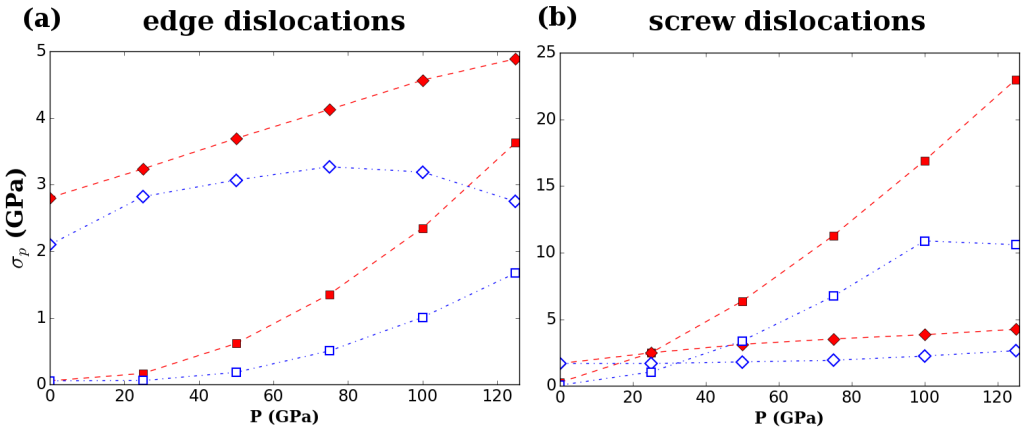

Fig. VII.6 Pressure dependence of the Peierls stresses calculated for (a) glide of edge dislocation, and (b) screw dislocations. Square and diamond symbols correspond to the {110} and {100} glide planes, while filled and hollow symbols are used to represent σ_p in anhydrous and hydrous MgO.

The 0 GPa Peierls stresses are thus comparable with those found in previous studies, albeit modestly higher for all dislocations studied. This difference can be attributed to the choice of xc-functional as Carrez et al. (2009) and Liu et al. (2012) used the PBE-GGA xc-functional (Perdew et al. 1996), which is known to significantly overestimate the cell volume, due to under-binding of the exchange-correlation energy. For MgO, the elastic constants C_{ij} increase with decreasing cell volume (i.e. increasing pressure) which means that, at a given pressure the PBE xc-functional underestimates the elastic constants. Consequently, PN simulations parameterized using the results of DFT calculations performed using the PBE xc-functional should consistently predict lower Peierls stresses than those parameterized using the PBEsol xc-functional, as is the case here.

In the previous section, it was shown that adsorption of $\{2H_{Mg}\}^X$ defects to the fault plane lowers GSF energies along the 1/2<110>{110} γ-line. When these γ-lines are used to parameterize PN calculations of dislocation glide, this translates into lower Peierls stresses for glide on the 1/2<110>{110} slip system. Although the edge and screw dislocations in this slip have comparable Peierls stresses at ambient pressure, above 0 GPa the Peierls stress of the 1/2<110> screw dislocation gliding on {110} is greater than that of the 1/2<110>{110} edge dislocation, and screw dislocation controls the mobility of this slip system. At 0 GPa, the Peierls stress of a 1/2<110>{110} edge dislocation is 0.06 GPa, indistinguishable from the Peierls stress for this slip system in dry MgO. However, as can be seen in Fig. VII.6a, the pressure derivative $d\sigma_p/dP$ is lowered by $\{2H_{Mg}\}^X$ defects and, at 125 GPa pressure, the σ_p calculated using the wet γ-line is 1.7 GPa, <50% of the value for this dislocation in dry MgO (3.6 GPa). For glide of 1/2<110> screw dislocations on {110}, the Peierls stress is 0.06 GPa when the wet γ-line is used, compared with 0.26 GPa under dry conditions; at 125 GPa the corresponding wet and dry values are 10.6 and 23.0 GPa.

The effect of protonated vacancies on the qualitative pressure dependence of dislocations gliding on {100} is more pronounced. Whereas, in dry MgO, the Peierls stress of 1/2<110>{100} edge dislocations increases monotonically with pressure, the addition of water leads to a pronounced negative curvature of $\sigma_p(P)$. This effect is sufficiently great that σ_p actually decreases above 75 GPa. The Peierls stress for glide of 1/2<110> screw dislocations on {100} is similar for anhydrous and hydrous MgO at ambient pressure (~1.7 GPa). However, the adsorption of protonated vacancies to the glide plane greatly reduces the pressure dependence of σ_p, which in hydrous MgO is just 2.7 GPa at 125 GPa,

compared with 4.2 GPa for dry MgO. As was found for dry MgO, the Peierls stress of the 1/2<110>{100} dislocation is greater than that of the 1/2<110> screw dislocation gliding on {100} at all pressures, although in wet MgO the Peierls stress for the edge and screw dislocation begin to converge at high pressure.

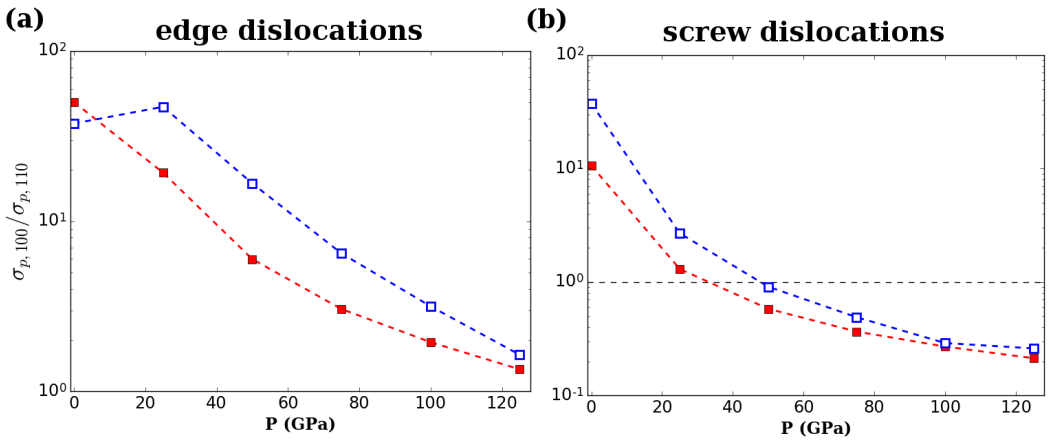

Fig. VII.7 Ratio of σ_p for glide on {100} and {110} for (a) edge and (b) screw dislocations, with (filled symbols) and without (hollow symbols) $\{2H_{Mg}\}^X$ defects present. The horizontal dashed line for the screw dislocations represents a Peierls stress ratio of 1.

For 1/2<110> screw dislocations in dry MgO, the relatively rapid increase in σ_p for glide on {110} with pressure means that glide on {100} becomes easier at high pressure. This results in a cross-over of the relative strengths of the two glide planes at high pressure. Using the Peierls stresses calculated for dry MgO, we that this occurs at a pressure of 24.8 GPa, comparable to the ~23 GPa measured in creep experiments (Girard et al. 2012). However, glide of 1/2<110> screw dislocations on {110} is preferentially enhanced by the presence of protonated vacancies over glide on {100}. While this effect is not sufficient to prevent the preferred glide plane from changing at mantle pressures, the slip system cross-over is shifted to higher pressures (Fig. VII.7b). For the $\{2H_{Mg}\}^X$ defect concentrations used in this

study, the cross-over pressure at which glide of 1/2<110> screw dislocation on {110} increases to 32.1 GPa. Assuming linear dependence of the Peierls stress on $\{2H_{Mg}\}^X$ defect, this implies that the cross-over pressure is shifted by ~29 GPa multiplied by the fraction of protonated cation sites at the glide plane. In anhydrous MgO, the 1/2<110>{110} edge dislocation slip system is weaker than the 1/2<110>{100} edge dislocation slip system at all mantle-relevant pressures (Fig. VII.7a), and this is not changed by the incorporation of $\{2H_{Mg}\}^X$ defects at the glide plane. However, the pressure at which the Peierls stress of 1/2<110> screw dislocation on {110} exceeds that of the 1/2<110>{100} edge dislocation increases from 30.6 GPa in dry MgO to 46.2 GPa for hydrous MgO with $\{2H_{Mg}\}^X$ present at the concentrations used in this study, giving a dependence of the cross-over pressure on $\{2H_{Mg}\}^X$ concentration of ~62 GPa times the fraction of occupied sites.

The hydrolytic weakening of the Peierls stress found here is a direct result of the reduction of the γ-line maximum by the insertion of suitably oriented $\{2H_{Mg}\}^X$ defects at the slip plane. This reduces the inelastic restoring force that balances the repulsive elastic interaction between components of the dislocation density distribution ρ at different lattice planes. What cannot be determined, however, is whether the reduction of the γ-line energies is due to the presence of hydrogen, or the vacancy generated when creating a $\{2H_{Mg}\}^X$ defect. Given that the 1/2<110> γ-line maxima on both {110} and {100} correspond to the points of closest approach between Mg atoms on either side of the stacking fault plane, it is likely that the mechanism by which protonated vacancies reduce the Peierls stress is by minimizing the repulsive interactions between adjacent Mg ions across the glide plane. In this case, the role of the H atoms is solely to charge-balance the creation of an Mg vacancy.

Creation of protonated defects is not the only mechanism by which vacancies can be generated in MgO or its iron-bearing analogue (Mg, Fe)O. Insertion of trivalent cations, such as Al^{3+} and Fe^{3+} into MgO/(Mg, Fe)O leads to the creation of M-site vacancies to maintain overall charge neutrality. Extrinsic vacancies associated with trivalent cations can vastly outnumber intrinsic vacancies, such as those associated with Schottky defects (Van Orman et al. 2009). In the case of MgO, doping with trivalent cations at the 100-200 ppm level decreases dislocation mobility and increases its critical resolved shear stress (Singh and Coble 1974ab). The increase in yield strength is nearly identical for Cr^{3+}, Al^{3+}, and Fe^{3+}, despite their different ionic radii, which suggests that this pinning is not caused by attractive elastic interactions between the trivalent cation and the dislocation core but the substantial change in the electrostatic energy of this complex when it is sheared by a passing dislocation (Ahlquist 1975). However, Otsuka et al. (2010) have suggested that under lower mantle conditions, ferric iron and $\{\square_M\}''$ vacancies dissociate. It is thus possible that, under oxidized conditions, there will be free vacancies, capable of inducing Peierls stress reductions comparable to those predicted here for protonated vacancies to dislocation cores, with similar geophysical implications. More work needs to be done to investigate the effects of Fe^{3+} on the deformation of (Mg, Fe)O with realistic Fe contents.

Iron-bearing (Mg, Fe)O is the weakest major phase in the Earth's lower mantle. In both numerical simulations of two-phase creep (Madi et al. 2005) and high-pressure deformation experiments on magnesiowustite + bridgmanite aggregates (Girard et al. 2016) the bulk of the strain in multi-phase lower mantle materials is accommodated by (Mg, Fe)O. When deformed under moderate stress conditions, (Mg, Fe)O polycrystals develop pronounced lattice preferred orientation (LPO) (Yamazaki and Karato 2002), although a recent

deformation experiment of a magnesiowustite + bridgmanite at 61 GPa found no evidence for the development of a coherent deformation fabric (Miyagi and Wenk 2016). MgO is highly elastically anisotropic over the entire pressure range of the Earth's mantle (Karki et al. 1999). (Mg, Fe)O is even more anisotropic than pure MgO and probably accounts for the majority of the observed seismic wave anisotropy in the Earth's lower mantle (Marquardt et al. 2009), especially as (Mg, Fe)SiO_3 bridgmanite, the other major component of the lower mantle, does not develop any significant LPO when deformed under mantle-relevant conditions (Merkel et al. 2003). At high pressure, the 1/2<110> screw dislocations experience more lattice friction for glide on {110} than on {100}, which results in a change in the LPO for a give pattern of mantle strain. Lattice preferred orientation of (Mg, Fe)O has also been invoked to explain seismic anisotropy in the D″ region of the lowermost mantle, on the assumption that the dominant slip system is 1/2<110>{100} (Karato 2014). In hydrous MgO, the greatest Peierls stress reduction was found for the 1/2<110>{110} slip system, so that the pressure at which {100} becomes the dominant slip for the 1/2<110> screw dislocations is displaced to higher pressures under hydrous conditions. At pressures representative of the deep lower mantle, the preferred slip system is the same for both hydrous and anhydrous MgO. However, $\{2H_{Mg}\}^X$ defects preferentially enhance 1/2<110>{110} slip by $\{2H_{Mg}\}^X$ defects, thereby altering the relative activities of the two major slip systems in MgO and changing its LPO, and potentially the observed pattern of seismic anisotropy.

VII.4. Conclusions

In this study, we have used the PN model, parameterized using *ab initio* calculated GSF energies to determine the effect of a common variety of protonated vacancy, $\{2H_{Mg}\}^X$, on the Peierls stress of MgO. Using DFT, 1/2<110> γ-lines were calculated for slip on the {110} and {100} families of planes, representing the most important slip systems in MgO, and these were used to parameterize Peierls-Nabarro calculations of edge and screw dislocation core structures and Peierls stresses. Calculations were performed using stoichiometric MgO simulation cells, in addition to simulation cells containing $\{2H_{Mg}\}^X$ defects, and it was found that the latter produced wider dislocation cores and lower Peierls stresses over the entire pressure range of the Earth's mantle. Although σ_p is decreased by the presence of protonated vacancies at the glide plane for slip on both {100} and {110}, we find that the Peierls stress reduction is greatest for 1/2<110>{110} slip (for both edge and screw dislocations). In the case of 1/2<110> screw dislocations, this leads to an increase in the pressure at which glide on {100} becomes easiest, meaning that the presence of water may influence the deformation fabric.

These calculations show that the presence of protonated defects near a dislocation core in MgO can reduce its Peierls stress. However, although we have considered only MgO, the results have implications for the glide controlled creep of other mantle minerals such as olivine or pyroxene. The easy glide planes of the dominant slip systems for dislocation are parallel to sheets of MO_6 octahedra (where M is typically Mg or Fe), for which MgO may be considered a structurally simple analogue. Glide lubrication by protonated defects may provide an explanation for the lower yield strength and different LPO of hydrous versus

anhydrous olivine, and this possibility warrants further exploration using atomistic simulations.

Chapter VIII. Lubrication of dislocation glide in forsterite by Mg vacancies: insights from Peierls-Nabarro modeling

VIII.1. Introduction

Forsterite-rich olivine is the dominant component of the Earth's upper mantle, composing ~60-70% of its bulk by volume. Olivine is also the weakest major phase in this region of the Earth's interior, and accordingly controls its rheology. Interpreting seismological models of the Earth's upper mantle in terms of the dynamics of plastic flow thus requires an intimate understanding of the atomic-scale mechanisms that contribute to the deformation of olivine. A number of mechanisms contribute to the rheology of olivine under mantle conditions. These include: grain boundary diffusion (e.g. Mei and Kohlstedt 2000); grain boundary sliding, accommodated by either elastic and diffusional relaxation of the grain boundary(Jackson et al. 2014) or dislocation-enabled deformation of individual grains (e.g. Hansen et al. 2011; Hansen et al. 2012ab); dislocation climb (e.g. Goetze and Kohlstedt 1973); and dislocation glide (e.g. Evans and Goetze 1979; Katayama and Karato 2008).

Dislocations, which are linear topological defects in the crystal lattice that act as carriers of plastic strain, play a particularly important role in the deformation of olivine under low temperature or moderate to high stress conditions, such as in the mantle wedge above a subducting slab. The strain rate in this creep regime is controlled by the rate of kink-pair nucleation, which depends on the elasticity of the crystal and the intrinsic lattice friction of the glide plane. This latter property is quantified by the Peierls stress, σ_p, the critical stress

required to initiate free glide of a dislocation at 0 K. Defect chemistry can therefore exert an important influence if immobile impurities segregate strongly to dislocation cores and inhibit glide creep by pinning dislocations, a phenomenon called solute drag (Cottrell and Bilby 1949).

Olivine is a plastically anisotropic mineral, and develops a measurable lattice preferred orientation (LPO) when deformed in the dislocation glide-controlled creep regime (e.g. Nicolas and Christensen 1987; Mainprice 2007; Long and Silver 2009; Long and Becker 2010). The dominant slip system for dislocation creep at low pressure is [100](010). Pressure changes the preferred dominant slip system of olivine, and much of the variation in seismic wave anisotropy in the upper mantle is explicable in terms of this pressure-induced transition (Mainprice et al. 2005; Ohuchi et al. 2011 Raterron et al. 2016). At high pressure, the dominant slip system is [001](010), as this slip system hardens less in response to increasing pressure than the [100](010) slip system (Raterron et al. 2011; Hilairet et al. 2012).

Experimental studies have reported Peierls stresses for olivine, ranging widely from as little as 3.8 GPa (Idrissi et al. 2016) to ~15 GPa (Demouchy et al. 2013), although typical values are in the range 5-10 GPa (e.g. Evans and Goetze 1979; Kranjc et al. 2016; Proietti et al. 2016). The Peierls stress measured in these studies represents a weighted average of the Peierls stresses of the individual slip systems that contribute to the total strain. While σ_p has not been measured experimentally for any individual slip system in olivine, this gap in our knowledge has been partially filled using atomic scale modeling. Mahendran et al. (2017) directly calculated σ_p for [001] and [100] screw dislocations gliding on several

crystallographic planes. Consistent with experimental observations, they found that [100](010) glide is easier than [001](010) glide in dry forsterite, with Peierls stresses of 3.1 and 7.2 GPa, respectively, within the range of Peierls stresses reported from experiments. Hydrous defects affect the deformation of olivine under conditions of low-temperature (<1273 K) and high-stress, reducing σ_p to 1.6-2.9 GPa (Katayama and Karato 2008). The incorporation of water as the "titanoclinohumite" defect, consisting of charge-coupled $\{Ti_M\}^{\cdot\cdot}$ and $\{2H_{Si}\}''$ defects apparently results in a systematic increase in strain rate (Faul et al. 2016).

In addition to enhancing strain rates, protonated vacancies may change the preferred slip system in olivine. Ohuchi et al. (2012) investigated the effect of increasing water content on the dominant slip system, and observed that the [001](010) slip was preferred over [100](010) slip at moderate water contents, with the transition occurring at ~650 ppm H/Si. Natural olivine crystals in subduction zone-derived peridotites show this B-type fabric (Mizukami et al. 2004), and 'wet' olivine fabrics have also been found in some peridotites sourced from the deep upper mantle (Katayama et al. 2005). Such a change in preferred slip system may explain the existence of trench-parallel orientation of 'fast' shear-wave polarizations in mantle wedges above subduction zones (Margheriti et al. 1996; Smith et al. 2001), which has previously been attributed to trench-parallel flow. A water-induced change of deformation fabric implies that protonated vacancies have a differential effect on the critical resolved shear stresses (CRSS) of the dominant slip systems, whether by stabilizing dislocation kinks or reducing the Peierls stress.

Atomistic calculations using density functional theory (DFT; Hohenburg and Kohn 1964; Kohn and Sham 1965) show that in the Earth's upper mantle, which is $MgSiO_3$-saturated, protonated M site vacancies in olivine are many orders of magnitude more abundant than protonated Si vacancies, except at very high water fugacities (Walker et al. 2007). The predominance of M site vacancies in mantle olivine could be reinforced in oxidized regions of the mantle, as the oxidation of Fe^{2+} to Fe^{3+} may be accompanied by the creation of M-site vacancies to maintain charge neutrality. The two mechanisms for creating mobile M-site vacancies may co-exist, particularly in mantle wedges above subduction zones, which are oxidized by fluid transfer from the subducting slab (Kelley and Cottrell 2009).

In this study we use computational simulations to investigate the possibility that cation vacancies may be able to lubricate dislocation glide in forsterite by reducing the Peierls stress σ_p. Core structures and Peierls stresses are calculated for important slip systems in forsterite using a semi-discrete Peierls-Nabarro (PN; Peierls 1940; Nabarro 1947) model. In the PN model, a dislocation is represented as a discrete array of partial dislocations distributed on the glide plane, with the balance between repulsive elastic forces and inelastic restoring forces determining the shape of the dislocation. The inelastic component of the dislocation energy is parametrized here using atomistic calculations of generalized stacking fault (GSF; Christian and Vítek 1970) energies on olivine slip planes, using empirical interatomic potentials to model interactions between ions. In this study, we consider only cation vacancies, such as can be expected to be created in mantle olivine by oxidation of Fe^{2+} to Fe^{3+} or through protonation of a cation site in hydrous systems. Vacancies on both the M1 and M2 sub-lattices, represented using Kroger-Vink notation (Kroger and Vink 1956) as $\{\square_{M1}\}''$ as $\{\square_{M2}\}''$, will be simulated.

VIII.2. Methods

As in the preceding chapter, the Peierls-Nabarro model is used to calculate the core structures and Peierls stresses for dislocations in forsterite, with the inelastic energy parameterized using atomistic calculations of GSF energies. Recall that, **i**n an atomistic simulation, a GSF is inserted by cutting a simulation cell with the appropriate orientation, and displacing one half with respect to the other by **u**, then allowing the atomic coordinates to relax to a local minimum energy configuration. For materials without rigid unit modes, such as simple oxides, atomic positions are typically constrained to relax normal to the fault plane. However, olivine contains SiO_4 polyhedra, which accommodate shear strain primarily through rotation rather than deformation. To replicate this, in our simulations oxygen atoms have been permitted to relax freely while Mg and Si atoms can only move normal to the stacking fault plane. This contrasts with the approach taken by Durinck et al. (2005), in which Mg atoms are also permitted to relax freely. The additional constraint applied here reflect the lateral constraints on atoms near a narrow-core dislocation, where the displacement field **u** varies rapidly, giving atoms in adjacent atomic planes have substantially dissimilar displacements. In contrast, all atoms in a simulation cell containing a GSF have the same displacement **u**, permitting greater relaxation in the x-y plane.

In all GSF calculations described here, a 15 Å thick vacuum layer was used to minimize interactions between the GSF and its periodic images. To ensure that the boundary conditions of the relaxation calculation match the bulk material, the coordinates of all atoms within 5 Å of the vacuum layer were held fixed. Calculated GSF energies depend on the thickness of the slab atoms used in the simulation.. For stacking faults on (010), a slab

thickness of 8*b*, where *b* is the length of the [010] lattice vector, was found to be sufficient to converge the [100](010) and [001](010) γ-line maxima to < 5 meV/Å^2. Note that care should be taken when creating a simulation slab bounded by a vacuum region as the surface may carry a dipole moment. However, the slabs used here are relatively large, and GSF energies are converged with respect to both slab and vacuum thickness.

In this study, owing to the large number of atoms in the simulation cells, atomic scale interactions are modeled using empirical interatomic potentials. These interatomic potential are from the widely-used THB1 model (Sanders et al. 1984; Lewis and Catlow 1985), which has been used earlier in this work to model segregation of vacancy-related defects to dislocation cores in MgO (Chapter IV) and forsterite (Chapter V). The model parameters are summarized in Table IV.1. All atomistic calculations are performed using the molecular mechanics software GULP (Gale 1997; Gale and Rohl 2003).

The two defect species considered in this study, $\{\square_{M1}\}''$ and $\{\square_{M2}\}''$, are charged, and inserting them into a simulation cell gives it a net charge. This is compensated for by applying a charge-neutralizing background. Creating a vacancy in the simulation cell is simple, and involves removing from the simulation cell a single atom of the desired type located a specified distance from the stacking fault plane. The slab thicknesses used to calculate GSF energies in the absence of Mg vacancies are sufficiently great to also ensure convergence of GSF energies with point defects present at the stacking fault plane.

VIII.3. Results

GSF energies in point defect free forsterite

In materials with complex lattices, like olivine, there may be several inequivalent planes on which slip can occur. We find that the lowest energy (010) stacking fault plane is located at $z = 0.25$ (or, equivalently, $z = 0.75$), intersecting the sheet of $M2O_6$ octahedra (Fig. VIII.1a). The THB1 potential model has previously been validated by Mahendran et al. (2017) at 0 GPa, who compared [100](010) and [001](010) γ-lines calculated with the interatomic potential with the earlier DFT calculations by Durinck et al. (2005). Although GSF energies calculated with THB1 are qualitatively consistent with the DFT calculations, the energies calculated with the interatomic potential are somewhat higher, particularly for displacement

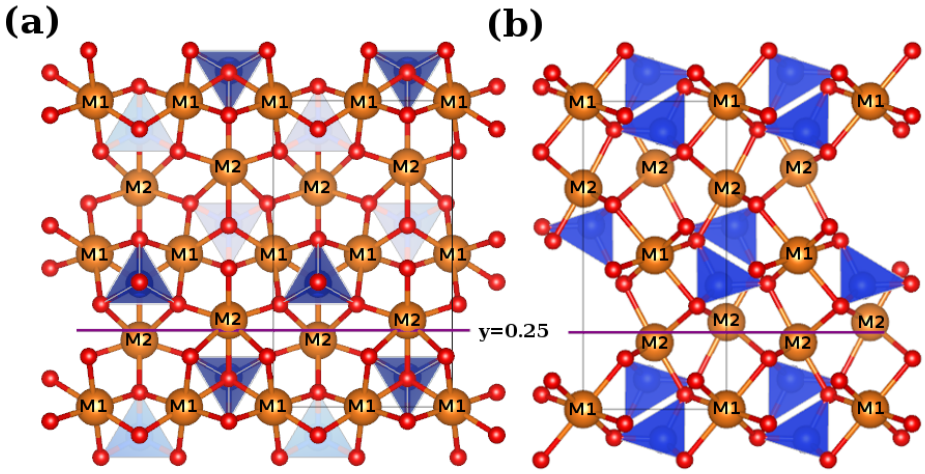

Fig. VIII.1 The olivine unit cell, viewed down the (a) [100] and (b) [001] cell directions, with the M1 and M2 sites labeled. The easy glide plane for dislocations gliding on (010) is marked. Visualization produced using VESTA 3 (Momma and Izumi 2011).

along [001](010). Indeed, the magnitude of the difference may actually be understated, as Durinck et al. (2005) used atomic slabs only a single unit cell thick along the stacking fault normal, so that their *ab initio* computed GSF energies are unlikely to be fully converged with respect to slab thickness.

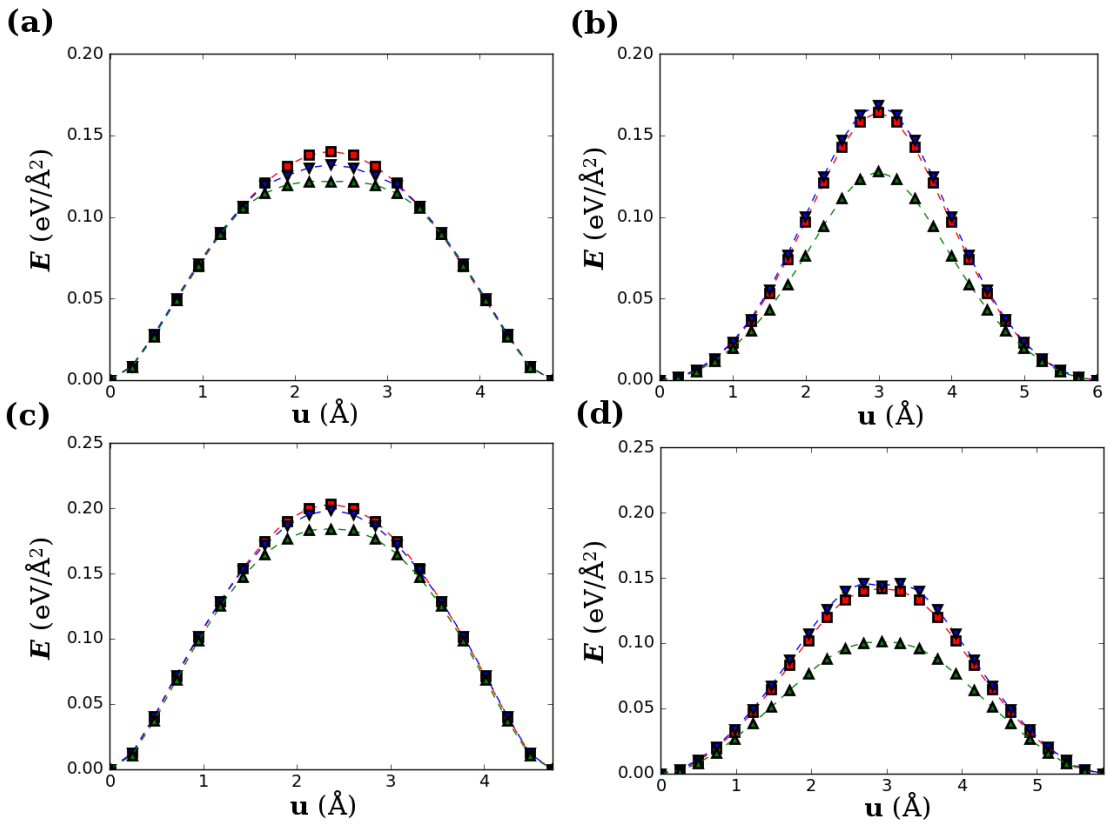

Fig. VIII.2 (a) [100](010) and (b) [001](010) γ-lines at 0 GPa. (c) [100](010) and (d) [001](010) γ-lines at 10 GPa. Square, triangle, and inverted triangle symbols correspond to GSFs without point defects, with $\{\square_{M2}\}''$ defects, and with $\{\square_{M1}\}''$ defects.

The difference between GSF energies obtained in *ab initio* and force field calculations may be due to the use of formal charges in the THB1 model. The introduction of a GSF into a simulation cell often brings ions at or near the stacking fault plane into close proximity with ions of like charge. GSF calculations for the oxide UO_2 using a diverse range of potential

models show that partially ionic models predict lower energies than models that employ formal charges (Chapter VI; Skelton and Walker 2017a). Although the ionicity ζ of an atom in a crystal is difficult to determine uniquely, refinements of electron density distributions obtained using theoretical calculations (Liu et al. 2009) and synchrotron x-ray diffraction (Kirfel et al. 2005) indicate that ζ is < 1 for forsterite. It is thus unsurprising that Durinck et al. (2005) find lower GSF energies than calculations that use the THB1 potential.

In our calculations, we find that in point defect-free forsterite the maximum energy along the [100](010) γ-line, which is the energy of a 1/2[100](010) GSF, increases monotonically with pressure from 0.140 eV/Å^2 at 0 GPa to 0.203 eV/Å^2 at 10 GPa (Fig. VIII.2). By comparison, the energy of the 1/2[001](010) GSF, which is the [001](010) γ-line maximum, decreases modestly over the same pressure range, from 0.163 eV/Å^2 at 0 GPa to 0.142 eV/Å^2 at 10 GPa. This contrasts with DFT calculations (Durinck et al. 2005), which predict a pressure-independent [001](010) γ-line maximum energy, although this is likely a consequence of the different simulation parameters, including simulation cell size and relaxation constraints. While, at ambient pressure, the energy of the [100](010) γ-line maximum is lower than that of the [001](010) γ-line maximum, the qualitatively different responses of the two γ-lines to applied pressure mean that the [001](010) γ-line has the lower maximum energy above ~3 GPa. The higher GSF energies reported here are partly due to the stricter relaxation constraints, particularly for Mg atoms, which were allowed to relax freely in previous studies (Durinck et al. 2005; Mahendran et al. 2017) but were here constrained to relax normal to the stacking fault plane.

Influence of Mg vacancies on GSF energies

In the mantle, where olivine coexists with $(Mg,Fe)SiO_3$ pyroxene, Mg vacancies are expected to be more abundant than Si vacancies. As discussed above in the introduction, and in Chapter V, the olivine crystal structure has two symmetrically distinct divalent cation sites, M1 and M2. In the bulk lattice, M1 vacancies are of lower energy than M2 vacancies (Brodholt 1997). Any change in the GSF energy will depend on the interaction between the Mg vacancy and the stacking fault, which can be expected to vary between the two sites. Considering first slip in the [100] direction, we find that the energy of the 1/2[100](010) GSF with a $\{\square_{M1}\}''$ defect adsorbed to the stacking fault plane is 0.132 eV/Å^2 at 0 GPa, 5.7% lower than the value computed without point defects. The 1/2[100](010) GSF energy increases with pressure (Fig. VIII.3), reaching 0.198 eV/Å^2 at 10 GPa, 2.5% less than the point defect-free value. $\{\square_{M2}\}''$ defects have a more substantial impact on the calculated 1/2[100](010) GSF energy, reducing it to 0.121 eV/Å^2 at 0 GPa, 13.6% lower than the point defect-free value. Pressure decreases the relative reduction of the 1/2[100](010) GSF energy with adsorption of $\{\square_{M2}\}''$; its value at 10 GPa (0.184 eV/Å^2) corresponds to a reduction of only 9.5%.

The 1/2[001](010) GSF energy calculated with a $\{\square_{M1}\}''$ defect at the fault plane is 0.168 eV/Å^2 at ambient pressure, decreasing to 0.145 eV/Å^2 at 10 GPa. Comparing these with the values reported above for point defect-free case, we see that M1 vacancies do not lubricate [001](010) slip, and may actually inhibit it. In contrast, $\{\square_{M2}\}''$ defects reduce the 1/2[001](010) GSF energy to 0.127 eV/Å^2 at 0 GPa, a decrease of -22.1%. At 10 GPa, the energy of this GSF is 0.101 eV/Å^2, corresponding to a -28.9% change in the GSF energy relative to

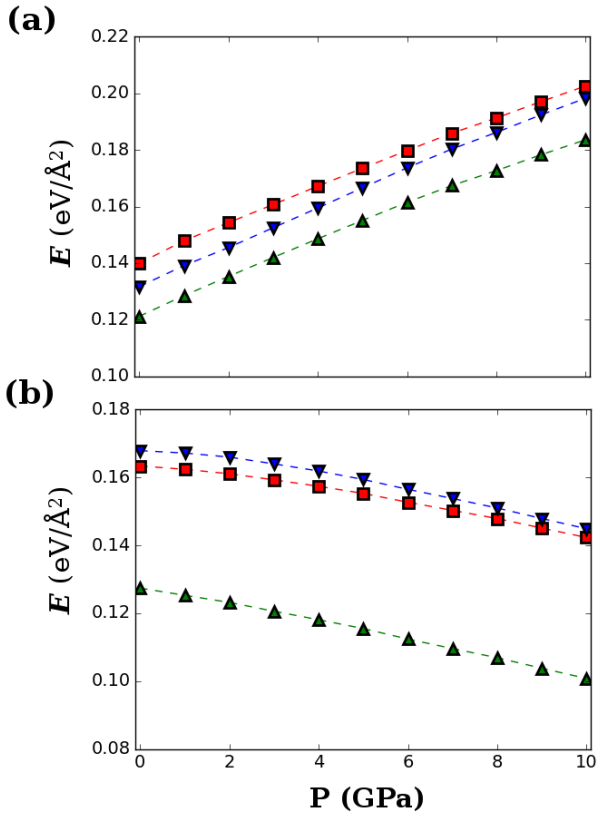

Fig. VIII.3 Maximum energies along the (a) [100](010) and (b) [001](010) γ-lines. Symbols have the same meaning as in Fig. VIII.2.

the point defect-free GSF case. Overall, (010) stacking fault energies are reduced much more by the presence of M2 than M1 vacancies, unsurprising given that the fault plane intersects the sheet of $M2O_6$ octahedra. The lubrication effect is greatest for [001](010) γ-line energies, as the minimum distance between M2 sites across the fault plane is 2.61 Å (at the γ-line maximum), compared with 3.89 Å for the [100](010) γ-line.

The markedly different sensitivities of the [100](010) and [001](010) γ-lines to adsorption of $\{\square_{M1}\}''$ versus $\{\square_{M2}\}''$ defects to the stacking fault are a direct consequence of the

location of the slip plane in the unit cell. As shown in Fig. VIII.1a, the lowest energy slip plane lies across the center of the sheet of $M2O_6$ octahedra that is parallel to the (010) plane and does not intersect $M1O_6$ octahedra (or SiO_4 tetrahedra). Consequently, M1 vacancies do not contribute to the population of vacant lattice sites at the slip plane. Nevertheless, $\{\square_{M1}\}''$ defects do still reduce the energy of the [100](010) γ-line, although [001](010) γ-line energies are essentially unchanged. This is because displacement of the upper half the simulation cell by 1/2[100] brings M2 and Si sites on opposite sites of the stacking plane into close proximity. Relaxing the atom in the M2 site away from the stacking fault reduces the energy of the slab, which is easier when a void has been created above the M2 site by the insertion of a $\{\square_{M1}\}''$ defect. At 0 GPa, this increases the relaxed M2-Si distance from 2.939 Å to 3.021 Å. Furthermore, a sub-periodic modulation of the M1 site coordinates is introduced, as the Mg atoms in the layer of M1 sites closest to the GSF stacking fault are displaced ~0.2 Å along the fault plane normal. The sign of the displacement vector alternates along [001]. For the olivine crystal structure, [001](010) slip does not cause cations to approach as closely as for [100](010) slip, so there is less potential for vacant cation sites away from the slip plane to reduce GSF energies by enabling relaxation away from the stacking fault.

Peierls stresses of dislocations in point defect-free forsterite

Core structures and Peierls stresses for edge and screw dislocations in forsterite have been calculated using the PN model (equation VI.2), with the misfit energy parameterized using the γ-lines calculated in the previous section. At 0 GPa, the Peierls stress calculated for the [100](010) edge dislocation in the point defect-free crystal is 2.4 GPa, ~25% greater than

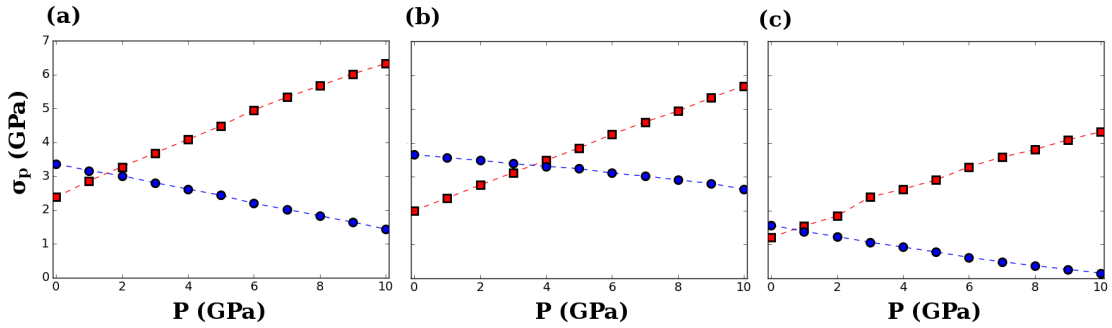

Fig. VIII.4 Pressure evolution of σ_p for (squares) [100](010) and (circles) [001](010) edge dislocations with (a) no point defects, (b) a $\{\square_{M1}\}''$ defect, and (c) a $\{\square_{M2}\}''$ defect at the glide plane. All Peierls stresses are plotted using the same scale. Symbols have the same meaning as in Fig. VIII.2.

the value computed by Durinck et al. (2007) using a DFT-parameterized continuous PN model. The Peierls stress increases with pressure (Fig. VIII.4), reaching 6.3 GPa at 10 GPa, much higher than the corresponding value of 2.2 GPa calculated by Durinck et al. The pressure derivative of the Peierls stress is thus $d\sigma_p/dP$ = 0.39. For the [001](010) edge dislocation, σ_p is calculated to be 3.4 GPa at ambient pressure, decreasing with increasing pressure to 1.4 GPa at 10 GPa, in qualitative agreement with DFT-parameterized PN calculations by Durinck et al. (2007). This gives a pressure derivative for the Peierls stress $d\sigma_p/dP$ = -0.19. The disagreement between this calculation and that of Durinck et al. may be partially attributed to the present use of a discrete PN model, in contrast to the continuous formulation employed by Durinck et al. However, the principal disagreement concerns the pressure dependence of the γ-line energies. Whereas in this study the [001](010) γ-line maximum decreases with pressure, the γ-line previously calculated is nearly pressure independent (Durinck et al. 2005; Durinck et al. 2007). The cores of [100](010)

and [001](010) edge dislocations are undissociated across the entire pressure range 0-10 GPa, consistent with previous PN calculations (Durinck et al. 2007).

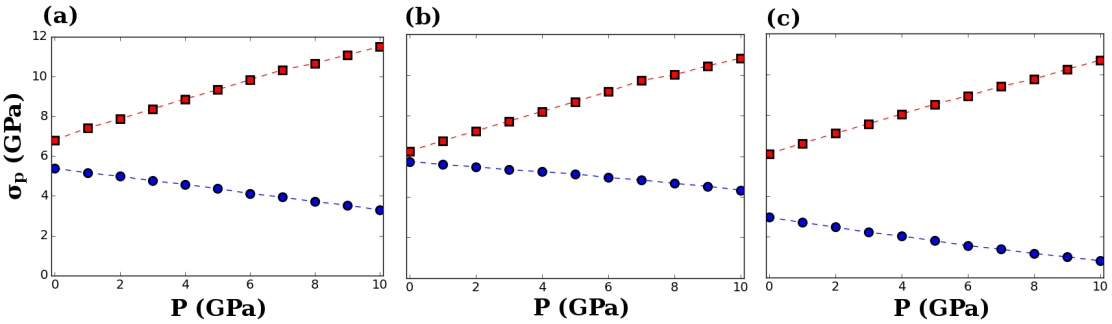

Fig. VIII.5 Pressure evolution of σ_p for (squares) [100](010) and (circles) [001](010) screw dislocations with (a) no point defects, (b) a $\{\square_{M1}\}''$ defect, and (c) a $\{\square_{M2}\}''$ defect at the glide plane. All Peierls stresses are plotted using the same scale.

A screw dislocation can glide on any lattice plane containing the dislocation line vector $\boldsymbol{\xi}$. Each glide plane has a different structure and a correspondingly different lattice resistance, giving rise to preferred glide planes. Here, we calculate the Peierls stress for [100] and [001] glide on (010), corresponding to the screw dislocations that enable deformation of the [100](010) and [001](010) slip systems. The Peierls stress for glide of [100] on the (010) plane at ambient pressure (Fig. VIII.5) is 6.8 GPa, comparable with the 6.3 GPa predicted by DFT-parametrized PN calculations (Durinck et al. 2007). However, we calculate $d\sigma_p/dP = 0.47$, slightly greater than the pressure derivative of $d\sigma_p/dP = 0.39$ calculated by Durinck et al. (2007). However, this is somewhat lower than the pressure derivative $d\sigma_p/dP$ ~0.67 measured in high-stress deformation experiments for the average Peierls stress, which is presumably controlled by the easy [100](010) slip system (Proietti et al. 2016).

The [001] screw dislocation glides on the (010) plane with a Peierls stress σ_p = 5.4 GPa at 0 GPa pressure (Fig. VIII.5), comparable to values calculated in previous theoretical studies, which range between 3.1 GPa (Durinck et al. 2007) and 7.2 GPa (Mahendran et al. 2017). As was found for the [001](010) edge dislocation, pressure enhances glide on this slip system by reducing its Peierls stress, with $d\sigma_p/dP$ = -0.21. Fully atomistic calculations show that the static [001] screw dislocation core has a labile non-planar structure and that the effect of applied stress is to transform into a high core energy-low Peierls stress planar configuration (Carrez et al. 2008). The critical stress for dislocation glide is thus the stress required to activate the locking-unlocking mechanism for this slip system (Mahendran et al. 2017). This locking-unlocking mechanism cannot be modeled within the PN formalism, and the σ_p reported in this study is for the glissile (i.e. unlocked) dislocation core gliding on the median plane of the $M2O_6$ sheet.

Effect of vacancies on the Peierls stress

For [100](010) edge dislocations, the adsorption of a $\{\square_{M1}\}''$ defect to the stacking fault plane reduces Peierls stress by -16% at ambient pressure, to 2.0 GPa. The pressure dependence of σ_p is not significantly changed by the presence of the defect as $d\sigma_p/dP$ = 0.37, compared with 0.39 calculated above for the point defect-free dislocation, and 10 GPa σ_p = 5.7 GPa. The effect of the $\{\square_{M2}\}''$ defect is more substantial, and for this defect σ_p = 1.2 GPa at ambient pressure, slightly more than half the Peierls stress calculated for a dislocation without adsorbed vacancies. Moreover, unlike the $\{\square_{M1}\}''$ defect, $\{\square_{M2}\}''$ defects reduce the pressure sensitivity of this slip system, as $d\sigma_p/dP$ = 0.31. At 10 GPa, σ_p = 4.3 GPa, -31% lower than the value calculated in section 3.2.

As can be seen in Fig. VIII.4, the [001](010) edge dislocation responds quite differently from [100](010) edge dislocation to the presence of Mg vacancies. The adsorption of a $\{\square_{M1}\}''$ defect to the stacking fault plane increases [001](010) γ-line energies, leading to considerably higher Peierls stresses for the [001](010) edge dislocation. At ambient pressure, σ_p = 3.7 GPa, nearly 10% greater than the Peierls stress without point defects. The Peierls stress decreases with pressure at a rate $d\sigma_p/dP$ = -0.10. Compared with the $d\sigma_p/dP$ calculated for this dislocation without adsorbed point defects, $\{\square_{M1}\}''$ reduces the pressure sensitivity of [001](010) slip by almost a factor of 2. Unlike $\{\square_{M1}\}''$ defects, $\{\square_{M2}\}''$ defects reduce the [001](010) γ-line energy. Correspondingly, as can be seen in Fig. VIII.4c, the Peierls stress of the [001](010) edge dislocation is considerably reduced by $\{\square_{M2}\}''$, to 1.6 GPa at 0 GPa applied pressure, decreasing to only 150 MPa at 10 GPa, giving $d\sigma_p/dP$ = -0.14. Due to the relative softness of this slip system, the relative Peierls stress reduction actually increases with pressure, from -52% at 0 GPa to -90% at 10 GPa.

For [100](010) screw dislocations (Fig. VIII.5), the presence of Mg vacancies at the glide plane reduces the Peierls stress. If the Mg vacancy is located on an M2 site, σ_p is calculated to be 6.1 GPa, 10.2% lower than in point defect-free forsterite, and increases with pressure to 10.7 GPa at 10 GPa. The pressure sensitivity of the [100] screw dislocation is unaffected by $\{\square_{M1}\}''$ defects as $d\sigma_p/dP$ = 0.46, nearly identical to the value found in section 3.2 for this dislocation. For an Mg vacancy located on an M1 site close to (but not on) the slip plane, calculated values for σ_p at these pressures are comparable, 6.3 GPa and 10.8 GPa at 0 and 10 GPa, respectively, as is the pressure derivative $d\sigma_p/dP$, which is 0.45.

The Peierls stresses of [001] screw dislocations gliding on (010) are similarly reduced by the presence of an Mg vacancy at one of the M2 sites located at the slip plane, to 3.0 GPa at ambient pressure and 0.8 GPa at 10 GPa (Fig. VIII.5). The pressure derivative $d\sigma_p/dP$ = -0.21, identical to the value above for point defect-free forsterite. Unlike the [100](010) screw dislocation, the relative Peierls stress reduction induced by the presence of M2 vacancies actually increases with pressure, from -44% at ambient pressure to -75% at 10 GPa. However, just as in the case of [001](010) edge dislocations, glide of [001] screw dislocations on (010) is modestly inhibited by the presence of M1 vacancies. At ambient pressure, σ_p = 5.7 GPa, decreasing to 4.3 GPa at 10 GPa pressure. The magnitude of $d\sigma_p/dP$ is reduced by ~1/3, to -0.14, relative to the point defect-free value.

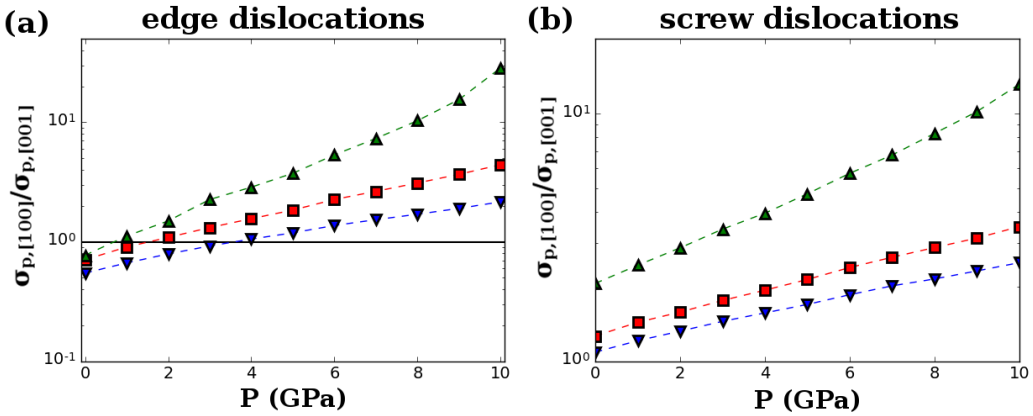

Fig. VIII.6 $\sigma_{p,[100]}/\sigma_{p,[001]}$ ratios for (a) edge, and (b) screw dislocations. Symbols have the same meaning as in Fig. VIII.2.

In vacancy-free forsterite, the ratio $\sigma_{p,[100]}/\sigma_{p,[001]}$ increases with *P* for both the edge and screw components of both slip systems. For edge dislocations, $\sigma_{p,[100]}/\sigma_{p,[001]}$ varies from 0.71 at ambient pressure, to 4.4 at 10 GPa (Fig. VIII.6a). The addition of $\{\square_{M1}\}''$ vacancies changes this ratio, decreasing it to 0.54 at ambient pressure and reducing the pressure

sensitivity so that, at 10 GPa, it is just 2.16. In contrast, $\{\square_{M2}\}''$ defects increase the ratio, to 0.77 at 0 GPa and 28.51 at 10 GPa. In each case, the ratio $\sigma_{p,[100]}/\sigma_{p,[001]} = 1$ corresponds to the pressure at which [100](010) glide becomes harder than [001](010) glide. This occurs at 1.5 GPa with no point defects present, increasing to 3.6 GPa when $\{\square_{M1}\}''$ defects are adsorbed to the stacking fault and decreases to 0.7 GPa upon adsorption of $\{\square_{M2}\}''$ defects to the stacking fault plane. In the case of screw dislocations, $\sigma_{p,[100]}/\sigma_{p,[001]}$ is strictly > 1. However, $\{\square_{M1}\}''$ defects reduce it from 1.26 to 1.09 at ambient pressure, and from 3.49 to 2.50 at 10 GPa. The $\{\square_{M2}\}''$ defect has the reverse effect on the two slip systems, increasing $\sigma_{p,[100]}/\sigma_{p,[001]}$ to 2.06 at ambient pressure and 13.10 and 10 GPa. From this, we conclude that, while $\{\square_{M1}\}''$ defects cause the relative activities of the two slip systems to converge at constant *P*, $\{\square_{M2}\}''$ defects enhance slip on [001](010).

VIII.4. Discussion

Experimental studies have reported a pressure-induced change in the deformation fabric of anhydrous olivine, caused by a change of the preferred slip system from [100](010) to [001](010) (Couvy et al. 2004; Raterron et al. 2016). This transition may be observable in seismological models for the Earth's upper mantle. The LPO of Fe-bearing Fo_{90} olivine suggests a change from dominant [100](010) to [001](010) slip at ~3 GPa, which corresponds to a mantle depth of approximately 70-80 km (Jung et al. 2009). At 0 GPa, the [100](010) edge dislocation has the lowest Peierls stress and so should be the dominant slip system during glide deformation. However, because pressure is calculated to suppress the activity of this slip system, the Peierls stress of the [001](010) edge dislocation is lower at high pressure. The P-σ_p curves of the two slip systems in point defect-free forsterite

intersect at 1.5 GPa (Fig. VIII.4a), slightly lower than the pressures reported in experiments.

Deformation experiments produce different olivine textures under dry and wet conditions. One plausible reason for this is that hydrated vacancies lubricate [001](010) glide more than [100](010) glide (Katayama et al. 2004), leading to the development of the flow normal B-type fabric associated with the mantle wedge. Ohuchi et al. (2012) have found that the transition between the two fabrics occurs at ~650 ppm H/Si. Consistent with this, we find that the Peierls stresses of [100](010) edge and screw dislocations are reduced less by the presence of M-site vacancies than [001](010) edge and screw dislocations. Realistic vacancy-related defect concentrations are insufficient to change the weakest slip system at ambient pressure. However, the differential effect on the Peierls stresses of the [100](010) and [001](010) edge dislocations is enough to reduce the pressure at which the Peierls stresses of the two slip systems cross over. When the inelastic restoring force in equation (VI.2) is parametrized using the γ-line, $P_{\text{cross-over}}$ decreases from 1.5 GPa to ~0.7 GPa. Higher defect concentrations at the dislocation core will cause the slip system cross-over to be displaced to even lower pressures. Similarly, differences between concentrations of vacancy-related defects at the glide planes of the two slip systems will displace the cross-over pressure. Increasing the concentration $\{\square_{M2}\}''$ defects adsorbed to the [100](010) dislocation or decreasing the concentration of defects adsorbed to the [001](010) dislocation will reduce $P_{cross\text{-}over}$. Changing either of the concentrations in the opposite direction increases $P_{cross\text{-}over}$.

The calculated influence of vacancy-related defects on the Peierls stress of olivine may be of significance for development of LPO during deformation. It has also been suggested that a distinct LPO may form in olivine when it is deformed via diffusion creep (Miyazaki et al. 2013). Similarly, a transition to a grain boundary sliding deformation mechanism may explain the presence of the B-type deformation fabric, rather than water-induced changes to the relative strengths of olivine slip systems. However, as these calculations show, the adsorption of vacancies, and by implication vacancy-related defects, is sufficient to induce a change in the deformation fabric of olivine similar to that observed by Katayama and Karato (2008) under hydrous conditions. In tomographic images of shear wave anisotropy, this might show up as a reduction of the depth at which the deformation fabric changes from A-type (i.e. [100](010)) to B-type (i.e. [001](010)). Alternatively, if water is present only at shallow depths, the shear wave anisotropy may match the B-type fabric at shallow depths, transitioning to the A-type deformation fabric as the modal abundance of water decreases. The B-type deformation fabric then re-emerges at high pressure as the relative activity of the [001](010) slip system increases. These conclusions carry over to the dislocation-accommodated grain-boundary sliding regime. This deformation mechanism leads to the development of a pronounced LPO that relates to the slip system accommodating grain boundary sliding (Hansen et al. 2011; Hansen et al. 2012ab), which will be altered by the presence of hydrous vacancies.

Incorporation of water is not the only mechanism by which vacancies can be generated in olivine minerals. Trivalent cations such as Al^{3+}, Sc^{3+} and Fe^{3+} can substitute for Mg^{2+} (or Fe^{2+}) in the olivine lattice, charge-balanced either the replacement of Si^{4+} by a trivalent

cation or, more commonly, the creation of M-site vacancies (Colson et al. 1989). The latter substitution mechanism can be written as

$$3\cdot\left(M_M^{2+}\right)^X + M_2^{3+}O_3 \rightleftharpoons 2\cdot\left(M_M^{3+}\right)^{\cdot} + \left(\square_M\right)'' + 3\cdot M^{2+}O \qquad \text{(VIII.1)}$$

where M^{2+} is typically Mg^{2+} or, in iron-bearing olivine, Fe^{2+} and M^{3+} is the substituting trivalent cation. The solubility of common trivalent elements in olivine is sufficiently high that vacancies created by the substitution reaction (VIII.1) can greatly outnumber intrinsic vacancies, such as those associated with Schottky defects (Van Orman et al. 2009). In $(Mg,Fe)_2SiO_4$, M-site vacancies are produced by oxidation of iron from Fe^{2+} to Fe^{3+}, and at high fO_2 $\{Fe^{3+}{}_M\}^{\cdot}$ and $\{\square_M\}''$ are the most abundant defects (Stocker 1978). Vacancies are also produced by a similar mechanism in the common oxide (Mg,Fe)O, and in this material they are frequently unassociated, especially at high pressure (Otsuka et al. 2010), and the same may be true for olivine as well. Decoupled bare vacancies would be able to lubricate dislocation glide in a similar way to protonated vacancies, with the same implications for deformation of lower mantle rocks and the development of LPO.

In addition to studying the effects of $\{\square_{M1}\}''$ and $\{\square_{M2}\}''$ defects on dislocation glide, an attempt was also made to calculate energies for [100](010) and [001](010) GSFs with $\{2H_{M1}\}^X$ and $\{2H_{M2}\}^X$ defects adsorbed to the stacking fault plane. However, while the [100](010) and [001](010) γ-line maxima were systematically reduced by the presence of protonated vacancies, the γ-line was insufficiently smooth to determine accurate Peierls stresses for any dislocation. This may be because the available potentials for the MgO-SiO_2-H_2O system treat oxygen atoms that are bonded to H differently from the regular

"oxide" oxygens. This means that the location of the hydroxyl oxygen must be selected *prior* to inserting the H atom. For segregation, this does not present a significant challenge, as the shape of the atomic site - and hence the optimal configuration of H ions - is already known (Chapter V). However, in a GSF calculation, the extreme shearing of the polyhedra that span the stacking fault causes the shape of an "M" site to change considerably through the simulation. Locating the optimal configuration of the H ions with their associated hydroxyl-type oxygens, O_H, in a $\{2H_M\}^X$ defect is thus non-trivial. This was not a problem for the DFT calculations used to investigate glide lubrication of dislocations in MgO (Chapter VII), as solving for the electron density distribution directly removes the need to treat oxygen atoms that are bonded to H differently from those that are not. Revisiting these GSF calculations with protonated vacancies might be possible using DFT, but would computationally demanding and require significant time on a national facility.

VIII.5. Conclusions

In this study, we used atomistic calculations of generalized stacking fault energies in forsterite, the Mg end-member of olivine, to parameterize Peierls-Nabarro models of pure edge and screw dislocation. To probe the possible influence of vacancy-related defects on the Peierls stress, energies were calculated for GSFs in point defect-free forsterite, and with $\{\square_{M1}\}''$ and $\{\square_{M2}\}''$ defects segregated to lattice sites in close proximity to the stacking fault plane. It was found that vacancies are capable of reducing γ-line energies and, correspondingly, Peierls stresses for many of the major slip systems in olivine. However, the magnitude of this decrease depends strongly on both the slip system and the site on which the vacancy is located. $\{\square_{M2}\}''$ defects at lattice sites adjacent to the glide plane have

the greatest influence on the Peierls stress of both slip systems, with the magnitude of the σ_p reduction being greatest for the [001](010) slip system. In the case of edge dislocations, this reduces the pressure at which the hardening of [100](010) glide cause [001](010) to become the dominant slip system.

Cation vacancies in olivine are associated with intrinsic defect mechanisms (Schottky and Frenkel defects). However, in natural olivine, vacancy concentrations are, in most cases, probably controlled by extrinsic defect mechanisms, such as the creation of protonated vacancies in hydrated systems, the oxidation of Fe^{2+} to Fe^{3+}, or the charge-balanced substitution of heterovalent impurities, such Al^{3+} or Cr^{3+}. Each of these mechanisms will be operative in at least some regions of the Earth's upper mantle. Hydration and oxidation are especially relevant in mantle wedges above subduction zones. There, concentrations of vacancy related defects are likely to be elevated, due to the combination of oxidizing conditions and the availability of liquid water from dehydrating phases in the subducting slab.

IX. Conclusions

IX.1. Summary of results

Phosphates at mantle pressures

Minor phases, particularly phosphates, have been suggested to be potential reservoirs of trace elements in some regions of the Earth's mantle. At upper mantle pressures, the dominant phosphate mineral is apatite. In Chapter II, DFT calculations were used to examine the compressibility and crystal structure of apatite at high pressure. It was found that under static (i.e. 0 K) conditions, apatite decomposes to form the calcium orthophosphate tuite at pressures >10 GPa, with the exact transition pressure depending on the apatite channel anion. Chapter III used a combination of DFT-parameterized lattice strain modeling and fully atomistic calculations of point defect energies in tuite and $CaSiO_3$ perovskite (cpv) to show that, under mantle *PT* conditions, tuite can incorporate considerably higher concentrations of incompatible elements like Sr and Ba than cpv. This suggests that phosphate minerals, where present, could play an important role in the distribution of incompatible trace elements in the mantle.

Segregation of bare and protonated cation vacancies to dislocations

In the second part of this study, atomistic simulations were used to investigate interactions between dislocations and vacancy-related defects in mantle minerals. The potential for dislocation cores to behave as reservoirs for vacancy-related defects was investigated by calculating energies for segregation of bare and protonated vacancies to a single dislocation embedded in a 1D periodic supercell. These fully atomistic calculations made use of the `disloPy` code developed as part of this study to facilitate high-throughput calculations of

dislocation properties at the atomic scale. The study focused on MgO, a structurally simple oxide (space group $Pm\bar{3}m$) which is both an industrially import ceramic and the Mg end-member of (Mg, Fe)O magnesiowüstite, the second most abundant mineral in the lower mantle, and Mg_2SiO_4 forsterite, the Mg end-member of the most common upper mantle mineral, olivine.

For both forsterite and periclase, minimum segregation energies to both edge and screw dislocations were substantially negative, with E_{seg} < -1.0 eV for the tightest binding sites around edge dislocations for vacancies, protonated and bare, in both minerals. However, segregation energies could be considerably lower; in the case of $\{2H_{Mg}\}^X$ defects segregating around 1/2<110>{100] edge dislocation in MgO, E_{seg} is -6 eV for the tightest binding site. This means that vacancy-related defect concentrations at dislocation cores in MgO and Mg_2SiO_4 will be far greater than in the bulk lattice. At mantle temperatures, the relative enrichment may be as high as 10^3-10^4. However, it is worth noting that I have calculated segregation energies in the dilute limit, and that interactions between point defects are likely to be significant at higher concentrations.

In the fully atomistic calculations of defect segregation to dislocation cores in forsterite detailed in Chapter V, it was noted that segregation energies for M1 and M2 vacancies depend on dislocation geometry (i.e. $\boldsymbol{\xi}$ and **b**). Around a dislocation in forsterite, the energy of a vacancy can be several eV lower than in the bulk, particularly around [100](010) and [001](010) edge dislocations. As was found for MgO, cation vacancies in forsterite are enriched around dislocation cores, relative to bulk concentrations. Segregation energies were different for the two symmetry distinct M sites. For some dislocations, particularly [100] screw and [100](010) edge dislocations, the segregation energy calculated for the

tightest binding M1 sites is considerably lower than that of the tightest binding M2 site, and M2 vacancy concentrations will be low in the dislocation. However, the lowest segregation energy sites for $\{\square_{M1}\}''$ and $\{\square_{M2}\}''$ defects in the [001](010) edge dislocation core are comparable. Concentrations of M1 vacancy-related defects are higher in the core regions of all four dislocations considered in this study, while only [001](010) edge dislocations are predicted to have a high concentration of M2 vacancy-related defects at the glide plane. This is potentially significant because the favored plane for dislocation glide on (010) is the median plane of the (010)-parallel sheet of $M2O_6$ octahedra.

Lubrication of dislocation glide by vacancy-related defects

The ability of dislocation core sites to bind protonated vacancies is of geophysical significance due to the potential for hydrous defects to lubricate dislocation glide, thereby reducing flow stresses in the exponential creep regime. In this study, the effect of water on the Peierls stress, one of the parameters that controls the rate of dislocation glide, was calculated using the Peierls-Nabarro method parameterized using atomic-scale calculations, as implemented in the newly-developed `disloPy` software package, and which was used to calculate Peierls stresses for dislocations in UO_2 in Chapter VI.

As demonstrated in chapter VII using DFT calculations, water, in the form of doubly-protonated magnesium vacancies (i.e. $\{2H_{Mg}\}^X$), reduces the energies of the <110>{110} and <110>{100} γ-lines in MgO. Peierls-Nabarro (PN) models parameterized using these γ-lines, showed that $\{2H_{Mg}\}^X$ defects reduce the Peierls stress for both slip systems. However, the 1/2<110>{110} and 1/2<110>{100} dislocations are affected differently, with the former being considerably more sensitive to the presence of protonated vacancies. This

results in an increase of the pressure at which the transition from dominant 1/2<110>{110} slip to 1/2<110>{100} slip occurs. At the defect concentration used in the GSF calculations presented in Chapter VII, the transition pressure increases by 7.3 GPa, from 24.8 GPa to 32.1 GPa. This gives a dependence of the transition pressure on concentration C_{2H_Mg} of $\{2H_{Mg}\}^X$ defects at the slip plane is ~30·C_{2H_Mg} GPa. The pressure at which the Peierls stresses of the 1/2<110>{100} screw dislocation and 1/2<110>{100} edge dislocation cross over is even more sensitive to the presence of $\{2H_{Mg}\}^X$ defects, rising by 30·C_{2H_Mg} GPa.

In Chapter VIII, I examined the effects of bare M1 and M2 site vacancies on glide of [100](010) and [001](010) dislocations in forsterite. The influence of Mg vacancies on the mobility of these slip systems in forsterite was determined by using the γ-lines calculated from simulation cells containing $\{\square_{M1}\}''$ or $\{\square_{M2}\}''$ defects adsorbed to the stacking fault plane. An attempt was also made to calculate energies for [100](010) and [001](010) GSFs with $\{2H_{M1}\}^X$ and $\{2H_{M2}\}^X$ defects adsorbed to the stacking fault plane. However, accurate γ-line energies could not be calculated due to problems with the potential model. Fortunately, the similarity of the segregation energies for $\{2H_M\}^X$ and $\{\square_M\}''$ defects in forsterite (see the Discussion of the similarity measures for the two defects in Chapter VIII) suggests that the two defect types might behave similarly, so that the results obtained for bare vacancies may provide a useful guide to the behavior of protonated vacancies.

Comparing calculated Peierls stresses for each of the dislocations, shown in Fig. VIII.4 for edge dislocations and Fig. VIII.5 for screw dislocations, I found that Mg vacancies generally lubricate glide on (010). The exception was $\{\square_{M1}\}''$ defects, which actually inhibited [001](010) glide. For all four dislocations, the $\{\square_{M2}\}''$ defect is more effective at lubricating glide, as the easy (010) glide plane is located at the median plane of the sheet of

$M2O_6$ octahedra. Moreover, $\{\square_{M2}\}''$ defects are more effective at lubricating glide on [001](010) than [100](010), and accordingly displace the pressure-induced transition from [100](010) dominant slip to [001](010) to lower *P*. At the defect concentrations used here, the transition pressure was reduced more than two-fold, from 1.5 GPa to ~0.7 GPa, which corresponds to a depth of ~28-30 km in the Earth's interior. This is approximately the depth at which the water-induced B-type fabric is thought to occur (Katayama and Karato 2008).

However, I note that the deformation fabric transition may actually occur at even lower pressures. In Chapter V, it was noted that M2 vacancy-related defects have lower energy around [001](010) edge dislocations than [100](010) edge dislocations in forsterite, and are thus more strongly concentrated around the former than the latter dislocation. Moreover, the tightest binding sites around a [001](010) edge dislocation are on the glide plane and close to the dislocation line, where their impact on dislocation glide is likely to be greatest. Thus, vacancy-weakening of the [001](010) slip system may be further enhanced by relative to [100](010).

In summary, these calculations have shown that vacancy-related defects segregate to dislocation cores in important mantle minerals, with often significant partitioning energies between the bulk and the dislocation core. As proposed by Katayama and Karato (2008), these defects can change the Peierls stresses of some slip systems, increasing strain rates and changing the lattice preferred orientation, and hence the deformation fabric. For forsterite, the change in LPO is consistent with the experiments on hydrous olivine reported by Katayama and Karato (2008), as is the magnitude of the Peierls stress reduction,

providing evidence that protonated vacancies can alter the rheology of olivine - and perhaps other mantle minerals - in the exponential creep regime.

IX.2. Future directions

Incompatible elements and dislocations in mantle minerals

In this study, tuite was studied as an example of a minor phase that may be able to make an outsize contribution to the trace element budget of the Earth's interior, particularly the lower mantle. However, extended defects, such as grain boundaries and dislocations, can act as point-defect sinks. Indeed, some elements may be found almost exclusively on grain boundaries, as is the case for K, P, and Ti in mantle peridotites, and grain boundary accommodation can determine whole-rock concentrations of these elements (Suzuki 1987). Moreover Cr, Al, Ti, and especially Ca are all enriched at grain boundaries in synthetic polycrystalline olivine (Hiraga et al. 2003; Marquardt and Faul 2018). Partitioning of these elements from the bulk to grain boundaries in olivine is so strong that it has been suggested that grain boundaries could be the most important storage sites for incompatible elements in the Earth’s mantle (Hiraga et al. 2004).

As regions of high strain, dislocations are likewise able to accommodate incompatible elements at concentrations exceeding bulk values. In their computational study of MgO dislocations, Zhang et al. (2010) used the cluster-based method to calculate energies for Sr and Ca defects segregating to 1/2<110>{110} edge dislocation, finding that defect energies in core sites were 1.0-2.5 eV lower than in the bulk. Even the lower value gives defect concentrations in the dislocation core a factor of 10^3-10^4 greater than in the bulk at mantle temperatures. Accommodation of trace elements at dislocation is also of interest in the

context of the Earth's crust. For instance, dislocations, which are commonly introduced into zircon grains during tectonic events (Reddy et al. 2007), sweep up impurities, including U, Al, and Pb, as they glide through the lattice during creep (Piazolo et al. 2016). Trapping of radiogenic Pb in dislocation loops within individual grains of $ZrSiO_4$ enables dating of individual metamorphic events (Peterman et al. 2016).

Binding between immobile impurities and a dislocation core reduces the mobility of a dislocation by increasing the energy required to separate the dislocation and point defect, a phenomenon known as dislocation pinning. Pinning of dislocations in olivine causes peaks in the attenuation spectrum associated with the reversible glide of dislocation segment bounded by two adjacent pinning points; the frequency of the attenuation depends on the length of the dislocation segment (e.g. Karato and Spetzler 1990). Above some threshold stress, determined by the binding energy between a dislocation and an immobile impurity, the dislocation breaks free from the pinning point; at high temperature, de-pinning is a thermally activated process (Cottrell and Bilby 1949). De-pinning is associated with the transition from recoverable anelastic strain to irreversible viscous strain.

I propose to calculate energies for segregation of a range of incompatible trace elements, such Ti, Sr, and Al, to dislocation cores in forsterite using `disloPy`, as has been done in this study for vacancy-related defects. In addition to providing quantitative information about the partitioning of incompatible elements between the bulk lattice and dislocation sites, this will allow us to map the binding energy between immobile point defects as a function of distance from the dislocation core. In turn, this will enable the calculation of threshold stresses for de-pinning of dislocations in forsterite, at least approximately.

Water and other mantle minerals

While this study has focused on the minerals periclase and forsterite, water weakening is observed in other mantle minerals, such as clinopyroxene, whose creep rate is enhanced by a factor of ~100 under "wet" conditions. The water-weakening effect in clinopyroxene is substantial enough that, although dry clinopyroxene is stronger than dry olivine, under wet conditions the relative strength of the two minerals is reversed (Chen et al. 2006). Conversely, the creep strengths of the high pressure polymorphs of olivine, wadsleyite and ringwoodite, are apparently unaffected by water-related defects during low temperature, high stress deformation (Chen et al. 1998). However, these two minerals are not entirely insensitive to water, as the bulk and shear moduli of wadsleyite (Mao et al. 2008; Chang et al. 2015) and ringwoodite (Smyth et al. 2004; Wang et al. 2006b) decrease with increasing water fugacity.

Of the major mantle minerals, wadsleyite is best able to accommodate water as hydrous defects, with a solubility limit of ~3.3% (Kudoh et al. 1996). However, ringwoodite can also dissolve significant amounts of water, ~1.7%, and even bridgmanite may dissolve between 0.1% (Inoue et al. 2010) and 0.2% water (Murakami et al. 2002). *Ab initio* quantum-chemical modeling suggests that bridgmanite is the main host for water in the lower mantle, especially if Al is present (Merli et al. 2016). It has been suggested that natural wadsleyite must contain at least 0.1-0.3% water to be compatible with the observed electrical conductivity of the transition zone (Dai and Karato 2009). High water contents in diamond-preserved ringwoodite from the transition zone likewise that this region, in contrast to the upper or lower mantle, is likely to be hydrated, containing up to ~1 wt. % water (Pearson et al. 2014).

The Python package `disloPy` developed as part of this study was designed to automate dislocation calculations. Calculating energies for segregation of vacancy-related defects to dislocation cores in these minerals is thus a relatively straightforward task. More interesting is the question of whether the Peierls stresses for dislocations in mantle silicates other than olivine are reduced by the presence of vacancy-related defects.

Glide lubrication in hyper-stoichiometric UO_2

In this study, it was found that vacancy-related defects lubricate dislocation glide in some mantle minerals. An analogous phenomenon has been described for UO_2, which is important both as the dominant ore mineral for uranium and as a major reactor fuel. Uranium has multiple valence states, with charge ranging between +3*e* and +6*e*, which enables the O/U ratio for UO_2 to vary with oxidation conditions. Oxidizing conditions increase the O/U ratio, giving the material the hyper-stoichiometric composition UO_{2+x}, with $x > 0$ (Willis 1964). Hyper-stoichiometry influences the physical and chemical properties of UO_2, for instance by enabling dissolution of various fission products (Grimes and Catlow 1991), increasing oxygen self-diffusion coefficients (Breitung 1978), enhancing the heat capacity (Grønvold et al. 1970), and increasing the bulk electrical conductivity (Garcia et al. 2017). The mechanical behavior of UO_2 is influenced by deviations from stoichiometry, and higher O/U leads to lower flow stresses (Nadeau 1969; Seltzer et al. 1972) and changes in the relative strengths of the major slip systems, with critical resolved shear stresses for 1/2<110>{110} and 1/2<110>{111} considerably lower in UO_{2+x} than UO_2 (Yust and McHargue 1971; Keller et al. 1988). In contrast, 1/2<110>{100} slip appears to be relatively insensitive to oxidation.

The increase of the O/U ratio in hyper-stoichiometric is driven by the incorporation of additional oxygen ions at interstitial sites in the UO_2 lattice, rather than the creation of U site vacancies. To maintain charge neutrality, the insertion of an oxygen interstitial results in nearby uranium atoms being oxidized to U^{5+} (Willis 1964; Thorn and Winslow 1966; Willis 1978).Interstitial oxygen atoms are thought to be responsible for the change in the relative strengths of the 1/2<110>{100}, 1/2<110>{110}, and 1/2<110>{111}, as the presence of interstitial oxygen increases the anion density on the glide plane and reduces the barrier to dislocation glide (Ashbee and Yust 1982). Atomic scale simulations find that the critical resolved shear stress decreases with increasing number of defects on the oxygen sub-lattice. (Fossati et al. 2013), but no one has attempted to calculate the Peierls stress, σ_p, for dislocation glide in UO_{2+x} directly.

The PN method, as implemented in `disloPy`, can be used to model the effect of point defect-dislocation interactions on the Peierls stress, as has been attempted in thesis for MgO and forsterite. In Chapter VI, it was established that the PN method can be used to calculate σ_p for the important slip systems in stoichiometric UO_2, obtaining values comparable to those from fully atomistic simulations. It is reasonable to assume, therefore, that it can also be applied to dislocation glide in hyper-stoichiometric UO_2. This would involve constructing γ-lines for the major slip systems from GSF calculations performed with interstitial oxygen defects inserted at the fault plane, charge balanced by nearby U^{5+}, and these γ-lines can be used to parameterize PN calculations.

References

Adams DJ, Oganov AR (2006) Ab initio molecular dynamics study of CaSiO3 perovskite at P-T conditions of Earth's lower mantle. Phys Rev B 73:184106. doi: 10.1103/PhysRevB.73.184106

Ahlquist CN (1975) Solution strengthening of MgO crystals. Journal of Applied Physics 46:14–17 . doi: 10.1063/1.322198

Amodeo J, Carrez P, Devincre B, Cordier P (2011) Multiscale modelling of MgO plasticity. Acta Materialia 59:2291–2301. doi: 10.1016/j.actamat.2010.12.020

Amodeo J, Carrez P, Cordier P (2012) Modelling the effect of pressure on the critical shear stress of MgO single crystals. Philosophical Magazine 92:1523–1541. doi: 10.1080/14786435.2011.652689

Ando J, Shibata Y, Okajima Y, et al. (2001) Striped iron zoning of olivine induced by dislocation creep in deformed peridotites. Nature 414:893–895. doi: 10.1038/414893a

Arey JS, Seaman JC, Bertsch PM (1999) Immob ilization of Uranium in Contaminated Sediments by Hydroxyapatite Addition. Environ Sci Technol 33:337–342. doi: 10.1021/es980425+

Arima T, Yamasaki S, Inagaki Y, Idemitsu K (2005) Evaluation of thermal properties of UO2 and PuO2 by equilibrium molecular dynamics simulations from 300 to 2000 K. Journal of Alloys and Compounds 400:43–50. doi: 10.1016/j.jallcom.2005.04.003

Asadi E, Zaeem MA, Moitra A, Tschopp MA (2014) Effect of vacancy defects on generalized stacking fault energy of fcc metals. J Phys: Condens Matter 26:115404. doi: 10.1088/0953-8984/26/11/115404

Ashbee KHG, Yust CS (1982) A mechanism for the ease of slip in UO2+x. Journal of Nuclear Materials 110:246–250. doi: 10.1016/0022-3115(82)90152-0

Bai Q, Kohlstedt DL (1993) Effects of chemical environment on the solubility and incorporation mechanism for hydrogen in olivine. Phys Chem Minerals 19:460–471. doi: 10.1007/BF00203186

Baranov VG, Lunev AV, Tenishev AV, Khlunov AV (2014) Interaction of dislocations in UO2 during high burn-up structure formation. Journal of Nuclear Materials 444:129–137. doi: 10.1016/j.jnucmat.2013.09.042

Basak CB, Sengupta AK, Kamath HS (2003) Classical molecular dynamics simulation of UO2 to predict thermophysical properties. Journal of Alloys and Compounds 360:210–216. doi: 10.1016/S0925-8388(03)00350-5

Berry AJ, Hermann J, O'Neill HSC, Foran GJ (2005) Fingerprinting the water site in mantle olivine. Geology 33:869–872. doi: 10.1130/G21759.1

Berry AJ, O'Neill HSC, Hermann J, Scott DR (2007a) The infrared signature of water associated with trivalent cations in olivine. Earth and Planetary Science Letters 261:134–142. doi: 10.1016/j.epsl.2007.06.021

Berry AJ, Walker AM, Hermann J, et al. (2007b) Titanium substitution mechanisms in forsterite. Chemical Geology 242:176–186. doi: 10.1016/j.chemgeo.2007.03.010

Bianchini F, Kermode JR, Vita AD (2016) Modelling defects in Ni–Al with EAM and DFT calculations. Modelling Simul Mater Sci Eng 24:045012. doi: 10.1088/0965-0393/24/4/045012

Blöchl PE (1994) Projector augmented-wave method. Phys Rev B 50:17953–17979. doi: 10.1103/PhysRevB.50.17953

Blundy J, Wood B (1994) Prediction of crystal-melt partition coefficients from elastic moduli. Nature 372:452–454. doi: 10.1038/372452a0

Bodinier J-I, Merlet C, Bedini RM, et al (1996) Distribution of niobium, tantalum, and other highly incompatible trace elements in the lithospheric mantle: The spinel paradox. Geochimica et Cosmochimica Acta 60:545–550. doi: 10.1016/0016-7037(95)00431-9

Boioli F, Tommasi A, Cordier P, et al. (2015) Low steady-state stresses in the cold lithospheric mantle inferred from dislocation dynamics models of dislocation creep in olivine. Earth and Planetary Science Letters 432:232–242. doi: 10.1016/j.epsl.2015.10.012

Bolfan-Casanova N, Keppler H, Rubie DC (2003) Water partitioning at 660 km depth and evidence for very low water solubility in magnesium silicate perovskite. Geophys Res Lett 30:1905. doi: 10.1029/2003GL017182

Born M (1940) On the stability of crystal lattices. I. Mathematical Proceedings of the Cambridge Philosophical Society 36:160–172. doi: 10.1017/S0305004100017138

Brantley SL, Crane SR, Crerar DA, et al. (1986) Dissolution at dislocation etch pits in quartz. Geochimica et Cosmochimica Acta 50:2349–2361. doi: 10.1016/0016-7037(86)90087-6

Breitung W (1978) Oxygen self and chemical diffusion coefficients in UO2±x. Journal of Nuclear Materials 74:10–18. doi: 10.1016/0022-3115(78)90527-5

Brice JC (1975) Some thermodynamic aspects of the growth of strained crystals. Journal of Crystal Growth 28:249–253. doi: 10.1016/0022-0248(75)90241-9

Brodholt J (1997) Ab initio calculations on point defects in forsterite (Mg2SiO4) and implications for diffusion and creep. American Mineralogist 82:1049–1053. doi: 10.2138/am-1997-11-1201

Brodholt JP, Refson K (2000) An ab initio study of hydrogen in forsterite and a possible mechanism for hydrolytic weakening. J Geophys Res 105:18977–18982. doi: 10.1029/2000JB900057

Browaeys JT, Chevrot S (2004) Decomposition of the elastic tensor and geophysical applications. Geophys J Int 159:667–678. doi: 10.1111/j.1365-246X.2004.02415.x

Brunet F, Allan DR, Redfern SAT, et al. (1999) Compressibility and thermal expansivity of synthetic apatites, Ca5(PO4)3X with X = OH, F and Cl. European Journal of Mineralogy 11:1023–1036. doi: 10.1127/ejm/11/6/1023

Bulatov V, Cai W (2006) Computer Simulations of Dislocations. OUP Oxford

Bulatov VV, Kaxiras E (1997) Semidiscrete Variational Peierls Framework for Dislocation Core Properties. Phys Rev Lett 78:4221–4224. doi: 10.1103/PhysRevLett.78.4221

Bullough R, Newman RC (1962) The interaction of vacancies with dislocations. The Philosophical Magazine: A Journal of Theoretical Experimental and Applied Physics 7:529–531. doi: 10.1080/14786436208212186

Bullough R, Newman RC (1963) The interaction of impurities with dislocations in silicon and germanium. Progress in semiconductors. 7:99-136.

Cai W, Bulatov VV, Chang J, et al. (2003) Periodic image effects in dislocation modelling. Philosophical Magazine 83:539–567. doi: 10.1080/0141861021000051109

Calderín L, Stott MJ, Rubio A (2003) Electronic and crystallographic structure of apatites. Phys Rev B 67:134106. doi: 10.1103/PhysRevB.67.134106

Caracas R, Wentzcovitch R, Price GD, Brodholt J (2005) CaSiO3 perovskite at lower mantle pressures. Geophys Res Lett 32:L06306. doi: 10.1029/2004GL022144

Carayannis G, Manolakis D, Kalouptsidis N (1983) A fast sequential algorithm for least-squares filtering and prediction. IEEE Transactions on Acoustics, Speech, and Signal Processing 31:1394–1402. doi: 10.1109/TASSP.1983.1164224

Carrez P, Walker AM, Metsue A, Cordier P (2008) Evidence from numerical modelling for 3D spreading of [001] screw dislocations in Mg2SiO4 forsterite. Philosophical Magazine 88:2477–2485. doi: 10.1080/14786430802363804

Carrez P, Ferré D, Cordier P (2009) Peierls–Nabarro modelling of dislocations in MgO from ambient pressure to 100 GPa. Modelling Simul Mater Sci Eng 17:35010. doi: 10.1088/0965-0393/17/3/035010

Carrez P, Godet J, Cordier P (2015) Atomistic simulations of ½〈1 1 0〉 screw dislocation core in magnesium oxide. Computational Materials Science 103:250–255. doi: 10.1016/j.commatsci.2014.10.019

Catlow CRA, Faux ID, Norgett MJ (1976) Shell and breathing shell model calculations for defect formation energies and volumes in magnesium oxide. J Phys C: Solid State Phys 9:419. doi: 10.1088/0022-3719/9/3/008

Chang Y-Y, Jacobsen SD, Bina CR, et al. (2015) Comparative compressibility of hydrous wadsleyite and ringwoodite: Effect of H2O and implications for detecting water in the transition zone. J Geophys Res Solid Earth 120:2015JB012123. doi: 10.1002/2015JB012123

Chen J, Inoue T, Weidner DJ, et al. (1998) Strength and water weakening of mantle minerals, olivine, wadsleyite and ringwoodite. Geophys Res Lett 25:575–578. doi: 10.1029/98GL00043

Chen J, Inoue T, Yurimoto H, Weidner DJ (2002) Effect of water on olivine-wadsleyite phase boundary in the (Mg, Fe)2SiO4 system. Geophys Res Lett 29:1875. doi: 10.1029/2001GL014429

Chen S, Hiraga T, Kohlstedt DL (2006) Water weakening of clinopyroxene in the dislocation creep regime. J Geophys Res 111:B08203. doi: 10.1029/2005JB003885

Christian JW, Vítek V (1970) Dislocations and stacking faults. Rep Prog Phys 33:307. doi: 10.1088/0034-4885/33/1/307

Clark SJ, Segall MD, Pickard CJ, et al. (2009) First principles methods using CASTEP. Zeitschrift für Kristallographie - Crystalline Materials 220:567–570. doi: 10.1524/zkri.220.5.567.65075

Clouet E (2006) The vacancy–edge dislocation interaction in fcc metals: A comparison between atomic simulations and elasticity theory. Acta Materialia 54:3543–3552. doi: 10.1016/j.actamat.2006.03.043

Clouet E (2009) Elastic energy of a straight dislocation and contribution from core tractions. Philosophical Magazine 89:1565–1584. doi: 10.1080/14786430902976794

Clouet E (2011) Dislocation core field. I. Modeling in anisotropic linear elasticity theory. Phys Rev B 84:224111. doi: 10.1103/PhysRevB.84.224111

Clouet E, Garruchet S, Nguyen H, et al. (2008) Dislocation interaction with C in α-Fe: A comparison between atomic simulations and elasticity theory. Acta Materialia 56:3450–3460. doi: 10.1016/j.actamat.2008.03.024

Comodi P, Liu Y (2000) CO3 substitution in apatite. European Journal of Mineralogy 12:965–974. doi: 10.1127/0935-1221/2000/0012-0965

Cooper MWD, Rushton MJD, Grimes RW (2014) A many-body potential approach to modelling the thermomechanical properties of actinide oxides. J Phys: Condens Matter 26:105401. doi: 10.1088/0953-8984/26/10/105401

Cordier P, Amodeo J, Carrez P (2012) Modelling the rheology of MgO under Earth/'s mantle pressure, temperature and strain rates. Nature 481:177–180. doi: 10.1038/nature10687

Cordier P, Demouchy S, Beausir B, et al. (2014) Disclinations provide the missing mechanism for deforming olivine-rich rocks in the mantle. Nature 507:51–56. doi: 10.1038/nature13043

Corgne A, Liebske C, Wood BJ, et al. (2005) Silicate perovskite-melt partitioning of trace elements and geochemical signature of a deep perovskitic reservoir. Geochimica et Cosmochimica Acta 69:485–496. doi: 10.1016/j.gca.2004.06.041

Costa F, Chakraborty S (2008) The effect of water on Si and O diffusion rates in olivine and implications for transport properties and processes in the upper mantle. Physics of the Earth and Planetary Interiors 166:11–29. doi: 10.1016/j.pepi.2007.10.006

Cottrell AH, Bilby BA (1949) Dislocation Theory of Yielding and Strain Ageing of Iron. Proc Phys Soc A 62:49. doi: 10.1088/0370-1298/62/1/308

Couvy H, Frost DJ, Heidelbach F, et al. (2004) Shear deformation experiments of forsterite at 11 GPa - 1400°C in the multianvil apparatus. European Journal of Mineralogy 16:877–889. doi: 10.1127/0935-1221/2004/0016-0877

Dai L, Karato S (2009) Electrical conductivity of wadsleyite at high temperatures and high pressures. Earth and Planetary Science Letters 287:277–283. doi: 10.1016/j.epsl.2009.08.012

Dal Corso A (2014) Pseudopotentials periodic table: From H to Pu. Computational Materials Science 95:337–350. doi: 10.1016/j.commatsci.2014.07.043

Demichelis R, Civalleri B, D'Arco P, Dovesi R (2010) Performance of 12 DFT functionals in the study of crystal systems: Al2SiO5 orthosilicates and Al hydroxides as a case study. Int J Quantum Chem 110:2260–2273. doi: 10.1002/qua.22574

Demontis P, Spanu S, Suffritti GB (2001) Application of the Wolf method for the evaluation of Coulombic interactions to complex condensed matter systems: Aluminosilicates and water. The Journal of Chemical Physics 114:7980–7988. doi: 10.1063/1.1364638

Demouchy S, Tommasi A, Boffa Ballaran T, Cordier P (2013) Low strength of Earth's uppermost mantle inferred from tri-axial deformation experiments on dry olivine crystals. Physics of the Earth and Planetary Interiors 220:37–49. doi: 10.1016/j.pepi.2013.04.008

Denoual C (2004) Dynamic dislocation modeling by combining Peierls Nabarro and Galerkin methods. Phys Rev B 70:24106. doi: 10.1103/PhysRevB.70.024106

Dick BG, Overhauser AW (1958) Theory of the Dielectric Constants of Alkali Halide Crystals. Phys Rev 112:90–103. doi: 10.1103/PhysRev.112.90

Dobson DP, Brodholt JP (2000) The electrical conductivity of the lower mantle phase magnesiowüstite at high temperatures and pressures. J Geophys Res 105:531–538. doi: 10.1029/1999JB900242

Durinck J, Legris A, Cordier P (2005) Pressure sensitivity of olivine slip systems: first-principle calculations of generalised stacking faults. Phys Chem Minerals 32:646–654. doi: 10.1007/s00269-005-0041-2

Durinck J, Carrez P, Cordier P (2007) Application of the Peierls-Nabarro model to dislocations in forsterite. European Journal of Mineralogy 19:631–639. doi: 10.1127/0935-1221/2007/0019-1757

Elliott JC, Mackie PE, Young RA (1973) Monoclinic Hydroxyapatite. Science 180:1055–1057. doi: 10.1126/science.180.4090.1055

Elsinger EC, Leal L (1996) Coralline hydroxyapatite bone graft substitutes. The Journal of Foot and Ankle Surgery 35:396–399. doi: 10.1016/S1067-2516(96)80058-5

Eshelby JD, Read WT, Shockley W (1953) Anisotropic elasticity with applications to dislocation theory. Acta Metallurgica 1:251–259. doi: 10.1016/0001-6160(53)90099-6

Evans B, Goetze C (1979) The temperature variation of hardness of olivine and its implication for polycrystalline yield stress. J Geophys Res 84:5505–5524. doi: 10.1029/JB084iB10p05505

Faul UH, Cline II CJ, David EC, et al. (2016) Titanium-hydroxyl defect-controlled rheology of the Earth's upper mantle. Earth and Planetary Science Letters 452:227–237. doi: 10.1016/j.epsl.2016.07.016

Faul UH, CIine II CJ, Berry A, et al. (2017) Constraints on oxygen fugacity within metal capsules. Phys Chem Minerals 1–13. doi: 10.1007/s00269-017-0937-7

Fei H, Wiedenbeck M, Yamazaki D, Katsura T (2013) Small effect of water on upper-mantle rheology based on silicon self-diffusion coefficients. Nature 498:213–215. doi: 10.1038/nature12193

Fleet ME, Liu X (2007) Letter: Hydrogen-carbonate ion in synthetic high-pressure apatite. American Mineralogist 92:1764–1767. doi: 10.2138/am.2007.2716

Fleet ME, Liu X, Shieh SR (2010) Structural change in lead fluorapatite at high pressure. Phys Chem Minerals 37:1–9. doi: 10.1007/s00269-009-0305-3

Foitzik A, Skrotzki W, Haasen P (1989) Correlation between microstructure, dislocation dissociation and plastic anisotropy in ionic crystals. Materials Science and Engineering: A 113:399–407. doi: 10.1016/0921-5093(89)90326-2

Fossati P, Van Brutzel L, Devincre B (2013) Molecular dynamics simulation of dislocations in uranium dioxide. Journal of Nuclear Materials 443:359–365. doi: 10.1016/j.jnucmat.2013.07.059

Gaetani GA, Grove TL (1998) The influence of water on melting of mantle peridotite. Contrib Mineral Petrol 131:323–346. doi: 10.1007/s004100050396

Gale JD (1997) GULP: A computer program for the symmetry-adapted simulation of solids. J Chem Soc, Faraday Trans 93:629–637. doi: 10.1039/A606455H

Gale JD, Rohl AL (2003) The General Utility Lattice Program (GULP). Molecular Simulation 29:291–341. doi: 10.1080/0892702031000104887

Gdoutos EE, Agrawal R, Espinosa HD (2010) Comparison of the Ewald and Wolf methods for modeling electrostatic interactions in nanowires. Int J Numer Meth Engng 84:1541–1551. doi: 10.1002/nme.2948

Giannozzi P, Baroni S, Bonini N, et al. (2009) QUANTUM ESPRESSO: a modular and open-source software project for quantum simulations of materials. J Phys: Condens Matter 21:395502. doi: 10.1088/0953-8984/21/39/395502

Girard J, Jihua C, Raterron P (2012) Deformation of periclase single crystals at high pressure and temperature: Quantification of the effect of pressure on slip-system activities. Journal of Applied Physics 111:112607 . doi: 10.1063/1.4726200

Girard J, Chen J, Raterron P, Holyoke CW (2013) Hydrolytic weakening of olivine at mantle pressure: Evidence of [100](010) slip system softening from single-crystal deformation experiments. Physics of the Earth and Planetary Interiors 216:12–20. doi: 10.1016/j.pepi.2012.10.009

Girard J, Amulele G, Farla R, et al. (2016) Shear deformation of bridgmanite and magnesiowüstite aggregates at lower mantle conditions. Science 351:144–147. doi: 10.1126/science.aad3113

Goel P, Choudhury N, Chaplot SL (2008) Atomistic modeling of the vibrational and thermodynamic properties of uranium dioxide, UO2. Journal of Nuclear Materials 377:438–443. doi: 10.1016/j.jnucmat.2008.03.020

Goyal A, Rudzik T, Deng B, et al. (2013) Segregation of ruthenium to edge dislocations in uranium dioxide. Journal of Nuclear Materials 441:96–102. doi: 10.1016/j.jnucmat.2013.05.031

Grimes RW, Catlow CRA (1991) The stability of fission products in uranium dioxide. Phil Trans R Soc Lond A 335:609–634. doi: 10.1098/rsta.1991.0062

Grimme S (2006) Semiempirical GGA-type density functional constructed with a long-range dispersion correction. J Comput Chem 27:1787–1799. doi: 10.1002/jcc.20495

Grønvold F, Kveseth NJ, Sveen A, Tichý J (1970) Thermodynamics of the UO2+x phase I. Heat capacities of UO2.017 and UO2.254 from 300 to 1000 K and electronic contributions. The Journal of Chemical Thermodynamics 2:665–679. doi: 10.1016/0021-9614(70)90042-X

Hansen LN, Zimmerman ME, Kohlstedt DL (2011) Grain boundary sliding in San Carlos olivine: Flow law parameters and crystallographic-preferred orientation. J Geophys Res 116:B08201. doi: 10.1029/2011JB008220

Hansen LN, Zimmerman ME, Kohlstedt DL (2012a) Laboratory measurements of the viscous anisotropy of olivine aggregates. Nature 492:415. doi: 10.1038/nature11671

Hansen LN, Zimmerman ME, Kohlstedt DL (2012b) The influence of microstructure on deformation of olivine in the grain-boundary sliding regime. J Geophys Res 117:B09201. doi: 10.1029/2012JB009305

Hartley CS, Mishin Y (2005a) Characterization and visualization of the lattice misfit associated with dislocation cores. Acta Materialia 53:1313–1321. doi: 10.1016/j.actamat.2004.11.027

Hartley CS, Mishin Y (2005) Representation of dislocation cores using Nye tensor distributions. Materials Science and Engineering: A 400–401:18–21. doi: 10.1016/j.msea.2005.03.076

Hazen RM, Finger LW (1979) Bulk modulus—volume relationship for cation-anion polyhedra. J Geophys Res 84:6723–6728. doi: 10.1029/JB084iB12p06723

He Q, Liu X, Hu X, et al. (2012) Solid solutions between lead fluorapatite and lead fluorvanadate apatite: compressibility determined by using a diamond-anvil cell coupled with synchrotron X-ray diffraction. Phys Chem Minerals 39:219–226. doi: 10.1007/s00269-011-0477-5

Henkelman G, Uberuaga BP, Harris DJ, et al. (2005) MgO addimer diffusion on MgO(100): A comparison of *ab initio* and empirical models. Phys Rev B 72:115437. doi: 10.1103/PhysRevB.72.115437

Hernández ER, Alfè D, Brodholt J (2013) The incorporation of water into lower-mantle perovskites: A first-principles study. Earth and Planetary Science Letters 364:37–43. doi: 10.1016/j.epsl.2013.01.005

Heuser BJ, Trinkle DR, Jalarvo N, et al. (2014) Direct Measurement of Hydrogen Dislocation Pipe Diffusion in Deformed Polycrystalline Pd Using Quasielastic Neutron Scattering. Phys Rev Lett 113:025504. doi: 10.1103/PhysRevLett.113.025504

Hilairet N, Wang Y, Sanehira T, et al. (2012) Deformation of olivine under mantle conditions: An in situ high-pressure, high-temperature study using monochromatic synchrotron radiation. J Geophys Res 117:B01203. doi: 10.1029/2011JB008498

Hill R (1952) The Elastic Behaviour of a Crystalline Aggregate. Proc Phys Soc A 65:349. doi: 10.1088/0370-1298/65/5/307

Hiraga T, Anderson IM, Kohlstedt DL (2003) Chemistry of grain boundaries in mantle rocks. American Mineralogist 88:1015–1019

Hiraga T, Anderson IM, Kohlstedt DL (2004) Grain boundaries as reservoirs of incompatible elements in the Earth's mantle. Nature 427:699–703. doi: 10.1038/nature02259

Hirth JP, Lothe J (1982) Theory of Dislocations, 2nd edn. John Wiley & Sons, Inc., USA

Hochrein O, Kniep R, Zahn D (2005) Atomistic Simulation Study of the Order/Disorder (Monoclinic to Hexagonal) Phase Transition of Hydroxyapatite. Chem Mater 17:1978–1981. doi: 10.1021/cm0401903

Hohenberg P, Kohn W (1964) Inhomogeneous Electron Gas. Phys Rev 136:B864–B871. doi: 10.1103/PhysRev.136.B864

Hÿtch MJ, Putaux J-L, Pénisson J-M (2003) Measurement of the displacement field of dislocations to 0.03 Å by electron microscopy. Nature 423:270. doi: 10.1038/nature01638

Idrissi H, Bollinger C, Boioli F, et al. (2016) Low-temperature plasticity of olivine revisited with in situ TEM nanomechanical testing. Science Advances 2:e1501671. doi: 10.1126/sciadv.1501671

Ikoma T, Yamazaki A, Nakamura S, Akao M (1999) Preparation and Structure Refinement of Monoclinic Hydroxyapatite. Journal of Solid State Chemistry 144:272–276. doi: 10.1006/jssc.1998.8120

Ingle KW, Crocker AG (1978) The interaction between vacancies and the ½〈111〉 {11¯0} edge dislocation in body centred cubic metals. Acta Metallurgica 26:1461–1469. doi: 10.1016/0001-6160(78)90161-X

Inoue T, Wada T, Sasaki R, Yurimoto H (2010) Water partitioning in the Earth's mantle. Physics of the Earth and Planetary Interiors 183:245–251. doi: 10.1016/j.pepi.2010.08.003

Ionov DA, Hofmann AW, Merlet C, et al. (2006) Discovery of whitlockite in mantle xenoliths: Inferences for water- and halogen-poor fluids and trace element residence in the terrestrial upper mantle. Earth and Planetary Science Letters 244:201–217. doi: 10.1016/j.epsl.2006.02.012

Ismail-Beigi S, Arias TA (2000) Ab Initio. Phys Rev Lett 84:1499–1502. doi: 10.1103/PhysRevLett.84.1499

Issa I, Amodeo J, Réthoré J, et al. (2015) In situ investigation of MgO nanocube deformation at room temperature. Acta Materialia 86:295–304. doi: 10.1016/j.actamat.2014.12.001

Jackson I, Faul UH, Skelton R (2014) Elastically accommodated grain-boundary sliding: New insights from experiment and modeling. Physics of the Earth and Planetary Interiors 228:203–210. doi: 10.1016/j.pepi.2013.11.014

Joachim B, Wohlers A, Norberg N, et al. (2012) Diffusion and solubility of hydrogen and water in periclase. Phys Chem Minerals 40:19–27. doi: 10.1007/s00269-012-0542-8

Jaoul O, Bertran-Alvarez Y, Liebermann RC, Price GD (1995) Fe–Mg interdiffusion in olivine up to 9 GPa at T = 600–900°C; experimental data and comparison with defect calculations. Physics of the Earth and Planetary Interiors 89:199–218. doi: 10.1016/0031-9201(94)03008-7

Jung H, Karato S (2001) Water-Induced Fabric Transitions in Olivine. Science 293:1460–1463 . doi: 10.1126/science.1062235

Jung H, Mo W, Green HW (2009) Upper mantle seismic anisotropy resulting from pressure-induced slip transition in olivine. Nature Geosci 2:73–77. doi: 10.1038/ngeo389

Jung DY, Oganov AR (2005) Ab initio study of the high-pressure behavior of CaSiO3 perovskite. Phys Chem Minerals 32:146–153. doi: 10.1007/s00269-005-0453-z

Karato S (2014) Some remarks on the origin of seismic anisotropy in the D” layer. Earth, Planets and Space 50:1019. doi: 10.1186/BF03352196

Karato S, Spetzler HA (1990) Defect microdynamics in minerals and solid-state mechanisms of seismic wave attenuation and velocity dispersion in the mantle. Rev Geophys 28:399–421. doi: 10.1029/RG028i004p00399

Karato S, Wu P (1993) Rheology of the Upper Mantle: A Synthesis. Science 260:771–778. doi: 10.1126/science.260.5109.771

Karki BB, Crain J (1998) First-principles determination of elastic properties of CaSiO3 perovskite at lower mantle pressures. Geophys Res Lett 25:2741–2744. doi: 10.1029/98GL51952

Karki BB, Ghosh DB, Verma AK (2015) First-principles prediction of pressure-enhanced defect segregation and migration at MgO grain boundaries. American Mineralogist 100:1053–1058 . doi: 10.2138/am-2015-5143

Karki BB, Khanduja G (2006) Vacancy defects in MgO at high pressure. American Mineralogist 91:511–516. doi: 10.2138/am.2006.1998

Karki BB, Wentzcovitch RM, Gironcoli S de, Baroni S (1999) First-Principles Determination of Elastic Anisotropy and Wave Velocities of MgO at Lower Mantle Conditions. Science 286:1705–1707. doi: 10.1126/science.286.5445.1705

Katayama I, Jung H, Karato S (2004) New type of olivine fabric from deformation experiments at modest water content and low stress. Geology 32:1045–1048. doi: 10.1130/G20805.1

Katayama I, Karato S, Brandon M (2005) Evidence of high water content in the deep upper mantle inferred from deformation microstructures. Geology 33:613–616. doi: 10.1130/G21332.1

Katayama I, Karato S (2008) Low-temperature, high-stress deformation of olivine under water-saturated conditions. Physics of the Earth and Planetary Interiors 168:125–133. doi: 10.1016/j.pepi.2008.05.019

Keller RJ, Mitchell TE, Heuer AH (1988) Plastic deformation in nonstoichiometric UO2+x single crystals—I. Deformation at low temperatures. Acta Metallurgica 36:1061–1071. doi: 10.1016/0001-6160(88)90160-5

Kelley KA, Cottrell E (2009) Water and the Oxidation State of Subduction Zone Magmas. Science 325:605–607. doi: 10.1126/science.1174156

Kirfel A, Lippmann T, Blaha P, et al. (2005) Electron density distribution and bond critical point properties for forsterite, Mg2 SiO4, determined with synchrotron single crystal X-ray diffraction data. Phys Chem Minerals 32:301–313. doi: 10.1007/s00269-005-0468-5

Kohlstedt DL, Keppler H, Rubie DC (1996) Solubility of water in the α, β and γ phases of (Mg,Fe)2SiO4. Contrib Mineral Petrol 123:345–357. doi: 10.1007/s004100050161

Kohn W, Sham LJ (1965) Self-Consistent Equations Including Exchange and Correlation Effects. Phys Rev 140:A1133–A1138. doi: 10.1103/PhysRev.140.A1133

Kocks UF, Argon AS, Ashby MF (1975) Thermodynamics and knetics of slip. Pergamon Press, Oxford

Koizumi H, Kirchner HOK, Suzuki T (1993) Kink pair nucleation and critical shear stress. Acta Metallurgica et Materialia 41:3483–3493. doi: 10.1016/0956-7151(93)90228-K

König S, Lissner M, Lorand J-P, et al. (2015) Mineralogical control of selenium, tellurium and highly siderophile elements in the Earth's mantle: Evidence from mineral separates of ultra-depleted mantle residues. Chemical Geology 396:16–24. doi: 10.1016/j.chemgeo.2014.12.015

Konzett J, Frost DJ (2009) The High P–T Stability of Hydroxyl-apatite in Natural and Simplified MORB—an Experimental Study to 15 GPa with Implications for Transport and Storage of Phosphorus and Halogens in Subduction Zones. J Petrology 50:2043–2062. doi: 10.1093/petrology/egp068

Konzett J, Rhede D, Frost DJ (2012) The high PT stability of apatite and Cl partitioning between apatite and hydrous potassic phases in peridotite: an experimental study to 19 GPa with implications for the transport of P, Cl and K in the upper mantle. Contrib Mineral Petrol 163:277–296. doi: 10.1007/s00410-011-0672-x

Kranjc K, Rouse Z, Flores KM, Skemer P (2016) Low-temperature plastic rheology of olivine determined by nanoindentation. Geophys Res Lett 43:2015GL065837. doi: 10.1002/2015GL065837

Kröger FA, Vink HJ (1956) Relations between the Concentrations of Imperfections in Crystalline Solids. Solid State Physics 3:307–435. doi: 10.1016/S0081-1947(08)60135-6

Kronenberg AK, Tullis J (1984) Flow strengths of quartz aggregates: Grain size and pressure effects due to hydrolytic weakening. J Geophys Res 89:4281–4297. doi: 10.1029/JB089iB06p04281

Kudoh Y, Inoue T, Arashi H (1996) Structure and crystal chemistry of hydrous wadsleyite, Mg1.75SiH0.5O4: possible hydrous magnesium silicate in the mantle transition zone. Phys Chem Minerals 23:461–469. doi: 10.1007/BF00202032

Kunz M, Leinenweber K, Parise JB, et al. (1996) The baddeleyite-type high pressure phase of Ca(OH)2. High Pressure Research 14:311–319. doi: 10.1080/08957959608201416

Lauzier J, Hillairet J, Vieux-Champagne A, Benoit W (1989) The vacancies, lubrication agents of dislocation motion in aluminium. J Phys: Condens Matter 1:9273. doi: 10.1088/0953-8984/1/47/001Lee KKM, Steinle-Neumann G, Akber-Knutson S (2009) Ab initio predictions of potassium partitioning between Fe and Al-bearing MgSiO3 perovskite and post-perovskite. Physics of the Earth and Planetary Interiors 174:247–253. doi: 10.1016/j.pepi.2008.09.003

Lee KKM, O'Neill B, Panero WR, et al (2004) Equations of state of the high-pressure phases of a natural peridotite and implications for the Earth's lower mantle. Earth and Planetary Science Letters 223:381–393. doi: 10.1016/j.epsl.2004.04.033

de Leeuw NH (2001) Density Functional Theory Calculations of Hydrogen-Containing Defects in Forsterite, Periclase, and α-Quartz. J Phys Chem B 105:9747–9754. doi: 10.1021/jp0109978

de Leeuw NH (2010) Computer simulations of structures and properties of the biomaterial hydroxyapatite. Journal of Materials Chemistry 20:5376–5389. doi: 10.1039/B921400C

de Leeuw NH, Parker SC, Catlow CRA, Price GD (2000) Modelling the effect of water on the surface structure and stability of forsterite. Phys Chem Min 27:332–341. doi: 10.1007/s002690050262

Lemaire C, Kohn SC, Brooker RA (2004) The effect of silica activity on the incorporation mechanisms of water in synthetic forsterite: a polarised infrared spectroscopic study. Contrib Mineral Petrol 147:48–57. doi: 10.1007/s00410-003-0539-x

Leslie M, Gillan MJ (1985) The energy and elastic dipole tensor of defects in ionic crystals calculated by the supercell method. J Phys C: Solid State Phys 18:973. doi: 10.1088/0022-3719/18/5/005

Lewis GV, Catlow CRA (1985) Potential models for ionic oxides. J Phys C: Solid State Phys 18:1149. doi: 10.1088/0022-3719/18/6/010

Li JCM (1972) Disclination model of high angle grain boundaries. Surface Science 31:12–26. doi: 10.1016/0039-6028(72)90251-8

Li B, Kung J, Liu W, Liebermann RC (2014) Phase transition and elasticity of enstatite under pressure from experiments and first-principles studies. Physics of the Earth and Planetary Interiors 228:63–74. doi: 10.1016/j.pepi.2013.11.009

Liao H, Xu Z (2015) Approaches to manage hesitant fuzzy linguistic information based on the cosine distance and similarity measures for HFLTSs and their application in qualitative decision making. Expert Systems with Applications 42:5328–5336. doi: 10.1016/j.eswa.2015.02.017

Lim SC, Baikie T, Pramana SS, et al. (2011) Apatite metaprism twist angle (φ) as a tool for crystallochemical diagnosis. Journal of Solid State Chemistry 184:2978–2986. doi: 10.1016/j.jssc.2011.08.031

Liu YH, Ma YM, He Z, et al. (2007) Phase transition and optical properties of CaCl 2 under high pressure by ab initio pseudopotential plane-wave calculations. J Phys: Condens Matter 19:425225. doi: 10.1088/0953-8984/19/42/425225

Liu L, Du J, Zhao J, et al. (2009) Elastic properties of hydrous forsterites under high pressure: First-principle calculations. Physics of the Earth and Planetary Interiors 176:89–97. doi: 10.1016/j.pepi.2009.04.004

Liu X, Fleet ME, Shieh SR, He Q (2011) Synthetic lead bromapatite: X-ray structure at ambient pressure and compressibility up to about 20 GPa. Phys Chem Minerals 38:397–406. doi: 10.1007/s00269-010-0413-0

Liu L, Wu XZ, Wang R, et al. (2012) High-pressure effect on elastic constants, stacking fault energy and correlation with dislocation properties in MgO and CaO. Eur Phys J B 85:1–10. doi: 10.1140/epjb/e2012-30032-4

Lorand J-P, Alard O (2010) Determination of selenium and tellurium concentrations in Pyrenean peridotites (Ariege, France): New insight into S/Se/Te systematics of the upper in mantle samples. Chemical Geology 278:120–130. doi: 10.1016/j.chemgeo.2010.09.007

Lu G, Zhang Q, Kioussis N, Kaxiras E (2001) Hydrogen-Enhanced Local Plasticity in Aluminum: An Ab Initio Study. Phys Rev Lett 87:95501. doi: 10.1103/PhysRevLett.87.095501

Lu G, Kaxiras E (2002) Can Vacancies Lubricate Dislocation Motion in Aluminum? Phys Rev Lett 89:105501. doi: 10.1103/PhysRevLett.89.105501

Lunev AV, Kuksin AY, Starikov SV (2017) Glide mobility of the 1/2[1 1 0](0 0 1) edge dislocation in UO2 from molecular dynamics simulation. International Journal of Plasticity 89:85–95. doi: 10.1016/j.ijplas.2016.11.004

Luo F, Cheng Y, Cai L-C, Chen X-R (2013) Structure and thermodynamic properties of BeO: Empirical corrections in the quasiharmonic approximation. Journal of Applied Physics 113:033517. doi: 10.1063/1.4776679

Ma G, Liu XY (2009) Hydroxyapatite: Hexagonal or Monoclinic? Crystal Growth & Design 9:2991–2994. doi: 10.1021/cg900156w

MacInnis IN, Brantley SL (1992) The role of dislocations and surface morphology in calcite dissolution. Geochimica et Cosmochimica Acta 56:1113–1126. doi: 10.1016/0016-7037(92)90049-O

Mackie PE, Elliot JC, Young RA (1972) Monoclinic structure of synthetic Ca5(PO4)3Cl, chlorapatite. Acta Crystallographica Section B Structural Crystallography and Crystal Chemistry 28:1840–1848. doi: 10.1107/S0567740872005114

Mackwell SJ, Kohlstedt DL, Paterson MS (1985) The role of water in the deformation of olivine single crystals. J Geophys Res 90:11319–11333. doi: 10.1029/JB090iB13p11319

Madi K, Forest S, Cordier P, Boussuge M (2005) Numerical study of creep in two-phase aggregates with a large rheology contrast: Implications for the lower mantle. Earth and Planetary Science Letters 237:223–238. doi: 10.1016/j.epsl.2005.06.027

Mahendran S, Carrez P, Groh S, Cordier P (2017) Dislocation modelling in Mg 2 SiO 4 forsterite: an atomic-scale study based on the THB1 potential. Modelling Simul Mater Sci Eng 25:054002. doi: 10.1088/1361-651X/aa6efa

Mainprice D, Tommasi A, Couvy H, et al. (2005) Pressure sensitivity of olivine slip systems and seismic anisotropy of Earth's upper mantle. Nature 433:731. doi: 10.1038/nature03266

Mao Z, Jacobsen SD, Jiang F, et al. (2008) Single-crystal elasticity of wadsleyites, β-Mg2SiO4, containing 0.37–1.66 wt.% H2O. Earth and Planetary Science Letters 266:78–89. doi: 10.1016/j.epsl.2007.10.045

Margheriti L, Nostro C, Cocco M, Amato A (1996) Seismic anisotropy beneath the Northern Apennines (Italy) and its tectonic implications. Geophys Res Lett 23:2721–2724. doi: 10.1029/96GL02519

Marquardt H, Speziale S, Reichmann HJ, et al. (2009) Elastic Shear Anisotropy of Ferropericlase in Earth's Lower Mantle. Science 324:224–226. doi: 10.1126/science.1169365

Marquardt K, Faul UH (2018) The structure and composition of olivine grain boundaries: 40 years of studies, status and current developments. Phys Chem Minerals 1–34. doi: 10.1007/s00269-017-0935-9

Martin RF, Donnay G (1972) Hydroxyl in the mantle. American Mineralogist **57:**554–570

McLean M, Hirth JP (1968) On the equilibrium shape of dislocation etch pits. Surface Science 11:25–36. doi: 10.1016/0039-6028(68)90036-8

Mei S, Kohlstedt DL (2000) Influence of water on plastic deformation of olivine aggregates: 1. Diffusion creep regime. J Geophys Res 105:21457–21469. doi: 10.1029/2000JB900179

Menéndez-Proupin E, Cervantes-Rodríguez S, Osorio-Pulgar R, et al. (2011) Computer simulation of elastic constants of hydroxyapatite and fluorapatite. Journal of the Mechanical Behavior of Biomedical Materials 4:1011–1020. doi: 10.1016/j.jmbbm.2011.03.001

Merkel S, Wenk HR, Badro J, et al. (2003) Deformation of (Mg0.9,Fe0.1)SiO3 Perovskite aggregates up to 32 GPa. Earth and Planetary Science Letters 209:351–360. doi: 10.1016/S0012-821X(03)00098-0

Merli M, Bonadiman C, Diella V, Pavese A (2016) Lower mantle hydrogen partitioning between periclase and perovskite: A quantum chemical modelling. Geochimica et Cosmochimica Acta 173:304–318. doi: 10.1016/j.gca.2015.10.025

Metsue A, Carrez P, Denoual C, et al. (2010) Plastic deformation of wadsleyite: IV Dislocation core modelling based on the Peierls–Nabarro–Galerkin model. Acta Materialia 58:1467–1478 . doi: 10.1016/j.actamat.2009.10.047

Metzger T, Höpler R, Born E, et al. (1998) Defect structure of epitaxial GaN films determined by transmission electron microscopy and triple-axis X-ray diffractometry. Philosophical Magazine A 77:1013–1025. doi: 10.1080/01418619808221225

Miller MK (2006) Atom probe tomography characterization of solute segregation to dislocations and interfaces. J Mater Sci 41:7808–7813. doi: 10.1007/s10853-006-0518-5

Miyagi L, Wenk H-R (2016) Texture development and slip systems in bridgmanite and bridgmanite + ferropericlase aggregates. Phys Chem Minerals 43:597–613 . doi: 10.1007/s00269-016-0820-y

Miyazaki T, Sueyoshi K, Hiraga T (2013) Olivine crystals align during diffusion creep of Earth/’s upper mantle. Nature 502:321–326. doi: 10.1038/nature12570

Mizukami T, Wallis SR, Yamamoto J (2004) Natural examples of olivine lattice preferred orientation patterns with a flow-normal a-axis maximum. Nature 427:432–436. doi: 10.1038/nature02179

Momma K, Izumi F (2011) *VESTA 3* for three-dimensional visualization of crystal, volumetric and morphology data. Journal of Applied Crystallography 44:1272–1276. doi: 10.1107/S0021889811038970

Monkhorst HJ, Pack JD (1976) Special points for Brillouin-zone integrations. Phys Rev B 13:5188–5192. doi: 10.1103/PhysRevB.13.5188

Moore WR, Graves SE, Bain GI (2001) Synthetic bone graft substitutes. ANZ Journal of Surgery 71:354–361. doi: 10.1046/j.1440-1622.2001.02128.x

Morelon N-D, Ghaleb D, Delaye J-M, Van Brutzel L (2003) A new empirical potential for simulating the formation of defects and their mobility in uranium dioxide. Philosophical Magazine 83:1533–1555. doi: 10.1080/1478643031000091454

Mouhat F, Coudert F-X (2014) Necessary and sufficient elastic stability conditions in various crystal systems. Phys Rev B 90:224104. doi: 10.1103/PhysRevB.90.224104

Murakami M, Hirose K, Yurimoto H, et al. (2002) Water in Earth's Lower Mantle. Science 295:1885–1887. doi: 10.1126/science.1065998

Murayama JK, Nakai S, Kato M, Kumazawa M (1986) A dense polymorph of Ca3(PO4)2: a high pressure phase of apatite decomposition and its geochemical significance. Physics of the Earth and Planetary Interiors 44:293–303. doi: 10.1016/0031-9201(86)90057-9

Murphy ST, Rushton MJD, Grimes RW (2014) A comparison of empirical potential models for the simulation of dislocations in uranium dioxide. Progress in Nuclear Energy 72:27–32. doi: 10.1016/j.pnucene.2013.09.010

Nabarro FRN (1947) Dislocations in a simple cubic lattice. Proc Phys Soc 59:256. doi: 10.1088/0959-5309/59/2/309

Nabarro FRN (1997) Fifty-year study of the Peierls-Nabarro stress. Materials Science and Engineering: A 234:67–76. doi: 10.1016/S0921-5093(97)00184-6

Nadeau JS (1969) Dependence of Flow Stress on Nonstoichiometry in Oxygen-Rich Uranium Dioxide at High Temperatures. Journal of the American Ceramic Society 52:1–7. doi: 10.1111/j.1151-2916.1968.tb11863.x-i1

Nakamura A, Schmalzried H (1983) On the nonstoichiometry and point defects of olivine. Phys Chem Minerals 10:27–37. doi: 10.1007/BF01204323

Nazarov AA, Shenderova OA, Brenner DW (2000a) Elastic models of symmetrical 〈001〉 and 〈011〉 tilt grain boundaries in diamond. Phys Rev B 61:928–936. doi: 10.1103/PhysRevB.61.928

Nazarov AA, Shenderova OA, Brenner DW (2000b) On the disclination-structural unit model of grain boundaries. Materials Science and Engineering: A 281:148–155. doi: 10.1016/S0921-5093(99)00727-3

Nerikar PV, Parfitt DC, Casillas Trujillo LA, et al. (2011) Segregation of xenon to dislocations and grain boundaries in uranium dioxide. Phys Rev B 84:174105. doi: 10.1103/PhysRevB.84.174105

Nguyen HV, Bai L (2010) Cosine Similarity Metric Learning for Face Verification. In: Computer Vision – ACCV 2010. Springer, Berlin, Heidelberg, pp 709–720

Nogita K, Une K (1995) Irradiation-induced recrystallization in high burnup UO2 fuel. Journal of Nuclear Materials 226:302–310. doi: 10.1016/0022-3115(95)00123-9

Ohuchi T, Kawazoe T, Nishihara Y, et al. (2011) High pressure and temperature fabric transitions in olivine and variations in upper mantle seismic anisotropy. Earth and Planetary Science Letters 304:55–63. doi: 10.1016/j.epsl.2011.01.015

Ohuchi T, Kawazoe T, Nishihara Y, Irifune T (2012) Change of olivine a-axis alignment induced by water: Origin of seismic anisotropy in subduction zones. Earth and Planetary Science Letters 317–318:111–119. doi: 10.1016/j.epsl.2011.11.022

Oganov AR, Brodholt JP, Price GD (2001) Ab initio elasticity and thermal equation of state of MgSiO3 perovskite. Earth and Planetary Science Letters 184:555–560. doi: 10.1016/S0012-821X(00)00363-0

Ono S (2008) Experimental constraints on the temperature profile in the lower mantle. Physics of the Earth and Planetary Interiors 170:267–273. doi: 10.1016/j.pepi.2008.06.033

O'Reilly SY, Griffin WL (2000) Apatite in the mantle: implications for metasomatic processes and high heat production in Phanerozoic mantle. Lithos 53:217–232. doi: 10.1016/S0024-4937(00)00026-8

O'Reilly, SY, Griffin WL (2013) Mantle metasomatism. In Metasomatism and the chemical transformation of rock: The role of fluids in terrestrial and extraterrestrial processes, ed. D. E. Harlov and H. Austrheim, 471-533. Berlin, Germany: Springer.

Otero-de-la-Roza A, Luaña V (2011) Treatment of first-principles data for predictive quasiharmonic thermodynamics of solids: The case of MgO. Phys Rev B 84:024109. doi: 10.1103/PhysRevB.84.024109

Otsuka K, McCammon CA, Karato S (2010) Tetrahedral occupancy of ferric iron in (Mg,Fe)O: Implications for point defects in the Earth's lower mantle. Physics of the Earth and Planetary Interiors 180:179–188. doi: 10.1016/j.pepi.2009.10.005

Pan Y, Fleet ME (2002) Compositions of the Apatite-Group Minerals: Substitution Mechanisms and Controlling Factors. Reviews in Mineralogy and Geochemistry 48:13–49. doi: 10.2138/rmg.2002.48.2

Parfitt DC, Bishop CL, Wenman MR, Grimes RW (2010) Strain fields and line energies of dislocations in uranium dioxide. J Phys: Condens Matter 22:175004. doi: 10.1088/0953-8984/22/17/175004

Pearson DG, Brenker FE, Nestola F, et al. (2014) Hydrous mantle transition zone indicated by ringwoodite included within diamond. Nature 507:221–224. doi: 10.1038/nature13080

Peierls R (1940) The size of a dislocation. Proc Phys Soc 52:34. doi: 10.1088/0959-5309/52/1/305

Perdew JP, Burke K, Ernzerhof M (1996) Generalized Gradient Approximation Made Simple. Phys Rev Lett 77:3865–3868. doi: 10.1103/PhysRevLett.77.3865

Perdew JP, Ruzsinszky A, Csonka GI, et al. (2008) Restoring the Density-Gradient Expansion for Exchange in Solids and Surfaces. Phys Rev Lett 100:136406. doi: 10.1103/PhysRevLett.100.136406

Peterman EM, Reddy SM, Saxey DW, et al. (2016) Nanogeochronology of discordant zircon measured by atom probe microscopy of Pb-enriched dislocation loops. Science Advances 2:e1601318. doi: 10.1126/sciadv.1601318

Peslier AH, Woodland AB, Bell DR, Lazarov M (2010) Olivine water contents in the continental lithosphere and the longevity of cratons. Nature 467:78–81. doi: 10.1038/nature09317

Pfrommer BG, Côté M, Louie SG, Cohen ML (1997) Relaxation of Crystals with the Quasi-Newton Method. Journal of Computational Physics 131:233–240. doi: 10.1006/jcph.1996.5612

Piazolo S, Fontaine AL, Trimby P, et al. (2016) Deformation-induced trace element redistribution in zircon revealed using atom probe tomography. Nature Communications 7:10490. doi: 10.1038/ncomms10490

Plimpton S (1995) Fast Parallel Algorithms for Short-Range Molecular Dynamics. Journal of Computational Physics 117:1–19. doi: 10.1006/jcph.1995.1039

Price GD, Parker SC, Leslie M (1987) The lattice dynamics and thermodynamics of the Mg2SiO4 polymorphs. Phys Chem Minerals 15:181–190. doi: 10.1007/BF00308782

Proietti A, Bystricky M, Guignard J, et al. (2016) Effect of pressure on the strength of olivine at room temperature. Physics of the Earth and Planetary Interiors 259:34–44. doi: 10.1016/j.pepi.2016.08.004

Puls MP (1980) Vacancy-dislocation interaction energies in MgO. Philosophical Magazine A 41:353–368. doi: 10.1080/01418618008239317

Puls MP (1983) Vacancy-dislocation interaction energies in MgO A re-analysis. Philosophical Magazine A 47:497–513. doi: 10.1080/01418618308245242

Puls MP, Norgett MJ (1976) Atomistic calculation of the core structure and Peierls energy of an (a/2)[110] edge dislocation in MgO. Journal of Applied Physics. 47(2):466-77. doi: 10.1063/1.322670

Qi Y-Y, Cheng Y, Liu M, et al. (2013) Phase transition and thermodynamic properties of CaF2 via first principles. Physica B: Condensed Matter 426:13–19. doi: 10.1016/j.physb.2013.05.033

Ranganathan SI, Ostoja-Starzewski M (2008) Universal Elastic Anisotropy Index. Phys Rev Lett 101:055504. doi: 10.1103/PhysRevLett.101.055504

Rao SI, Varvenne C, Woodward C, et al. (2017) Atomistic simulations of dislocations in a model BCC multicomponent concentrated solid solution alloy. Acta Materialia 125:311–320. doi: 10.1016/j.actamat.2016.12.011

Raterron P, Chen J, Geenen T, Girard J (2011) Pressure effect on forsterite dislocation slip systems: Implications for upper-mantle LPO and low viscosity zone. Physics of the Earth and Planetary Interiors 188:26–36. doi: 10.1016/j.pepi.2011.06.009

Raterron P, Chen J, Li L, et al. (2016) Pressure-induced slip-system transition in forsterite: Single-crystal rheological properties at mantle pressure and temperature. American Mineralogist 92:1436–1445. doi: 10.2138/am.2007.2474

Reddy SM, Timms NE, Pantleon W, Trimby P (2007) Quantitative characterization of plastic deformation of zircon and geological implications. Contrib Mineral Petrol 153:625–645. doi: 10.1007/s00410-006-0174-4

Ringwood T (1975) Composition and Petrology of the Earth's Mantle. McGraw-Hill.,USA

Robinson K, Gibbs GV, Ribbe PH (1971) Quadratic Elongation: A Quantitative Measure of Distortion in Coordination Polyhedra. Science 172:567–570. doi: 10.1126/science.172.3983.567

Ropo M, Kokko K, Vitos L (2008) Assessing the Perdew-Burke-Ernzerhof exchange-correlation density functional revised for metallic bulk and surface systems. Phys Rev B 77:195445. doi: 10.1103/PhysRevB.77.195445

Rulis P, Ouyang L, Ching WY (2004) Electronic structure and bonding in calcium apatite crystals: Hydroxyapatite, fluorapatite, chlorapatite, and bromapatite. Phys Rev B 70:155104. doi: 10.1103/PhysRevB.70.155104

Sakaguchi I, Yurimoto H, Sueno S (1992) Self-diffusion along dislocations in single-crystals MgO. Solid State Communications 84:889–893. doi: 10.1016/0038-1098(92)90453-G

Sanchez JM, Ducastelle F, Gratias D (1984) Generalized cluster description of multicomponent systems. Physica A: Statistical Mechanics and its Applications 128:334–350. doi: 10.1016/0378-4371(84)90096-7

Sanders MJ, Leslie M, Catlow CRA (1984) Interatomic potentials for SiO2. J Chem Soc, Chem Commun 1271–1273. doi: 10.1039/C39840001271

Schröder K-P, Sauer J, Leslie M, et al. (1992) Bridging hydrodyl groups in zeolitic catalysts: a computer simulation of their structure, vibrational properties and acidity in protonated faujasites (H□Y zeolites). Chemical Physics Letters 188:320–325. doi: 10.1016/0009-2614(92)90030-Q

Seltzer MS, Clauer AH, Wilcox BA (1972) The influence of stoichiometry on compression creep of uranium dioxide single crystals. Journal of Nuclear Materials 44:43–56. doi: 10.1016/0022-3115(72)90127-4

Sempolinski DR, Kingery WD (1980) Ionic Conductivity and Magnesium Vacancy Mobility in Magnesium Oxide. Journal of the American Ceramic Society 63:664–669. doi: 10.1111/j.1151-2916.1980.tb09857.x

Shanno DF (1970) Conditioning of quasi-Newton methods for function minimization. Math Comp 24:647–656. doi: 10.1090/S0025-5718-1970-0274029-X

Shannon RD (1976) Revised effective ionic radii and systematic studies of interatomic distances in halides and chalcogenides. Acta Crystallographica Section A 32:751–767. doi: 10.1107/S0567739476001551

Shen P, Feng H, Wu X, et al. (2015) The Core Structure and Peierls Stress of 〈 11 2 ¯ 0 〉 Dislocations in MgB2 with Mg and B Vacancies. J Supercond Nov Magn 28:1743–1748. doi: 10.1007/s10948-015-3001-1

Shim S-H, Jeanloz R, Duffy TS (2002) Tetragonal structure of CaSiO3 perovskite above 20 GPa. Geophys Res Lett 29:2166. doi: 10.1029/2002GL016148

Singh RN, Coble RL (1974a) Dynamic dislocation behavior in ``pure'' magnesium oxide single crystals. Journal of Applied Physics 45:981–989 . doi:10.1063/1.1663445

Singh RN, Coble RL (1974b) Dynamic dislocation behavior in iron-doped magnesium oxide crystals. Journal of Applied Physics 45:990–995 . doi: 10.1063/1.1663446

Sinogeikin SV, Bass JD (1999) Single-crystal elasticity of MgO at high pressure. Phys Rev B 59:R14141–R14144. doi: 10.1103/PhysRevB.59.R14141

Skelton R, Walker AM (2017a) Peierls-Nabarro modeling of dislocations in UO2. Journal of Nuclear Materials 495:202–210. doi: 10.1016/j.jnucmat.2017.08.024

Skelton R, Walker AM (2017b) Ab initio crystal structure and elasticity of tuite, γ-Ca3(PO4)2, with implications for trace element partitioning in the lower mantle. Contrib Mineral Petrol 172:87. doi: 10.1007/s00410-017-1406-5

Skelton R, Walker AM (2018) Lubrication of dislocation glide in MgO by hydrous defects. Phys Chem Minerals 1–14. doi: 10.1007/s00269-018-0957-y

Smith GP, Wiens DA, Fischer KM, et al. (2001) A Complex Pattern of Mantle Flow in the Lau Backarc. Science 292:713–716. doi: 10.1126/science.1058763

Smyth JR, Holl CM, Frost DJ, Jacobsen SD (2004) High pressure crystal chemistry of hydrous ringwoodite and water in the Earth's interior. Physics of the Earth and Planetary Interiors 143–144:271–278. doi: 10.1016/j.pepi.2003.08.011

Smyth JR, Frost DJ, Nestola F, et al. (2006) Olivine hydration in the deep upper mantle: Effects of temperature and silica activity. Geophys Res Lett 33:L15301. doi: 10.1029/2006GL026194

Sommer H, Regenauer-Lieb K, Gasharova B, Siret D (2008) Grain boundaries: a possible water reservoir in the Earth's mantle? Miner Petrol 94:1–8. doi: 10.1007/s00710-008-0002-9

Song W, Li CH, Park SC (2009) Genetic algorithm for text clustering using ontology and evaluating the validity of various semantic similarity measures. Expert Systems with Applications 36:9095–9104. doi: 10.1016/j.eswa.2008.12.046

Stackhouse S, Brodholt JP, Wookey J, et al. (2005) The effect of temperature on the seismic anisotropy of the perovskite and post-perovskite polymorphs of MgSiO3. Earth and Planetary Science Letters 230:1–10. doi: 10.1016/j.epsl.2004.11.021

Stocker RL (1978) Influence of oxygen pressure on defect concentrations in olivine with a fixed cationic ratio. Physics of the Earth and Planetary Interiors 17:118–129. doi: 10.1016/0031-9201(78)90053-5

Stocker RL, Ashby MF (1973) On the rheology of the upper mantle. Rev Geophys 11:391–426. doi: 10.1029/RG011i002p00391

Stocker RL, Smyth DM (1978) Effect of enstatite activity and oxygen partial pressure on the point-defect chemistry of olivine. Physics of the Earth and Planetary Interiors 16:145–156. doi: 10.1016/0031-9201(78)90085-7

Stokes HT, Hatch DM (2005) FINDSYM: program for identifying the space-group symmetry of a crystal. J Appl Cryst 38:237–238. doi: 10.1107/S0021889804031528

Stroh AN (1958) Dislocations and Cracks in Anisotropic Elasticity. Philosophical Magazine 3:625–646. doi: 10.1080/14786435808565804

Sudarsanan K, Young RA (1972) Structure of strontium hydroxide phosphate, Sr5(PO4)3OH. Acta Cryst B Struct Crystallogr Cryst Chem 28:3668–3670. doi: 10.1107/S0567740872008544

Sudarsanan K, Young RA (1980) Structure of partially substituted chlorapatite (Ca2Sr)5(PO4)3Cl. Acta Cryst B Struct Crystallogr Cryst Chem 36:1525–1530. doi: 10.1107/S0567740880006516

Sugiyama K, Tokonami M (1987) Structure and crystal chemistry of a dense polymorph of tricalcium phosphate Ca3 (PO4)2: A host to accommodate large lithophile elements in the earth's mantle. Phys Chem Minerals 15:125–130. doi: 10.1007/BF00308774

Sun T, Zhang D-B, Wentzcovitch RM (2014) Dynamic stabilization of cubic CaSiO3 perovskite at high temperatures and pressures from *ab initio* molecular dynamics. Phys Rev B 89:094109. doi: 10.1103/PhysRevB.89.094109

Suzuki K (1987) Grain-boundary enrichment of incompatible elements in some mantle peridotites. Chemical Geology 63:319–334. doi: 10.1016/0009-2541(87)90169-0

Taketomi S, Matsumoto R, Miyazaki N (2008) Atomistic simulation of the effects of hydrogen on the mobility of edge dislocation in alpha iron. J Mater Sci 43:1166–1169. doi: 10.1007/s10853-007-2364-5

Tarrat N, Benoit M, Caillard D, et al. (2014) Screw dislocation in hcp Ti : DFT dislocation excess energies and metastable core structures. Modelling Simul Mater Sci Eng 22:055016. doi: 10.1088/0965-0393/22/5/055016

Taylor GI FRS (1934) The mechanism of plastic deformation of crystals. Part I.—Theoretical. Proc R Soc Lond A 145:362–387. doi: 10.1098/rspa.1934.0106

Thorn RJ, Winslow GH (1966) Nonstoichiometry in Uranium Dioxide. The Journal of Chemical Physics 44:2632–2643. doi: 10.1063/1.1727104

Thompson RM, Xie X, Zhai S, et al. (2013) A comparison of the Ca3(PO4)2 and CaSiO3 systems, with a new structure refinement of tuite synthesized at 15 GPa and 1300 °C. American Mineralogist 98:1585–1592. doi: 10.2138/am.2013.4435

Tielke JA, Zimmerman ME, Kohlstedt DL (2016) Direct shear of olivine single crystals. Earth and Planetary Science Letters 455:140–148. doi: 10.1016/j.epsl.2016.09.002

Tielke JA, Zimmerman ME, Kohlstedt DL (2017) Hydrolytic weakening in olivine single crystals. J Geophys Res Solid Earth 122:2017JB014004. doi: 10.1002/2017JB014004

Trombe JC, Montel G (1978) Some features of the incorporation of oxygen in different oxidation states in the apatitic lattice—I On the existence of calcium and strontium oxyapatites. Journal of Inorganic and Nuclear Chemistry 40:15–21. doi: 10.1016/0022-1902(78)80298-X

Tsuru T, Udagawa Y, Yamaguchi M, et al. (2013) Solution softening in magnesium alloys: the effect of solid solutions on the dislocation core structure and nonbasal slip. J Phys: Condens Matter 25:022202. doi: 10.1088/0953-8984/25/2/022202

Udagawa Y, Yamaguchi M, Tsuru T, et al. (2011) Effect of Sn and Nb on generalized stacking fault energy surfaces in zirconium and gamma hydride habit planes. Philosophical Magazine 91:1665–1678. doi: 10.1080/14786435.2010.543651

Ulian G, Tosoni S, Valdrè G (2013a) Comparison between Gaussian-type orbitals and plane wave ab initio density functional theory modeling of layer silicates: Talc [Mg3Si4O10(OH)2] as model system. The Journal of Chemical Physics 139:204101. doi: 10.1063/1.4830405

Ulian G, Valdrè G, Corno M, Ugliengo P (2013b) Periodic ab initio bulk investigation of hydroxylapatite and type A carbonated apatite with both pseudopotential and all-electron basis sets for calcium atoms. American Mineralogist 98:410–416. doi: 10.2138/am.2013.4171

Ulian G, Tosoni S, Valdrè G (2014) The compressional behaviour and the mechanical properties of talc [Mg3Si4O10(OH)2]: a density functional theory investigation. Phys Chem Minerals 41:639–650. doi: 10.1007/s00269-014-0677-x

Vanderbilt D (1990) Soft self-consistent pseudopotentials in a generalized eigenvalue formalism. Phys Rev B 41:7892–7895. doi: 10.1103/PhysRevB.41.7892

Vanderbilt D (1998) First-principles theory of structural phase transitions in cubic perovskites. Journal of the Korean Physical Society 32:S103–S106

Van Orman JA, Fei Y, Hauri EH, Wang J (2003) Diffusion in MgO at high pressures: Constraints on deformation mechanisms and chemical transport at the core-mantle boundary. Geophys Res Lett 30:1056. doi: 10.1029/2002GL016343

Van Orman JA, Li C, Crispin KL (2009) Aluminum diffusion and Al-vacancy association in periclase. Physics of the Earth and Planetary Interiors 172:34–42. doi: 10.1016/j.pepi.2008.03.008

van Westrenen W, Allan NL, Blundy JD, et al. (2000) Atomistic simulation of trace element incorporation into garnets—comparison with experimental garnet-melt partitioning data. Geochimica et Cosmochimica Acta 64:1629–1639. doi: 10.1016/S0016-7037(00)00336-7

Ventelon L, Lüthi B, Clouet E, et al. (2015) Dislocation core reconstruction induced by carbon segregation in bcc iron. Phys Rev B 91:220102. doi: 10.1103/PhysRevB.91.220102

Vinet P, Ferrante J, Smith JR, Rose JH (1986) A universal equation of state for solids. J Phys C: Solid State Phys 19:L467. doi: 10.1088/0022-3719/19/20/001

Volterra (1907). Sur l'équilibre des corps élastiques multiplement connexes. In *Annales scientifiques de l'École normale supérieure* 24:401-517.

Walker AM (2012) The effect of pressure on the elastic properties and seismic anisotropy of diopside and jadeite from atomic scale simulation. Physics of the Earth and Planetary Interiors 192–193:81–89. doi: 10.1016/j.pepi.2011.10.002

Walker AM, Slater B, Gale JD, Wright K (2004) Predicting the structure of screw dislocations in nanoporous materials. Nat Mater 3:715–720. doi: 10.1038/nmat1213

Walker AM, Gale JD, Slater B, Wright K (2005a) Atomic scale modelling of the cores of dislocations in complex materials part 1: methodology. Phys Chem Chem Phys 7:3227–3234. doi: 10.1039/B505612H

Walker AM, Gale JD, Slater B, Wright K (2005b) Atomic scale modelling of the cores of dislocations in complex materials part 2: applications. Phys Chem Chem Phys 7:3235–3242. doi: 10.1039/B505716G

Walker AM, Demouchy S, Wright K (2006) Computer modelling of the energies and vibrational properties of hydroxyl groups in α- and β-Mg2SiO4. European Journal of Mineralogy 18:529–543. doi: 10.1127/0935-1221/2006/0018-0529

Walker AM, Hermann J, Berry AJ, O'Neill HSC (2007) Three water sites in upper mantle olivine and the role of titanium in the water weakening mechanism. J Geophys Res 112:B05211. doi: 10.1029/2006JB004620

Walker AM, Tyer RP, Bruin RP, Dove MT (2008) The compressibility and high pressure structure of diopside from first principles simulation. Phys Chem Minerals 35:359–366. doi: 10.1007/s00269-008-0229-3

Walker AM, Woodley SM, Slater B, Wright K (2009) A computational study of magnesium point defects and diffusion in forsterite. Physics of the Earth and Planetary Interiors 172:20–27. doi: 10.1016/j.pepi.2008.04.001

Wang D, Mookherjee M, Xu Y, Karato S (2006a) The effect of water on the electrical conductivity of olivine. Nature 443:977–980. doi: 10.1038/nature05256

Wang J, Sinogeikin SV, Inoue T, Bass JD (2006b) Elastic properties of hydrous ringwoodite at high-pressure conditions. Geophys Res Lett 33:L14308. doi: 10.1029/2006GL026441

Watson GW, Kelsey ET, Parker SC (1999) Atomistic simulation of screw dislocations in rock salt structured materials. Philosophical Magazine A 79:527–536. doi: 10.1080/01418619908210314

Watson EB, Capobianco CJ (1981) Phosphorus and the rare earth elements in felsic magmas: an assessment of the role of apatite. Geochimica et Cosmochimica Acta 45:2349–2358. doi: 10.1016/0016-7037(81)90088-0

Webb SL, Jackson I (1990) Polyhedral rationalization of variation among the single-crystal elastic moduli for the upper-mantle silicates garnet, olivine, and orthopyroxene. American Mineralogist 75:731–738

Wentzcovitch RM, Ross NL, Price GD (1995) Ab initio study of MgSiO3 and CaSiO3 perovskites at lower-mantle pressures. Physics of the Earth and Planetary Interiors 90:101–112. doi: 10.1016/0031-9201(94)03001-Y

Willis BTM (1964) Structures of UO2, UO2+x andU4O9 by neutron diffraction. J Phys France 25:431–439. doi: 10.1051/jphys:01964002505043100

Willis BTM (1978) The defect structure of hyper-stoichiometric uranium dioxide. Acta Cryst A: Cryst Phys Diffr Theor Gen Crystallogr 34:88–90. doi: 10.1107/S0567739478000157

Wolf D, Keblinski P, Phillpot SR, Eggebrecht J (1999) Exact method for the simulation of Coulombic systems by spherically truncated, pairwise r−1 summation. The Journal of Chemical Physics 110:8254–8282. doi: 10.1063/1.478738

Wood BJ (2000) Phase transformations and partitioning relations in peridotite under lower mantle conditions. Earth and Planetary Science Letters 174:341–354. doi: 10.1016/S0012-821X(99)00273-3

Wood BJ, Blundy JD (1997) A predictive model for rare earth element partitioning between clinopyroxene and anhydrous silicate melt. Contrib Mineral Petrol 129:166–181. doi: 10.1007/s004100050330

Wright K, Catlow CRA (1994) A computer simulation study of (OH) defects in olivine. Phys Chem Minerals 20:515–518. doi: 10.1007/BF00203222

Xie X, Minitti ME, Chen M, et al. (2003) Tuite, γ-Ca3(PO4)2: a new mineral from the Suizhou L6 chondrite. European Journal of Mineralogy 15:1001–1005. doi: 10.1127/0935-1221/2003/0015-1001

Xie X, Gu X, Chen M (2016) An occurrence of tuite, γ-Ca3(PO4)2, partly transformed from Ca-phosphates in the Suizhou meteorite. Meteorit Planet Sci 51:195–202. doi: 10.1111/maps.12577

Xie M-Y, Tasnádi F, Abrikosov IA, et al. (2012) Elastic constants, composition, and piezolectric polarization in InxAl1−xN: From ab initio calculations to experimental implications for the applicability of Vegard's rule. Phys Rev B 86:155310. doi: 10.1103/PhysRevB.86.155310

Yakub E, Ronchi C, Staicu D (2009) Computer simulation of defects formation and equilibrium in non-stoichiometric uranium dioxide. Journal of Nuclear Materials 389:119–126. doi: 10.1016/j.jnucmat.2009.01.029

Yakub E, Ronchi C, Staicu D (2010) Diffusion of helium in non-stoichiometric uranium dioxide. Journal of Nuclear Materials 400:189–195. doi: 10.1016/j.jnucmat.2010.03.002

Yamazaki D, Karato S (2002) Fabric development in (Mg,Fe)O during large strain, shear deformation: implications for seismic anisotropy in Earth's lower mantle. Physics of the Earth and Planetary Interiors 131:251–267. doi: 10.1016/S0031-9201(02)00037-7

Yund RA, Smith BM, Tullis J (1981) Dislocation-assisted diffusion of oxygen in albite. Phys Chem Minerals 7:185–189. doi: 10.1007/BF00307264

Yust CS, McHargue CJ (1971) Deformation of Hyperstoichiometric UO2 Single Crystals. Journal of the American Ceramic Society 54:628–635. doi: 10.1111/j.1151-2916.1971.tb16019.x

Zhai S, Xue W, Yamazaki D, et al. (2011) Compressibility of strontium orthophosphate Sr3(PO4)2 at high pressure. Phys Chem Minerals 38:357–361. doi: 10.1007/s00269-010-0409-9

Zhai S, Liu X, Shieh SR, et al. (2009) Equation of state of γ-tricalcium phosphate, γ-Ca3(PO4)2, to lower mantle pressures. American Mineralogist 94:1388–1391. doi: 10.2138/am.2009.3160

Zhai S, Yamazaki D, Xue W, et al. (2013) P-V-T relations of γ-Ca3(PO4)2 tuite determined by in situ X-ray diffraction in a large-volume high-pressure apparatus. American Mineralogist 98:1811–1816. doi: 10.2138/am.2013.4403

Zhai S, Xue W, Yamazaki D, Ma F (2014) Trace element composition in tuite decomposed from natural apatite in high-pressure and high-temperature experiments. Sci China Earth Sci 57:2922–2927. doi: 10.1007/s11430-014-4980-7

Zhang F, Walker AM, Wright K, Gale JD (2010) Defects and dislocations in MgO: atomic scale models of impurity segregation and fast pipe diffusion. J Mater Chem 20:10445–10451. doi: 10.1039/C0JM01550D

Zhang F, Gale JD, Uberuaga BP, et al. (2013) Importance of dispersion in density functional calculations of cesium chloride and its related halides. Phys Rev B 88:054112. doi: 10.1103/PhysRevB.88.054112

Zhou L, Holec D, Mayrhofer PH (2013) First-principles study of elastic properties of cubic Cr1−xAlxN alloys. Journal of Applied Physics 113:43511. doi: 10.1063/1.4789378

Zunger A, Wei S-H, Ferreira LG, Bernard JE (1990) Special quasirandom structures. Phys Rev Lett 65:353–356. doi: 10.1103/PhysRevLett.65.353